

1N-23

NASA Conference Publication 10193

1941

074451

# Physics & Process Modeling (PPM) and Other Propulsion R&T

**Volume II: Applied Life Models, Design,  
Vibration Control, Mechanical  
Components, Tribology**

*Proceedings of the PPM and Other Propulsion R&T Conference  
held at the Cleveland Airport Marriott  
sponsored by NASA Lewis Research Center  
Cleveland, Ohio  
May 1, 1997*



# **Physics & Process Modeling (PPM) and Other Propulsion R&T**

## **Volume II: Applied Life Models, Design, Vibration Control, Mechanical Components, Tribology**

*Proceedings of the PPM and Other Propulsion R&T Conference  
held at the Cleveland Airport Marriott  
sponsored by NASA Lewis Research Center  
Cleveland, Ohio  
May 1, 1997*



National Aeronautics and  
Space Administration

Office of Management

**Scientific and Technical  
Information Program**

1997



Trade names or manufacturers' names are used in this report for identification only. This usage does not constitute an official endorsement, either expressed or implied, by the National Aeronautics and Space Administration.

## FOREWORD

The Propulsion Systems Program is one of six Propulsion Systems Research and Technology Base Programs within the NASA Aeronautics Enterprise. This program, which consists of a number of projects that are structured to address the critical technology needs of a range of vehicle classes, focuses on the goals of safety, environment, capacity, efficiency, affordability, performance, and survivability.

The Propulsion Systems Program relies on a number of critical technical competencies to perform research and develop technologies. Among these competencies are propulsion materials and structures. On May 1, 1997, individuals involved in materials and structures research under several of the Propulsion Systems Program projects met at the Cleveland Airport Marriott, in Cleveland, Ohio, to discuss their progress at the PPM and Other Propulsion R&T Conference. Representatives of government, industry, and universities heard presentations on material processing, material characterization, modeling, lifing, applied life models, design, vibration control, mechanical components, and tribology. This publication contains figures and supporting text from those presentations.

The majority of the research discussed was performed under the Physics & Process Modeling (PPM) project, which is focused on using physics-based models and process modeling techniques to reduce time, cost, and risk barriers to revolutionizing turbine engines and power systems. Other Propulsion Systems Program projects represented in the conference were Smart, Green Engine (SGE); Fast, Quiet Engine (FQE); High Temperature Engine Materials Program (HITEMP); and Hybrid Hyperspeed Propulsion (HHP). Also represented were the Rotorcraft Systems Program and the NASA Lewis Director's Discretionary Fund.

This conference was held in conjunction with three other conferences at the NASA Lewis Materials and Structures Technology Symposium. The other conferences addressed Advanced Subsonic Technology, Enabling Propulsion Materials, and the High Temperature Engine Materials and Structures Project.

Conference Chairs:

Douglas A. Rohn  
L. James Kiraly

## PROGRAMS AND PROJECTS

Papers contained herein support the goals of the following projects:

Program or Project	Paper Numbers
Propulsion Systems Program	
Physics and Process Modeling (PPM) project	3, 4, 8, 10, 11, 12, 15, 16, 17, 19, 20, 24, 25, 26, 27, 30, 31, 32, 33, 34, 35, 36
Smart Green Engine (SGE) project	28, 29
Fast, Quiet Engine (FQE) project	1, 6
High Temperature Engine Materials Program (HITEMP)	14, 18
Hybrid Hyperspeed Propulsion (HHP) project	2, 7, 9, 13
Rotorcraft Systems Program	22, 23, 37
Lewis Director's Discretionary Fund	5

## CONTENTS OF VOLUME II

### APPLIED LIFE MODELS

	Paper
An Extreme Value Theory Applicable to a Wide Variety of Random Processes Frederic A. Holland, Jr., NASA LeRC .....	20 - 1
Paper Withdrawn .....	21 - 6
Gear Crack Propagation Life Studies David G. Lewicki, U.S. Army Research Laboratory; and Roberto Ballarini, Case Western Reserve University .....	22 - 2
Surface Fatigue Evaluation of Gear Materials and Lubricants Dennis P. Townsend, NASA LeRC .....	23 - 3

### DESIGN

Computational Infrastructure for Engine Structural Performance Simulation Christos C. Chamis, NASA LeRC .....	24 - 4
Efficient Evaluation and Optimization of Structural Reliability Using Adaptive Approximations Ramana V. Grandhi, Wright State University; and Dale A. Hopkins, NASA LeRC .....	25 - 5
Optimization of Air-Breathing Propulsion Engine Concepts Surya N. Patnaik, Ohio Aerospace Institute; and Dale A. Hopkins, NASA LeRC .....	26 - 6
Technology Needs for Reduced Design and Manufacturing Cost of Commercial Transport Engines Douglas A. Rohn, NASA LeRC .....	27 - 7

### VIBRATION CONTROL

Damping Experiment of Spinning Composite Plates With Embedded Viscoelastic Material Oral Mehmed, NASA LeRC; and John B. Kosmatka, University of California, San Diego .....	28 - 8
Magnetic Excitation for Spin Vibration Testing Dexter Johnson, Oral Mehmed, and Gerald V. Brown, NASA LeRC .....	29 - 9
A New 1000 °F Magnetic Bearing Test Rig Albert F. Kascak, U.S. Army Research Laboratory; Gerald V. Brown, NASA LeRC; and Alan Palazzolo, Texas A&M .....	30 - 10

Neural Network Control of a Magnetically Suspended Rotor System Benjamin Choi, Gerald V. Brown, and Dexter Johnson, NASA LeRC .....	31	-11
--	----	-----

## **LUBRICATION**

Diamond Film Lubricants for Ceramics Kazuhisa Miyoshi, NASA LeRC .....	32	-12
---	----	-----

A High Temperature Vapor Phase Lubrication Study Utilizing a Thioether Liquid Lubricant Wilfred Morales, NASA LeRC; and E. Earl Graham and Thomas Galvin, Cleveland State University .....	33	-13
---	----	-----

## **MECHANICAL COMPONENTS & TRIBOLOGY**

The Role of Tribology in the Development of an Oil-Free Turbocharger Christopher DellaCorte, NASA LeRC .....	34	-14
---	----	-----

Tuft Testing for Advanced Oil-Free Turbomachinery Brush Seals James A. Fellenstein, Ohio Aerospace Institute .....	35	-15
---	----	-----

Rotordynamic Design Analysis of an Oil-Free Turbocharger Samuel A. Howard, Case Western Reserve University .....	36	-16
---	----	-----

Recent Advances in the Analysis of Spiral Bevel Gears Robert F. Handschuh, U.S. Army Research Laboratory .....	37	-17
---	----	-----

A NEW APPROACH TO EXTREME VALUE ESTIMATION  
APPLICABLE TO A WIDE VARIETY OF RANDOM VARIABLES

FREDERIC A. HOLLAND, JR.  
NASA Lewis Research Center  
Cleveland, Ohio

51-39  
029100  
10P.  
278114

Introduction

Designing reliable structures requires an estimate of the maximum and minimum values (i.e., strength and load) that may be encountered in service. Yet designs based on very extreme values (to insure safety) can result in extra material usage and hence, uneconomic systems. In aerospace applications, severe over-design cannot be tolerated making it almost mandatory to design closer to the assumed limits of the design random variables. The issue then is predicting extreme values that are practical, i.e. neither too conservative or non-conservative.

Obtaining design values by employing safety factors is well known to often result in overly conservative designs (refs. 1 and 2). Safety factor values have historically been selected rather arbitrarily, often lacking a sound rational basis. To answer the question of how safe a design needs to be has lead design theorists to probabilistic and statistical methods. The so-called three-sigma approach is one such method and has been described as the first step in utilizing information about the data dispersion (ref. 3). However, this method is based on the assumption that the random variable is dispersed symmetrically about the mean and is essentially limited to normally distributed random variables. Use of this method can therefore result in unsafe or overly conservative design allowables if the common assumption of normality is incorrect.

Perhaps the most widely used probabilistic approach in engineering is the Weibull distribution function (ref. 4). This function has been hailed for its ability to model a wide spectrum of distributions by merely changing the value of its shape parameter. However, the three-parameter form of the function has been shown to predict extremely conservative minimum values for random variables that are significantly skewed left. Often in such cases this function gives minimum values that are physically impossible (i.e., tensile strengths  $< 0$ ), calling for the use of the two-parameter formulation which inherently assumes a minimum value of zero. The user is then required to accept a specified risk of nonperformance in order to obtain a practical design value. The magnitude of this risk is subjective and again leads back to the question of how safe a design needs to be.

In view of the aforementioned and the objectives listed in Fig. 1, a new method is proposed for estimating the *practical* extreme values of random variables. This method is proposed as an alternative approach to establishing design values and is not intended as a determiner of *absolute* extremes. This method was designed to be simple, utilizing common statistical parameters (Fig. 2). The approach considers the major factors

believed to affect the maximum expected deviation from the mean or expected value—central tendency, dispersion, and skewness. These properties can be measured by the mean, standard deviation and the mode (most frequently occurring value). The method is based on the assumption that the minimum values of random variables have increased deviation from the mean as the frequency distribution becomes more skewed left while the deviation of the maximum value from the mean decreases (Fig. 3). The reverse is true as the distribution becomes more skewed right or positively skewed. The proposed generalized equation describing this behavior is given in Fig. 4.

The parameters of the generalized equation, given in Fig. 5, are based on theoretical and experimental results. These parameters make the proposed function compatible with the theoretical minimum values of the exponential distribution and the assumed practical limits of the normal distribution. The assumption therefore is that distributions of zero skew are normal and distributions having a skew of one are exponential. The function approximates the relationship between the standardized minimum values and the skewnesses of positively skewed theoretical probability distributions in the Weibull family (Fig. 6).

The proposed function should be interpreted as the assumed lower limit of the value of the random variable with respect to skew. This assumption was substantiated by plotting the standardized minimum experimental fracture strengths of 165 metal alloys against the skew of the distributions from which they came. As theorized, the function appeared to provide a close lower bound with the data.

The function works very well in theory as illustrated in Fig. 6. However, the challenge in applying the theory to real data is in obtaining the estimate of the population mode. The mode is not a directly calculable parameter as are the mean and standard deviation. In many cases a good estimate of the population mode may be unavailable, especially with smaller sample sizes. This can often be resolved by using the empirical relationship between the mean, mode and median (Fig. 8) allowing the function to be written in terms of the median value instead of the mode. The median is easily obtainable from a set of observations as it is the value at which half of the observations are smaller in magnitude and half are greater. This is a convenient approach which can give reasonable results compared with other methods of estimating the mode (Fig. 9). However, this equation is primarily limited to moderately skewed distribution and the error in using this relationship tends to increase as the skew of the distribution increases. Another alternative is to estimate the population mode from Weibull analysis. It is assumed that this method offers the most consistently reliable estimates of the population modes, especially for small sample sizes.

The use of the function for estimating minimum strength values for design are demonstrated in Figs. 10-12 in comparison with the three-parameter Weibull minimum value, the three-sigma approach, and use of a 1.2 safety factor on the mean. Predictions using the proposed function were done using the Weibull mode for reasons cited above and to have comparisons with three-parameter Weibull predictions on the same mode

basis. In Fig. 10 it is seen that several observations of fracture occurred at values *below* that allowed by the three-sigma approach. In this case this method has proven to be non-conservative (as expected since the distribution is not normal and skewed left). A three-parameter Weibull analysis was inappropriate in this case as it resulted in a minimum tensile strength below zero. In contrast the proposed method appeared to give a reasonable estimate of the minimum expected fracture strength. The safety factor approach (1.2) was more conservative.

Whereas a safety factor of 1.2 was conservative for the previously examined metals, this value was demonstrated to be insufficient for establishing a safe design strength for the ceramic shown in Fig. 11. However, the proposed method predicted a relatively safe minimum expected strength in comparison with the experimental observations. This demonstrates the proposed function's accounting of the nature of the random variable distribution. The three-parameter Weibull minimum value was significantly more conservative in this case.

The fracture strength distribution of the material shown in Fig. 12 suggests a definitive threshold strength. This behavior is captured by the proposed method and the three-parameter Weibull method, the predicted minimum values of which are nearly identical. The safety factor and the three-sigma approaches appear to give values that are very conservative.

An estimation of maximum expected rainfall from storm data in Fig. 13 demonstrates application to maxima. The proposed method predicts a practical maximum value not very far above the maximum observed value. Note that the mode of the two-parameter Weibull fit of the data was undefined. Therefore it was necessary (and reasonable in this case) to use the mode determined from the histogram in the proposed equation.

The proposed method offers a simple approach to reasonably estimate the practical extremes of random variables suitable for many engineering purposes (Figs. 15 and 16). As a general rule the proposed function is assumed applicable to random variables that can reasonably be approximated by the Weibull distribution function.

## References

1. Haugen, E. B., 1968, Probabilistic Approaches to Design, John Wiley & Sons, Inc., New York, NY.
2. Ullman, David, "Less Fudging on Fudge Factors," Machine Design, October 9, 1986, pp. 107-111.
3. Duffy, S. F., Hu, J. and Hopkins, D. A., 1995, "An Overview of Engineering Concepts and Current Design Algorithms for Probabilistic Structural Analysis," *ASME Proceedings of the 1995 Design Engineering Technical Conferences*, DE-Vol. 83, pp. 3-16.
4. Weibull, W., 1951, "A Statistical Distribution Function of Wide Applicability," *ASME Journal of Applied Mechanics*, Vol. 18, No. 3, pp. 293-297.



## Objectives

- Predict the limits of design random variables that are more consistently reliable and practical than current design methods.
- Simplify the statistical design process.
  - Utilize simple statistics.
  - Establish statistical design standard.

Fig. 1

## Statistical Parameters Characterize Random Variables

### •Central Tendency:

$\mu$  = Population Mean

$\theta$  = Population Mode

$\chi_{50}$  = Population Median

### •Dispersion:

$\sigma$  = Population Standard Deviation

### •Shape (Manner of Dispersion):

$$\delta = skew = \frac{\mu - \theta}{\sigma}$$

### •Random Variable x:

Standardized Variable:  $x^* = \frac{x - \mu}{\sigma}$

Expected Extrema of x:

$$\varepsilon_x = \begin{Bmatrix} x_{\min} \\ x_{\max} \end{Bmatrix} \Rightarrow x_{\min} < x < x_{\max}$$

Probability of occurrence:  $P(x)$

Fig. 2

## Concept: Expected Extrema Affected by Skewness

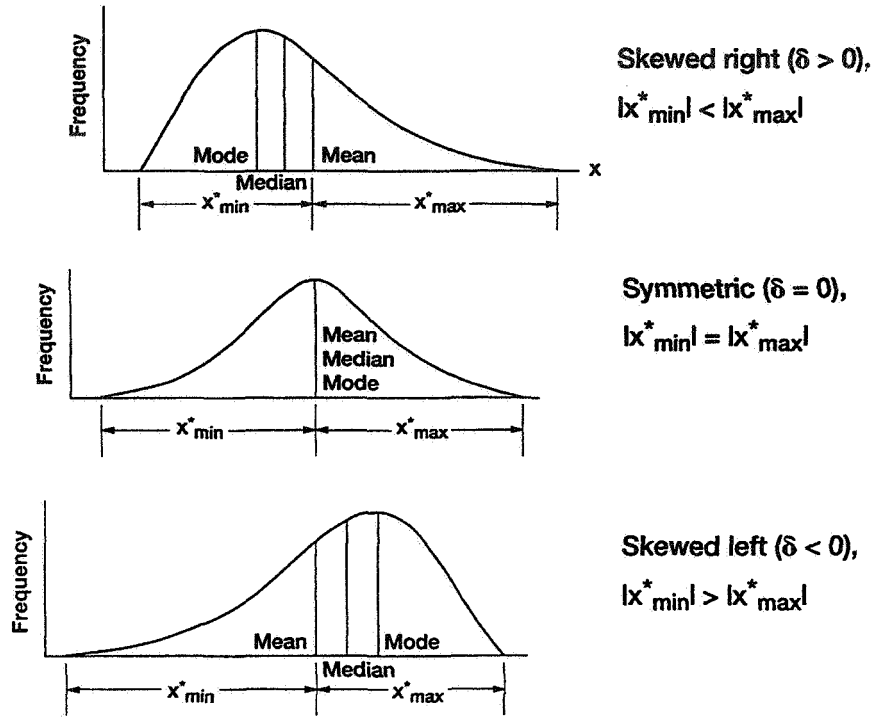


Fig. 3

## Proposed Generalized Equation Relating Expected Extrema to Simple Statistics\*

$$\frac{|\varepsilon - \mu|}{\sigma} = A^{1 \pm \frac{\delta}{B}}$$

- A = base parameter, expected or allowable extrema when  $\delta = 0$  (standard units)
- B = slope parameter or characteristic skew, value of skew where  $|\varepsilon| = 1$  standard unit
- $\delta$  = skew
- $\varepsilon$  = expected or allowable extrema, minimum (-) or maximum (+)
- $\mu$  = population mean
- $\sigma$  = population standard deviation

\* Applicable to a large class of unimodal random variable distributions.

Fig. 4

# Proposed Function for Estimating Practical Limits of Random Variables for Optimum Design [A = $\pi$ (3.14), B = 1]

$$\varepsilon(\mu, \sigma, \delta) = \mu \pm \sigma \cdot \pi^{1 \pm \delta} \quad \left\{ \begin{array}{l} x_{\min} = \mu - \sigma \cdot \pi^{1-\delta} \\ x_{\max} = \mu + \sigma \cdot \pi^{1+\delta} \end{array} \right.$$

Result: Practical Design Allowables for a Wide Range of Distributions

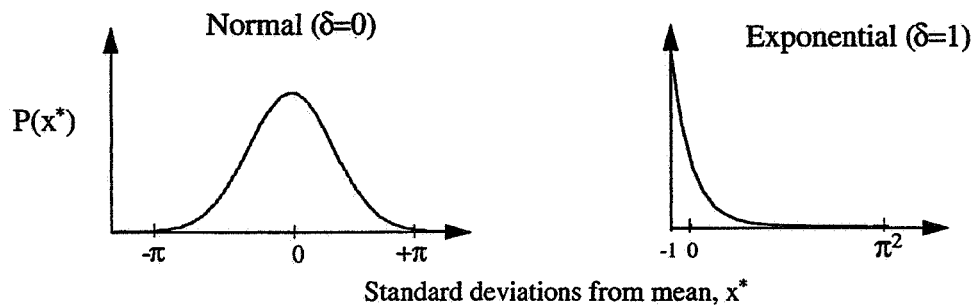
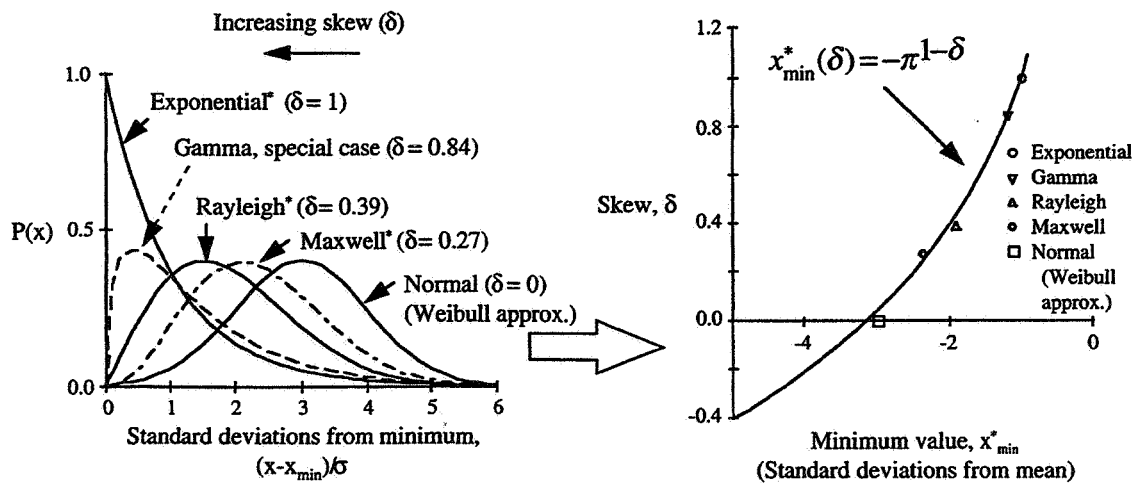


Fig. 5

## Proposed Function Models Threshold Behavior of Theoretical Probability Distributions



\*Single parameter distributions.

Fig. 6

## Proposed Function Provides Lower Bound on Observed Strength as Theorized

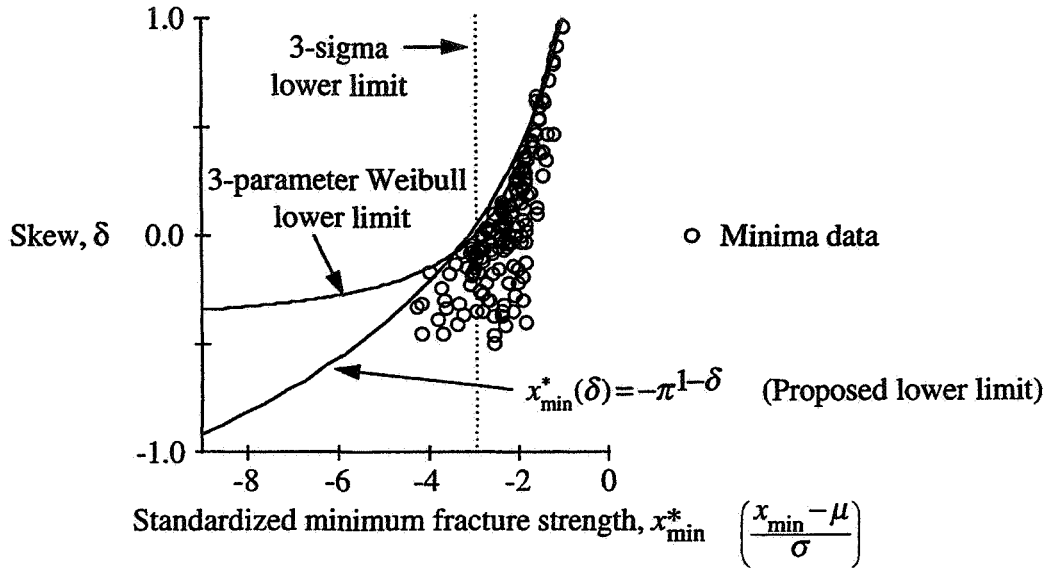


Fig. 7

## Empirical Relation Allows Median Based Predictions Using Proposed Function

$\mu$  = mean

$\theta$  = mode

$\chi_{50}$  = median

$\delta$  = skew

$$\delta = \frac{\mu - \theta}{\sigma} \approx \frac{3(\mu - \chi_{50})}{\sigma}$$

$$x_{\min}(\mu, \sigma, \theta) = \mu - \sigma \cdot \pi^{1 - \left( \frac{\mu - \theta}{\sigma} \right)}$$

$$x_{\min}(\mu, \sigma, \chi_{50}) = \mu - \sigma \cdot \pi^{1 - 3 \cdot \left( \frac{\mu - \chi_{50}}{\sigma} \right)}$$

Fig. 8

## Effect of Population Mode Estimates on Minima Predictions Using Proposed Function

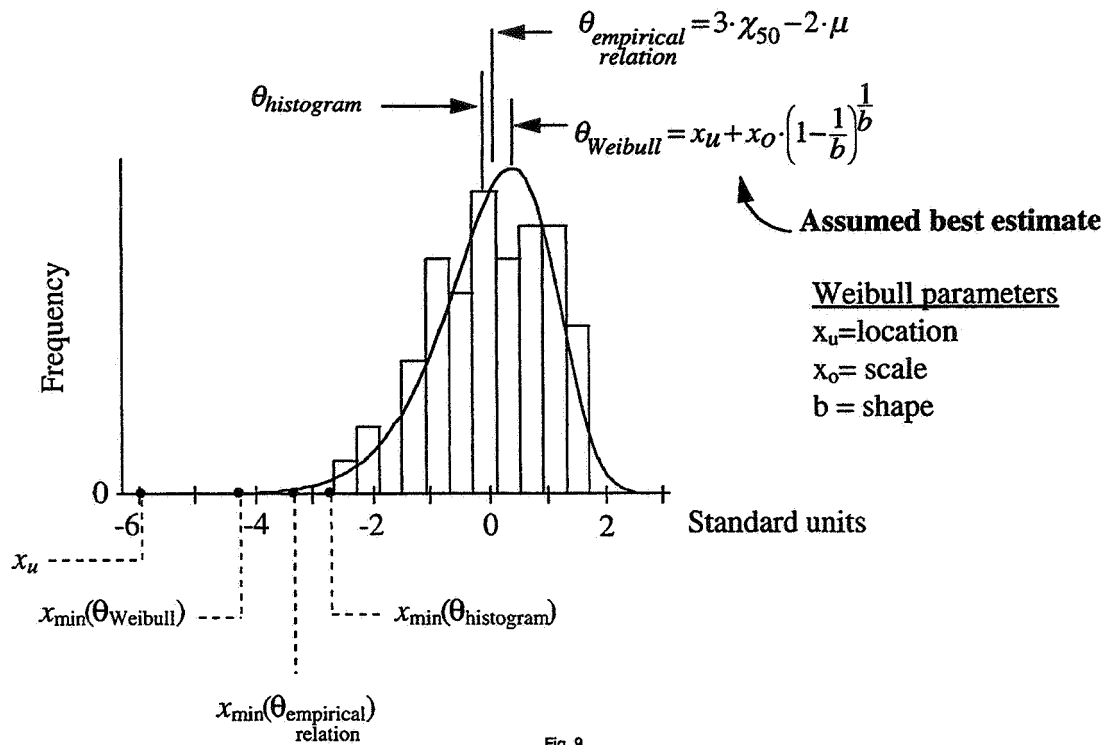


Fig. 9

## Design Strengths for A357-T6 Cast Aluminum

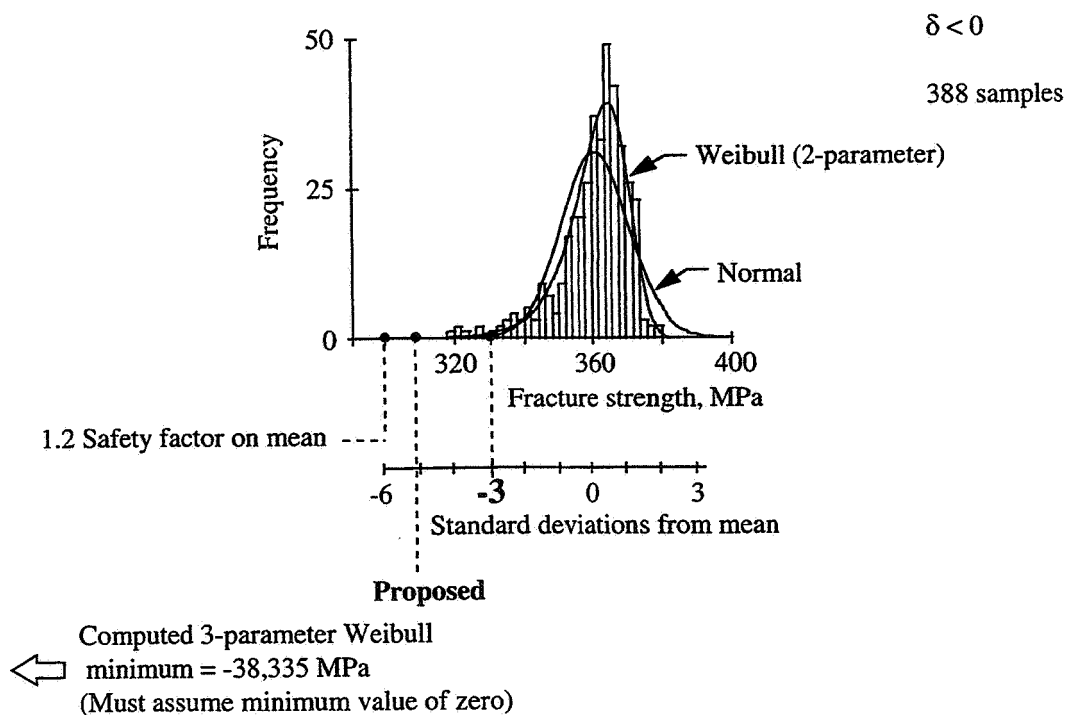


Fig. 10

## Design Strengths for $\text{Si}_3\text{N}_4$

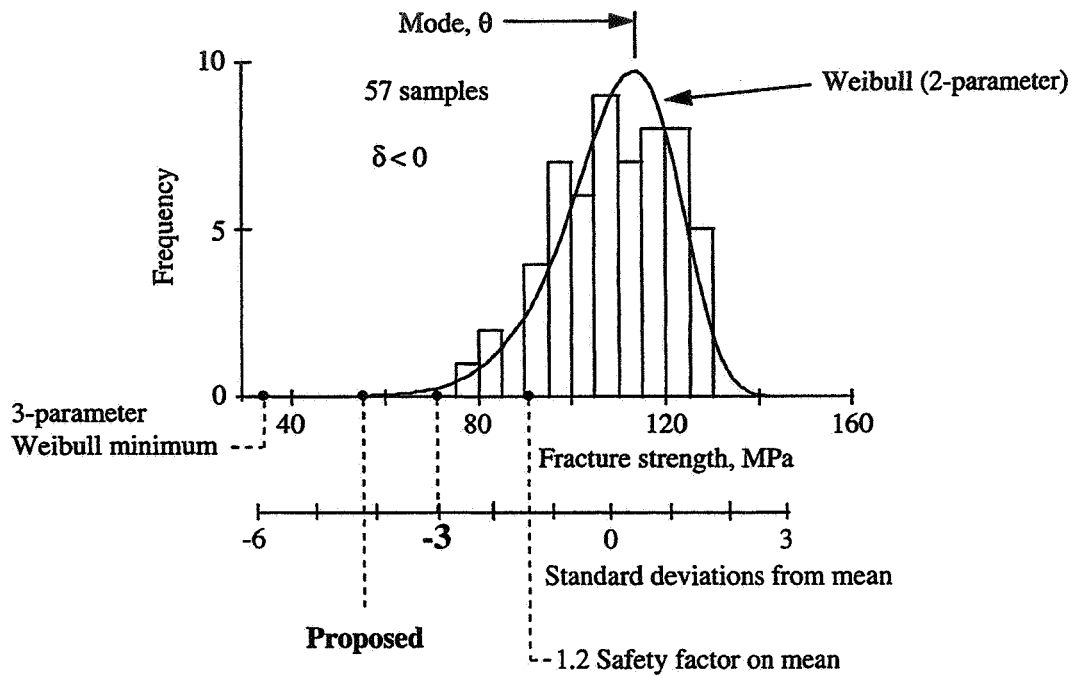


Fig. 11

## Design Strengths for a Low-Alloy Steel

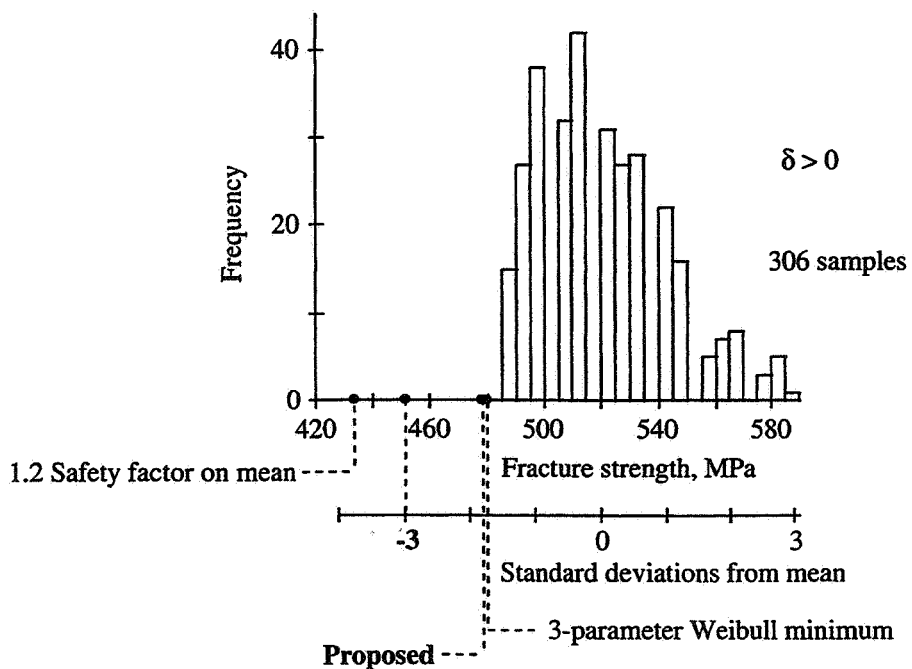


Fig. 12

## Determination of Maximum Assumed Value

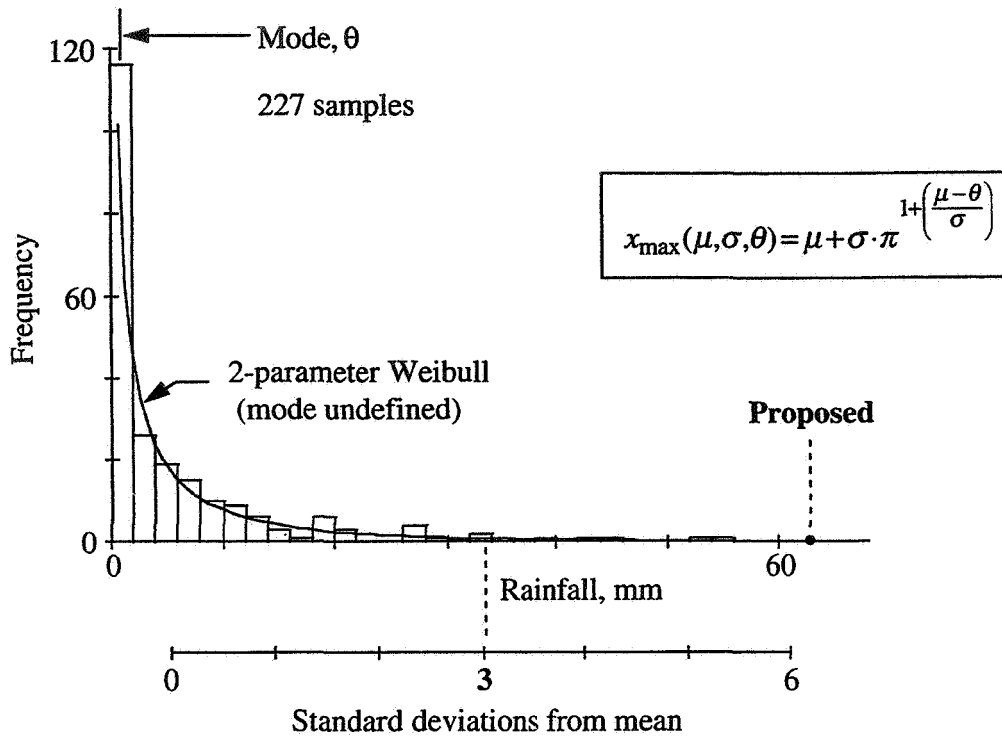


Fig. 13

## Summary of Results

- Safety factor (unadjusted) and three-sigma approaches can lead to uneconomical or unsafe design values.
- Three-parameter Weibull minimum values found to be very conservative for distributions of significant negative skew.
- Weibull mode estimate very compatible with proposed method.
- Proposed method gave consistently safe design strengths without excessive conservatism as compared with data.

Fig. 14

## Conclusions

- Skewness is important in predicting extreme values of random variables.
- Practical minimum values of random variables can be estimated from simple population statistics (mean, mode (or median), standard deviation).
- Proposed function gives reasonably conservative design values for fracture strength of materials.

Fig. 15

## Focus of Future Research

- Adapt function to allow utilization of coefficient of skew statistic, eliminating need for mode value when individual data points are available.
- Investigate relationship between probability of occurrence and predicted extrema.
- Expand theory to include probability of occurrence at any specified level.
- Confirm applicability to predictions of maxima.

Fig. 16



**Paper Withdrawn**

## GEAR CRACK PROPAGATION LIFE STUDIES

DAVID G. LEWICKI  
U.S. Army Research Laboratory  
NASA Lewis Research Center  
Cleveland, Ohio

and

Roberto Ballarini  
Case Western Reserve University  
Cleveland, Ohio

S2-39  
029101  
10P.  
078115

### Introduction

A common design goal for gears in helicopter or turboprop power transmissions is reduced weight. To help meet this goal, some gear designs use thin rims. Rims that are too thin, however, may lead to bending fatigue problems and cracks. The most common methods of gear design and analysis are based on standards published by the American Gear Manufacturers Association. Included in the standards are rating formulas for gear tooth bending to prevent crack initiation [1]. These standards can include the effect of rim thickness on tooth bending fatigue [2]. The standards, however, do not give any indication of the crack propagation path or the remaining life once a crack has started. Fracture mechanics has developed into a useful discipline for predicting strength and life of cracked structures.

The objective of this study was to determine the effect of gear rim thickness on crack propagation path and propagation life (Fig. 1). The major emphasis was to predict the direction in which a crack will grow, either through the gear tooth or through the rim. From an extensive study [3], linear elastic fracture analysis was used to analyze gear tooth bending fatigue in standard and thin-rim gears. Finite element computer programs were used to determine stress distributions and model crack propagation. Experimental tests were performed to validate predicted crack propagation results.

### Crack Propagation Simulation

The analysis of this present study used the FRANC (FRacture ANalysis Code) computer program described by Wawrzynek [4]. FRANC is a general purpose, two-dimensional, finite element code for the static analysis of cracked structures. Among the variety of capabilities, a unique feature of FRANC is the ability to model a crack in a structure and the ability to simulate crack propagation. Included in FRANC is an automated meshing algorithm that connects the user-created finite element mesh to a rosette of quarter-point, six-node triangular elements around the crack tip to model the inverse square-root stress singularity (Fig. 2). A sample finite element mesh of an uncracked gear is shown in Fig. 3. This model had 2353 8-node, plane stress, quadrilateral elements. An initial crack was placed in the fillet region on the tooth with the refined mesh. FRANC was then used to simulate propagation of the crack.

### Experimental Tests

Crack propagation experiments were performed in the NASA Lewis Spur Gear Fatigue Rig (Fig. 4). The test stand has been used quite extensively at Lewis to determine material, material processing, and lubricant effects on tooth pitting fatigue life [5]. The test gears were 28-tooth, 8-pitch, 20° pressure angle external

spur gears with a face width of 6.35 mm (0.25 in). The teeth had involute profiles with linear tip relief. All test gears used in the experiments were fabricated and machined from a single batch of consumable-electrode vacuum-melted AISI 9310 steel. The gears were case-carburized and ground. Four different test gear designs were considered with the backup ratios,  $m_B$ , (defined as the ratio of rim thickness divided by tooth height) from 3.3 to 0.3 (Fig. 5).

It was believed that tooth bending fatigue cracks would be difficult to initiate based on the load capacity of the test rig. Due to this, notches were fabricated in the fillet region (loaded side) on one tooth of each of the test gears to promote crack initiation (Fig. 6). The notches were fabricated using electrodischarge machining. The nominal notch dimensions were 0.20 mm (0.008 in) in length and 0.13 mm (0.005 in) in width along the full face width of the tooth. The notches were located at the same location for all test gears. This location was at a radius of 40.49 mm (1.594 in) on the fillet, which was the position of the greatest tensile stress for the solid gear ( $m_B=3.3$ ). The notches produced a stress concentration factor of approximately three as determined using a finite element analysis.

On two of the test gears ( $m_B=3.3$  and 0.3), special crack propagation gages were fabricated for installation in the tooth fillet region (Fig. 7). The gages had ten circular strands designed to break as the crack propagated through them, which in turn, increased the electrical resistance of the gage. A gage was installed on each side of the tooth flank for each gear instrumented with crack gages. The electrical resistance of the crack gages was monitored along with the load cycle count to estimate cycles as a function of crack length.

## Results

The predicted crack propagation paths for the models of the test gears are shown in Fig. 8. Also shown for comparison are the results of the experiments. For backup ratios  $m_B \geq 1.0$ , the cracks propagated through the teeth and the correlation between predicted crack paths and experiments was rather good. For the other extreme of  $m_B=0.3$ , the cracks propagated through the rim, and again, the correlation between predictions and experiments was good. A discrepancy occurred for the  $m_B=0.5$  cases. The predicted crack paths for these cases propagated in a fairly straight path with a slight tendency back toward the tooth. The crack paths from the experiments, however, propagated through the rims. The predictions for the  $m_B=0.5$  case was unstable and the crack paths were dependent on initial conditions. Various conditions such as initial crack angles, load positions, or small perturbations of the backup ratio affected the stress field in the tooth and rim region enough to significantly alter crack path direction.

Fig. 9 shows, as an example, the measured crack growth for the test gear with  $m_B=3.3$ . Crack initiation and crack propagation was fairly uniform throughout the tooth face width which supports the two-dimensional, planar analysis used in the predictions. Fig. 10 shows a sample comparison of predicted and measured crack growth. The stress intensity factors as predicted using the finite element analysis were used with the Paris crack growth model [6] to calculate predicted crack propagation life. In addition, the fatigue crack closure concept [7] was used. The cycles were defined as the number of crack propagation cycles after an initial crack of 0.64 mm (0.025 in).

Fig. 11 displays the effect of rim thickness on predicted mode I stress intensity factors and predicted crack propagation cycles. The stress intensity factors were determined from FRANC using the appropriate finite element models. The Paris equation was used along with the appropriate effective stress intensity range ratios. The initial cracks of the various models were placed at the location of the maximum tensile stress in the tooth fillet. The stress intensity factors were lowest for the  $m_B=0.5$  case. This gave the highest predicted number of cycles for the cases studied. The cycles all were defined as the number of crack propagation cycles after an initial crack of 0.28 mm (0.011 in). The stress intensity factors were highest

for the  $m_B=0.3$  case. However, the predicted life for this was somewhere between the case of  $m_B=0.5$  and 1.0 due to the fatigue crack closure effect. The cases of  $m_B=3.3$  and 1.0 gave nearly the same predicted life.

### Conclusions and Future Work

Analytical and experimental studies were performed to investigate the effect of rim thickness on gear tooth crack propagation path and life. Gear tooth crack propagation was simulated using a finite element based computer program which used principles of linear elastic fracture mechanics. In addition to the analysis, experimental studies were performed in the NASA Lewis Spur Gear Fatigue Rig. Gears with various backup ratios were tested to validate crack path and life predictions. Conclusions were (Fig. 12):

For backup ratios (defined as rim thickness divided by tooth height) of  $m_B=3.3$  and 1.0, the analysis predicted cracks that would propagate through the teeth and not the rims. This was validated by the experiments. For  $m_B=0.3$ , the analysis predicted cracks that would propagate through the rim, which was also validated by experiments. For  $m_B=0.5$ , the experiments produced rim fractures while the analysis showed instability (tooth or rim fracture) when various initial conditions were changed. In addition, good correlation between predicted and measured gear crack growth was achieved when the predictions used the Paris crack growth equation and the concept of fatigue crack closure.

The focus of future research is shown in Fig. 13. Future plans include further studies to refine the two-dimensional fracture analysis. Also, three-dimensional fracture analysis studies have begun. The ultimate goal is to develop design charts which would be used by the gear designer to establish lightweight but safe and reliable drive systems for future rotorcraft.

### References

1. "Fundamental Rating Factors and Calculation Methods for Involute Spur and Helical Gear Teeth", ANSI/AGMA 2001-B88, American Gear Manufacturers Association, Alexandria, VA, 1990.
2. Drago, R.J., and Lutthans, R.V., "Combined Effects of Rim Thickness and Pitch Diameter on Spur Gear Tooth Stresses", Journal of the American Helicopter Society, Vol. 28, Jul., pp 13-19, 1983.
3. Lewicki, D.G., "Crack Propagation Studies to Determine Benign or Catastrophic Failure Modes for Aerospace Thin-Rim Gears", Ph.D. Dissertation, Case Western Reserve University, May 1995.
4. Wawrzynek, P.A., "Discrete Modeling of Crack Propagation: Theoretical Aspects and Implementation Issues in Two and Three Dimensions", Ph.D. Dissertation, Cornell University, 1991.
5. Townsend, D.P., and Bamberger, E.N., "Surface Fatigue Life of Carburized and Hardened M50NiL and AISI 9310 Spur Gears and Rolling-Contact Test Bars", Journal of Propulsion and Power, Vol. 7, No. 4, pp. 642-649, 1991.
6. Paris, P.C., and Erdogan, F., "A Critical Analysis of Crack Propagation Laws", Journal of Basic Engineering, Vol. 85, pp. 528-534, 1963.
7. Elber, W., "The Significance of Fatigue Crack Closure", Damage Tolerance in Aircraft Structures, ASTM STP 486, pp. 230-242, 1971.

## OBJECTIVE

Determine effect of rim thickness on crack propagation life.

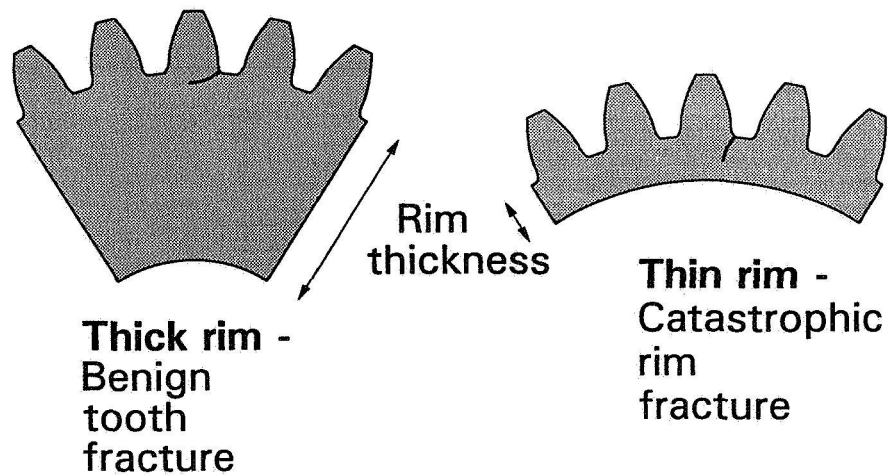


Fig. 1

## FRANC MODELING OF A CRACK

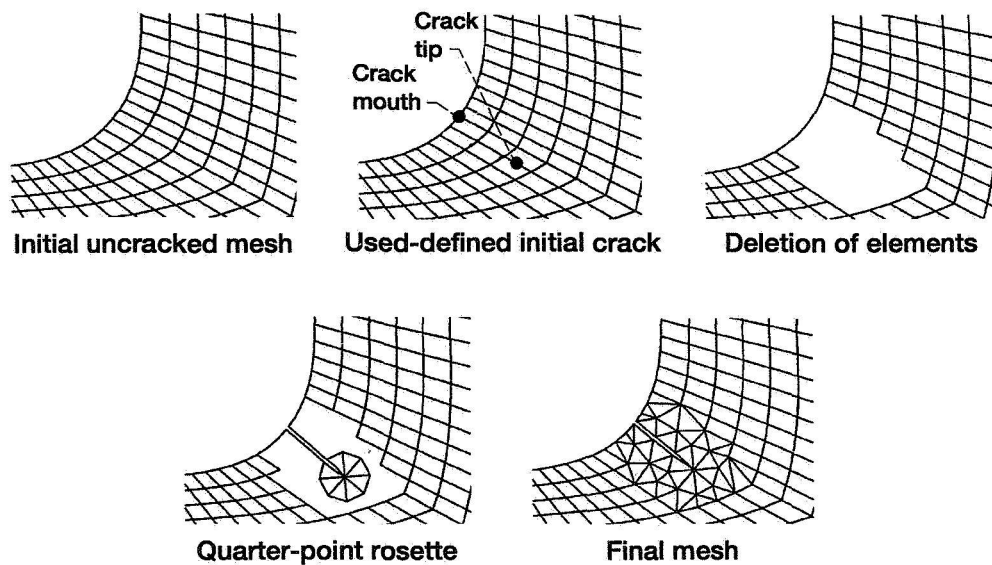


Fig. 2

CD-96-73642

## FINITE ELEMENT MODEL OF GEAR USED IN CRACK PROPAGATION STUDIES

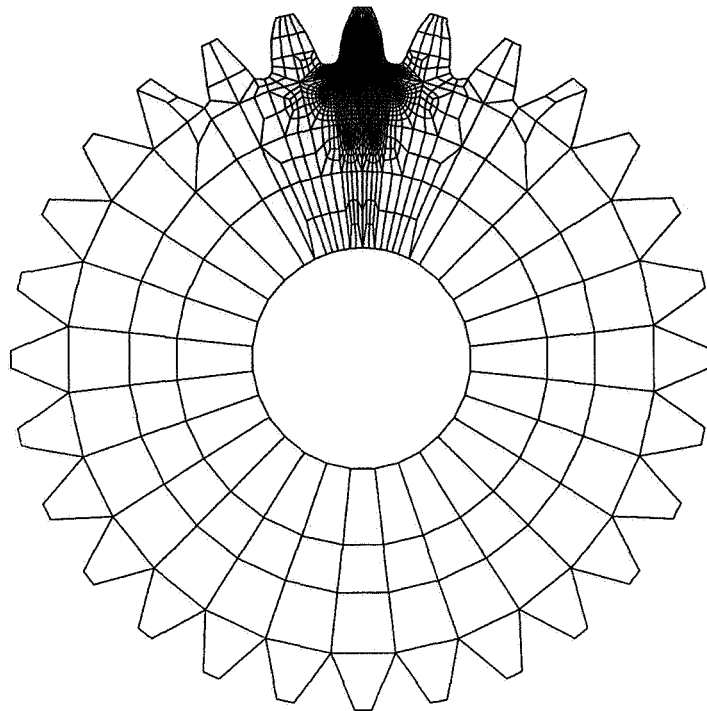


Fig. 3

CD-96-72854

## NASA LEWIS SPUR GEAR FATIGUE RIG

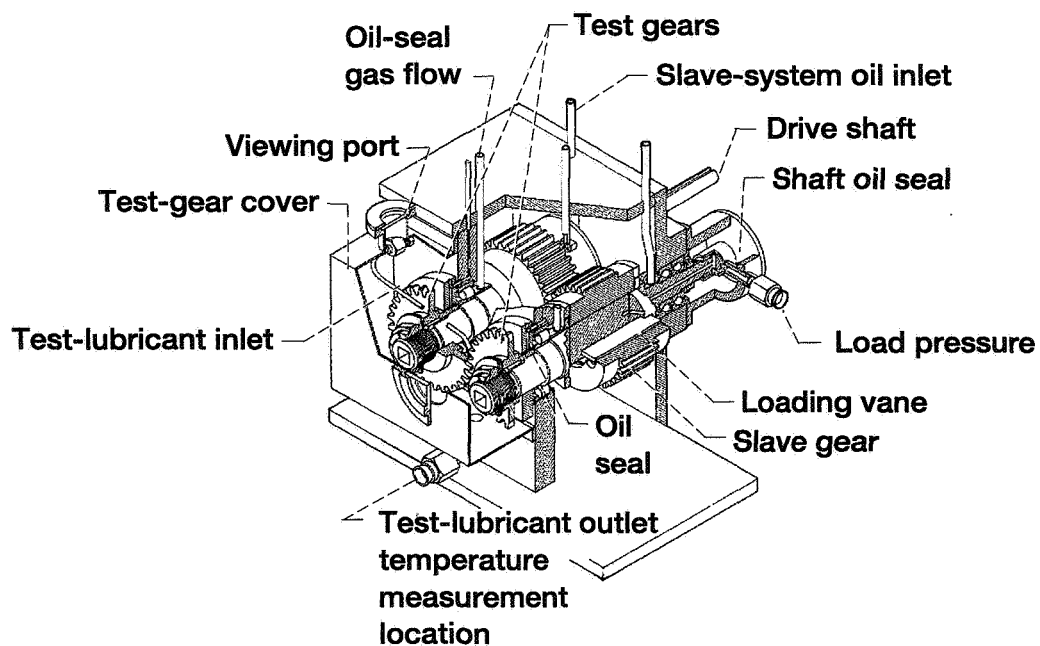


Fig. 4

CD-96-72849

## TEST GEARS

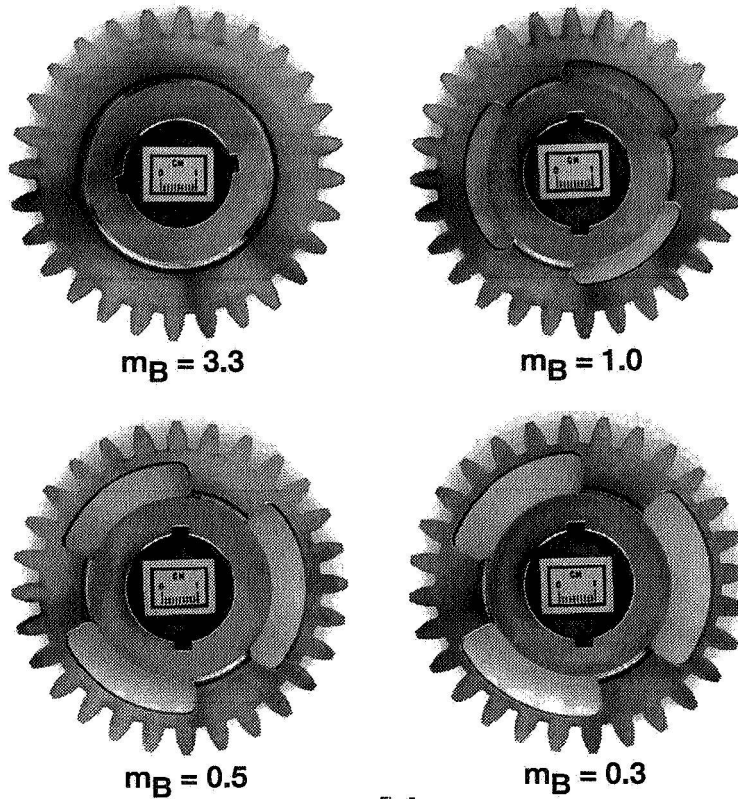


Fig. 5

CD-96-73637

## FABRICATED NOTCH IN TOOTH FILLET REGION

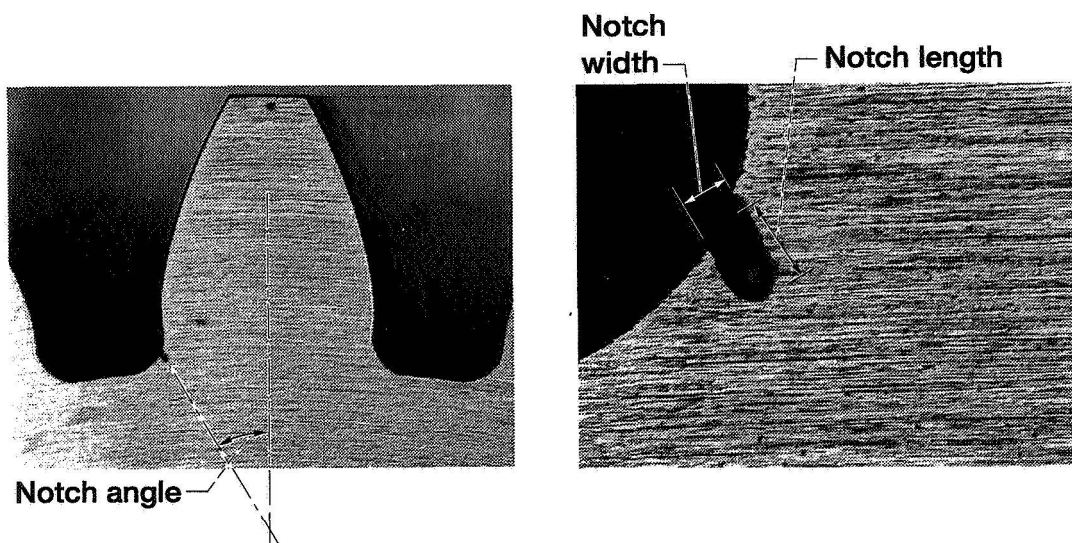


Fig. 6

CD-96-72846

## CRACK PROPAGATION GAGES

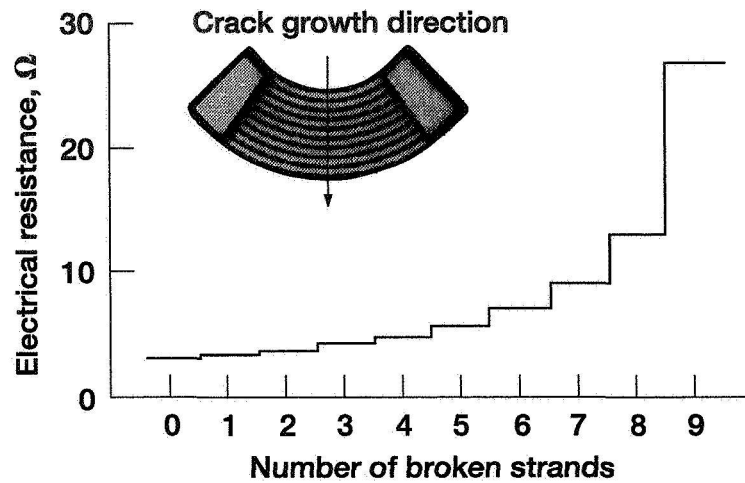


Fig. 7

CD-96-72851

## COMPARISON BETWEEN PREDICTED AND EXPERIMENTAL CRACK PROPAGATION PATHS

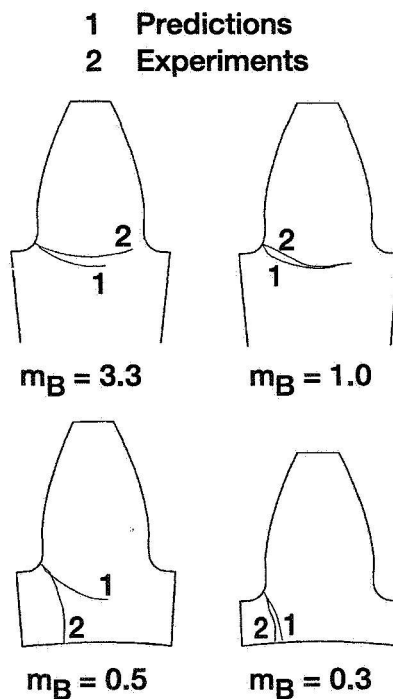


Fig. 8

CD-96-73638



## CRACK PROPAGATION FATIGUE GROWTH (Backup Ratio = 3.3, Thick Rim)

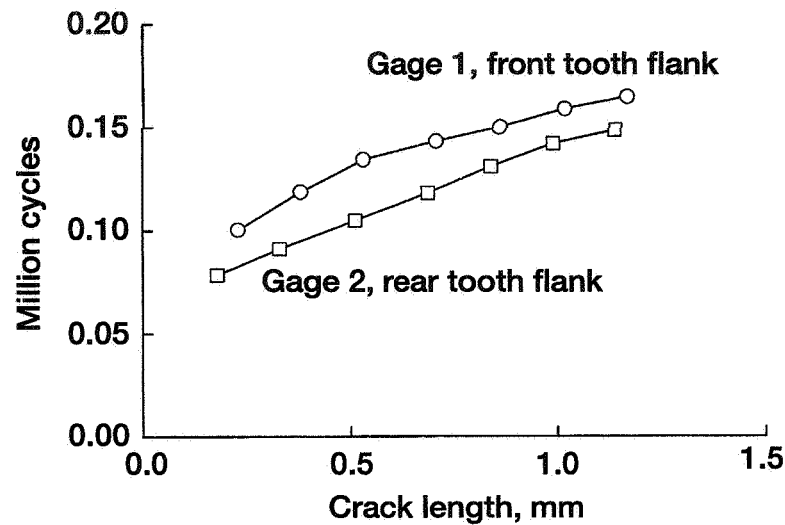


Fig. 9

CD-96-72853

## COMPARISON OF PREDICTED AND EXPERIMENTAL CRACK PROPAGATION (Paris Crack Growth Model With Crack Closure Adjustment)

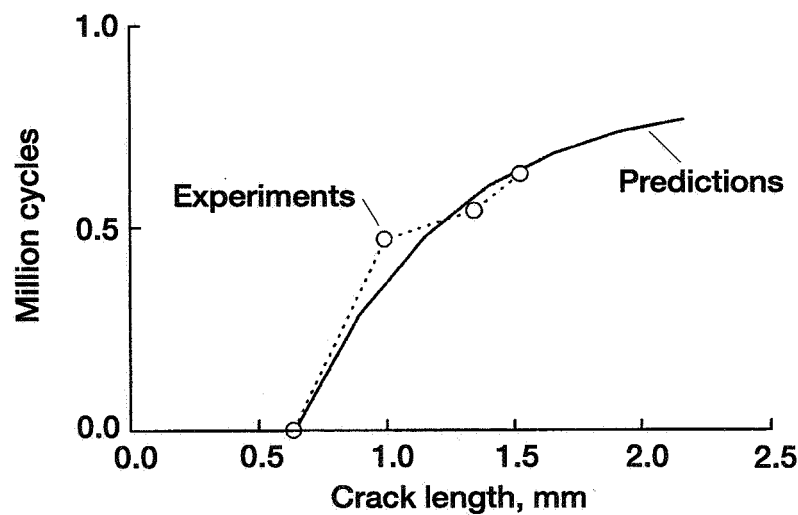


Fig. 10

CD-96-72857

## PREDICTED EFFECT OF RIM THICKNESS ON CRACK PROPAGATION LIFE

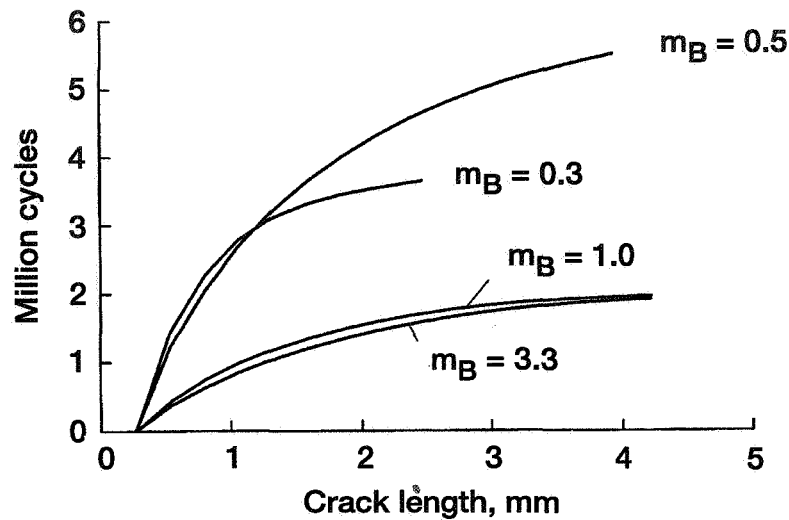


Fig. 11

CD-96-72859

## CONCLUSIONS

- Backup ratios (defined as rim thickness divided by tooth height) of 3.3 and 1.0 produced tooth fractures.
- Backup ratio of 0.3 produced rim fracture.
- Backup ratio of 0.5 produced rim fracture from tests and instability from analysis.
- Good correlation between predicted and measured gear crack growth rate was achieved when FEM stress intensity predictions were used with the Paris crack growth equation and the concept of fatigue crack closure.

Fig. 12

## **FOCUS OF FUTURE RESEARCH**

- Determine effect of rotating inertia force on crack propagation.
- Automate 2-D meshing process.
- Perform parametric studies (effects of initial crack position, dynamic load, tooth, root, rim, and support geometry).
- Initiate 3-D crack propagation studies.
- Develop gear design charts.

Fig. 13

# SURFACE FATIGUE EVALUATION OF GEAR MATERIALS AND LUBRICANTS

Dennis P. Townsend  
NASA Lewis Research Center  
Cleveland, Ohio

53-39

029102

078116

147

## Summary

The surface fatigue life of several gear materials, gear processes and gear lubricants were evaluated in the NASA spur gear fatigue test rig during the last several years. Some of these materials include VIM-VAR AISI 9310, EX-53, CBS-1000M, CBS-600, VASCO-X2, M50-NiL, VASCO Matrix II, VASCO Max 350, and Nitralloy N. Some of the various processes include shot peening at different intensities and hot forged powder metal AISI 4620. Several aircraft gear lubricants with different viscosity's and additives were evaluated for their effect on surface fatigue of standard spur gears. These materials and lubricants were evaluated for possible use in aircraft gear applications. The fatigue life of the gear materials and lubricants were compared with the life of the standard AISI 9310 aircraft gear material and the NASA base lubricant. Surface fatigue tests were conducted at a lubricant inlet temperature of 321K (120° F), a lubricant outlet temperature of 350K (170° F), a maximum Hertz stress of 1.71 GPa (248ksi) and a speed of 10000 rpm.

## Introduction

Aircraft turbine engine requirements are increasing the demand for higher reliability and higher operating temperature in many advanced and high power density applications for gears and rolling element bearings. The surface temperature of power gearing normally operates considerably higher than the bulk oil temperature; thereby, requiring improved lubricants and gear material that will provide long life at increased operating temperature.. Previous testing with rolling element bearings has shown that at high stress loads the surface fatigue life of bearings is much longer when the surface hardness at the operating temperature is Rockwell Rc 58 or higher and is drastically reduced when the hardness is less than Rc 58.

The objective of the research work reported in this paper was to compare under closely controlled test conditions the fatigue lives and failure modes of test spur gears made of advanced materials or improved material processing and the fatigue lives of standard test gears using advanced gear lubricants and compare the results with the standard aircraft gear material AISI 9310 using standard lubricants.

## Test Gears, Materials and Lubricants

The test gears used in the tests reported herein are shown in figure 2. Dimensions for the test gears are summarized in table I. All gears had a minimal surface finish on the tooth flank of  $0.406 \mu\text{m}$  cla (16  $\mu\text{in}$  cla) and a standard 20° involute tooth profile with a small profile tip relief.

The standard test gears were manufactured from AISI 9310. Two sets of standard test gears were shot peened at different intensities. The other gear materials tested were VIM-VAR AISI 9310, EX-53, CBS-600, CBS 1000M, M50-NiL, Vasco max 350, Vasco matrix II, Vasco X-2, Nitralloy N and hot forged powder metal AISI 4620. Table II is a list of the chemical composition of the materials discussed in this report. Most of the gears were case carburized and hardened, however the Vasco max 350 and matrix II were through hardened and the nitralloy N was nitrided. All the test gears had a nominal surface hardness of Rc 60.

Seven lubricants were selected for surface fatigue endurance tests with the CVM AISI 9310 steel gear test specimens. Lubricant properties are given in table III and include an unformulated base stock lubricant with no lubricant additives, a 5 cSt lubricant meeting the MIL-L-23699 specification, a lubricant meeting the MIL-L-7808J specification, a 5 cSt lubricant developed for helicopter gearboxes under the specification DOD-L-85734, a 7.5 cSt lubricant with an anti wear additive package meeting a special development specification DERD-2487, and two 9 cSt ester based lubricants with and without an additive package. Six of the seven lubricants could be classified as synthetic polyol-ester base stock lubricants while lubricant E is a polyalkylene-glycol with a small amount of boundary lubrication additive.

### Apparatus, and Procedure

#### Gear Test Apparatus

The gear fatigue tests were performed in the NASA Lewis Research Center's gear test apparatus. A schematic of the test rig is shown in figure 1. Oil pressure and leakage flow are supplied to the load vanes through a shaft seal. The two identical test gears can be started under no load, and the load can be applied gradually, without changing the running track on the gear teeth.

Separate lubrication systems are provided for the test gears and the main gearbox.. The test gear lubricant is filtered through a 5- $\mu$ m-nominal fiberglass filter.

A vibration transducer mounted on the gearbox is used to automatically shut off the test rig when a gear surface fatigue occurs. The gearbox is also automatically shut off if there is a loss of oil flow to either the main gearbox or the test gears, if the test gear oil overheats, or if there is a loss of seal gas pressurization. The operating speed for the test reported herein was 10,000 rpm.

#### Test Procedure

After the test gears were cleaned to remove the preservative, they were assembled on the test rig. The 0.635-cm (0.25-in.) wide test gears were run in an offset condition with a 0.30-cm (0.12-in.) tooth-surface overlap to give a load surface on the gear face of 0.28 cm (0.11 in.), thereby allowing for the edge radius of the gear teeth. All tests were run in at a pitch-line load of 1225 N/cm (700 lb/in) for 1 hour, which gave a maximum Hertz stress of 0.756 GPa (111 ksi). The load was then increased to 5784 N/cm (3305 lb/in), which gave a pitch-line maximum Hertz stress of 1.71 GPa (248 ksi) and a bending stress of 0.26 GPa (37 ksi).

Operating the test gears at 10 000 rpm gave a pitch-line velocity of 46.55 m/sec (9163 ft/min). Lubricant was supplied to the inlet mesh at 800 cm<sup>3</sup>/min (0.21 gpm) at 321K (120° F). The lubricant outlet temperature was nearly constant at 350 K (170° F).

The pitch-line elastohydrodynamic (EHD) film thickness was calculated by the Dawson and Higginson method. The EHD film thickness for the gear materials test conditions was computed to be 0.33  $\mu$ m (13 in.), which gave an  $h/\sigma$  of 0.55. The EHD film thickness for the lubricant tests are given in table III.

### Conclusions

There were 13 different gear material tests and seven different lubricant tests reported in this study. Nine of the materials tested had surface fatigue lives that were greater than the standard test gears. Four of these materials had surface fatigue lives that were several times the standard test gears with the M50-NiL having a fatigue life more than ten times the standard gears. The lubricant test demonstrated that the surface fatigue life of standard gears can be increased approximately ten times by a lubricant that has a good additive package and provides an EHD film thickness with an  $h/\sigma$  greater than one.

### References

1. Townsend, Dennis P. and Zaretsky, E. V. "Endurance and Failure Characteristics of Modified Vasco X-2, CBS 600 and AISI 9310 Spur Gears" NASA TM 81421 Aug. 1980
2. Townsend, Dennis P. and Zaretsky, Erwin V. "Effects of Shot Peening on Surface Fatigue Life of Carburized and Hardened AISI 9310 Spur Gears" NASA TP 2047 Aug. 1982
3. Townsend, Dennis P. "Surface Fatigue Life and Failure Characteristics of EX-53, CBS 1000M, and AISI 9310 Gear Materials". NASA TP 2513 Oct. 1985
4. Townsend, Dennis P. "Surface Fatigue and Failure Characteristics of Hot Forged Powder Metal AISI 4620, AISI 4640, and Machined AISI 4340 Steel Spur Gears". NASA TM 87330 May 1986.
5. Townsend, D. P. and Bamberger, E. N. "Surface Fatigue Life of M50NiL and AISI 9310 Gears and Rolling-Contact Bars". AIAA Journal of Propulsion and Power, Vol. 7, NO 4, July 1991 pp 642-649.
6. Townsend, Dennis P. "Improvement in Surface Fatigue Life of Hardened Gears by High-Intensity Shot Peening". NASA TM 105678, AVSCOM TR 91-C-042 Sept 1992.
7. Townsend, Dennis P. "Surface Fatigue Life of High Temperature Gear Materials". NASA TM 106562, AVSCOM TR ARL-TR-401 June 1994
8. Townsend, Dennis P. and Shimski, John "Evaluation of the EHL Film Thickness and Extreme Pressure Additives on Gear Surface Fatigue Life". NASA TM 106663, ARL TR ARL-TR-477 Dec. 1994

# NASA Lewis Research Center's Gear Fatigue Test Apparatus

## Gearbox

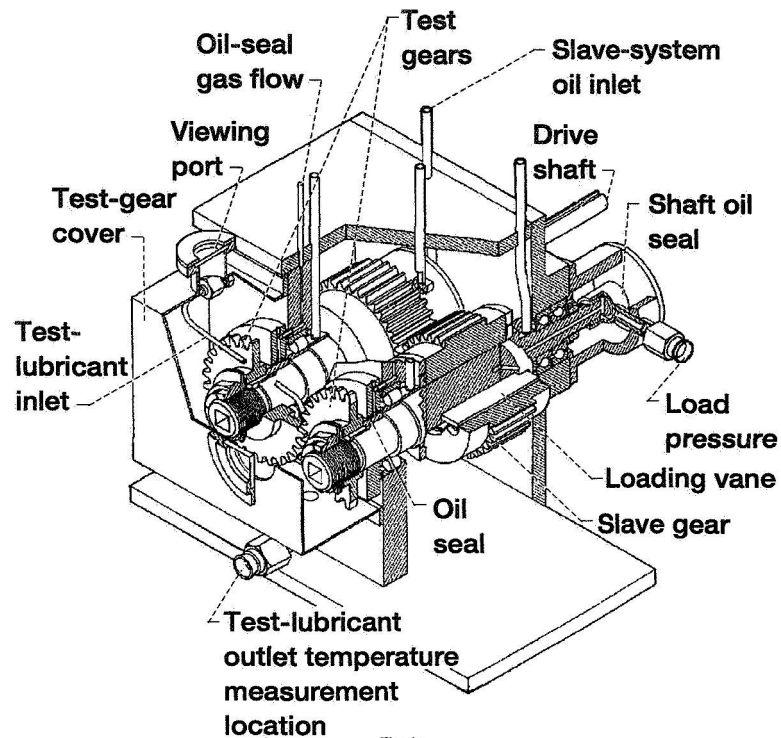


Fig. 1a

# NASA Lewis Research Center's Gear Fatigue Test Apparatus

## Schematic

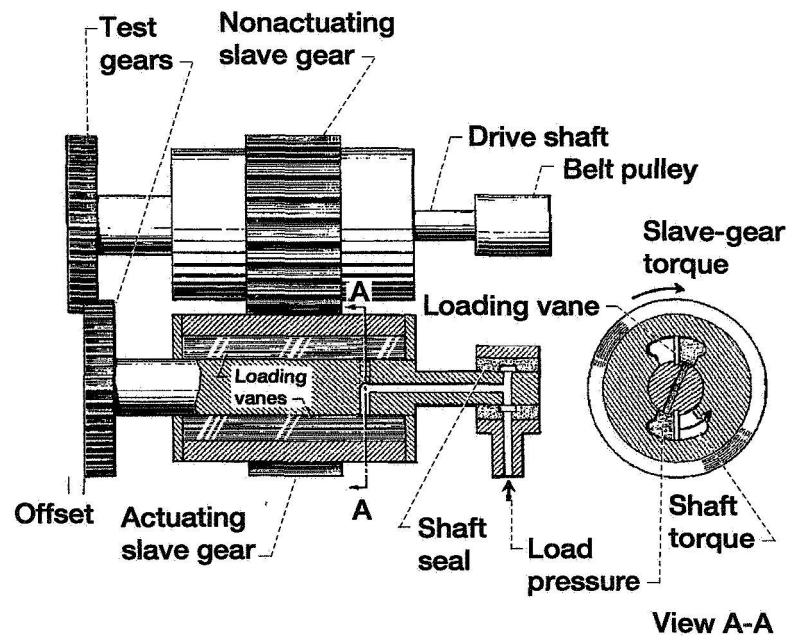
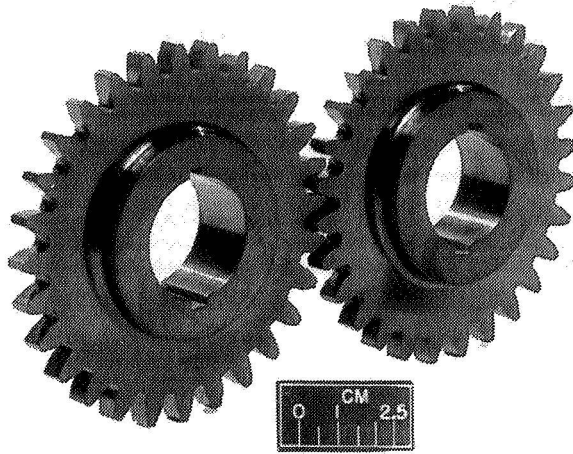


Fig. 1b

## Test-Gear Configuration



### Spur Gear Data

[Gear tolerance per AGMA class 12.]

Number of teeth	28
Diametral pitch	8
Circular pitch, cm (in.)	0.9975 (0.3297)
Whole depth, cm (in.)	0.762 (0.300)
Addendum, cm (in.)	0.318 (0.125)
Chordal tooth thickness (reference), cm (in.)	0.485 (0.191)
Tooth width, cm (in.)	0.635 (0.25)
Pressure angle, deg	20
Pitch diameter, cm (in.)	8.890 (3.500)
Outside diameter, cm (in.)	9.525 (3.750)
Root fillet, cm (in.)	0.102 to 0.152 (0.04 to 0.06)
Measurement over pins, cm (in.)	9.603 to 9.630 (3.7807 to 3.7915)
Pin diameter, cm (in.)	0.549 (0.216)
Backlash reference, cm (in.)	0.0254 (0.010)
Tip relief, cm (in.)	0.001 to 0.0015 (0.0004 to 0.0006)

Fig. 2

## Nominal Chemical Composition of Gear Materials

ELEMENT	AISI9310	VASCO Matrix II	VASCO Max 350	Nitralloy N	EX-53	CBS 600	CBS 1000	VASCO X-2	M50- NiL	AISI 4620
Carbon	0.1	0.51	0.01	0.24	0.01	0.19	0.14	0.14	0.13	0.11
Nickel	3.22	—	18.5	3.5	2.13	0.18	2.94	0.1	3.44	1.82
Chromium	1.21	4.0	—	1.18	1.05	1.5	1.12	4.9	4.21	—
Molybdenum	0.12	5.0	4.8	0.25	3.3	0.95	4.77	1.36	4.3	0.4
Cobalt	—	8.0	12.0	—	—	—	—	0.02	0.01	—
Manganese	0.63	0.15	0.05	0.55	0.37	0.61	0.48	0.25	0.28	0.25
Silicon	0.27	0.2	0.05	0.3	0.98	1.05	0.43	0.91	0.18	0.03
Sulfur	0.005	0.03	0.01	0.03	0.006	0.01	0.019	0.01	0.002	0.03
Phosphorous	0.005	0.03	0.01	0.03	0.009	0.01	0.018	0.01	0.002	0.03
Aluminum	—	—	0.1	1.08	—	—	—	—	—	—
Copper	0.13	—	—	—	2.07	—	—	0.07	0.05	—
Tungsten	—	1.0	—	—	—	—	—	1.35	—	—
Vanadium	—	1.0	—	—	0.12	—	0.1	0.42	1.19	—
Titanium	—	—	1.40	—	—	—	—	—	—	—
Boron	—	—	0.003	—	—	—	—	—	—	—
Calcium	—	—	0.05	—	—	—	—	—	—	—
Zirconium	—	—	0.02	—	—	—	—	—	—	—
Iron	Bal.	Bal.	Bal.	Bal.	Bal.	Bal.	Bal.	Bal.	Bal.	Bal.

Fig. 3



## Typical Fatigue Spalls and Cross Section of Test Gears

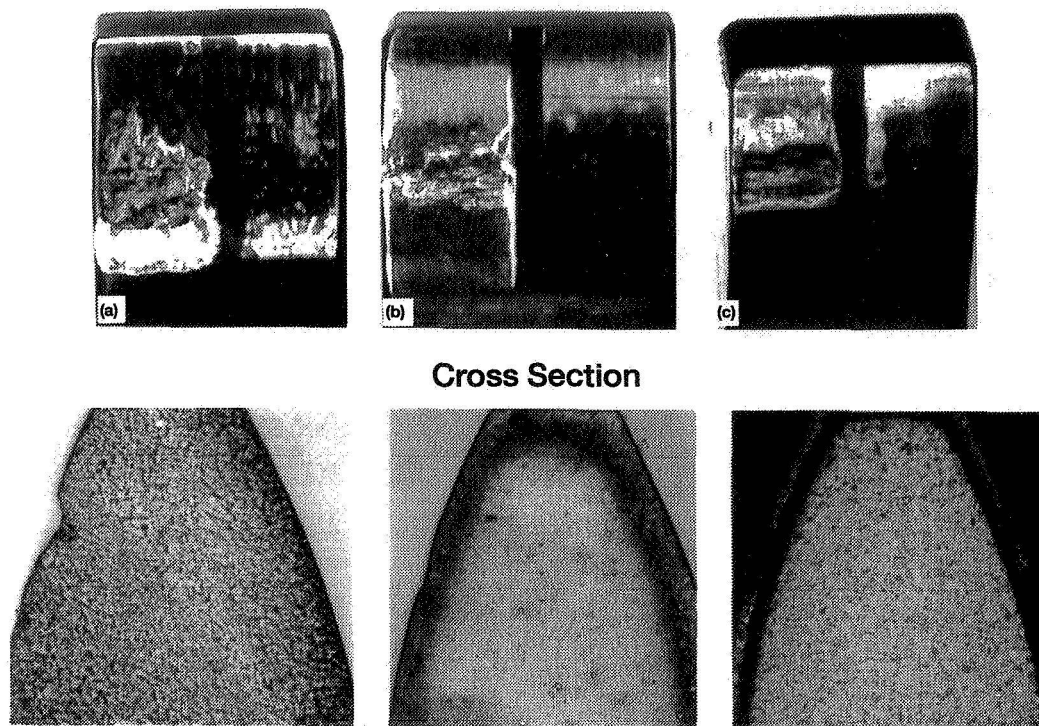


Fig. 4

## Surface Fatigue Life of CBS 600

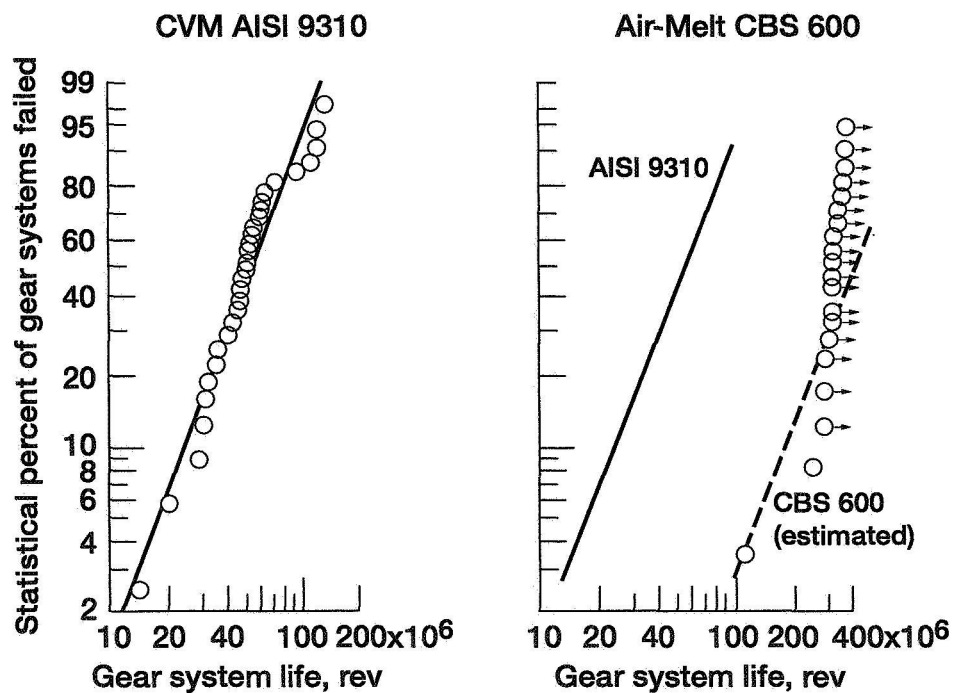
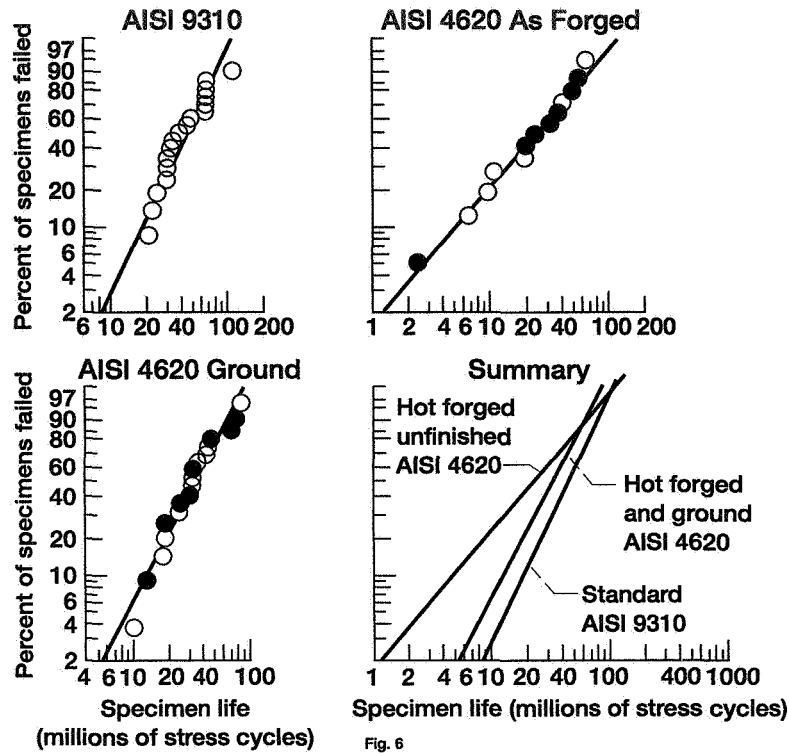


Fig. 5

## Surface Pitting Fatigue Life of Hot Forged Powder Metal Spur Gears



## Surface Fatigue Life of VIM-VAR EX-53 and CBS 1000M

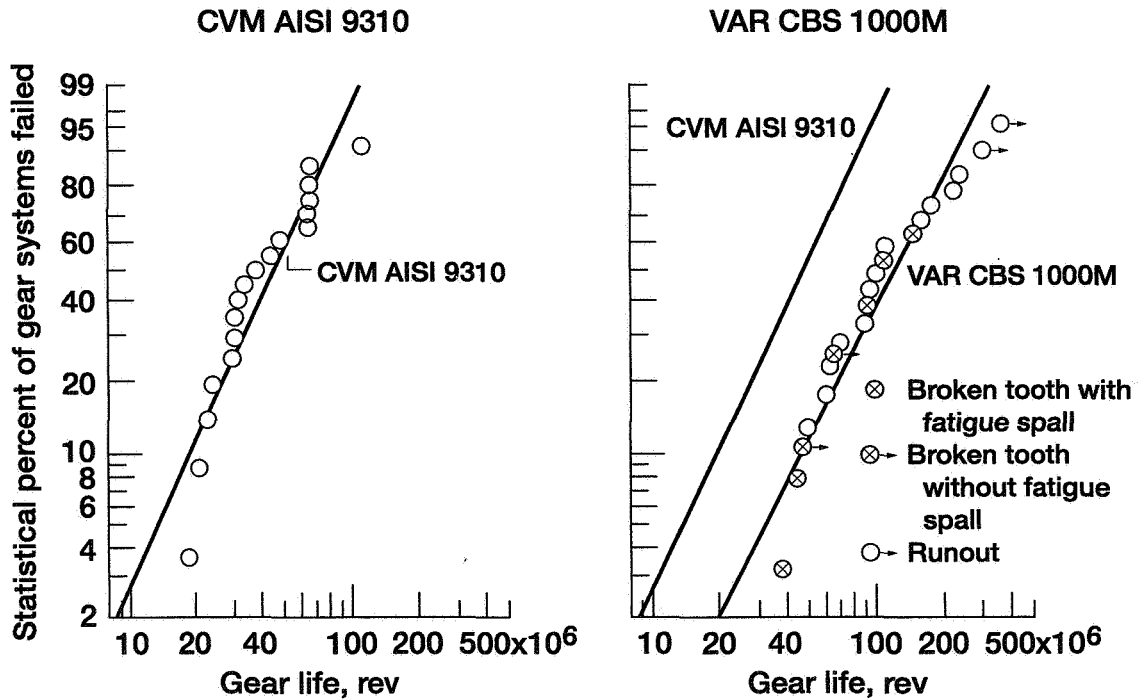


Fig. 7a

## Surface Fatigue Life of VIM-VAR EX-53 and CBS 1000M

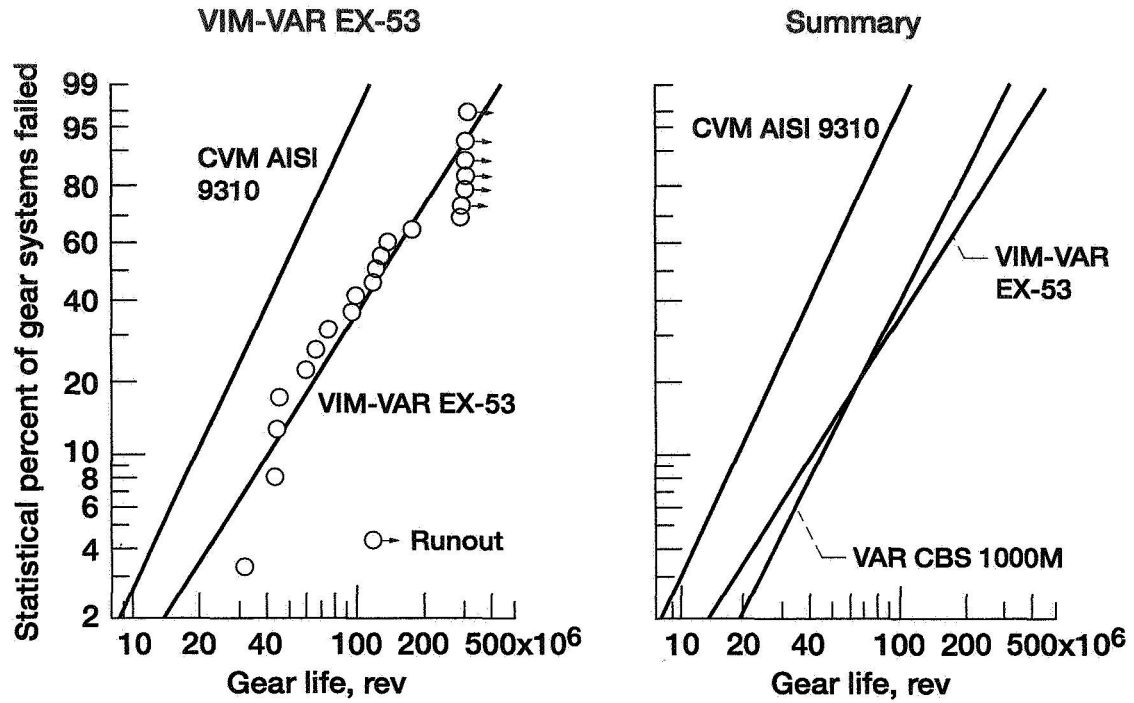
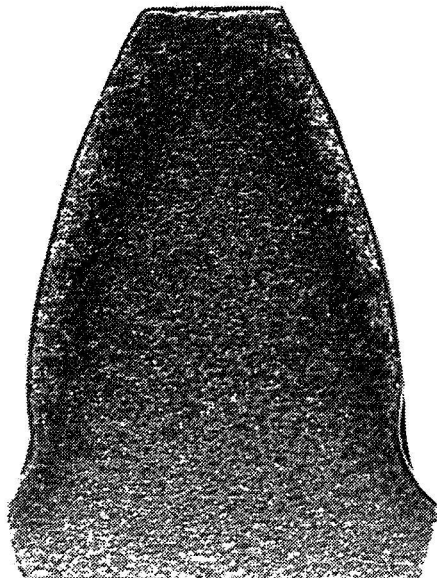


Fig. 7b

## End View of Shot Peened Gears

Medium-Intensity Shot Peened



High-Intensity Shot Peened

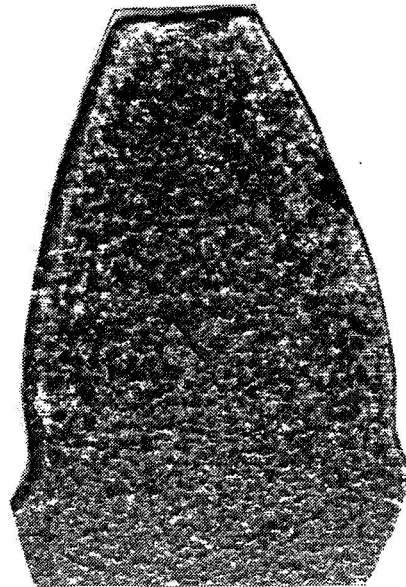


Fig. 8

## Measure of Subsurface Residual Stress of Gear Tooth

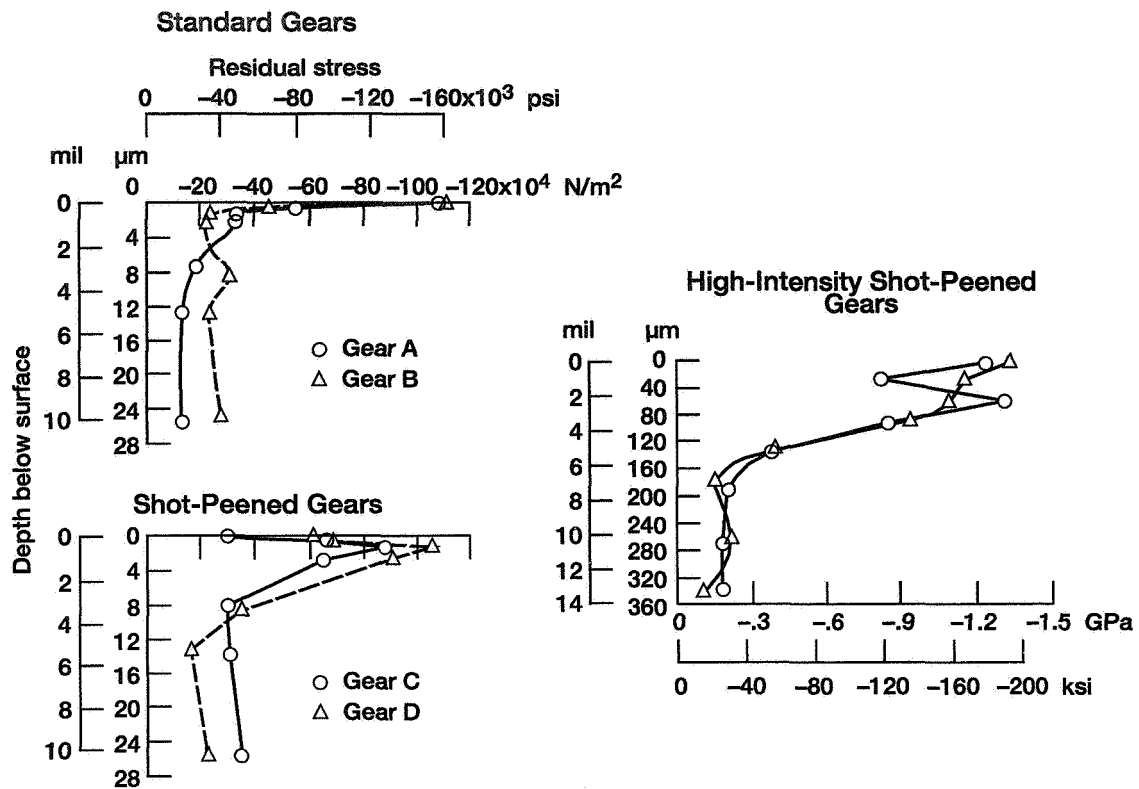


Fig. 9

## Surface Fatigue Life of Shot Peened Gears

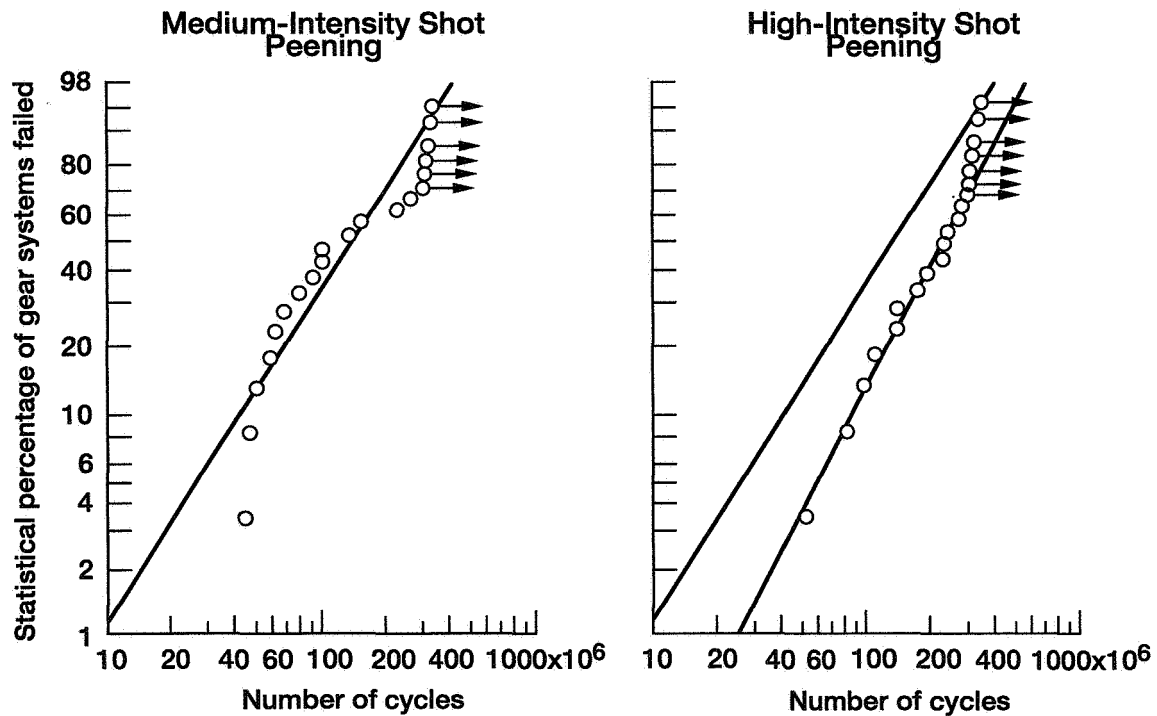


Fig. 10

## Surface Fatigue Life of VASCO X-2

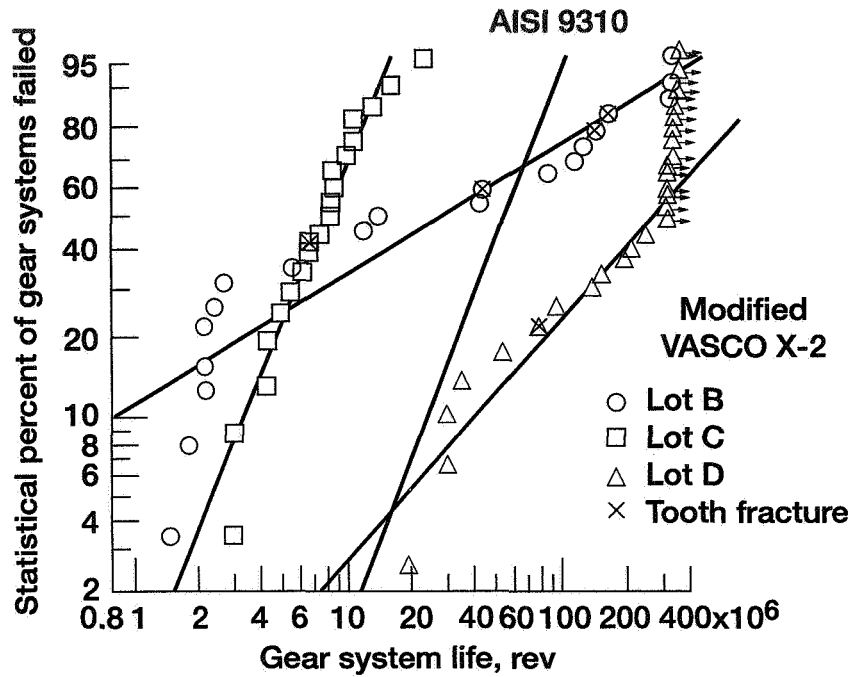


Fig. 11

## Surface Fatigue Life of High-Temperature Steels

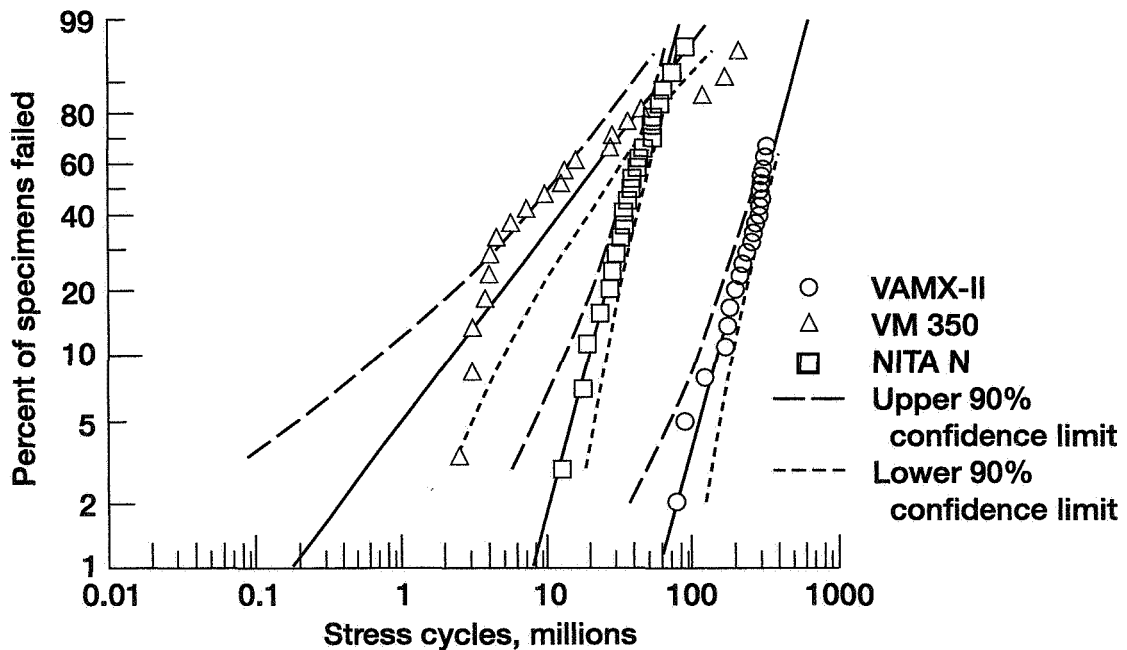


Fig. 12

## Surface Fatigue Life of 9310 and M50 NiL

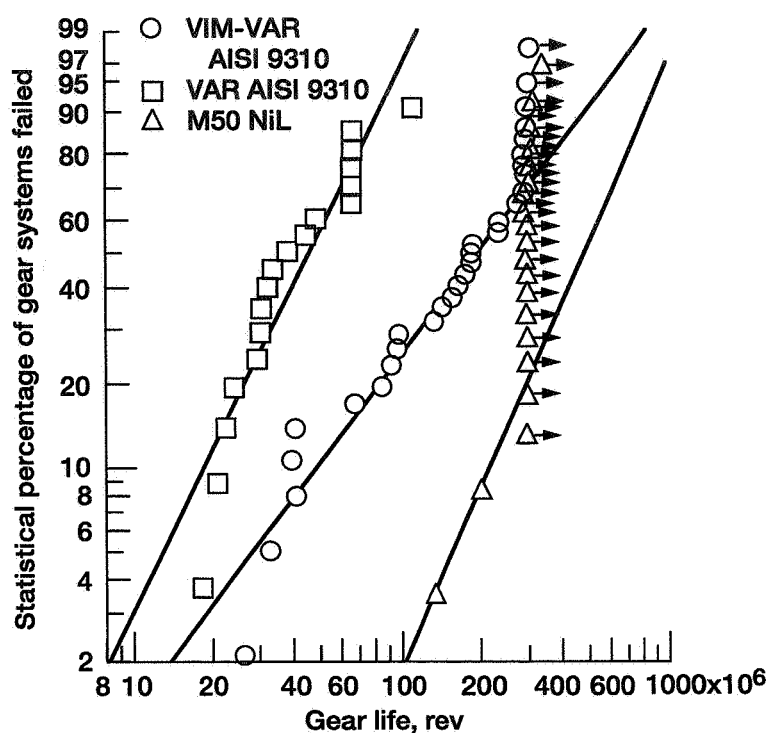


Fig. 13

## Surface Pitting Fatigue Lives of AISI 9310 With Different Lubricants

Lubricant code	Lubricant basestock	Gear system life, millions of stress cycles		Weibull slope	Failure index <sup>a</sup>	Confidence number, <sup>b</sup> percent
		10 percent	50 percent			
A	polyol-ester	5.1	20.4	1.36	30 of 30	—
B	polyol-ester	12.1	76	1.02	20 of 20	84
C	polyol-ester	5.7	20.7	1.46	20 of 20	55
D	polyol-ester	11.8	50.8	1.29	17 of 20	83
E	polyalkylene-glycol	46.5	152	1.59	15 of 19	99
F	polyol-ester	45.2	276	1.04	7 of 17	99
G	polyol-ester	103	568	1.1	5 of 18	99

<sup>a</sup> Number of failures out of number of tests.

<sup>b</sup> Percent of time that 10 percent life obtained with each lubricant will have the same relation to the 10 percent life of lubricant NASA A.

Fig. 14

## Surface Pitting Fatigue Lives of AISI 9310 Gears Run With Seven Different Lubricants

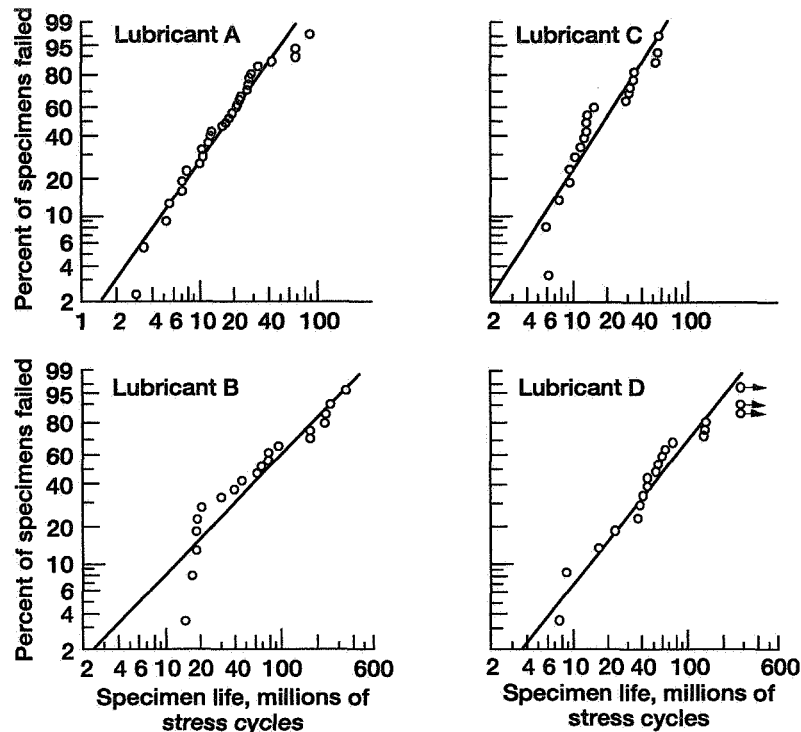


Fig. 15a

## Surface Pitting Fatigue Lives of AISI 9310 Gears Run With Seven Different Lubricants

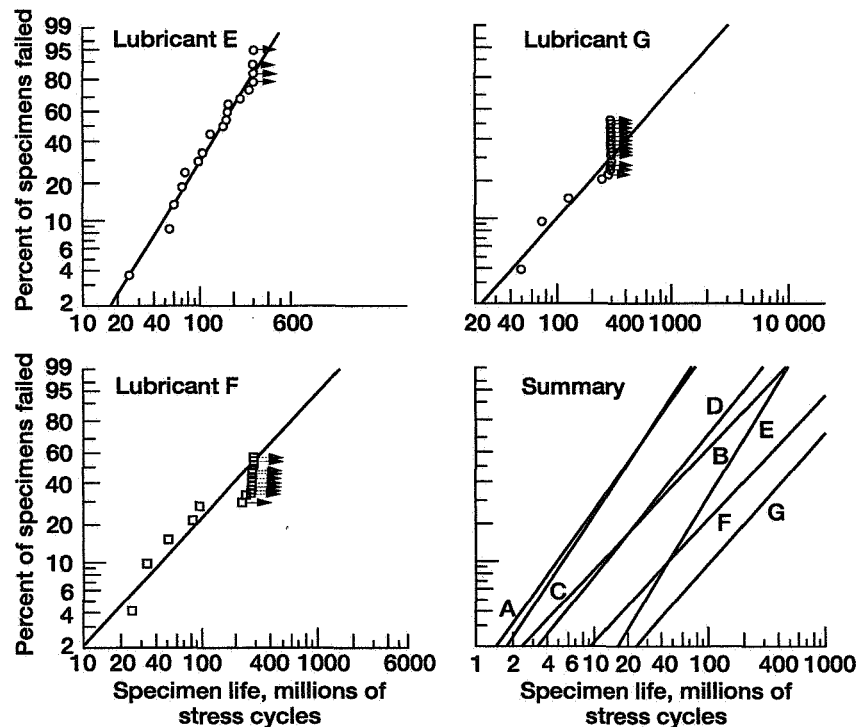


Fig. 15b

## Surface Fatigue Life at 248-ksi Hertz Stress

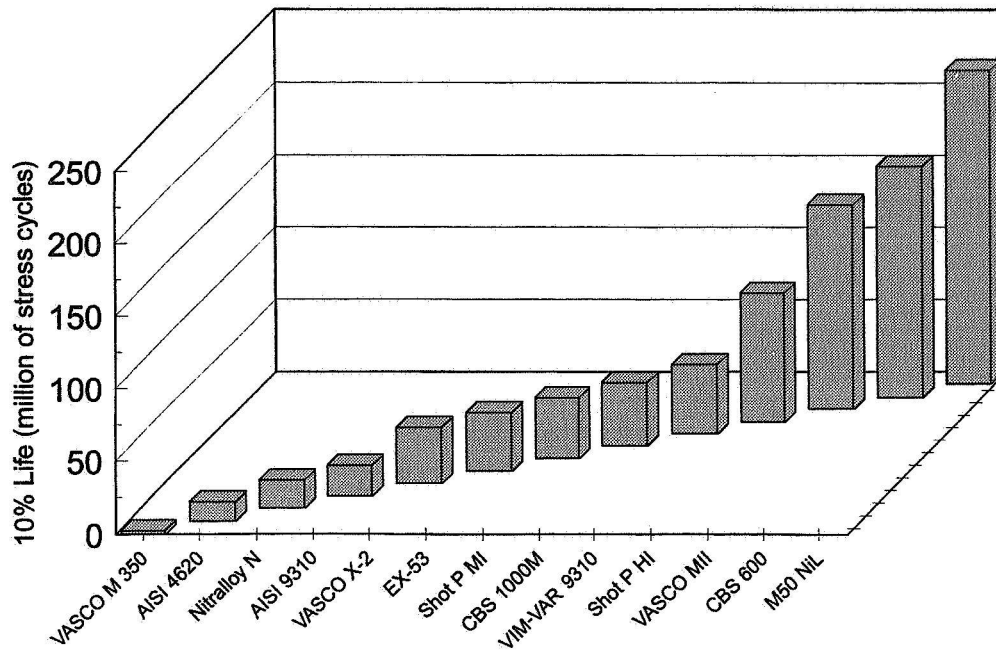


Fig. 16

## Relative Gear Surface Fatigue Life Versus Specific Film Thickness Ratio

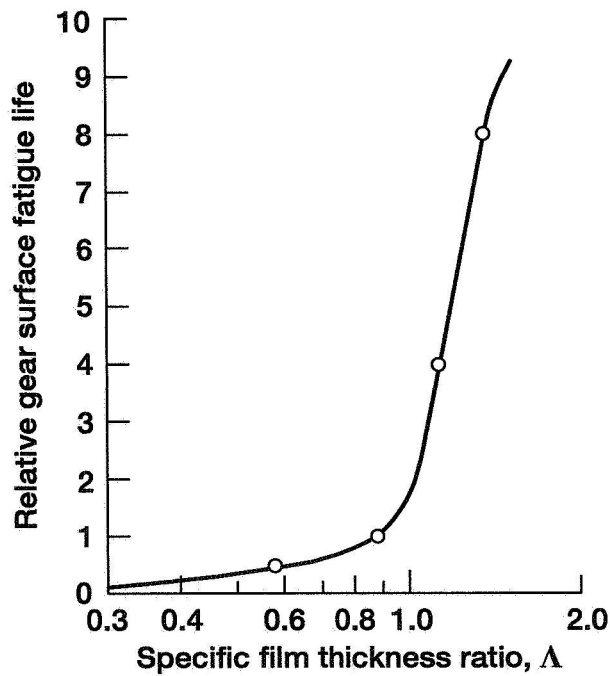


Fig. 17



54-07  
029 103

## COMPUTATIONAL INFRASTRUCTURE FOR ENGINE STRUCTURAL PERFORMANCE SIMULATION

078117

10P.

CHRISTOS C. CHAMIS  
NASA Lewis Research Center  
Cleveland, Ohio 44135

### Abstract

Select computer codes developed over the years to simulate specific aspects of engine structures are described. These codes include blade impact integrated multidisciplinary analysis and optimization, progressive structural fracture, quantification of uncertainties for structural reliability and risk, benefits estimation of new technology insertion and hierarchical simulation of engine structures made from metal matrix and ceramic matrix composites. Collectively these codes constitute a unique infrastructure readiness to credibly evaluate new and future engine structural concepts throughout the development cycle from initial concept, to design and fabrication, to service performance and maintenance and repairs, and to retirement for cause and even to possible recycling. Stated differently, they provide "virtual" concurrent engineering for engine structures total-life-cycle-cost.

### Introduction

The performance and reliability of propulsion structural systems depend on the interaction of their subsystems which, in-turn, depend on the interaction of their respective components (ref. 1). The performance of a specific component depends on the coupled effects of the system multi-disciplinary interaction on the component response (Fig. 1). Further, the integrated system response depends on the progressive and interacting influence of the coupled service loads/environment at all levels from sub-component, to component, to sub-system, to system. Interaction phenomena of interest include flutter, rotor instability, fatigue, flow separation, nonuniform combustion, blade containment, and noise suppression. The determination of aerothermodynamic system performance has traditionally relied on prototype tests whereas structural reliability has been determined from field data. Over the years, several integrated structural computer codes have been developed. Collectively, the codes constitute an inclusive infrastructure to computationally simulate engine structural performance. The most versatile of these are summarized in Fig. 2. A brief description of the capability of each computer code with a typical result from each follows:

**BLASIM** (Blade Assessment for Ice Impact) assesses the damage caused by foreign objects impact on engine blades. Examples of foreign objects include bird and ice. Also, this codes is capable of performing a variety of structural analyses including fatigue and flutter (Ref. 2). It consists of special finite element, composite mechanics, approximate design methods, dedicated substructuring and an optimization algorithm. A typical result obtained from BLASIM is shown in Fig. 3.

**CODSTRAN** (Composite Durability Structural Analysis) assesses the progressive structural damage in composite structures from damage initiation to structural fracture (Ref. 3). It is a combination of composite mechanics, finite element structural analysis and damage tracking. CODSTRAN accounts for all failure modes in composites, residual stresses and environmental effects. The failure modes evaluated using strength criteria thereby by-passing fracture toughness parameters. Though configured primarily for composites, it has been used for conventional metals and even reinforced concrete. It has also been used to simulate blade containment. A typical result is shown in Fig. 4.

**CSTEM** (Coupled Structural Thermal Acoustic Electromagnetic Tailoring) simulates analysis/design of multi-disciplinary, nonlinear behavior of composite structures (Ref. 4). It combines several 3-D finite element modules for the different disciplines with composites mechanics for polymer matrix, metal matrix and ceramic matrix composites and with an optimization routine. It has been used for structural problems, heat transfer, ice formation and more recently for fabrication processing. A typical result is shown in Fig. 5.

**NESSUS** (Nonlinear Evaluation of Stochastic Structures Under Stress) is the only code of its kind to quantify expected uncertainties in specified structural response by uncertainties specified at the lowest level of the formulation (Ref. 5). The lowest level usually consists of material properties, structural configuration, support conditions, loading conditions, etc. NESSUS combined finite element structural analysis with probabilistic concepts and can assess reliability and risk. A typical result is shown in Fig. 6.

**IPACS** (Integrated Probabilistic Assessment of Composite Structures) assesses the uncertainties in composite structures (Ref. 6). It combines NESSUS with probabilistic composites mechanics. Specified uncertainties at the lowest level include (in addition to those in NESSUS): constituent material properties, fabrication parameters laminate configuration variables and environmental effects. IPACS includes a resident data bank for several fibers and matrices. IPACS has been used to evaluate reliability and risk in a variety of composite structures. Typical results are shown in Fig. 7.

**T/BEST** (Technology Benefits Estimator) assesses the benefits gained by new technology insertions. This computer code may be considered as a “virtual” engine structure development facility. It has been under continuous development at Lewis Research Center for about three years. The computer code is identified as T/BEST (Ref. 7). T/BEST performs computational simulation to estimate the benefits of introducing new

technologies into existing or new propulsion systems at any level as shown in Fig. 8. The discipline modules used in T/BEST are: engine cycle (thermodynamic), engine weight, internal fluid mechanics, cost, mission, and coupled structural/thermal/tailoring. The executive system of T/BEST operates on stand-alone or networked workstations. Input files for all modules are generated automatically. T/BEST's modular approach allows for modifications and addition of analyses modules. All modules in T/BEST intercommunicate via a central neutral file. The modular structure of T/BEST is shown in Fig. 9. The execution sequence starts with the NNEPWATE (engine cycle) module in a clockwise direction and terminates with graphical display. A typical result is shown in Fig. 10.

HS/HTCS (Hierarchical Simulation of Hot Composite Structures) assesses the structural behavior of hot composite structures made from metal and ceramic matrix composites. Several different computer codes are included in this hierarchical structure as shown in Fig. 11. Each of these codes simulates a specific behavior at a specific scale starting from nanomechanics, through structural tailoring. The codes that have been used most frequently include METCAN (Metal Matrix Composite Analyzer, Ref. 8), CEMCAN (Ceramic Matrix Composite Analyzer, Ref. 9), and MMLT (Metal Matrix Laminate Tailoring, Ref. 10). A typical result from MMLT is shown in Fig. 12.

## Conclusions

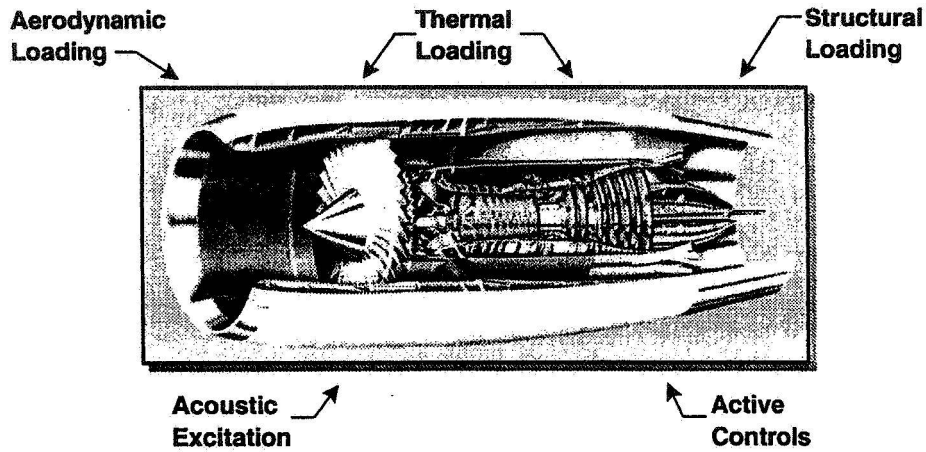
Select codes are available at the Structures and Acoustics Division at NASA Lewis Research Center to computationally simulate all aspects of engine structural response including tailoring, reliability and risk and benefits of new technology insertion. Typical results obtained from these codes are: (1) blade ice impact, (2) fan blade composite containment, (3) composite acoustic fatigue, (4) reliability of turbine blade, (5) reliability of fatigue life of a composite airfoil section, (6) benefits gained by using composites in engines and, (7) metal matrix laminate tailoring for improved load carrying capacity. Collectively, these codes constitute a "virtual" concurrent engineering and "virtual" engine structures development facility.

## References

1. Nichols, L. D. and Chamis, C. C., "Numerical Propulsion Systems Simulation: An Interdisciplinary Approach," NASA TM 10581, 1991.
2. E.S. Reddy and G.H. Abumeri, "Blade Assessment for Ice Impact (BLASIM) User's Manual, Version 1.0", NASA CR 191075, 1993.
3. Chamis, C.C., Murthy, P.L.N and Minnetyan, L: Progressive Fracture of Polymer Matrix Composite Structures: A New Approach. NASA TM 105574, January 1992.
4. Hartle, M., et. al, "CSTEM User's Manual," NASA Document , 1990.

5. "Probabilistic Structural Analysis for Select Space Propulsion System Structural Components," Annual Report by SwRI, Rocketdyne, University of Arizona, MARC Analysis Corp. and Columbia University for NASA LeRC, Contract NAS3-24389, 1986.
6. Chamis, C. C. and Murthy, P. L. N.: Probabilistic Composite Analysis. NASA CP 3104, Part 2, 1991, pp. 891-900.
7. Generazio, E. R., Chamis, C. C. and Abumeri, G. H. , "Technology Benefit Estimator (T/BEST) User's Manual," NASA TM 106785, December 1994.
8. Lee, H.J., Murthy, P.L.N. and Chamis, C.C: Metcan Updates for High Temperature Composite Behavior: Simulation/Verification. NASA TM 103682, 1991.
9. Mital, S. K., Murthy, P.L.N., and Chamis, C.C: "Ceramic Matrix Composites Properties/Microstresses With Complete and Partial Interphase Bond". NASA TM 106136, 1993.
10. Morel, M.R., Saravanos, D.A. and Chamis, C.C., "Tailored Metal Matrix Composites for High Temperature Performance", NASA TM 105816, 1992.

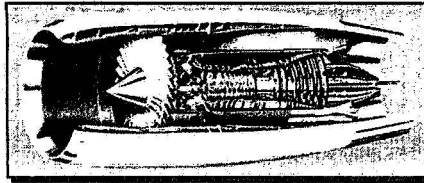
## *Engine Components Under Service-Environment Loadings*



*The structure is the natural multi-discipline integrator.*

Fig. 1

## *Engine Structures Computational Simulation Methods*



*BLASIM* -- *Low Impact Evaluation*

*CODSTRAN* -- *Progressive Structural Fracture Assessment*

*CSTEM* -- *Acoustic Fatigue and Coupled Multi-Discipline Analyses.*

*NESSUS* -- *Reliability/Risk of Metallic Structures*

*IPACS* -- *Reliability/Risk of Composite Structures*

*T-BEST* -- *System-Type Benefits Accrued From Structural Concepts/Technologies*

*HS/HTCS* -- *Inclusive of All Aspects of High Temperature Metal Matrix Composite Structures.*

Fig. 2

### Effect of Impact Location on Root Response

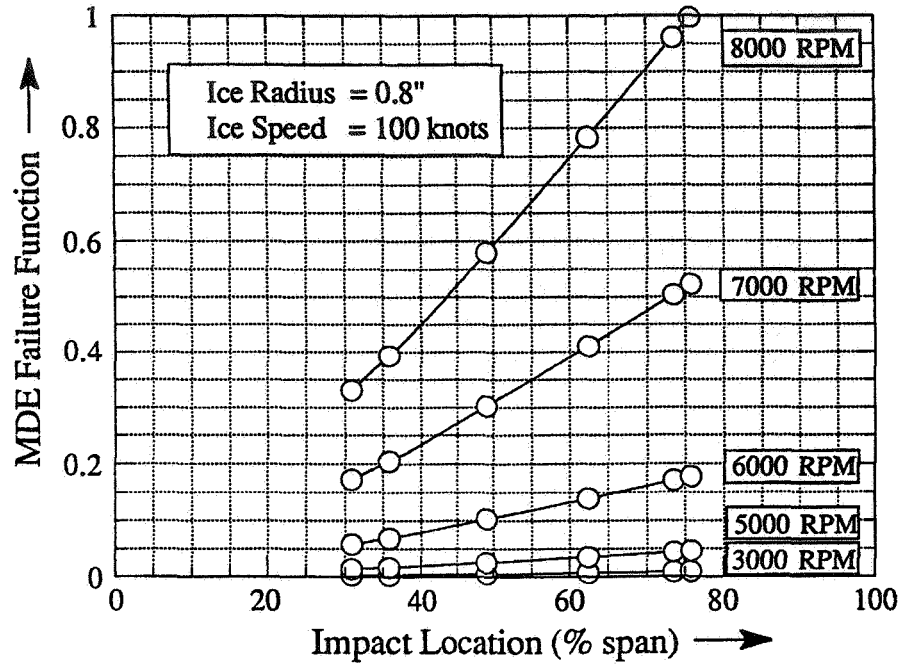


Fig. 3

### Effect of Shell Thickness on Damage

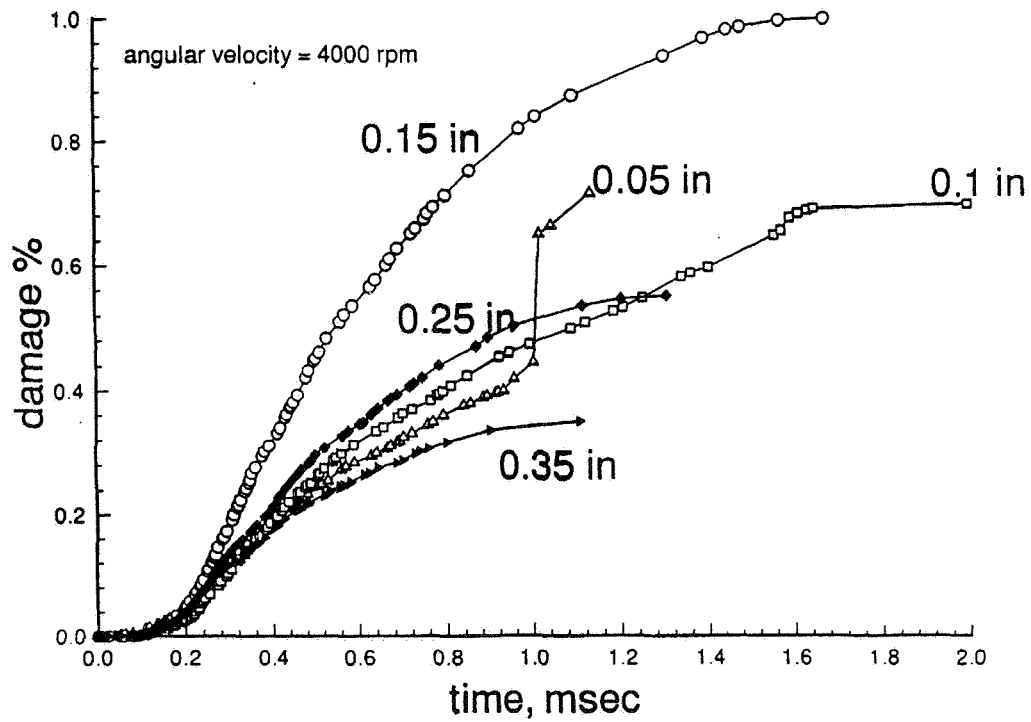


Fig. 4

## Acoustic Tailoring of Composite Fan Blades — Effect of Environment

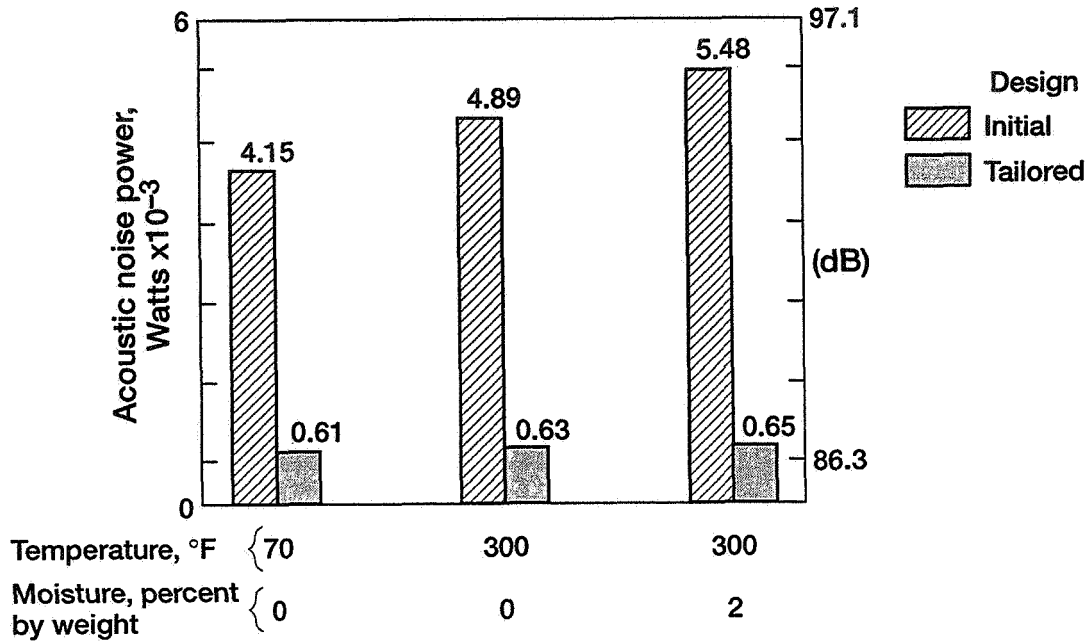


Fig. 5

CD-97-74646

## Results for the Creep Rupture Analysis

- By Varying  $t$ , a Distribution of Failure Probabilities can be Generated
- FEM Calculations are not Required for Each New  $t$  — only P2 and the Resulting Probability of Failure are Computed
- More Accurate (but Significantly More Costly) Combined Analysis Shows the Proposed Approach to be Efficient and Acceptably Accurate

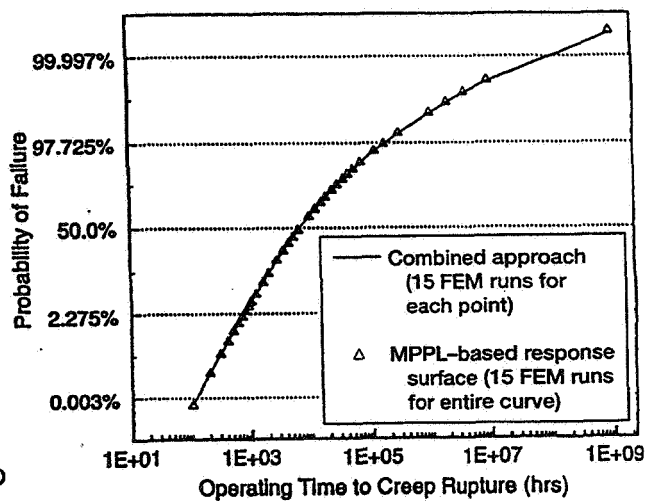


Fig. 6

## Compressive Fatigue Life of a Composite Wing (200 °F, 1% Moisture Content)

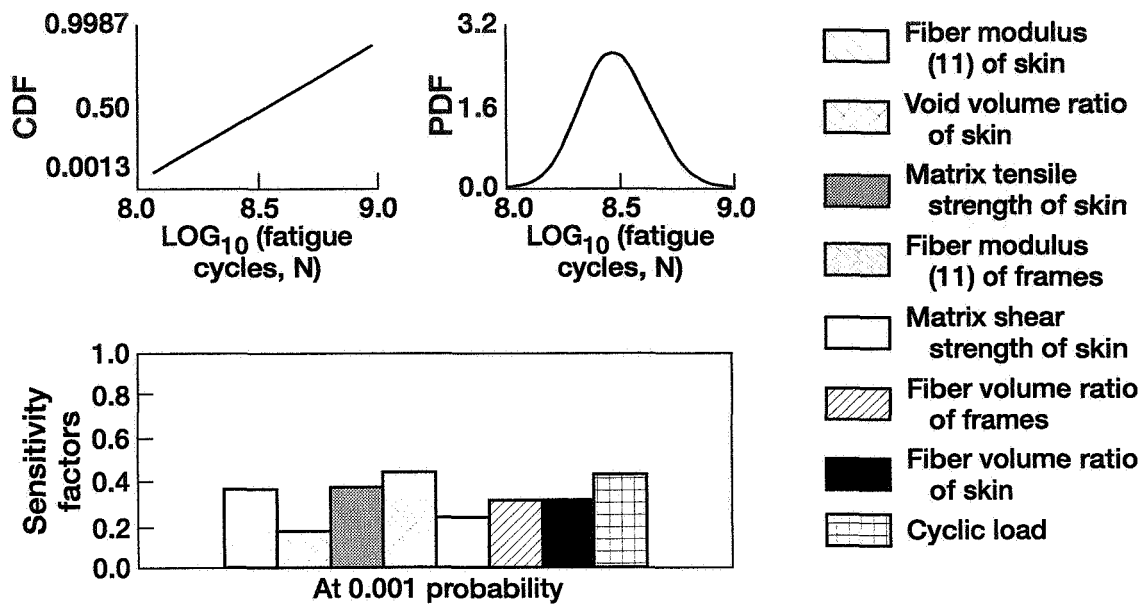
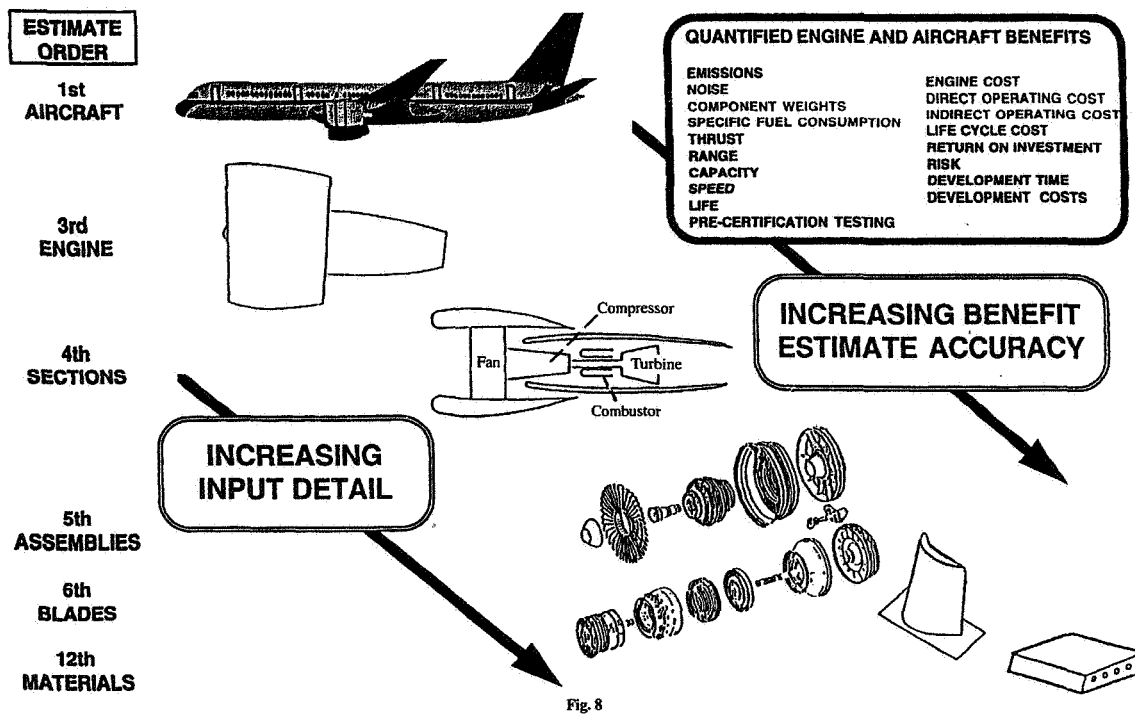


Fig. 7

## Hierarchical Technology Benefit Estimator





# T/BEST Modular Structure

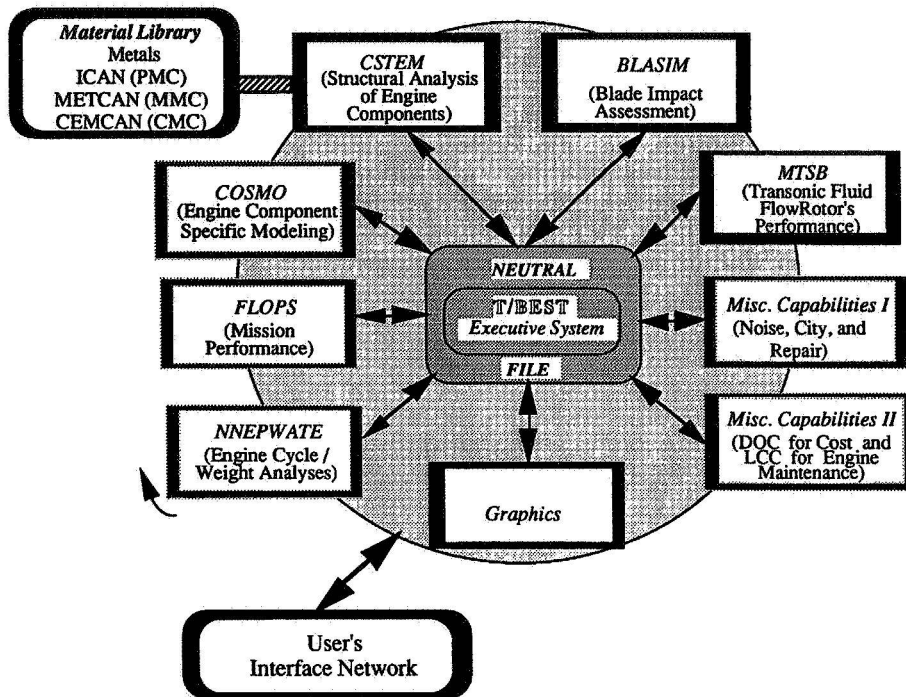


Fig. 9

## Aircraft Operating Cost Benefits of Advanced Composites Over Conventional Metals — Subsonic Transport

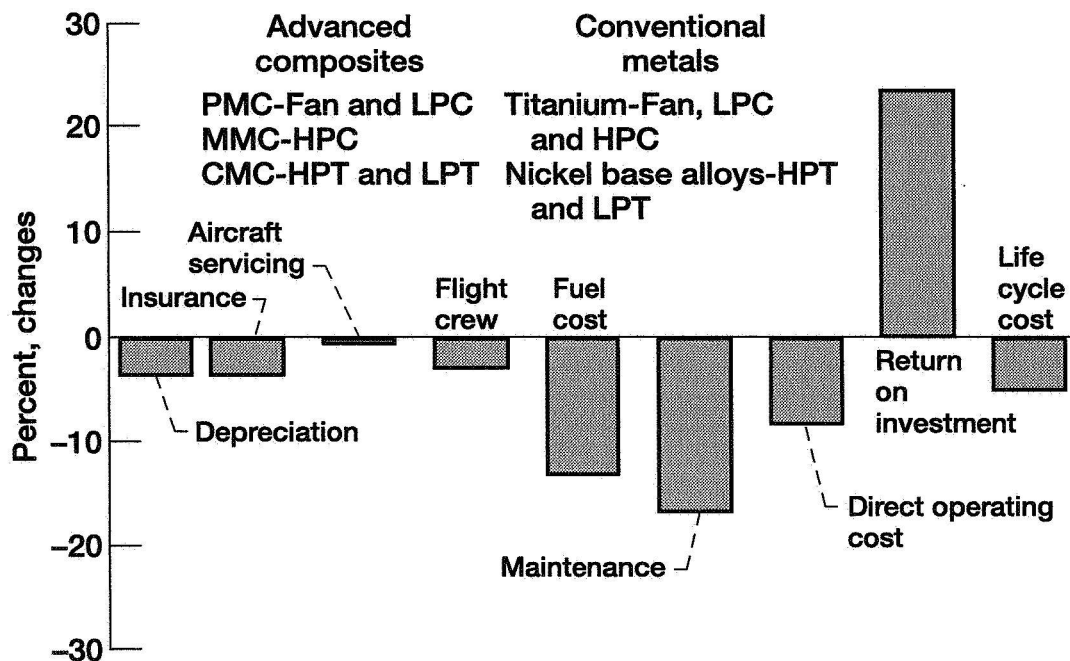


Fig. 10

# Hierarchical Computational Simulation/Tailoring of Hot Composite Laminates/Structures

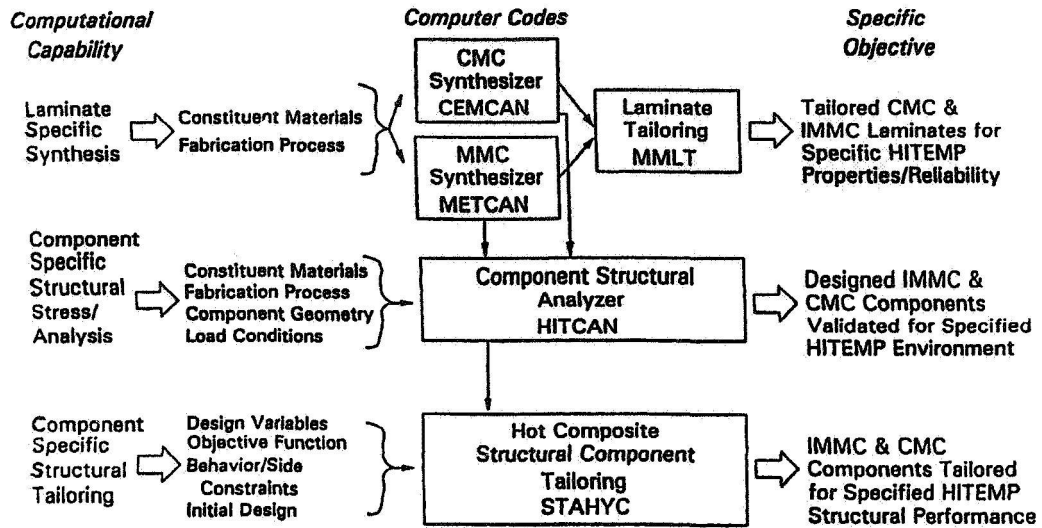


Fig. 11

## Effect of Optimal Processing on Fatigue Life

[0] SCS6/Ti-24Al-11Nb, 0.35 FVR (70 °F (23 °C), R = 0.1)

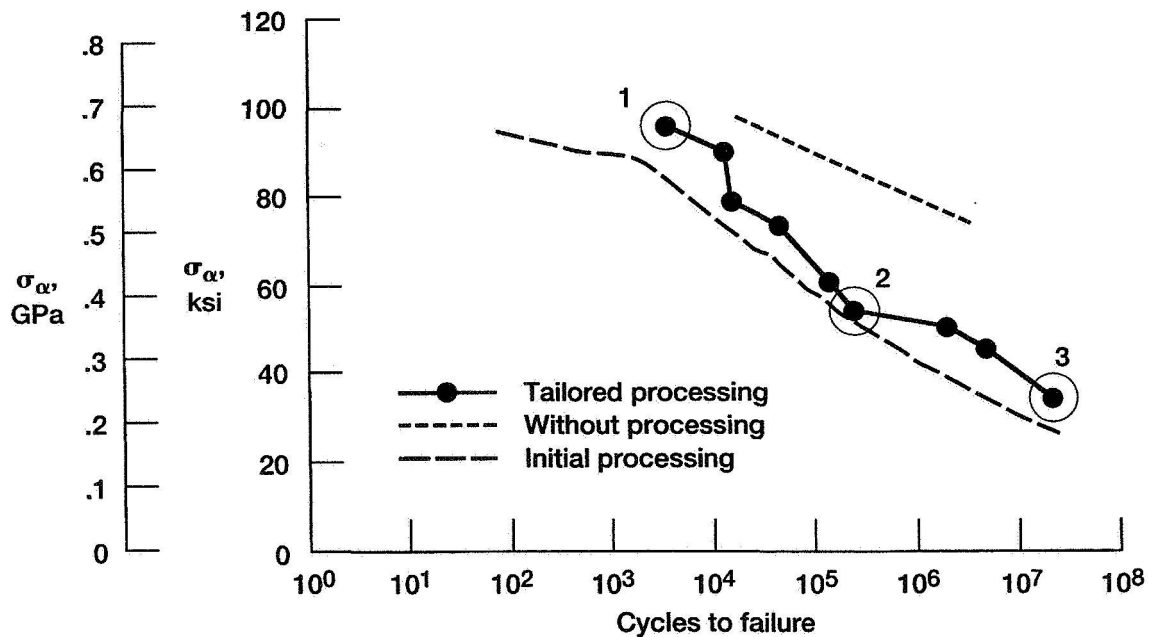


Fig. 12

55-38  
029104  
101.  
278118

# EFFICIENT EVALUATION AND OPTIMIZATION OF STRUCTURAL RELIABILITY\*

RAMANA V. GRANDHI  
Wright State University  
Dayton, OH 45435

and

Dale A. Hopkins  
NASA Lewis Research Center  
Cleveland, OH 44135

## Introduction

Use of approximations for calculating the structural failure probability under uncertainties is a necessary aspect. But efficient use of suitable approximations at different stages of reliability prediction and design makes this valuable tool practical for many large scale structures. This research addresses the modern approximation concepts and their utility in structural reliability estimation. Emphasis is placed on building higher order approximations using intervening variables to closely represent the nonlinear limit state functions. Several test problems with highly nonlinear performance functions are used to demonstrate the accuracy of the proposed method.

Many of the structural problems are modeled and simulated using the finite element methods (FEM) for obtaining a detailed structural response. FEM is a computationally intensive numerical procedure with a large number of degrees of freedom. With an increase in the complexity of the structural model and the multidisciplinary nature of analyses, the number of limit states and their computation increases very significantly. The requirement of frequent repetitive analysis of the structure hinders the utility of any tool and discourages that approach from being used. One particular tool which faces this difficulty is the computation of the structural reliability under parametric uncertainties.

A fundamental difficulty in calculating the structural reliability is the computation of the multifold integral representing uncertain quantities such as loads, geometry, material properties, and boundary conditions. The computation of the multiple integral is generally extremely complex and difficult for most of the practical problems. For numerically integrating, the inherent difficulties are that the limit state function has to be computed at many points of the  $n$ -dimensional domain using FEM, which is quite impractical. Therefore, relatively simple and accurate approximate techniques to evaluate the failure probability are demanded.

Typically, in reliability analysis methods, approximations are made in the space of independent, standard and normal variables,  $U$ , obtained from transformations. Accordingly, the limit state surface is also mapped to one in the new state space. In the standard space, the approximate failure probability is calculated by (i) first identifying the design point, also called the most probable failure point (MPP), which has a minimal distance from the origin, (ii) approximating the limit state surface using a first-order or second-order surface at the MPP, and (iii) evaluating the failure

---

\* Work funded under NASA Grant NAG 3-1489

probability defined by the approximating surface by exact or approximate means. In the first-order reliability method (FORM), the failure surface is approximated by the tangent plane at the MPP. FORM works well when the limit state surface has only one minimal distance point and the function is nearly linear in the neighborhood of the MPP. However, if the failure surface has large curvatures ( high nonlinearity ), the failure probability estimated using the safety index  $\beta$  by FORM may give unreasonable and inaccurate results [1]. In these cases more accurate approximate methods have to be applied. Several researchers [2,3] have developed second-order reliability methods (SORM) using quadratic approximations to replace the original failure surfaces. However, most of the methods do not work well in the case of negative or large curvatures. Also, the computation of the exact second-order derivatives matrix in all the SORM algorithms can be prohibitively expensive for the problems having a large number of random variables and the limit state functions computed using FEM. Furthermore, in some cases, the computed curvatures do not provide a realistic picture of the limit state surface in the neighborhood of the design point. For example, when the design point is an inflection point, the curvatures are zero and curvature-fitted paraboloid reduces to the tangent plane, thus, providing no improvement over the first-order approximation.

In this NASA Grant, efficient safety index search procedures were developed [4-8]. Wang and Grandhi calculated approximate second-order derivatives of the limit state function by using a two-point adaptive nonlinear approximation (TANA) [7] that was constructed during the safety index computation. Then the failure probability was calculated based on Tvedt's formula. The second-order derivatives were computed from the nonlinear approximation of the limit state function. Hence, the exact calculation of the higher order derivatives was avoided and significant computational savings were realized. Der Kiureghian, *et al* [3] used two semiparabola approximations to perform the second-order reliability approximations. The approximating paraboloid was defined by fitting a set of discrete points selected on the limit state surface at prescribed distances from the MPP,  $Y^*$ . This method had computational savings when the number of variables was large, and it approximately accounted for the higher-order terms. Also, it can be used for problems with an inflection point at  $Y^*$  since two semiparabolas were used.

In this research, a higher-order failure probability algorithm based on an adaptive nonlinear approximation is developed. The nonlinear approximation is constructed by using the function values and the first-order gradients of two points selected on the limit state surface, and its nonlinearity is automatically changed for different problems. The first-order Taylor series expansion in terms of the intervening variables gives closed form formulae of the nonlinear approximation. This higher-order reliability method (HORM) can be used for all  $\beta$  values and all curvatures, particularly for problems with highly nonlinear limit state functions or with an inflection point of the MPP. The method provides an exact result if an infinitely large number of terms are utilized. Since the exact second-order derivatives are not required, the method can realize significant computational savings for large scale problems. Large scale structural examples are used to demonstrate the developed methods.

## References

1. Melchers, R.E., Structural Reliability Analysis and Prediction, Ellis Horwood Limited, UK., 1987.
2. Cai, G.Q., and Elishakoff, I., "Refined Second-order Reliability Analysis," Structural Safety, Vol. 14, No. 4, July 1994, pp. 267-276.
3. Der Kiureghian, A., Lin, H.Z. and Hwang, S.J., "Second Order Reliability Approximations," Journal of Engineering Mechanics, ASCE, Vol. 113, 1987, pp. 1208-1225.

4. Reddy, M.V., Grandhi, R.V. and Hopkins, D.A., "Reliability Based Structural Optimization: A Simplified Safety Index Approach," *Journal of Computers and Structures*, Vol. 53, No. 6, 1994, pp. 1407-1418.
5. Wang, L.P. and Grandhi, R.V., "Intervening Variables and Constraint Approximations In Safety Index and Failure Probability Calculations," *Structural Optimization*, Vol. 10, No. 1, 1995, pp. 2-8.
6. Wang, L.P. Grandhi, R.V. and Hopkins, D.A., "Structural Reliability Optimization Using an Efficient Safety Index Calculation Procedure," *International Journal for Numerical Methods in Engineering*, Vol. 38, No. 10, 1995, pp. 1721-1738.
7. Wang, L.P. and Grandhi, R.V., "Improved Two-Point Function Approximations for Design Optimization," *AIAA Journal*, Vol. 33, No. 9, Sept. 1995, pp. 1720-1727.
8. Wang, L.P. and Grandhi, R.V., "Safety Index Calculation Using Intervening Variables for Structural Reliability Analysis," *Journal of Computers and Structures*, Vol. 59, No. 6, 1996, pp. 1139-1148.

## Research Objective

- Apply the modern approximation concepts and validate their utility in structural reliability estimation
- Build a high quality approximation to closely represent the nonlinear limit state functions
- Develop an accurate Higher–Order Reliability Method (HORM) for all  $\beta$  values, all curvatures, particularly for the problems with high nonlinearity or with an inflection point of MPP
- Demonstrate the accuracy of the proposed HORM using several examples

## Mathematical Model for Failure Probability

● Review

$$P_f = \int_{\Omega} f_X(X) dX$$

$X$ : Random variables (loads, geometry, material properties, etc.)

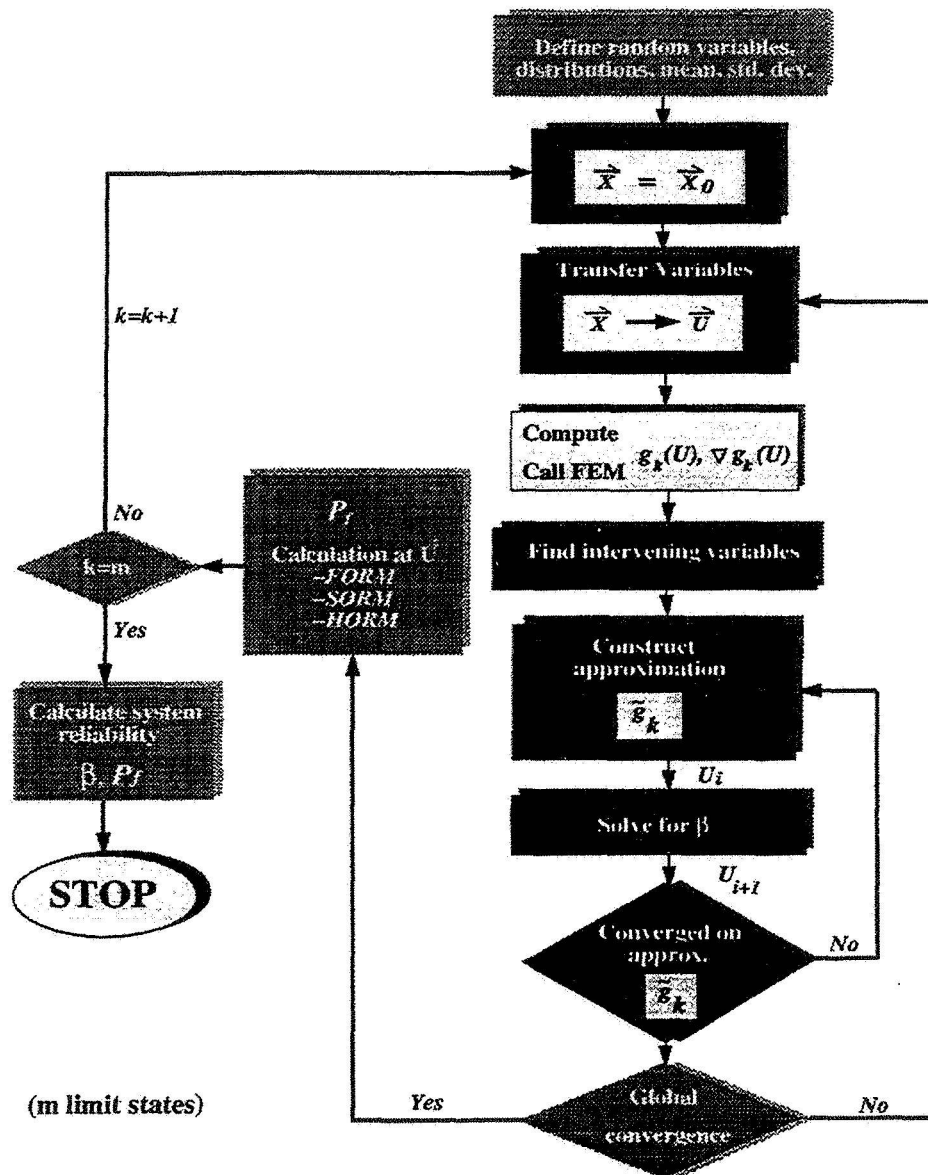
$\Omega$ : Failure region modeled by limit state functions  $g(X) \leq 0$

$f_X(X)$ : Joint probability density function

$P_f$  : Structural failure Probability

- Direct numerical integration and Monte Carlo simulation are time consuming. Relatively simple and accurate approximate techniques are demanded.

## Approximations in Failure Probability Calculations



## Two-point Adaptive Nonlinear Approximation for searching $\beta$

● **HORM**

### ● Intervening variables

$$y_i = x_i^{p_i} \quad i=1, 2, \dots, n$$

$x_i$ : original variable

$p_i$ : nonlinearity index for each variable

### ● Approximate function

$$\tilde{g}(X) = g(X_2) + \sum_{i=1}^n \frac{\partial g(X_2)}{\partial x_i} \frac{x_{i,2}^{1-p_i}}{p_i} (x_i^{p_i} - x_{i,2}^{p_i}) + 0.5 \varepsilon_2 \sum_{i=1}^n (x_i^{p_i} - x_{i,2}^{p_i})^2$$

Approximation is a second-order Taylor expansion at the current point  $X_2$  in terms of the intervening variables  $y_i$ , and the Hessian matrix has only diagonal elements of the same value  $\varepsilon_2$ .

## Two-point Adaptive Nonlinear Approximation for searching $\beta$

● **HORM**

### ● Establish n equations by matching the derivatives of exact and approximate function at the previous point $X_1$ .

$$\text{Exact} \rightarrow \frac{\partial g(X_1)}{\partial x_i} = \frac{\partial g(X_2)}{\partial x_i} \frac{x_{i,2}^{1-p_i}}{x_{i,2}^{p_i}} + \varepsilon_2 p_i (x_{i,1}^{p_i} - x_{i,2}^{p_i}) x_{i,1}^{p_i-1} \leftarrow \text{Approx.}$$

### ● Establish the (n+1)th equation by matching the exact and approximate function values at the previous point $X_1$ .

$$\text{Exact} \rightarrow g(X_1) = g(X_2) + \sum_{i=1}^n \frac{\partial g(X_2)}{\partial x_i} \frac{x_{i,2}^{1-p_i}}{p_i} (x_{i,1}^{p_i} - x_{i,2}^{p_i}) + 0.5 \varepsilon_2 \sum_{i=1}^n (x_{i,1}^{p_i} - x_{i,2}^{p_i})^2 \leftarrow \text{Approx.}$$

### ● Solve n+1 equations to obtain $p_i$ and $\varepsilon_2$

### ● Employ this approximation instead of exact FEM analysis for $\beta$ search and update the approximations at converged solution using exact analysis

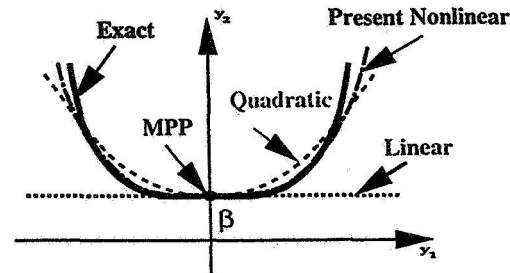


## First-Order Reliability Method (FORM)

● Review

- Approximate the failure surface using a tangent plane at MPP

$$P_f = \Phi(-\beta)$$



- FORM works well for the problems with linear or nearly linear limit state functions, but it may produce unreasonable and inaccurate results for highly nonlinear problems

## Proposed Higher-Order Reliability Method (HORM)

- Adaptive nonlinear approximations are used to approximate the limit state surface.
- Approximation closely represents the nonlinear limit state function.
- Accurate for all  $\beta$  values and all curvatures.
- Accurate for the problems with highly nonlinear limit state functions and with an inflection point.
- Significant reduction in computational effort for large scale problems because exact second-order derivatives are not needed.

## Two-point Adaptive Nonlinear Approximation for $P_f$ Calculation

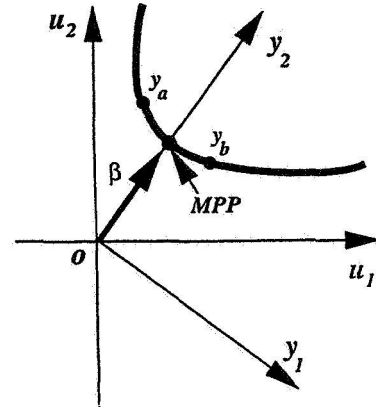
● **HORM**

- Rotate U-space to a new standard normal Y-space

$$Y = R U$$

In Y-space,  $y_n$  axis is in coincidence with the  $\beta$  vector

- Find two points,  $y_a$  and  $y_b$ , based on the approximate performance function constructed for computing  $\beta$
- No extra calculations are needed in finding  $y_a$  and  $y_b$



### Example 1

- Performance function:

$$g(x_1, x_2) = 2.2257 - 0.00131 (x_1 + x_2 - 20)^3 + 0.23570 (x_1 - x_2)$$

Normal distributions

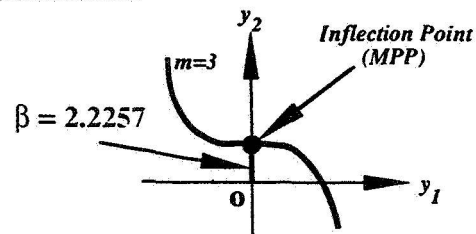
Mean:  $\bar{x}_1 = \bar{x}_2 = 10$

Standard deviation:  $\sigma_1 = \sigma_2 = 3$

- 3 g-function and 2 gradient calculations for MPP search
- No extra exact analyses for finding  $y_a$  and  $y_b$
- The approximation obtained for  $P_f$  calculation

$$y_2 = 2.2257 - 0.1 y_1^3$$

$m=3, a_1 = -0.1 < 0, \text{ Case 4}$



## Failure Probability Comparisons for Example 1

Method	Exact Analysis for $P_f$			
	g – calculation	First-order Gradients	Second-order Gradients	Failure Probability $P_f$
<b>FORM</b>	0	0	0	0.013014
<b>Breitung</b>	0	1	1	0.013014
<b>Tvedt</b>	0	1	1	0.013014
<b>Cai–Elishakoff</b>	0	1	1	0.013014
<b>Koyluoglu–Nielsen</b>	0	1	1	0.013014
<b>Monte Carlo</b>	Simple Size = 1,000,000			0.019188
<b>Present</b>	0	0	0	0.018180

### Example 3 : Circular Shaft

- **Performance function (U-space):**

$$g(u_1, u_2, u_3) = (u_1 + \frac{\bar{u}_1}{\sigma}) + (u_2 + \frac{\bar{u}_2}{\sigma}) + (u_3 + \frac{\bar{u}_3}{\sigma}) - e$$

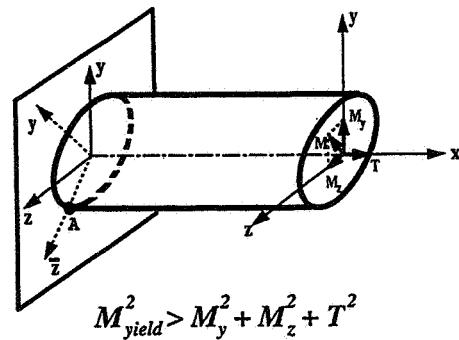
- **Normal distributions**

- *e* is the radius of the non-central sphere (safe domain in U-space)

- *m* = 2, the Koyluoglu–Nielsen formula is used

- Curvatures  $a_i$  are calculated by the proposed nonlinear approximation

- Four cases are tested for different *r* values (  $r = (\frac{\bar{u}_1}{\sigma})^2 + (\frac{\bar{u}_2}{\sigma})^2 + (\frac{\bar{u}_3}{\sigma})^2$  )



## Summary Remarks

- **Higher-order reliability method (HORM) is developed based on two-point adaptive nonlinear approximation**
- **HORM doesn't require any second-order or higher-order gradients**
- **HORM overcomes the drawbacks of Breitung, Tvedt and Cai-Elishakoff SORMs**
- **HORM extends the use of Koyluoglu-Nielsen method to the problems with highly nonlinear limit state functions and with an inflection point at MPP**
- **HORM is accurate for all  $\beta$  and all curvatures**
- **Significant reduction in computational effort for large scale problems**

## Focus of Future Research

- **Structural Optimization based on higher-order reliability analysis.**
- **Application on a turbine blade structure with multi-disciplinary limit state functions.**
- **System reliability analysis and optimization.**

56-07  
029105  
12P.  
578119

# **Optimization of Air-Breathing Propulsion Engine Concepts\***

**SURYA N. PATNAIK\***  
Ohio Aerospace Institute  
22800 Cedar Point Road  
Brook Park, Ohio 44142

and

**Dale A. Hopkins**  
NASA Lewis Research Center  
Cleveland, Ohio 44135

## **Introduction**

Air-breathing propulsion engines play an important role in the development of both civil and military aircraft. Design optimization of such engines can lead to higher power, or more thrust for less fuel consumption. A multimission propulsion engine design can be modeled mathematically as a multi-variable global optimization problem, with a sequence of subproblems, which are specific to the mission events defined through Mach number, altitude, and power setting combinations.

## **Solution Strategy**

A solution strategy has been developed for design optimization of air-breathing propulsion engine concepts through a soft coupling of the engine performance analyzer NEPP, an acronym for NASA Engine Performance Program (ref. 1), with the design optimization test bed CometBoards, which stands for Comparative Evaluation Test Bed of Optimization and Analysis Routines for the Design of Structures (refs. 2 and 3). Direct solution of such problems encountered convergence difficulties because of the large number of mission points, diverse constraint types, and overall ill-conditioning of the design space. However, some of the unique features of CometBoards, which include a cascade strategy, variable and constraint formulations, and scaling especially devised for difficult multi-disciplinary applications, could successfully optimize the performance of both subsonic and supersonic engines over their flight envelopes. The CometBoards and NEPP combined strategy converged to the same global optimum solution even when initiated from different design points. Typically, the NEPP code alone required many cycles of manual interventions to extract an acceptable solution,

---

\*Work funded under NASA-OAI cooperative agreement-NCC 3-453.

especially because of the unreliable nature of its optimization scheme. The reliable and robust NEPP and CometBoards combined design tool has eliminated manual interventions, and it is much easier to use, thus adding value to the engine cycle analysis procedure.

### Numerical Examples

Solutions for two numerical examples, consisting of a wave-rotor-topped subsonic engine and a mixed-flow turbofan engine design are included to illustrate the capability of the combined design tool. Design optimization of the wave-rotor-topped engine with four ports was carried out for a 47-mission-point flight envelope. To assess benefits that accrued from wave rotor topping, most base-line variables and constraints were declared passive, while rotational speed, heat added, and fuel flow were considered as active variables. Important active constraints included limits on maximum speed on all compressors, surge margin for all compressors, temperature, etc. Engine thrust was the merit function. The cascade strategy successfully solved the design, which consisted of 47 sub-problems, one for each mission point. For the mission point defined by Mach = 0.1 and altitude = 5000 ft, the convergence of the two-optimizer cascade strategy is shown in figure 10. The first optimizer produced an infeasible design at 67 060.87 lb thrust. The second optimizer produced a feasible optimum solution at 66 901.28 lb thrust, which has been verified graphically (fig. 11).

Design of a mixed-flow supersonic engine with constraints specified on the maximum compressor speed, acceptable surge margins, discharge temperatures, pressure ratios, mixer extreme Mach number, etc. has been cast as an optimization problem with engine thrust as the merit function, and bypass ratio, mixer pressure balance, r-values for fan and compressor, fuel flow, etc. as active design variables. The 122-mission-point flight envelope required the solution of 122 optimization sub-problems. The combined tool, using a four-optimizer cascade strategy, successfully solved the engine problem and converged to the same global solution even when initiated from different initial points. The engine solutions were normalized with respect to NEPP answers and depicted in figure 18. The current solution was found superior for most of the 122 mission points. In brief, the CometBoards and NEPP combined tool successfully solved the 122-mission-point, mixed-flow turbofan engine design optimization problem.

### References

1. Klann, J.L., Snyder, C.A., NEPP Programmers Manual, NASA TM-106575, 1994.
2. Patnaik, S.N., Coroneos, R. M., and Hopkins, D.A., Comparative Evaluation of Different Optimization Algorithms for Structural Design Applications, Int. Jnl. Num. Meth. Engrg. Vol. 39, 1996, pp. 1761-1774.
3. Guptill, J.D., Coroneos, R., Patnaik, S.N., D.A. Hopkins, and Berke, L., CometBoards Users Manual, NASA TM-4537, 1996.

## Outline

- Background
- COMETBOARDS Test-Bed
- NEPP Analyzer
- Wave-Rotor-Topped Subsonic Engine
- Mixed-Flow Turbofan Supersonic Engine
- Concluding Remarks

Fig. 1

CD-97-74761

## A Background for Design Test Bed COMETBOARDS

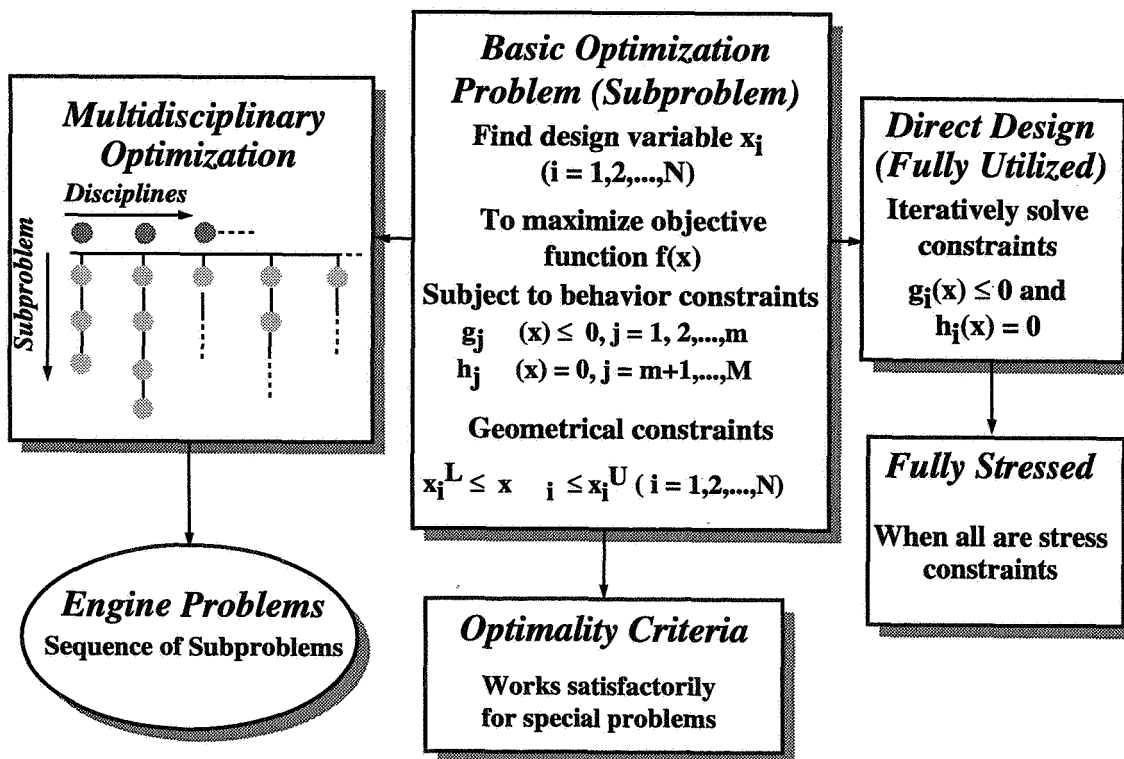


Fig. 2

CD-97-74762

## Issues and Solution Strategies for Engine and Aircraft Problems

- Distortion of Design Space
  - Engine thrust in kilopounds differs from bypass ratio—a small number
  - Velocity and field length differ in magnitude and units of measure

– Solution—Global Scaling of All Parameters

- Large Sequence of Optimization Subproblems

– Solution—Cascade Strategy

- Intensive Computation in Reanalysis and Gradients

– Solution—Neural Network and Regression Approximations

Fig. 3

CD-97-74763

## COMETBOARDS

General-Purpose Optimization Engine for Multidisciplinary Design Problems

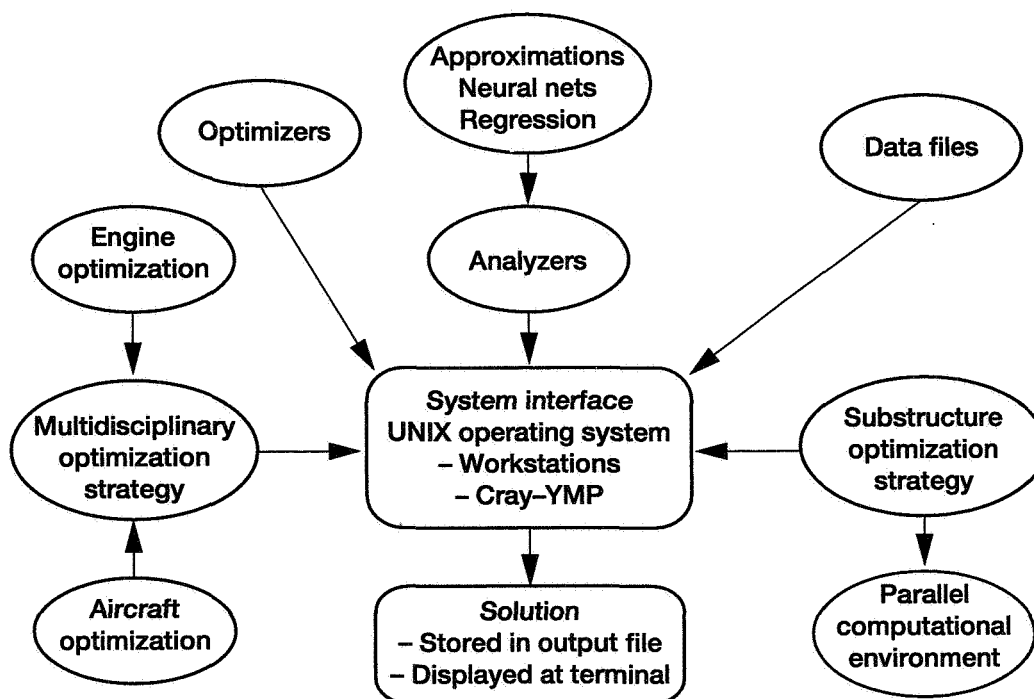


Fig. 4

CD-97-74764



## Key Features of COMETBOARDS

- Multidisciplinary Optimization
- State-of-the-Art Optimization Algorithms
- Substructure Optimization in Sequential and Parallel Computational Platforms
- Other Unique Strengths
  - Cascade Optimization Strategy
  - Design Variable Formulation
  - Constraint Formulation
  - Global Scaling Strategy
  - Quick Analyzer Integration Through 'Soft Coupling'
  - Analysis Approximations

Fig. 5

CD-97-74765

### Cascade Solution for a Subsonic Aircraft

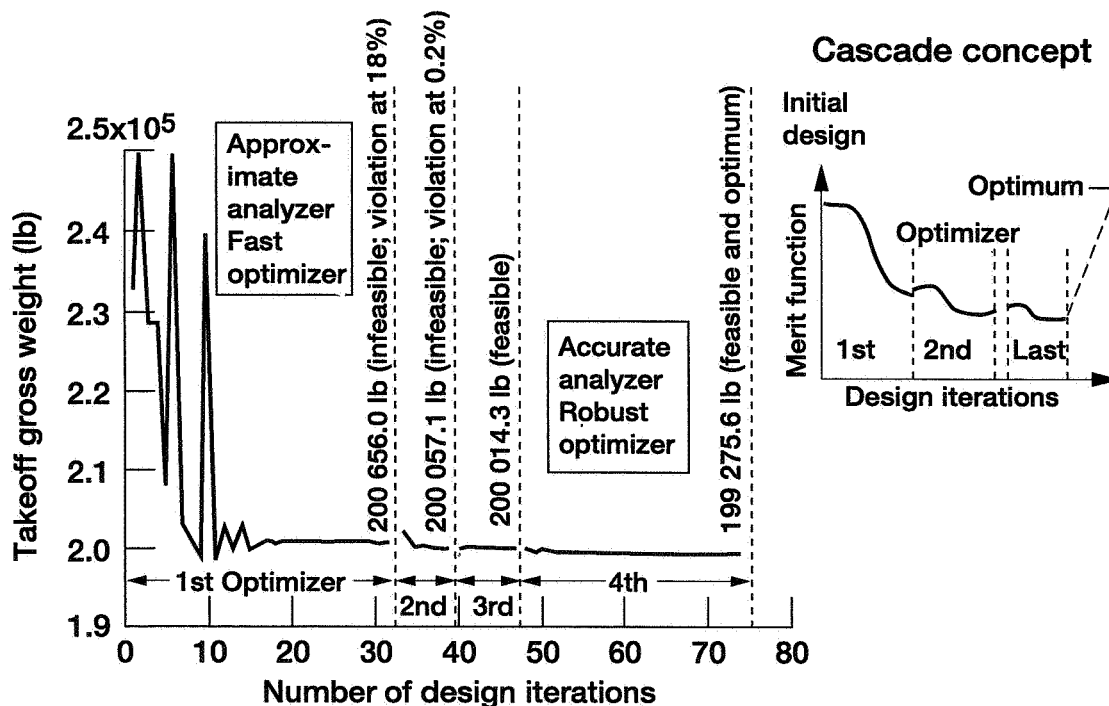


Fig. 6

CD-97-74766

## NASA Engine Performance Program—NEPP

- NEPP is used to predict engine performance
- NEPP is a zero-dimensional, steady-state engine analyzer
- Combines component maps to predict engine performance

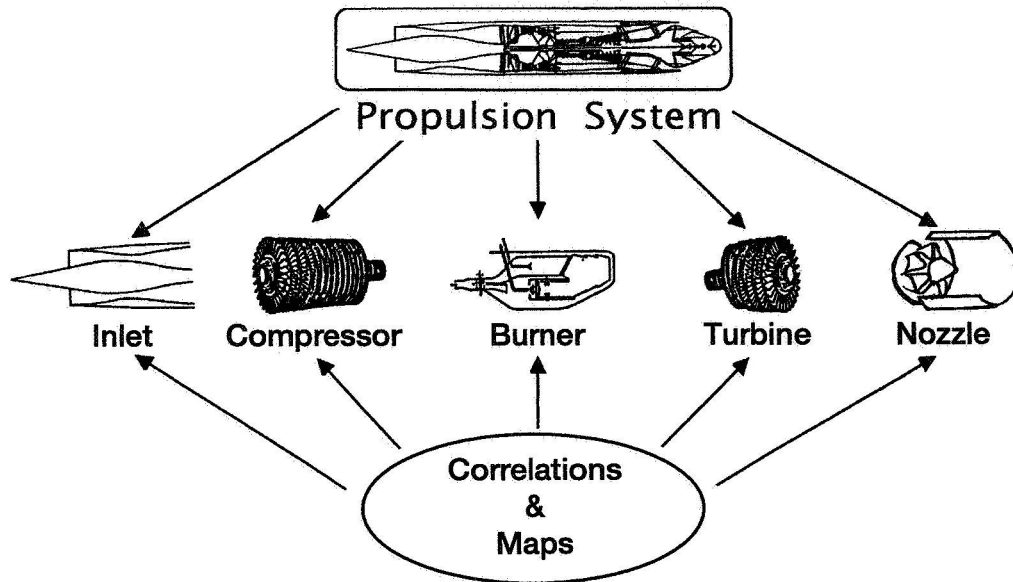
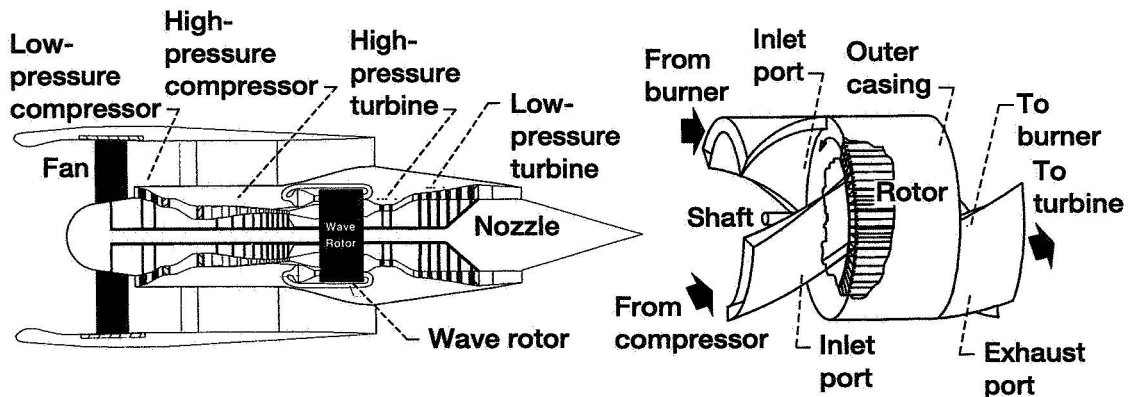


Fig. 7

CD-97-74774

## Optimization of Wave-Rotor-Topped Engine



**Objective:** Maximize engine thrust over 47-mission flight envelope

**Design variables:**

- Heat added in wave rotor
- Wave rotor rotational speed

**Behavior constraints:**

- Compressor speeds
- Wave rotor temperature
- Compressor surge margins

Fig. 8

CD-97-74767

# Flight Envelope for Subsonic Turbofan With Wave Rotor

47 Mission Points

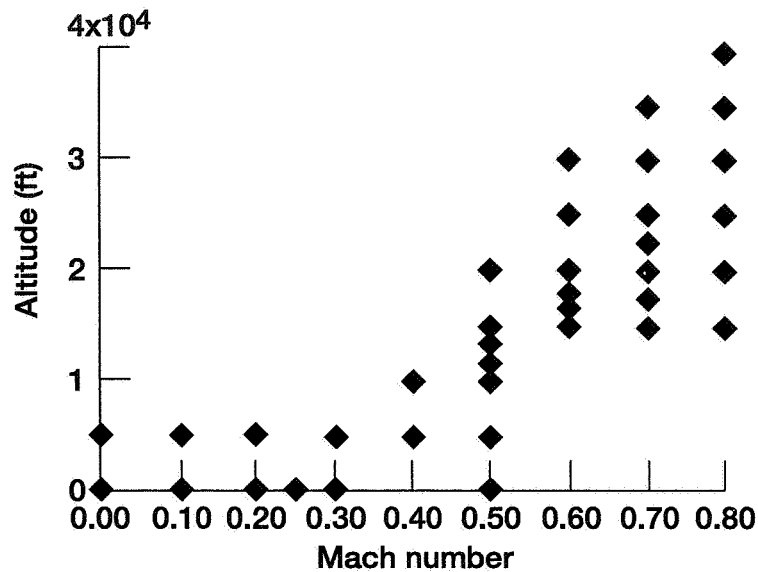


Fig. 9

CD-97-74768

## Convergence History of Cascade Strategy for a Wave-Rotor-Enhanced Subsonic Engine

Altitude = 5000 ft; Mach = 0.1

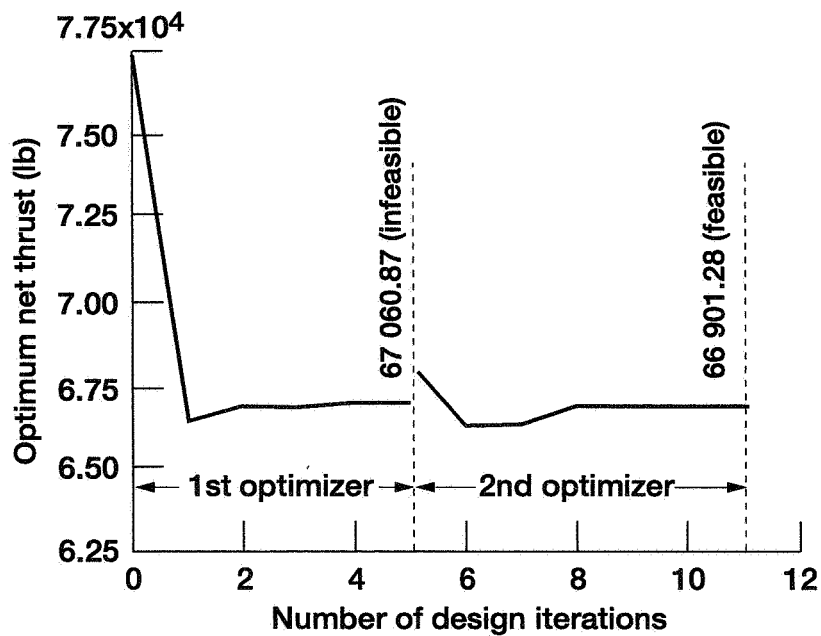


Fig. 10

CD-97-74769

## Graphical Verification for Subsonic Wave Rotor

Mach 0.4; Alt = 5000 ft

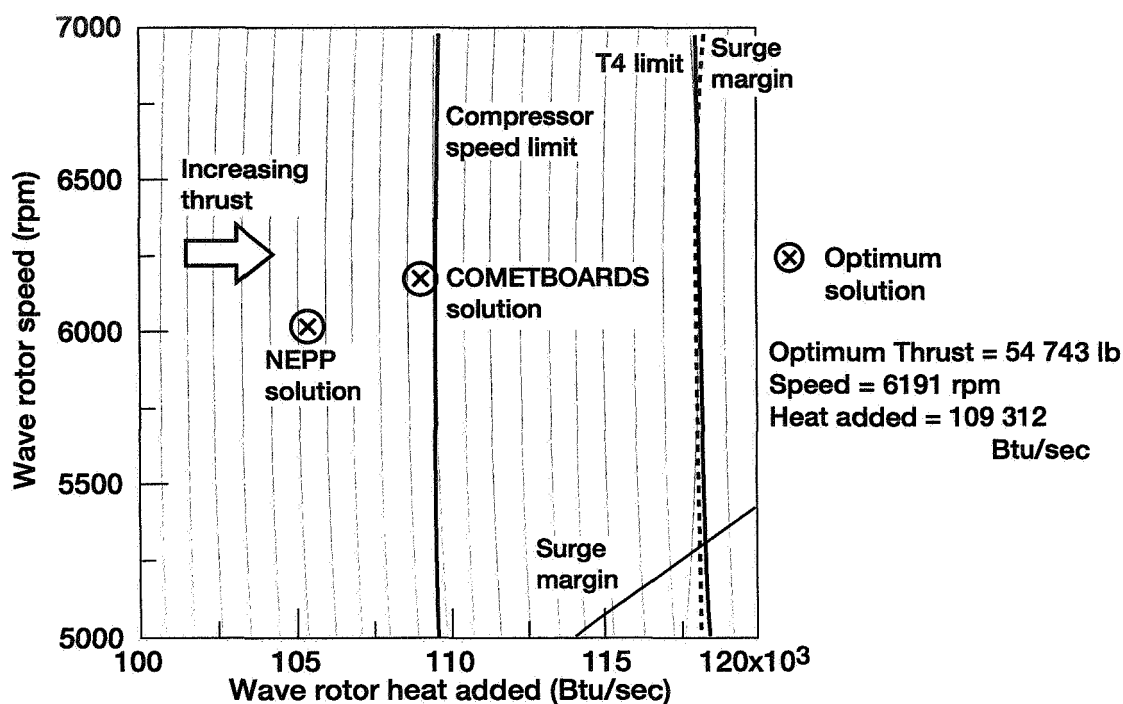


Fig. 11

CD-97-74770

## Wave Rotor Concept in a 47-Mission Subsonic Engine Design

Mission			Optimum thrust, lb		COMETBOARDS improvement over NEPP, percent	Number of Active constraints*
No.	Altitude, ft	Mach	COMETBOARDS	NEPP		
1	Sea level	0.25	70 075	70 075	0.00	3 (1, 7, 18)
13	10 000	0.40	45 135	43 072	4.80	4 (1, 3, 14, 18)
20	20 000	0.51	29 279	29 221	0.20	4 (1, 3, 14, 18)
26	30 000	0.60	18 827	17 898	5.20	4 (1, 3, 14, 18)
32	30 000	0.70	19 161	18 203	5.26	3 (1, 3, 14, 18)
38	20 000	0.80	30 898	30 110	2.62	3 (1, 3, 18)
47	40 000	0.85	12 684	12 611	0.58	3 (1, 3, 18)

\*1—maximum fan speed  
14—surge margin on fan

3—maximum compressor speed  
18—surge margin on compressor

7—maximum wave rotor outlet temperature

Fig. 12

CD-97-74771

## Value-Added Benefit in Design of a Subsonic Wave Rotor

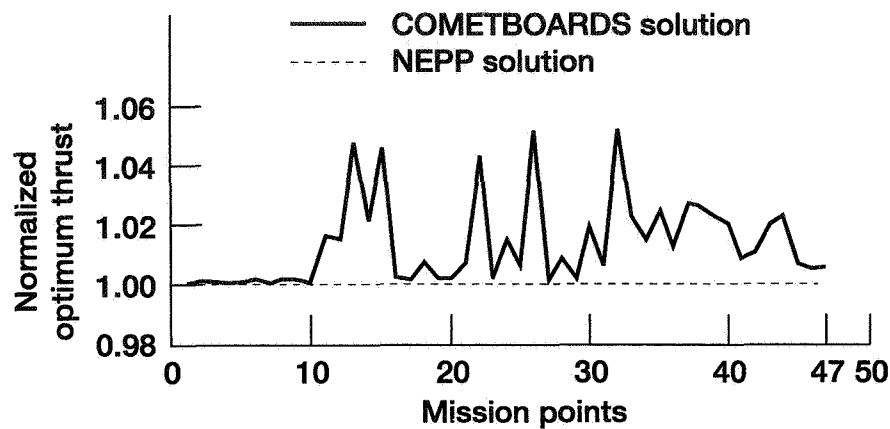


Fig. 13

CD-97-74772

## Design Optimization of Mixed-Flow Turbofan Engine Concepts

**Objective:** Maximize engine thrust for entire flight envelope

**Typical Design (or Free) Variables:**

- Pressure balance in mixer
- Surge margin
- Bypass ratio
- R-value for fan and compressor

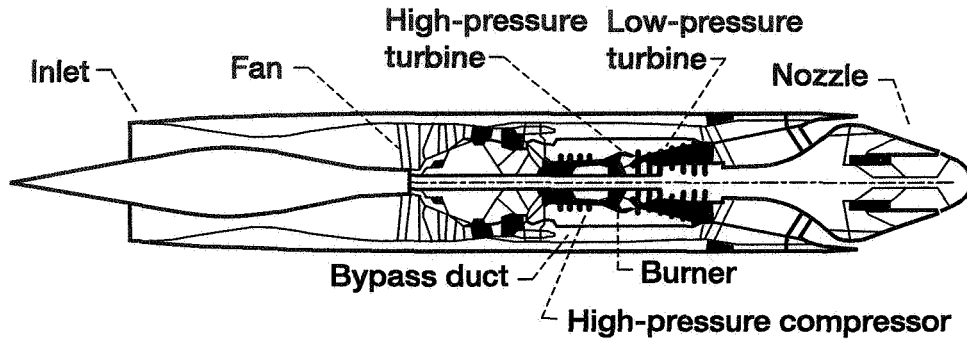
**Important Behavior Constraints:**

- Maximum speed on all compressors
- Mixer entrance Mach number
- Acceptable surge margin on all compressors
- Compressor discharge temperature

Fig. 14

CD-97-74773

## Optimization of Mixed-Flow Turbofan Performance



**Objective:** Maximize engine thrust over entire flight envelope

**Design variables:**

- Bypass ratio
- Fan speed
- Fan surge margin

**Behavior constraints:**

- Compressor speeds
- Compressor surge margins
- Compressor exit temperature
- Mixer corrected flow

Fig. 15

CD-97-74775

## Flight Envelope for HSCT Mixed-Flow Turbofan Engine

Problem 2: 122 Mission Points

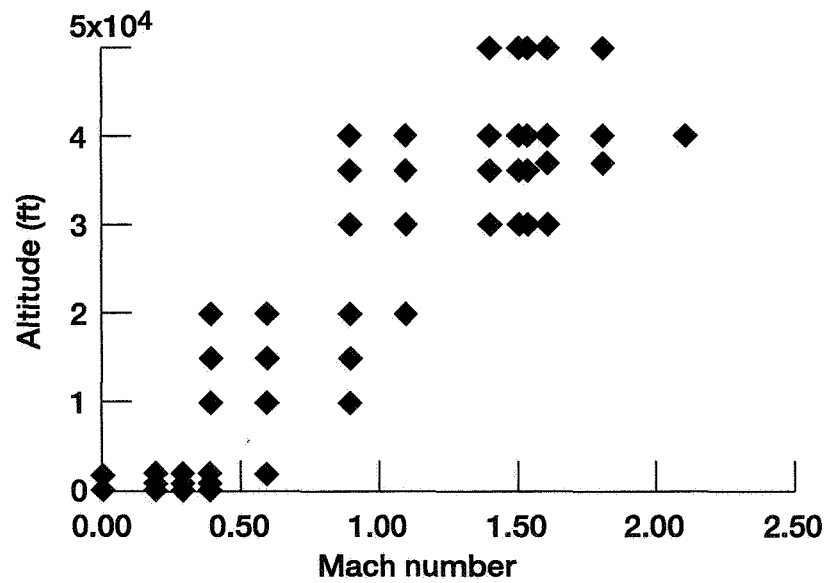


Fig. 16

CD-97-74776

## Design of an MFTF-HSCT Engine for a 122-Mission Flight Envelope

Mission			Optimum thrust, lb		COMETBOARDS improvements, percent
No.	Altitude, ft	Mach	COMETBOARDS	NEPP Optimizer	
20	Sea level	0.3	47 570	46 000	3.41
31	689	0.3	19 119	18 690	2.30
57	10 000	0.9	46 384	44 674	3.83
68	30 000	0.9	14 566	13 827	5.34
85	36 089	1.1	10 080	9 857	2.26
100	40 000	1.5	14 403	14 311	0.64
122	56 000	1.8	20 127	19 773	1.79

Fig. 17

CD-97-74777

## Value-Added Benefit in Design of an MFTF-HSCT Engine

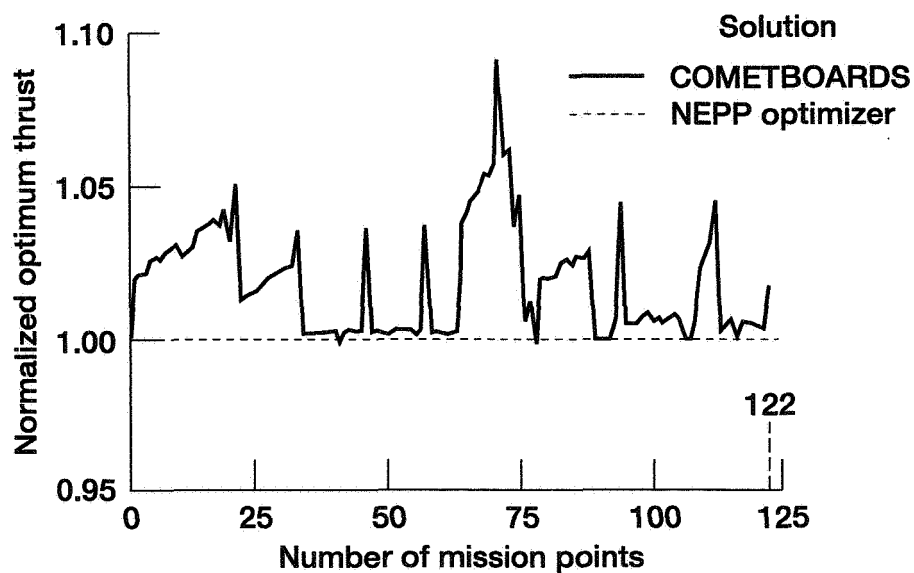


Fig. 18

CD-97-74778

## **Concluding Remarks**

- **Engine design required solutions of a large sequence of optimization subproblems**
- **Cascade strategy efficiently handled multimission engine design problems**
- **COMETBOARDS–NEPP combined tool successfully solved**
  - (1) High bypass wave-rotor-topped subsonic engine**
  - (2) Mixed-flow turbofan supersonic engine****Converged to same global optimum from different starting points**
- **COMETBOARDS offers value-added benefit to engine performance optimization**

Fig. 19

CD-97-74779



57-07  
029106

## TECHNOLOGY NEEDS FOR REDUCED DESIGN AND MANUFACTURING COST OF COMMERCIAL TRANSPORT ENGINES

10P.

DOUGLAS A. ROHN  
NASA-Lewis Research Center  
Cleveland, OH

278100

### Background

A NASA-led team studied the technology that would be needed to reduce the development cycle time and acquisition cost of commercial transport aircraft, including airframe and propulsion. This paper summarizes the needs identified by the propulsion team, which included members from Allied Signal Engines, Allison Engine Company, GE Aircraft Engines, Ladish Co., Pratt & Whitney, and Wyman Gordon, as well as NASA-Lewis.

The study team heard from all elements of the aeronautics community that the basis of competition is cost, and that performance is not a driver by itself. Basically, all customers demand lower costs, and producers of aircraft components and systems must respond. In addition, the time required to develop new or derivative products has a large impact on the market. Design and manufacturing were identified as fruitful areas for cost and time reduction.

It was recognized that application of advanced technologies to design and manufacturing would help. However, these technologies are higher-risk than have been traditionally applied in the area, so NASA involvement was appropriate. Also, a pre-competitive setting was formulated, where teamwork, both among the engine manufacturers and between the manufacturers and their suppliers, would be critical.

### Objective

The objective of the study was to assess the needs in the design and manufacturing processes and identify areas where technology could impact in cost and cycle-time reduction. At the highest level, the team first identified the goals that were in line with long-range needs of the aeropropulsion industry, and to which technology and process improvements would be required to contribute. These goals are to reduce the time and costs in the development cycle of aircraft engines by a factor of two, reduce production cycle time by a factor of four, and to reduce production costs by 25%. Also, it was the intent of the team to identify the highest impact technologies that could be developed and demonstrated in five years.

### Assessment

The initial selection of the propulsion system components to focus on was based on their value in the overall engine manufacturing, and the potential for cost and cycle time reductions. Note that the study was limited to state-of-the-art engine systems, recognizing that the current gas turbine engine configurations (*i.e.*: fan, compressor, combustor, turbine, associated structure, and other

components) will stay approximately the same for the foreseeable future. As shown in figure 2, the rotor system of the engine contributes the highest portion of hardware cost. Categorizing the rotor system components by primary shape manufacturing process, as in figure 3, it can be seen that forged components make up the largest fraction of the overall production cost. As shown in figure 2, these also have the highest potential for cost and time reduction.

The forging and related ring-rolling process is used to make components such as disks, spools, seals and airfoils from titanium and nickel-base super-alloys. The sequence of steps defining the forging process, as shown in figure 4, includes the steps from billet formation through all machining and surface treatments prior to engine final assembly. Technology has advanced to accommodate increasing demands on the reliability and performance of the engine components, with newer alloys, better inspection, unique methods, and more attention to processing parameters. However, the steps have remained basically the same since World War II, and the operational paradigms of the industry often limit attempts to improve productivity.

Operationally, analytically, and financially, each step is often viewed in isolation which prevents optimization of interacting steps and neglects upstream and downstream considerations. However, the development cycle is concurrent to the extent that forging development begins before the final design is complete. The development process generates a considerable amount of data to substantiate the process. New alloys, not having an extensive design data base, require even more. The iterative nature of the process and the evolution of new technology makes it cumbersome to manage this data. The process also promotes physical inefficiency. Given an incomplete understanding of the process, producers add conservatism to the design and production process. A substantial material envelope is added to the forging shape to counter distortion, surface cracking, and incomplete die fill. Further, several forging and heat-treatment iterations are often required to overcome unexpected problems such as low property values or residual excessive stresses.

Some of these and other barriers to time and cycle efficiency are summarized in figure 6. As a detailed example, figure 7 shows how material added to the forging shape results in only 20% of the billet actually being in the final part. Removal of 80% represents a very large production cost, both from the high material value of super-alloy stock (although there is some scrap value to the chips), as well as the machining cost.

### Study Results

To combat these issues and barriers, the team identified a vision for advanced forging processes, figure 8. A number of the elements of this vision require the advancement of technology across a range of applications, from a better understanding of the physics in the process steps, to integration of design and manufacturing analysis tools, to better process control, to improved production equipment. While some of these activities are beyond NASA's interest, the application of high-risk technology could help overcome the barriers to all the elements of this vision.

Technical need categories were identified, along with details of the technical advancements needed and their impact on the overall forging process time and cost. The categories and needs are listed in figures 9, 10 and 11.

These technical needs can be further summarized, as in figure 12, by: better analysis methods describing critical phenomena in processing; integration of computational tools for manufacturing steps, and linkage to design tools; and modified processing for higher productivity and lower cost. The study team envisioned an integrated toolset, figure 13, that would be built around an architecture of advanced computing power, optimization tools, and data management. Advanced 3-D analysis tools based on the physics of the multiple steps of the process would be coupled to the tools and technologies used to actually execute the forging process. These would, in turn, be linked to cost models and the best business practices so that design and manufacturing demands would be considered in the light of affordability and rapid cycle time.

### Status & Future Work

The team identified the potential for progress toward the vision of future forged product processing. Work would be centered around the development and application of: a design and processing toolset; enhanced physics-based processing analysis techniques; a better understanding and thus control of the manufacturing process; and more efficient teaming and information exchange within the industry.

One of the elements in the Propulsion Systems Base Research and Technology Program, the Physics & Process Modeling (PPM) project, has a general focus on physics-based analysis. PPM is supporting enhancement of some of the analysis tools used in the forging process. Other needs may be addressed in various other ways.

### Acknowledgment

The author would like to thank the members of the study team who gathered the information reported in this paper: Daniel Backman, Barbara Dubrosky, David Furrer, Timothy Grant, Ken Green, Timothy Howson, Mansoor Khan, Charles Lawrence, Howard Merrick, David Rice, Robert Rowe, Kamar Singh, Robert Stusrud, Stacy Thompson, and Raymond Walker.

## BACKGROUND

- **Drivers**
  - Basis of competition is cost
  - Need to maintain market share
- **Technology**
  - Focus on precompetitive technology
  - Emphasize high risk
- **Teamwork**
  - NASA involvement
  - Horizontal and vertical
- **Study team members**
  - AlliedSignal, Allison, GE, Ladish, NASA LeRC, Pratt & Whitney, Wyman-Gordon
- **High level objective**
  - Focus on highest impact elements
  - Final goal to reduce development time and cost by 50 percent, production cost by 25 percent

Fig. 1

## ASSESSMENT OF ENGINE COMPONENTS

Generic engine component	Current portion of engine hardware cost, percent	Cost reduction potential, percent		Cycle time reduction potential, percent	
		Development	Production	Development	Production
<b>Rotor system</b>	<b>32</b>	<b>50</b>	<b>30</b>	<b>60</b>	<b>25</b>
<b>Stator system</b>	<b>28</b>	<b>25</b>	<b>25</b>	<b>25</b>	<b>25</b>
<b>Frames and structures</b>	<b>20</b>	<b>25</b>	<b>20</b>	<b>35</b>	<b>20</b>
<b>Combustor</b>	<b>7</b>	<b>25</b>	<b>10</b>	<b>25</b>	<b>10</b>
<b>Lube system</b>	<b>3</b>	<b>10</b>	<b>5</b>	<b>5</b>	<b>10</b>
<b>Controls and externals</b>	<b>10</b>	<b>20</b>	<b>10</b>	<b>25</b>	<b>10</b>

Fig. 2

## APPORTIONMENT OF MANUFACTURING COST

Generic engine module	Manufacturing cost of primary shape-making process, percent		
	Forged component (bulk deformation: forging, ring rolling, extrusion)	Cost component (investment casting)	Fabricated component (sheet metal, SPFDB, brazing welding)
Rotor system	80	15	<5
Stator system	50	35	<10
Frames and structures	<10	70	<15
Combustor system	<10	<5	85

Fig. 3

## FORGING PROCESS

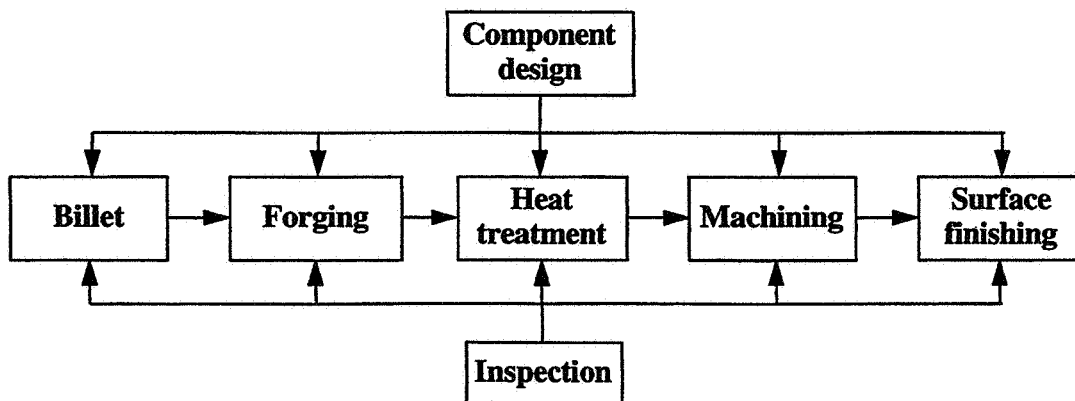


Fig. 4

- **Process issues**
  - **Compartmentalization**
  - **Conservative response to process uncertainty**
  - **Challenges from contemporary engine design and new materials**

# CYCLE TIME AND COST

- **Issues**
  - Forging development often begins before disk design is complete
  - Process involves considerable data
    - New materials generate new design and processing data
    - Evolutionary process makes it cumbersome to manage
  - Physical inefficiencies are built in
    - Initial disks are overweight so that later design changes can be accommodated
    - Forging and heat treatment iterations are needed to overcome unexpected problems

Fig. 5

# FORGING ASSESSMENT

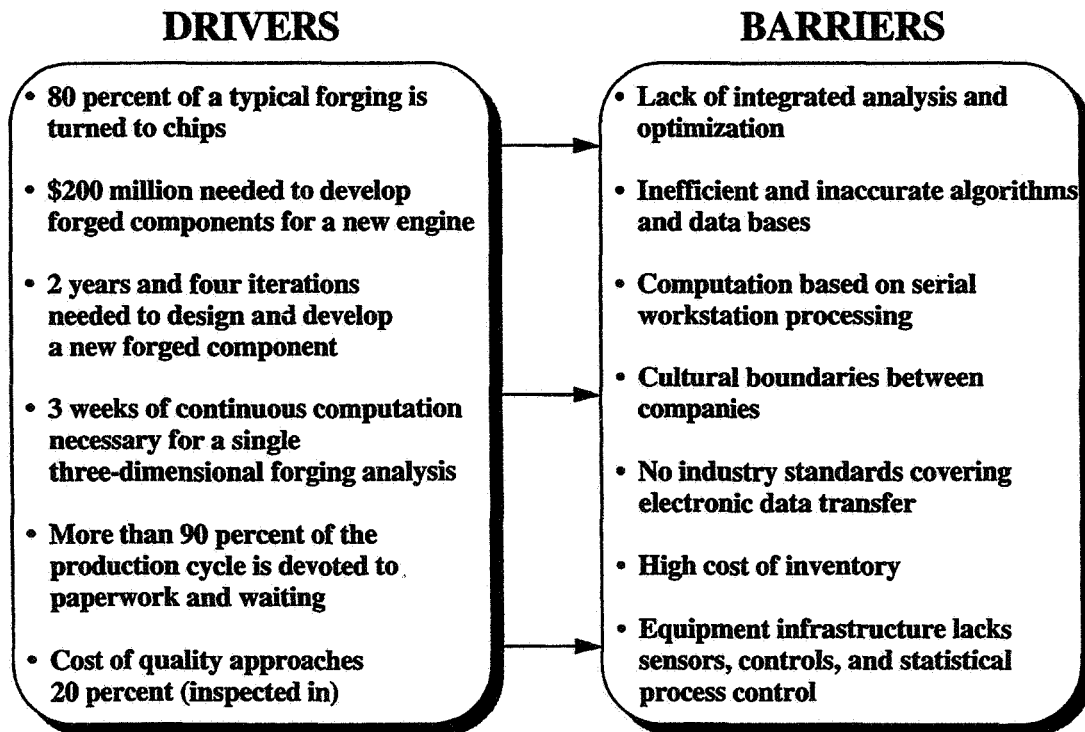


Fig. 6

## EXAMPLE: REDUCE FORGING WEIGHT

- **Current forging designs and practices waste material**
  - Utilization (part weight/billet weight) is typically 20 percent
  - Losses are associated with enlarged envelope to deal with die fill, sonic inspection, and distortion

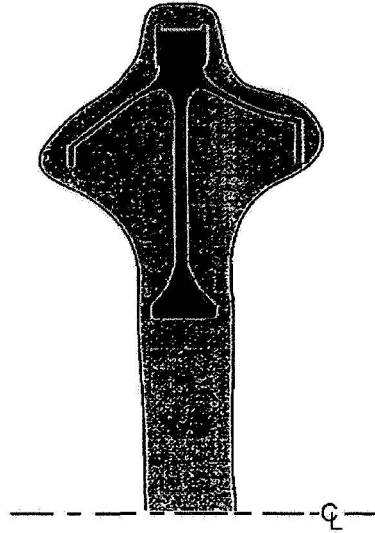


Fig. 7

## FUTURE FORGED PRODUCT PROCESSING

- **“Vision”**
  - Integrated approach for design through manufacturing
  - Better materials for parts, dies, tooling
  - Nearer net-shape parts and better process control
  - Next-generation presses which emphasize small lot sizes, rapid cycles, and agile manufacturing

Fig. 8

## TECHNOLOGY NEEDS

<u>Category</u>	<u>Need</u>
Process and design physics	<ul style="list-style-type: none"> <li>- Physics-based microstructure and property prediction</li> <li>- Die lubrication</li> </ul>
Design for manufacturing	<ul style="list-style-type: none"> <li>- Knowledge base of manufacturing constraints</li> <li>- Cost modeling input to design optimization</li> </ul>
Analysis methods	<ul style="list-style-type: none"> <li>- More complete CFD to predict heat transfer coefficients</li> <li>- Application of three-dimensional heat treatment codes</li> <li>- Three-dimensional prediction of machining distortion</li> <li>- Robust, efficient three-dimensional forging models</li> </ul>

Fig. 9

## TECHNOLOGY NEEDS (cont.)

<u>Category</u>	<u>Need</u>
Integrated tool set	<ul style="list-style-type: none"> <li>- Computer environment that links processes</li> <li>- Reduction in run-time for three-dimensional model execution</li> <li>- Optimization tools</li> </ul>
Processes and equipment	<ul style="list-style-type: none"> <li>- Novel computer-controlled manufacturing processes</li> <li>- Real-time statistical process control linking manufacturing, testing, and analysis</li> <li>- Lower-cost tooling</li> <li>- Improved methods and sensors for flaw detection</li> <li>- New approaches to reduce setup time</li> <li>- Three-dimensional design for manufacturing</li> </ul>

Fig. 10



## TECHNOLOGY NEEDS (concl.)

<b><u>Category</u></b>	<b><u>Need</u></b>
<b>Standards</b>	<ul style="list-style-type: none"><li>- Industry-standard specifications and property tests</li><li>- Common formats for product representation</li></ul>
<b>Validation and testing</b>	<ul style="list-style-type: none"><li>- Improved residual stress measurement techniques</li><li>- Approaches for applying the toolset for certification and qualification</li></ul>
<b>Business practices</b>	<ul style="list-style-type: none"><li>- Streamlined, electronic commerce</li><li>- Prediction of factory loading and cycle time for small lot sizes</li><li>- Visibility tools for integrated design and manufacturing environment</li></ul>

Fig. 11

## TECHNICAL NEEDS SUMMARY

- **Better analysis methods that describe critical phenomena in processing**
- **Integration of computational tools for manufacturing steps, and linkage to design tools**
- **Modified processing for higher productivity and lower cost**

Fig. 12

## STUDY CONCLUSION: INTEGRATED TOOLSET

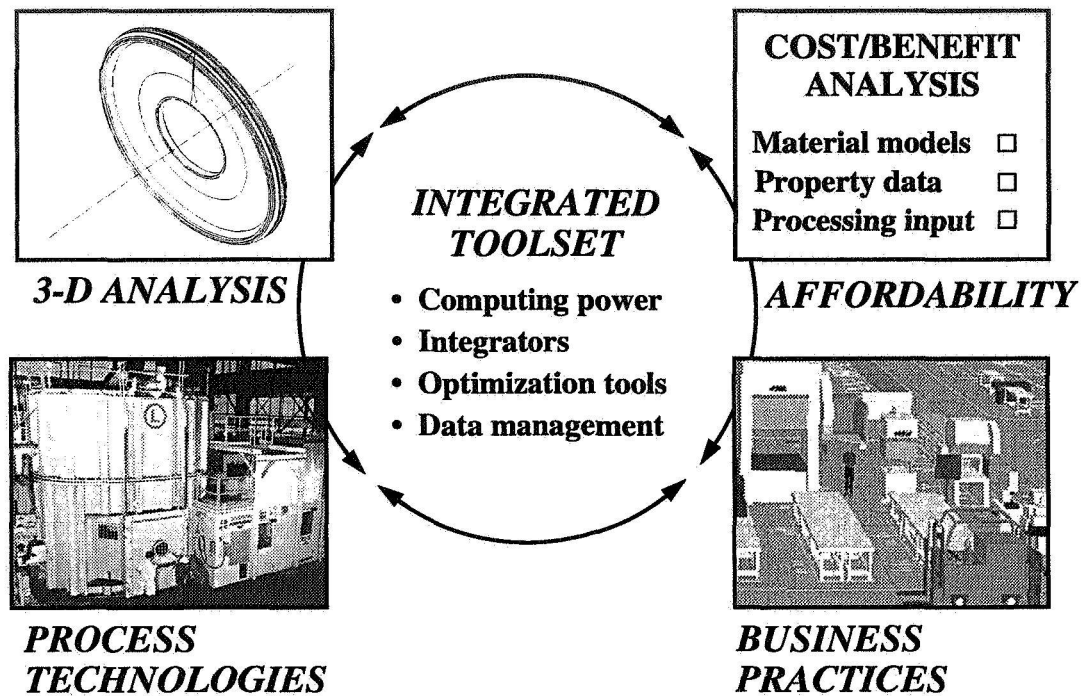


Fig. 13

## FUTURE PLANS

- **Develop and apply**
  - **Manufacturing process and product design integrated toolset**
  - **Physics-based enhanced processing analysis techniques**
  - **Better understanding and control of manufacturing processes**
  - **More efficient teaming and information exchange within the industry**

Fig. 14

58-39  
009107

# DAMPING EXPERIMENT OF SPINNING COMPOSITE PLATES WITH EMBEDDED VISCOELASTIC MATERIAL\*

14p.

078/01

by

ORAL MEHMED  
Machine Dynamics Branch  
NASA Lewis Research Center

and

John B. Kosmatka  
Division of Structural Engineering  
Department of Applied Mechanics and Engineering Sciences  
University of California, San Diego

## Introduction

One way to increase gas turbine engine blade reliability and durability is to reduce blade vibration. It is well known that vibration reduction can be achieved by adding damping to metal and composite blade-disk systems. This experiment was done to investigate the use of integral viscoelastic damping treatments to reduce vibration of rotating composite fan blades. It is part of a joint research effort with NASA LeRC and the University of California, San Diego (UCSD). Previous vibration bench test results obtained at UCSD (Ref. 1) show that plates with embedded viscoelastic material had over ten times greater damping than similar untreated plates; and this was without a noticeable change in blade stiffness. The objectives of this experiment, Fig. 1, were to verify the structural integrity of composite plates with viscoelastic material embedded between composite layers while under large steady forces from spinning, and to measure the damping and natural frequency variation with rotational speed.

The experiment was performed in the NASA LeRC Dynamic Spin Facility, a photo of the installation is shown in Fig. 2. This is a spin rig facility where the shaft can be vibrated while stationary or spinning to cause blade vibration by base motion. The shaft is air turbine driven, has a vertical axis of rotation, and is supported at the top end by a ball bearing on compliant mounts to allow small shaft motions. There is a magnetic bearing at the lower end. The magnetic bearing is used both to support the shaft and to force shaft vibration. Proximity probes are used to sense shaft motion for control of the magnetic bearing. There are two strain gauged flat plates which are attached to a hub structure with a set of clamps. The clamps are designed to allow quick plate changeover. Each clamp has two small accelerometers installed to sense bending and torsion vibration. The diameter of the blade tips is 396.2 mm (15.6 in).

---

\* Work funded under NASA Grants NCC3-309 and NCC3-493

Four flat plates and six thirty degree twisted plates were tested, see Figs. 3 and 4. The plates are laminated composite structures and are 1.14 mm (45 mils) thick, each has a cantilevered length of 228.6 mm (9 in) and a chord of 76.2 mm (3 in). There is a center layer .127 mm (5 mils) thick composed of a border material of either 90 degree graphite/epoxy or AF-32 resin, and a viscoelastic damping patch of 3M ISD-113; except the baseline plates have no patch. A loose weave E-glass scrim cloth (not shown) is embedded in the damping material to keep the damping material from creeping out of the cavity under the large steady state forces from spinning. The center layer is covered on each side by a .508 mm (20 mil) thick, 8-ply, graphite/epoxy T300/934 face sheet. The variables among the plates are: (1) border material, (2) face sheet stacking sequence, (3) patch size, and (4) patch location. The largest damping patch is designed to damp all the modes, whereas, the smaller patches are designed to damp specific modes.

Plate damping data were collected at dwells of rotation speed, up to 8000 rpm, while vibrating the shaft with the magnetic bearing. A random noise signal centered in bandwidth about the plate modes of interest was used for the excitation. There were signal-to-noise problems with the data above 4000 rpm which made it difficult to get accurate damping values. The slip ring brushes and line electrical interference are believed to be the major sources of the noise. The best data were obtained from a Wheatstone bridge on each plate that had four active blade strain gauges. Signals from bridges with only one active blade gauge were not as high in amplitude, and in general, were closer to the noise floor. Good signal amplitude is also dependent on locating gauges for the best sensitivity to the modes of interest.

The plate natural frequencies and damping levels in the spin rig have been obtained from measured transfer functions of plate strain gauge to clamp accelerometer signals. Transfer function data for the first chord-wise mode of the two baseline flat plates and a damped flat plate (1-19a) at zero rpm are shown in Fig. 5. The damping level of plate 1-19a, with the second mode patch, is over two times that of the baseline plates; and the damping would be greater if the patch had been optimized for the chord-wise mode. This is the only chord-wise mode data obtained from the experiment because the strain gauges were not located to be very sensitive to this mode. However, chord-wise modes are causing fatigue problems in modern engines and need to be damped. Future tests should concentrate more on this mode.

The signal to noise ratio was a problem at rotor speeds above 4000 rpm. The amplitude of the plate response signal decreased and the amplitude of slip ring noise increased with rotation speed. The decrease of plate response was caused by centrifugal stiffening and is discussed below. The change in the quality of the data can be seen in Fig. 6. Shown are first and second bending mode response signals at zero and 4000 rpm. A decrease of blade response and an increase of signal noise has occurred at 4000 rpm, and these trends became worse with rotation speed. Forty averages of each data record was taken to reduce the noise, but because of remaining noise curve fitting of the transfer function data was required before calculating damping values.

Increasing rotation speed usually had a stiffening effect on the plates and is seen by an increase in the plate natural frequency. This effect is called centrifugal stiffening. However, increasing rotation speed caused damping to decrease. Both these effects are shown by the solid lines in Figs. 7 - 9. The damping decrease can be explained by the natural frequency increase as follows. Loss factor is defined as vibration energy dissipated divided by vibration energy stored in the structure. As the structure stiffens the denominator increases, causing the loss factor decrease as shown by the data. The *calculated* changes in loss factor caused by the measured natural frequency changes are shown by the dashed lines. In general, the dashed lines follow the trend of the measured damping curves and account for the decrease of measured loss factor. Hence, we may conclude that the material damping is not changing much with rotational speed, and the loss factor decrease is caused mainly by the stiffening of the structure.

The measured natural frequencies for the first torsion mode of the plate in Fig. 10 shows a *decrease* with increasing rotation speed. Here, the centrifugal forces are causing a softening of the torsion mode because this plate is pre-twisted and is untwisting as rotation speed increases. The dashed line on the lower frame is the *calculated* increase in loss factor due to the natural frequency decrease. Although the measured damping data has a lot of scatter, we may again conclude from the general trends that the material damping is not changing much with rotation speed.

### Summary and Conclusions

Experimental data has been presented from a vibration spin experiment of flat and twisted graphite composite plates damped with 3M ISD 113 viscoelastic material embedded between composite layers. Damping was calculated from measured transfer functions of blade strain to blade base acceleration. Damping was repeatable and there were no failures or delaminations of the plates. This is significant since 3M ISD 113 has a very low creep modulus at room temperature, and the plates had up to 28,000 g's centrifugal load at the tip. Centrifugal stiffening was large for the plates and caused a significant drop in damping. However, real fan blades have smaller increases in natural frequency with rotational speed, and therefore, the decrease in fan blade damping should be smaller than measured in this experiment. To further improve damping new designs should use a stiffer damping material than used here.

### References

1. J.B. Kosmatka, Lapid A.J. and Mehmed O: Passive Vibration Reduction of Advanced Composite Pretwisted Plates Using Integral Damping Materials, Proceedings , SPIE - The International Society for Optical Engineering, vol. 2445, pp. 72 to 83, 1995.

# Objectives

- Verify the structural integrity of rotating composite plates with 3M ISD 113 viscoelastic material embedded between composite layers.
- Measure the damping and natural frequency variation with rotational speed.

Fig. 1

## Viscoelastic Damped Composite Plates in the NASA Dynamic Spin Facility

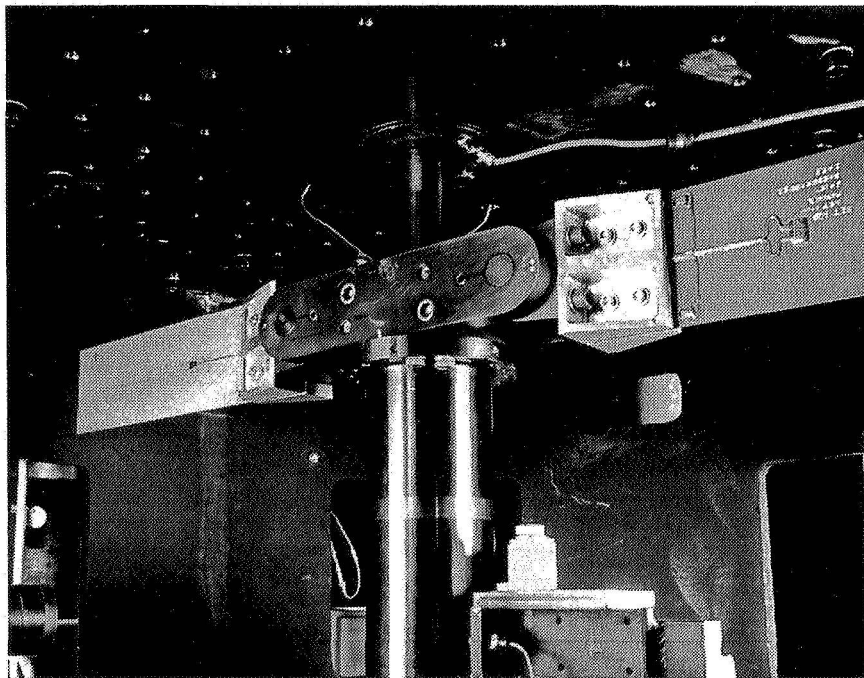


Fig. 2

CD-97-74607

## Flat Plate Configurations

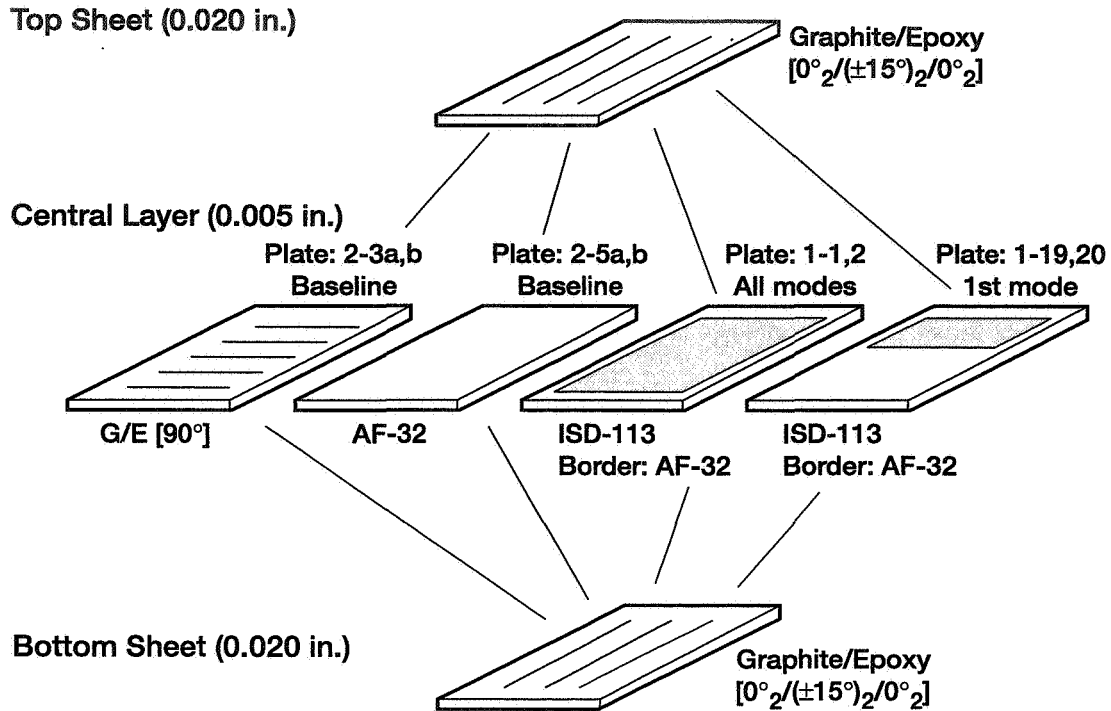


Fig. 3

CD-97-74608

## Twisted Plate Configurations

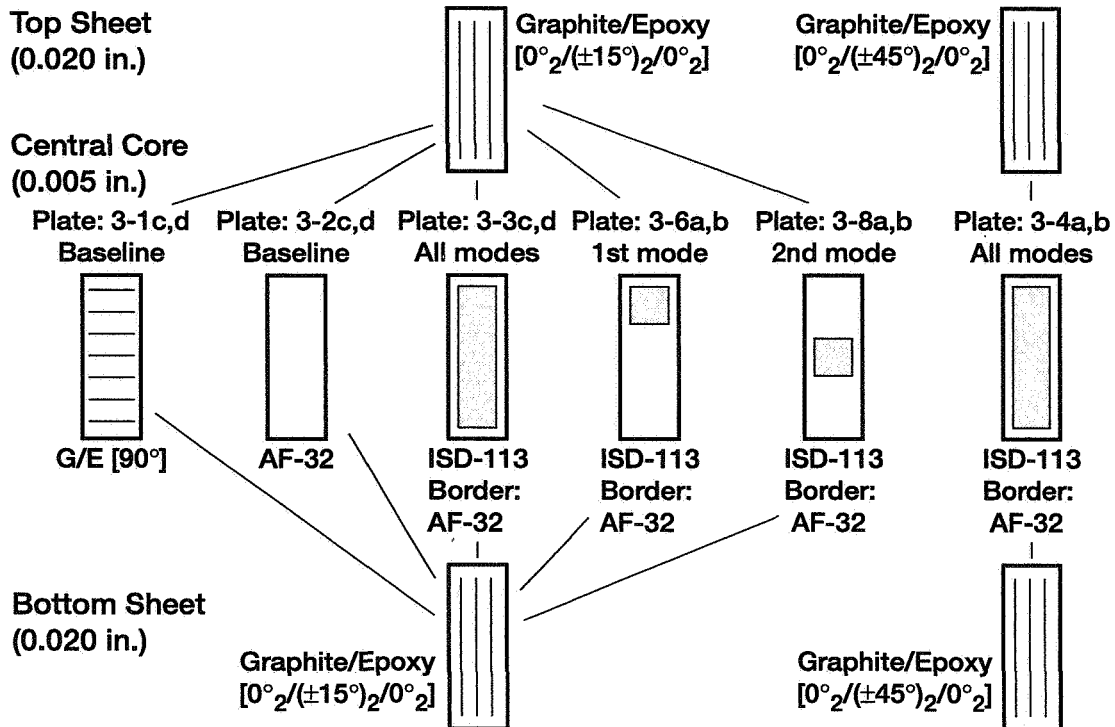


Fig. 4

CD-97-74609

## First Chordwise Mode Frequency Response Functions for Flat Plates at Zero RPM

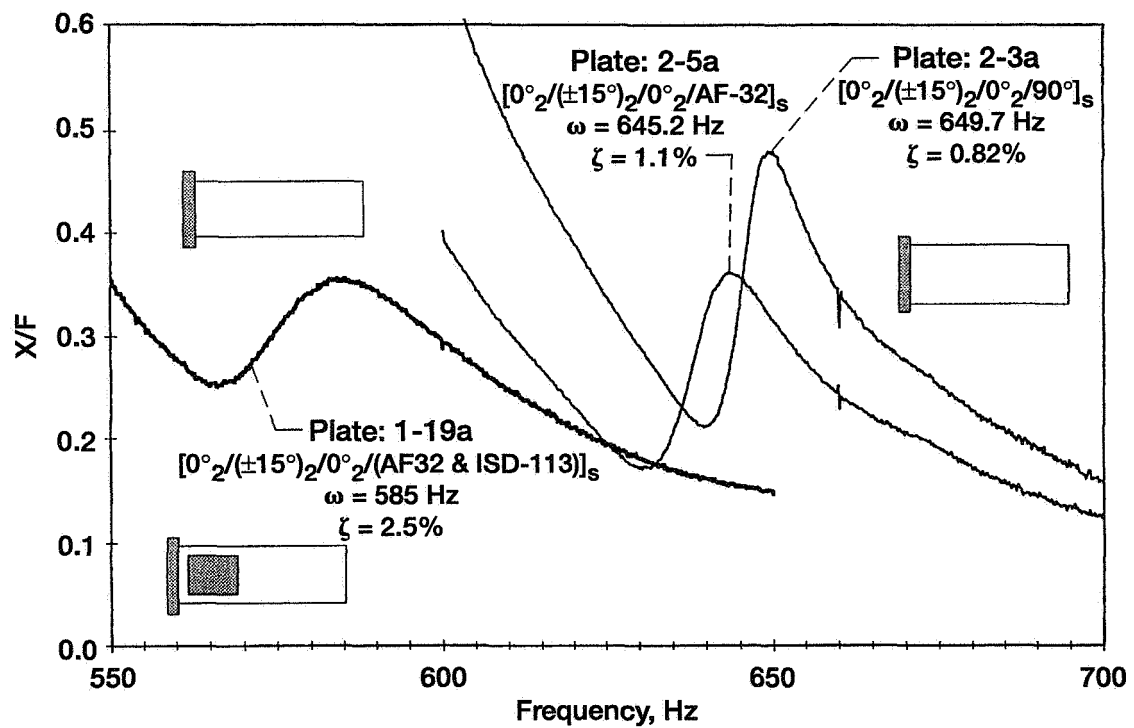


Fig. 5

CD-97-74610



# First and Second Bending Mode Frequency Response Functions for Flat Plates

$\Omega = 0$  rpm

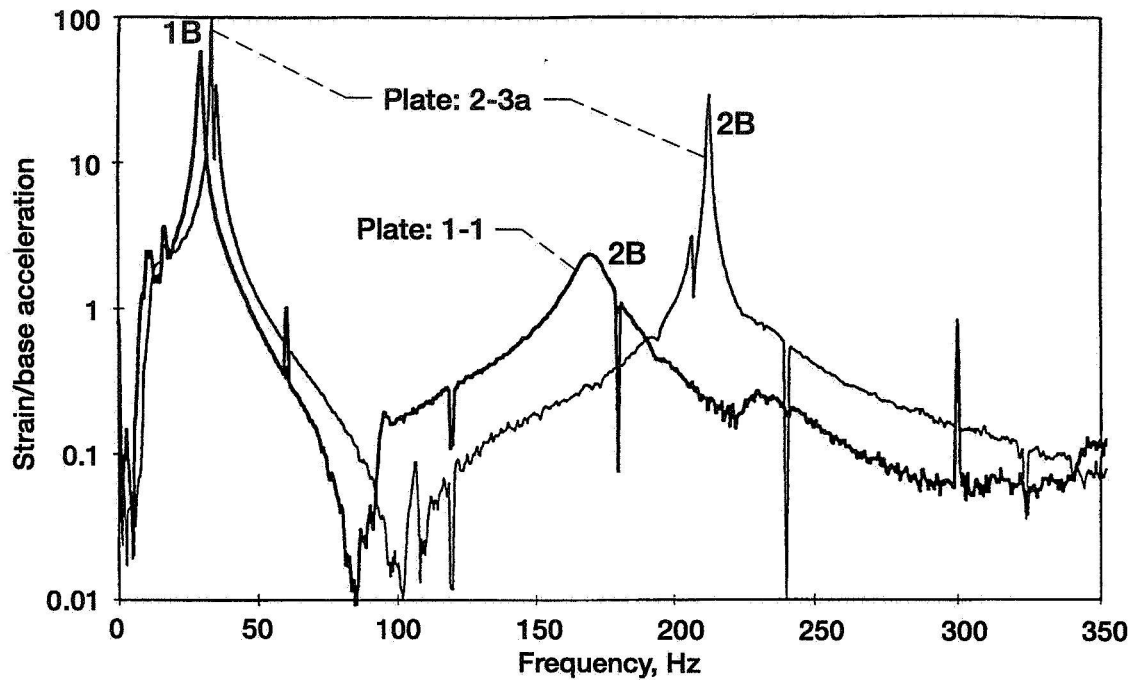


Fig. 6a

CD-97-74611

$\Omega = 4000$  rpm

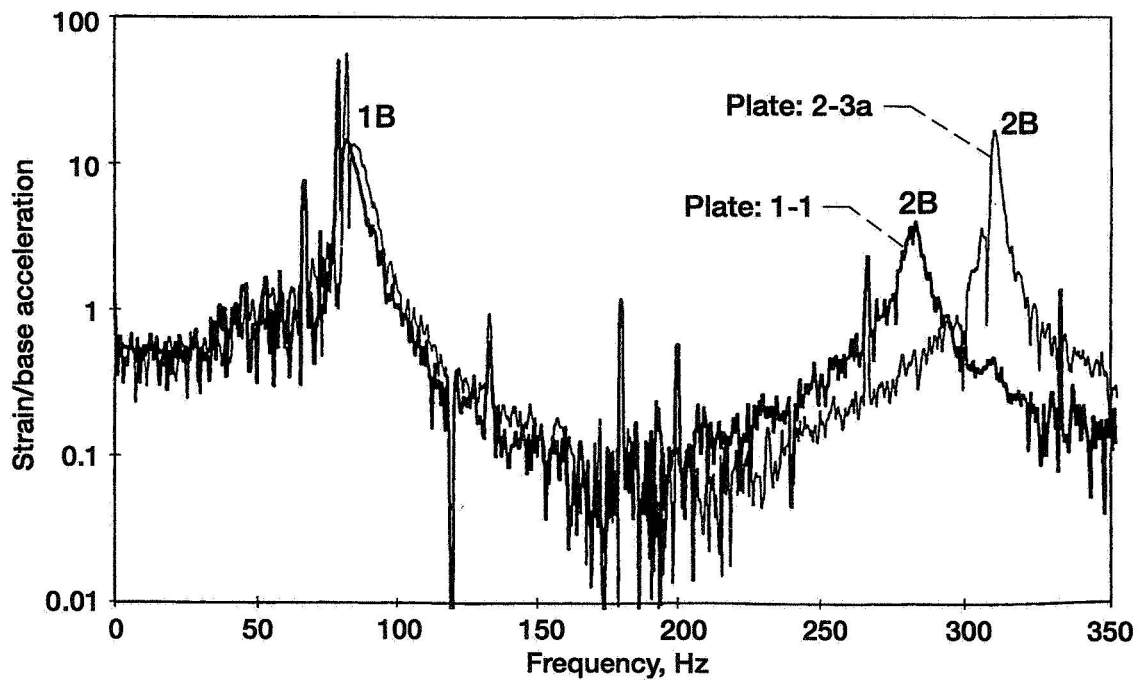


Fig. 6b

CD-97-74612

## Variation of First Torsion Mode Frequency With Rotor Speed for Flat Plates

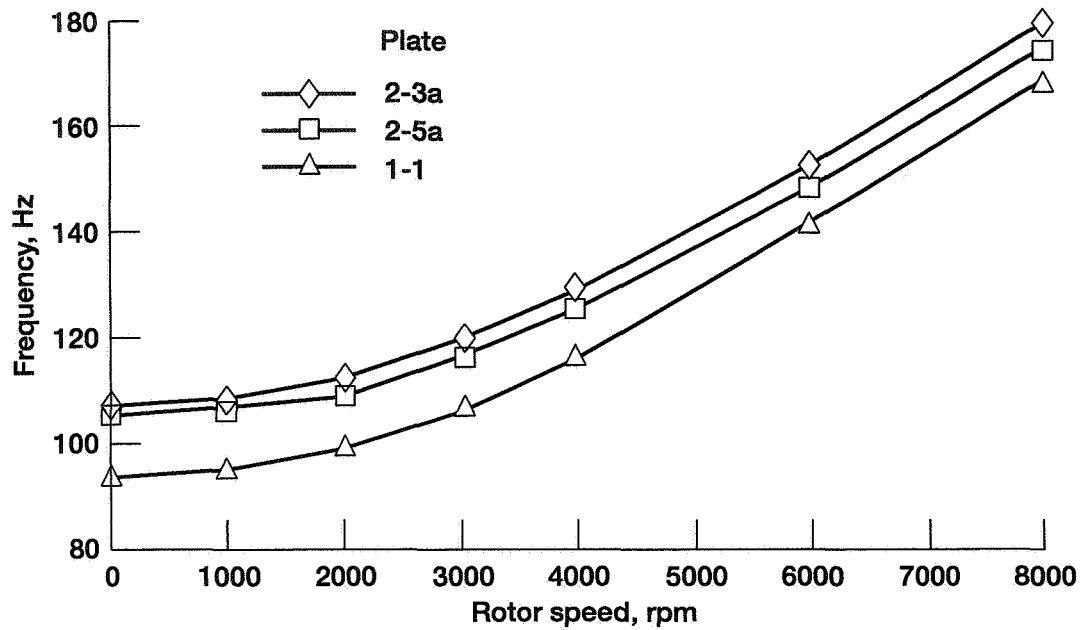


Fig. 7a

CD-97-74613

## Variation of First Torsion Mode Damping With Rotor Speed for Flat Plates

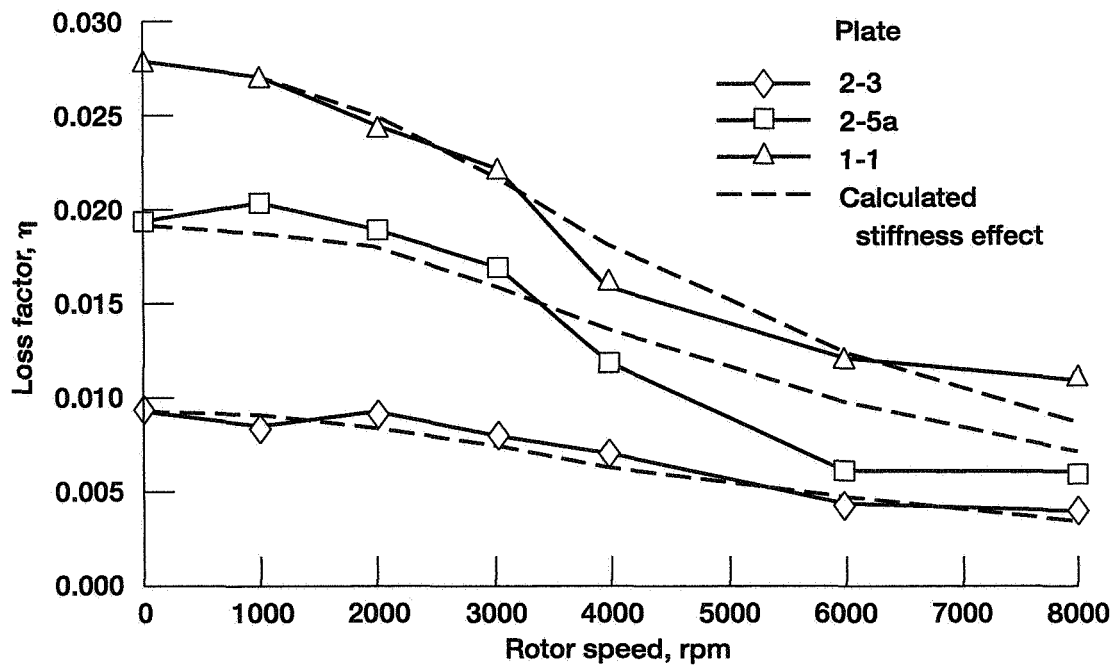


Fig. 7b

CD-97-74614

## Variation of First Bending Mode Frequency With Rotor Speed for Twisted Plates

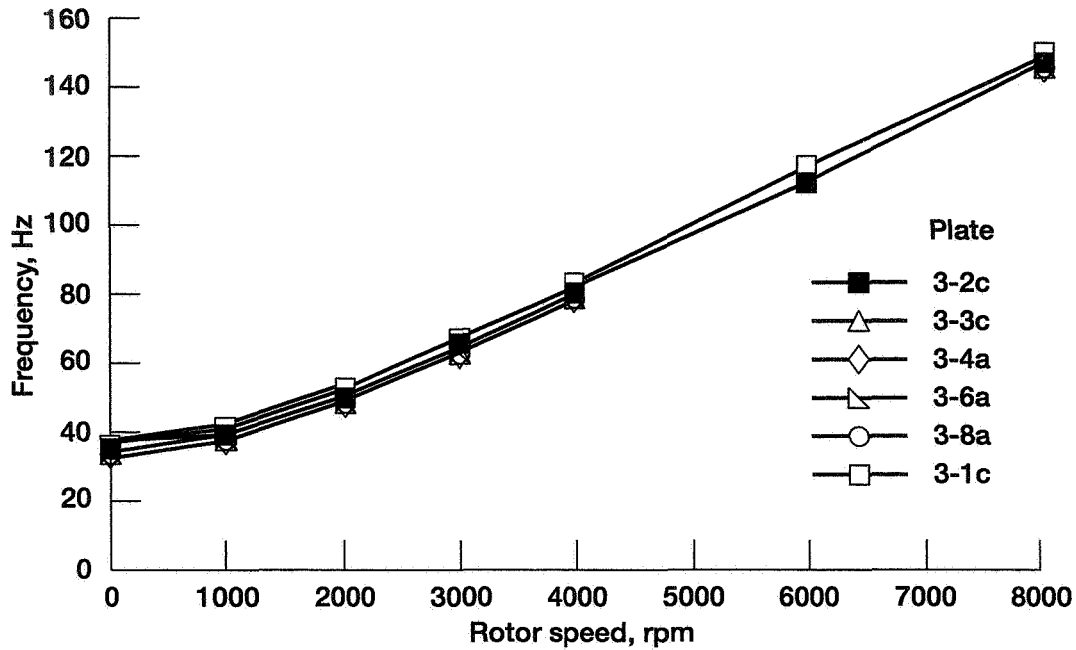


Fig. 8a

CD-97-74615

## Variation of First Bending Mode Damping With Rotor Speed for Twisted Plates

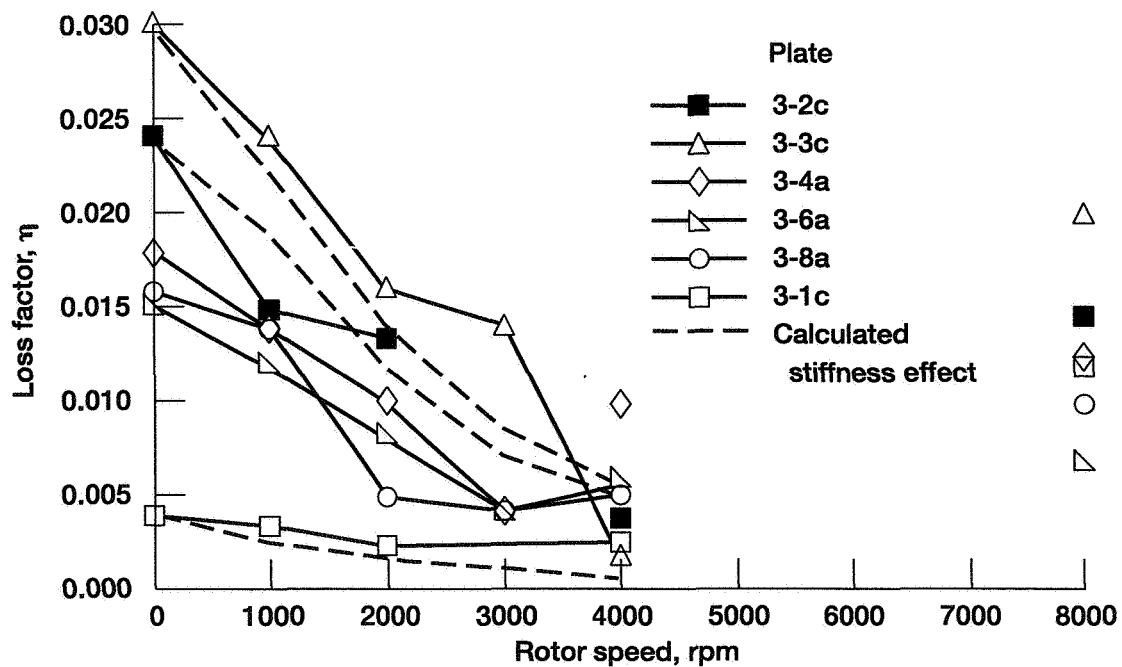


Fig. 8b

CD-97-74616

## Variation of Second Bending Mode Frequency With Rotor Speed for Twisted Plates

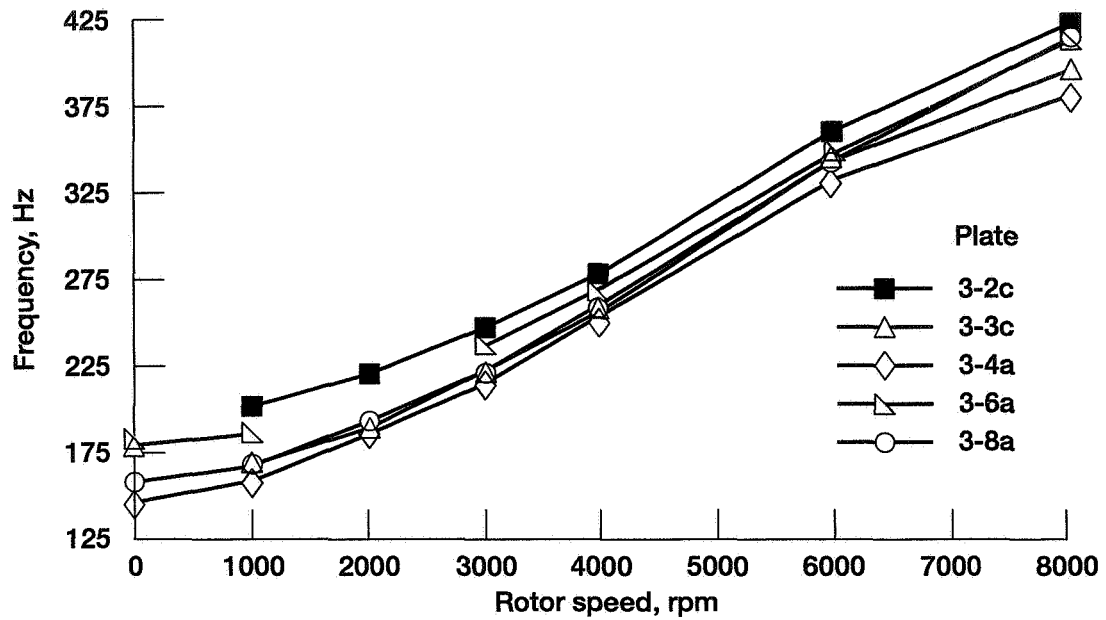


Fig. 9a

CD-97-74617

## Variation of Second Bending Mode Damping With Rotor Speed for Twisted Plates

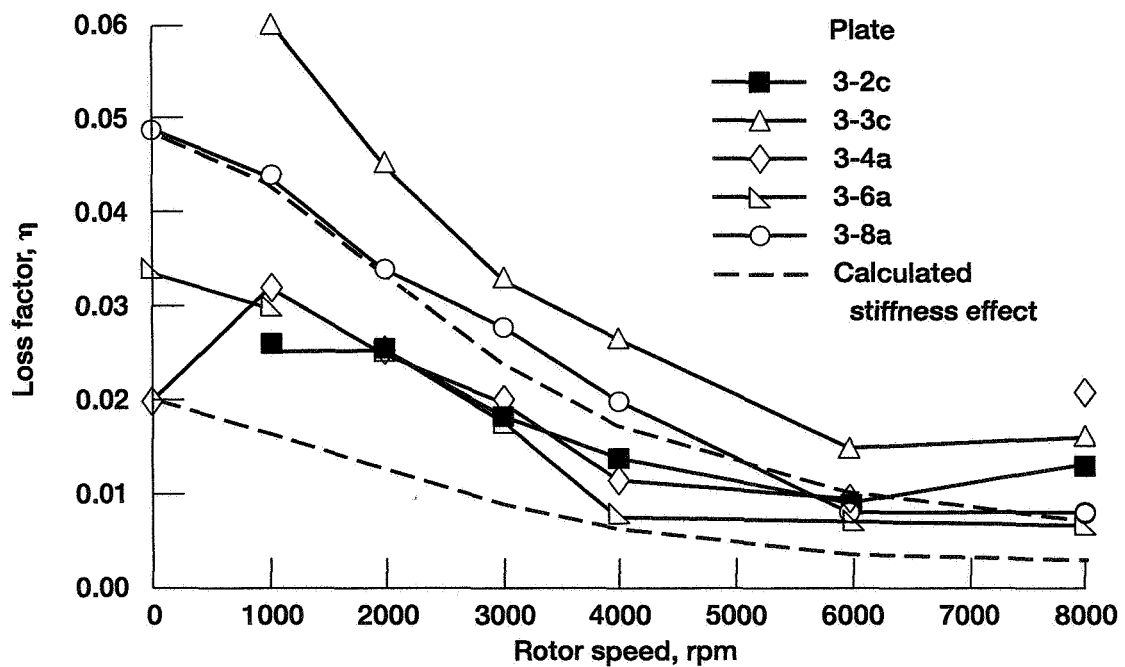


Fig. 9b

CD-97-74618

## Variation of First Torsion Mode Frequency With Rotor Speed for Twisted Plates

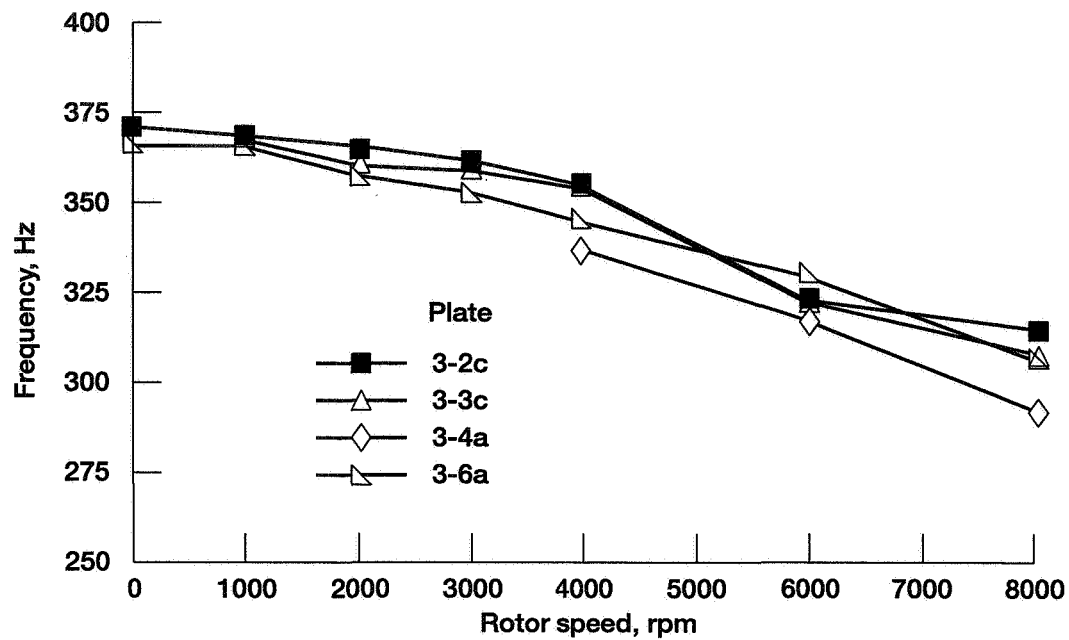


Fig. 10a

CD-97-74619

## Variation of First Torsion Mode Damping With Rotor Speed for Twisted Plates

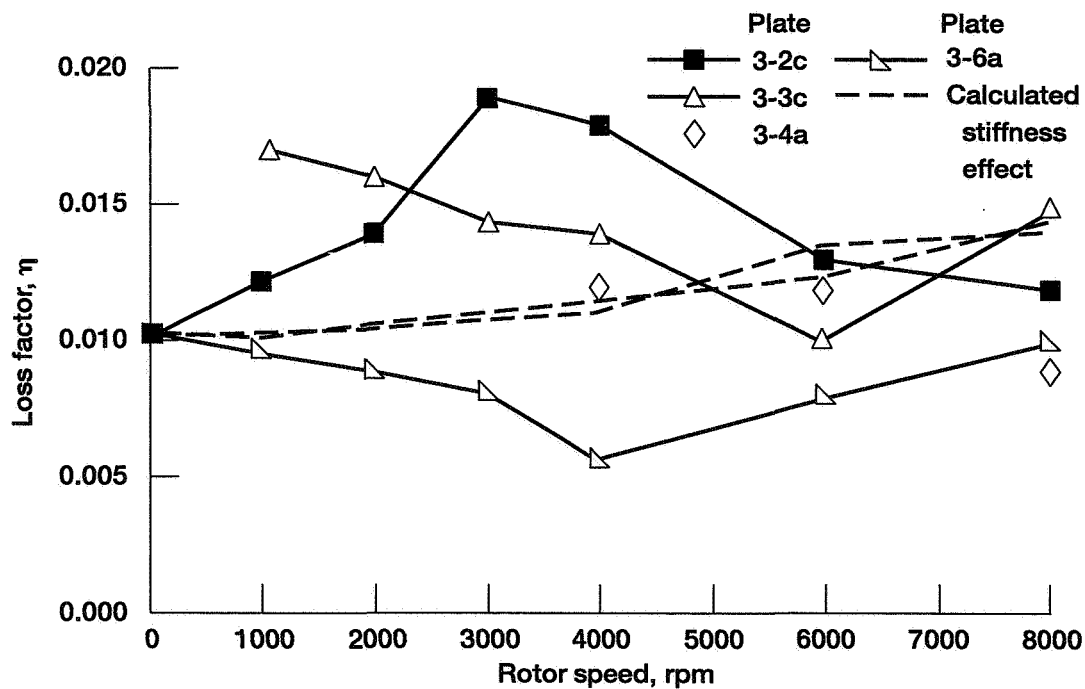


Fig. 10b

CD-97-74620

# Summary of Results

- No failures or delaminations of the rotating plates occurred with 3M ISD 113 viscoelastic material up to 28,000 g's.
- Repeatable damping values were obtained.
- Centrifugal stiffening was large for the plates tested and caused a significant drop in damping.

Fig. 11

## Conclusions

- Viscoelastic damping is a feasible and effective way to reduce engine fan blade vibration.
- Real fan blades have smaller increases in centrifugal stiffening, and should have smaller decreases in damping than the plates used in the experiment.

Fig. 12

## Focus of Future Research

- Transition the technology to engine blades:
  - Use actual fan blade geometries.
  - Perform aerodynamic rig experiments.
  - Concentrate on chord-wise modes.
  - Use stiffer damping materials.
  - Design patches to reduce the decrease in damping from centrifugal effects.

Fig. 13

# MAGNETIC EXCITATION FOR SPIN VIBRATION TESTING

DEXTER JOHNSON

Oral Mehmed

Gerald V. Brown

NASA Lewis Research Center  
Cleveland, Ohio 44135

59-39  
029108  
10P  
078103

## Abstract

The Dynamic Spin Rig Laboratory (DSRL) at the NASA Lewis Research Center is a facility used for vibration testing of structures under spinning conditions. The current actuators used for excitation are electromagnetic shakers which are configured to apply torque to the rig's vertical rotor. The rotor is supported radially and axially by conventional bearings. Current operation is limited in rotational speed, excitation capability, and test duration. In an effort to enhance its capabilities, the rig has been initially equipped with a radial magnetic bearing which provides complementary excitation and shaft support. The new magnetic feature has been used in actual blade vibration tests and its performance has been favorable. Due to the success of this initial modification further enhancements are planned which include making the system fully magnetically supported. This paper reports on this comprehensive effort to upgrade the DSRL with an emphasis on the new magnetic excitation capability.

## Introduction

The Machine Dynamics Branch at the NASA Lewis Research Center is currently involved in structural dynamic research and testing that supports NASA projects such as Smart Green Engine and AST, and other aeronautical and space programs. Our research emphasis is in the area of active vibration analysis and control (AVC), aeroelasticity (AE), and system dynamics. In the area of AVC there is a concentrated effort in using magnetic actuation and suspension. In the area of AE there is a primary focus on investigating the interaction of aerodynamic loading with the dynamics of rotating structures, such as fan blades. One facility used in testing rotating components at the NASA Lewis Research Center is the Dynamic Spin Rig Laboratory (DSRL), (see Figure 2). It is located in cell CW-18 in the Engine Research Building (ERB, Bldg. 5). In a combined effort with the AVC and AE areas, a radial magnetic suspension and excitation device has been incorporated into the DSRL. This initial implementation was highly successful and subsequent enhancements are planned which will provide an all magnetic support system with extended excitation capabilities.

## The DSRL

The DSRL currently is used to test turbomachinery blades and components which are rotated in a vacuum to obtain stress and deflection measurements. The rotor can be rotated up to 20,000 rpm.



The rotor is driven by an air turbine which is rated at 40,000 rpm. The current mode of excitation uses two (2) electromagnetic shakers that apply a torque to the rotor in a plane coplanar with the rotor axis. The rotor has a vertical axis of rotation. The stress and deflection measurements are made using strain gages, accelerometers, and a state-of-the-art optical blade deflection measurement system. The measurements signals are made accessible through the use of a 100 channel slip ring. Additionally, the vacuum chamber can be evacuated to 0.01 psia.

### **DSRL Issues**

The issues that are of concern with current DSRL use involves the need for enhanced testing capabilities in light of the more extensive testing requirements for today's turbomachinery components. Rotating components are expected to be used at very high rotational speeds, have extended life, and have better static and dynamic properties. The current rotational speed in the DSRL is limited due to heating problems with the mechanical bearings. Additionally, the life of the mechanical bearing is limited. The current electromagnetic shaker excitation system is limited in the excitation energy it can provide and it can only excite in one plane. Magnetic suspension provides no physical contact at the support position which eliminates heating due to mechanical contact. Also, mechanical life is substantially extended. Additionally, increased flexibility in excitation orientation (direction and phasing) can be achieved.

### **DSRL Issues Addressed via Magnetic Suspension and Excitation**

In response to the issues surrounding the use of the DSRL, magnetic suspension and excitation has been chosen as a way to address them. The initial magnetic suspension and excitation device is a radial magnetic bearing. For the extended upgrade, two (2) radial and one (1) thrust magnetic bearing will be used. The magnetic bearings will provide magnetic actuation for excitation and support, increase excitation energy and orientation flexibility, extend life due to no mechanical contact, attain higher rotational speeds, and increase test duration (life cycles).

The current single magnetic bearing that is being used is a 4-pole heteropolar type (see Figure 4.). Each pole has 160 coil turns. Its outer diameter is 4.7 in. It is operated using a maximum of 4 amps per coil. Measurements have produced stiffness values up to 60,000 lb./in. (see Figure 7.). The nominal radial gap distance is 0.020 in. with an operating radial gap distance of about 0.005 in. The total system bandwidth, including computer controller, power amplifiers, etc..., is about 500 Hz. It has been installed in the rig in place of the lower mechanical bearing (see Figure 8.).

The control system uses proportional-derivative (PD) control implemented using Turbo Pascal programming language on a 486-PC. This control system allows modification of magnetic bearing parameters such as stiffness and damping (see Figure 9.). By having this flexibility certain gains can be programmed for various operating conditions. In order to determine what combination of gains are useful and produce stable operation, a stability map was obtained by observing and recording what gains combinations produced instability. These gains can be

plotted to show a stability surface under which stable operation of the system is achieved (see Figure 10).

A frequency domain representation of the systems dynamic characteristic can be examined to obtain another perspective of the system. A transfer function between the excitation signal and the shaft position sensor gives a spectral profile that indicates how well we can transmit energy to the system (see Figure 11.).

### **Blade Vibration Tests Using New Magnetic Feature**

Dynamic tests have been performed using this new capability. Blade-like structures, provided by the University of California at San Diego, were tested and essential dynamic data was obtained (see Figure 12.). They were quite pleased with the flexibility of applying the excitation and its increased energy capabilities.

Off-shoots of this effort enable a preliminary investigation of using the magnetic bearing system to provide shaft actuation to suppress blade vibrations using blade strain gage feedback (see Figure 13.). Initial results were favorable and were presented at the High Cycle Fatigue Initiative Workshop - Active Vibration Control/Engine Health Monitoring Session, December 10, 1996. The presentation was titled "Active Control of Blade Vibration Using Magnetic Forcing of Shafts".

### **Summary**

In summary, a single radial magnetic bearing has been initially integrated into the DSRL to provide vibration excitation. Later, the rig was modified to have the magnetic bearing replace a conventional bearing support thereby providing vibration excitation and control. The preliminary performance of the magnetic bearing has been assessed and the results were favorable. Consequently, it was decided to convert the system to an all magnetically supported one. This full conversion will enable the rig to provide enhanced testing capabilities. It is the mission of the project team to design, develop, and implement a magnetic suspension system which will meet the conversion upgrade requirements by December 31, 1997.

## Dynamic Spin Facility

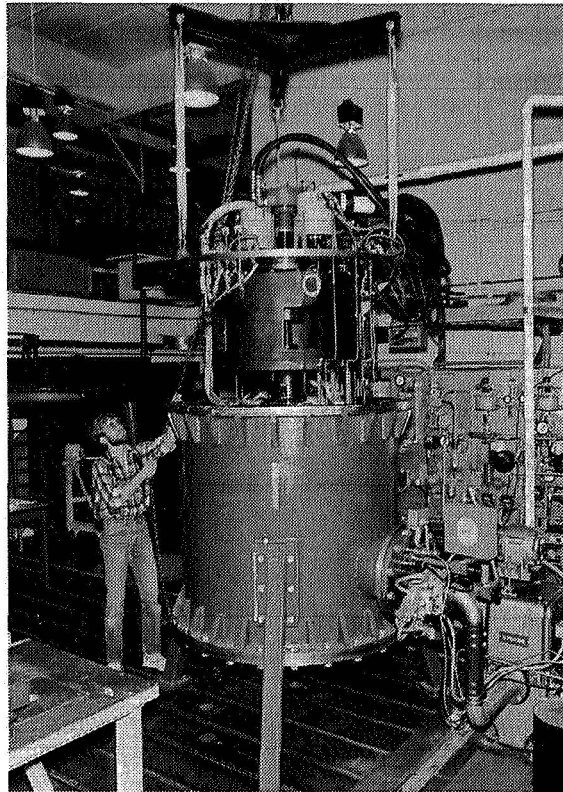


Fig. 1

CD-97-74655

## *Dynamic Spin Rig Lab Facilities*

- *Location: Building 5 - Test Cell CW-18*
- *Description: Turbomachinery blades and components are rotated in a vacuum to obtain stress and deflection measurements.*
- *Features:*
  - Rotor speeds to 20,000 rpm*
  - Air turbine rated @ 40,000 rpm*
  - 100 channel slip ring*
  - Chamber evacuated to 0.01 psia*
  - Vertical axis of rotation*
  - Electromagnetic shaker*
    - vibrates shaft and blades*
  - Optical blade deflection*
    - measurement system*

Fig. 2

## Magnetic Bearing Stator Laminations

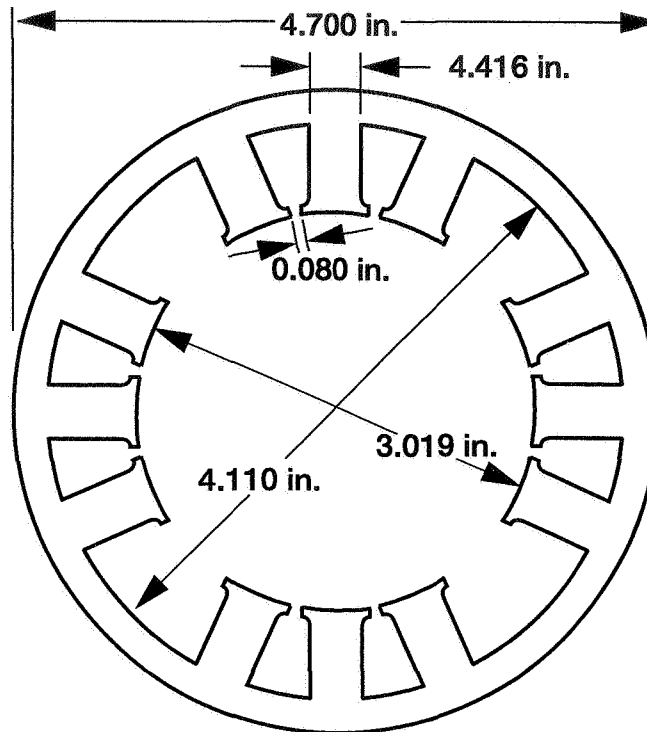


Fig. 3

CD-97-74648

## *Current Dynamic Spin Rig Issues*

- *Speed is limited because of current*
- *mechanical bearings (heating problem).*
- *Life of mechanical bearing is limited.*
- *More excitation energy is needed.*
- *Existing electromagnetic shakers can excite only in one plane.*

Fig. 4

## *Response to Spin Rig Issues: Magnetic Excitation and Suspension*

- *Use a magnetic bearing as magnetic actuator for excitation and support*
- *Increase excitation energy and orientation flexibility*
- *Extend life: no mechanical contact*
- *Attain higher rotational speeds*
- *Increase test duration (life cycles)*

Fig. 5

### **Dynamic Spin Rig Magnetic Bearing Load Curve** Gain = 160; Stiffness > 60,000 lb/in.

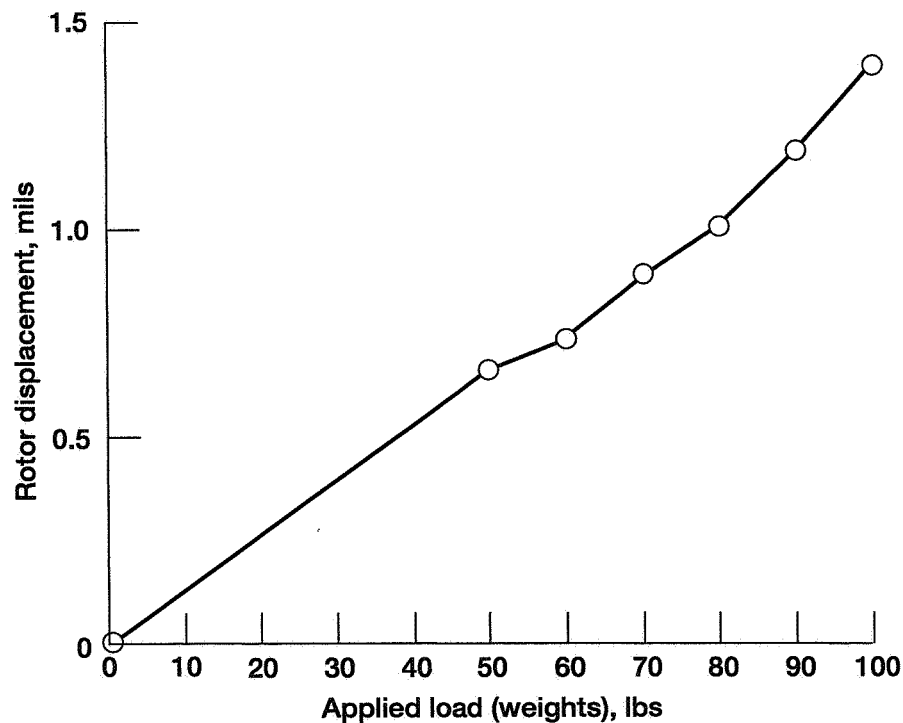


Fig. 6

CD-97-74649

## Magnetic Bearing Installed in Dynamic Spin Rig

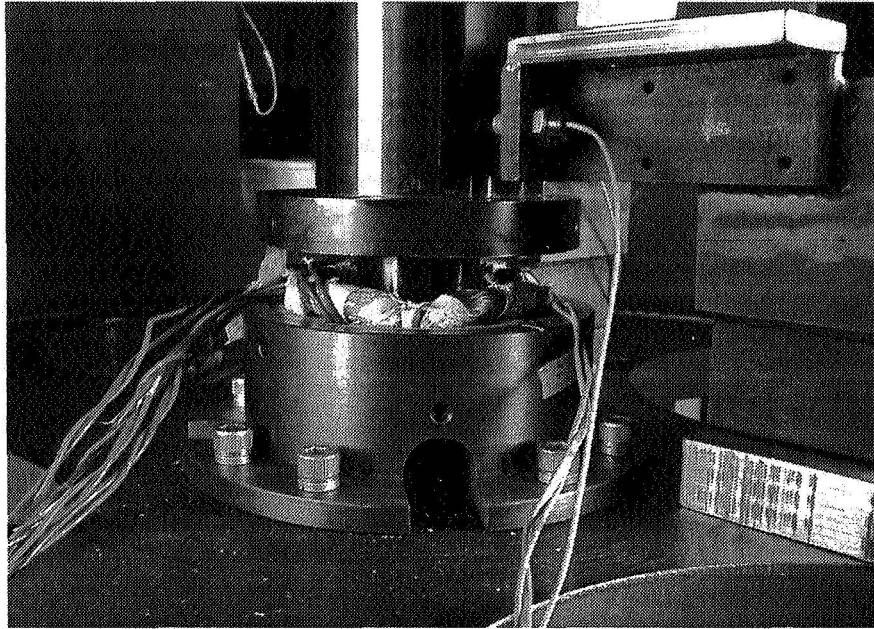


Fig. 7

CD-97-74650

## Block Diagram for Spin Rig Excitation System

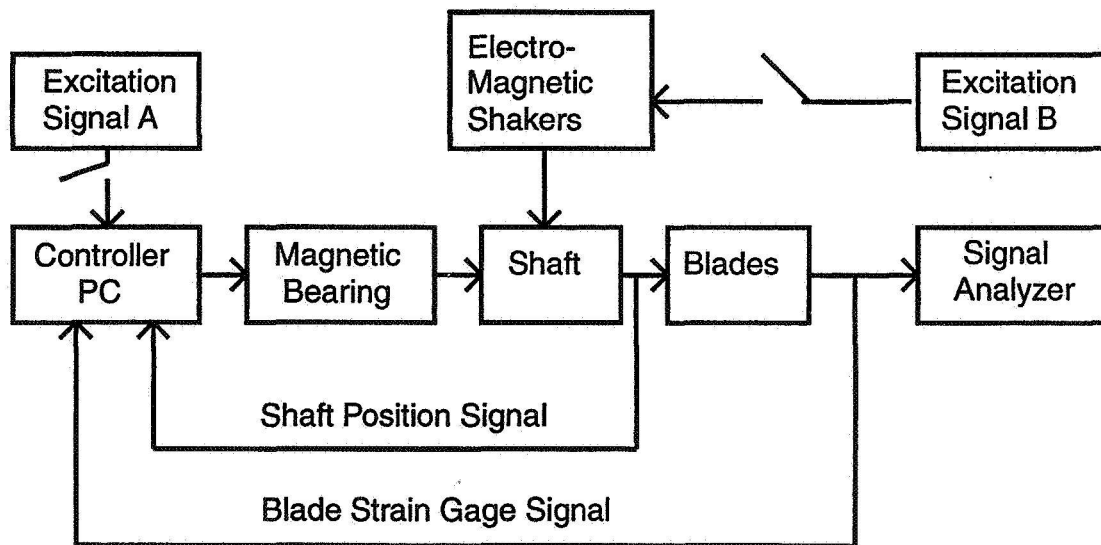


Fig. 8

CD-97-74651

## Dynamic Spin Rig Magnetic Bearing Control System Stability Limit Surface

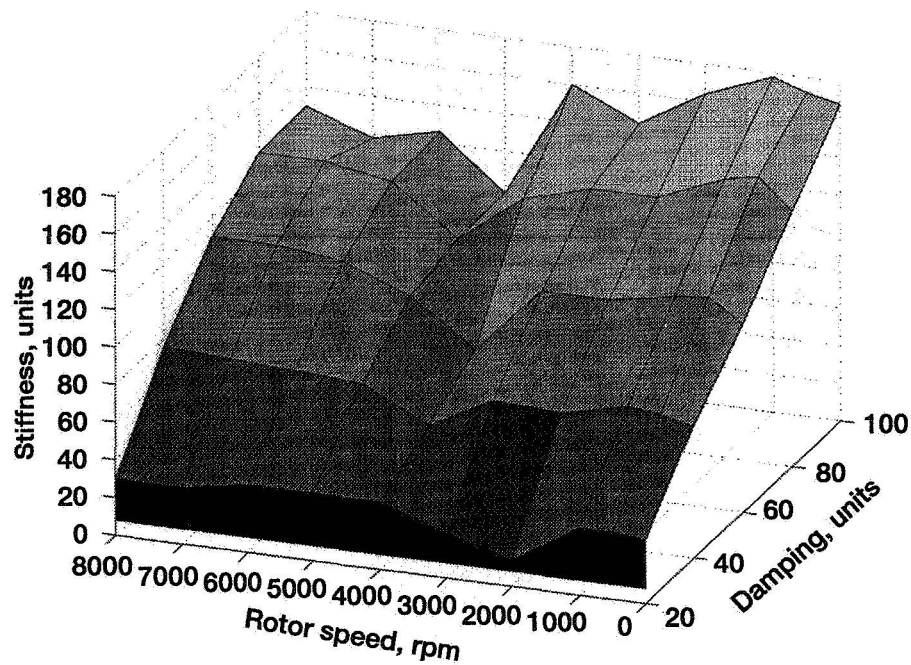


Fig. 9

CD-97-74652

## Spin Rig Magnetic Bearing/Rotor Transfer Function (in Vacuum) — Y Axis

Constant K, Variable D

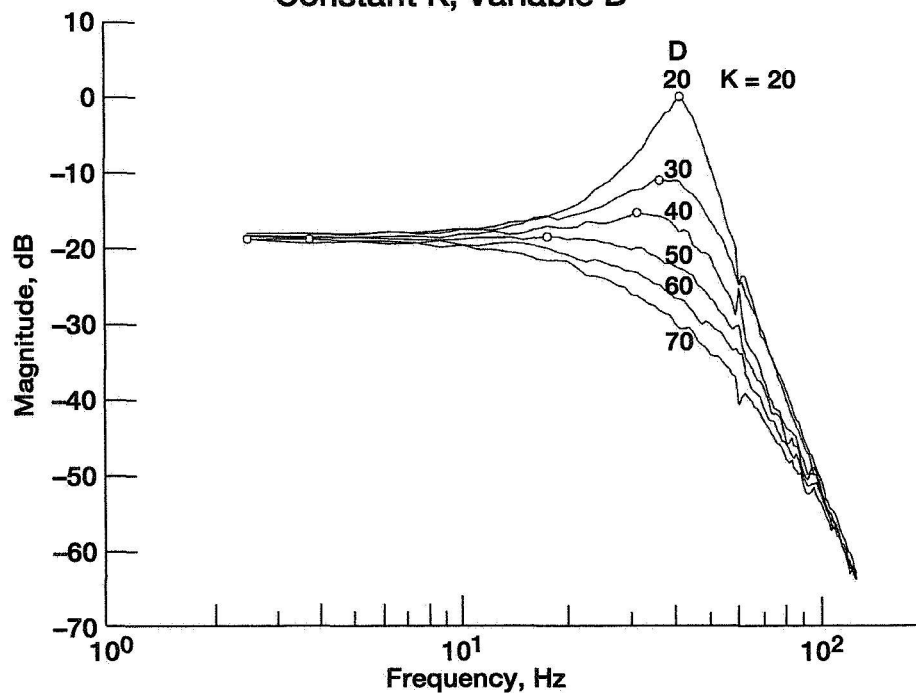


Fig. 10

CD-97-74653

## Viscoelastic Damped Composite Plates in the NASA Dynamic Spin Facility

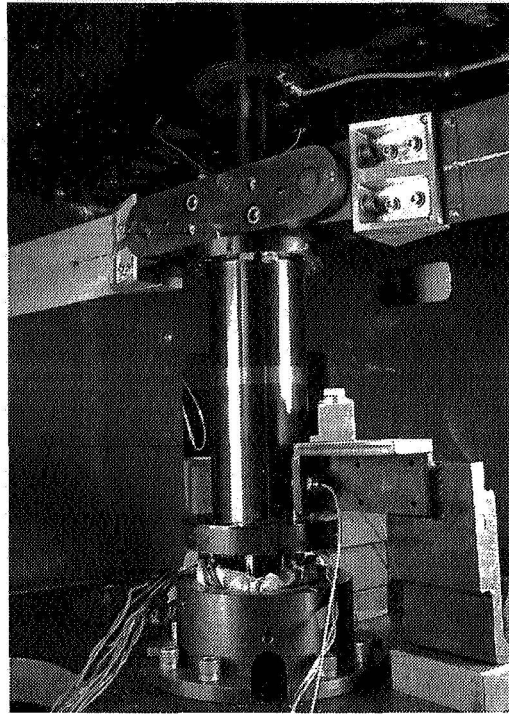


Fig. 11

CD-97-74607

### Transient Decay of Flat Plate With Damping Patch

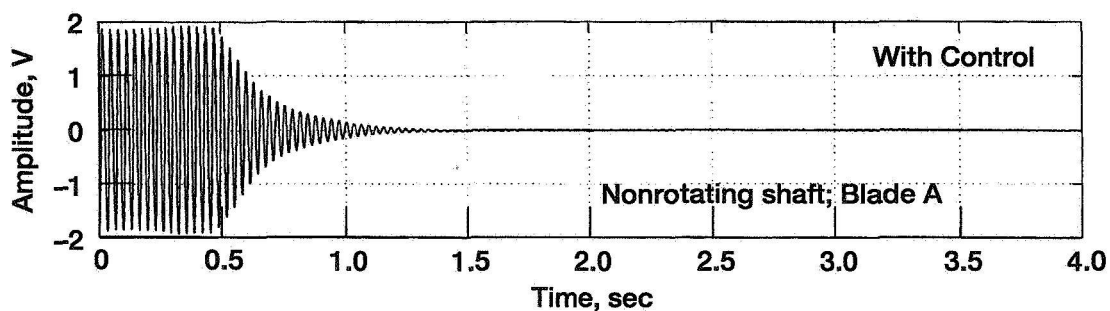
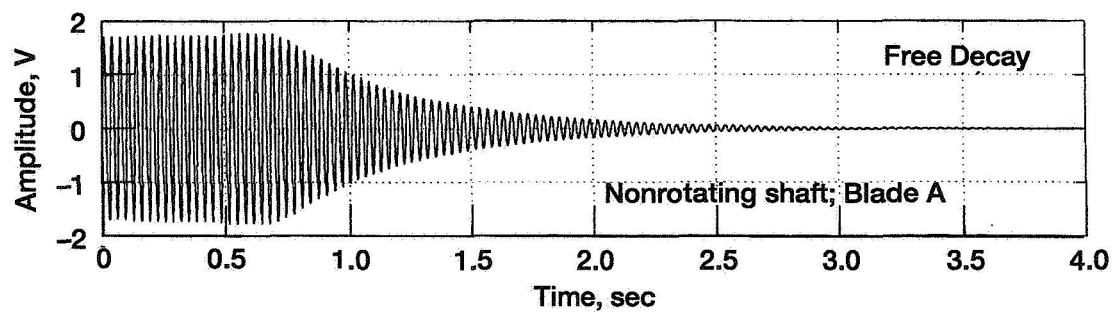


Fig. 12

CD-97-74654



## *Dynamic Spin Rig Conversion Project Summary*

- *Initially, a single radial magnetic bearing was integrated into the Dynamic Spin Rig to provide vibration excitation.*
- *Later, the rig was modified so that a magnetic bearing replaced a conventional bearing support, thereby providing vibration excitation and control.*
- *An assessment of the preliminary performance of the magnetic bearing showed favorable results.*
- *Consequently, a decision was made to convert the mechanical support system for the rotor to a fully magnetic one, which will enable the rig to provide the desired enhanced testing capabilities.*

Fig. 13

# A NEW 1000°F MAGNETIC BEARING TEST RIG

ALBERT F. KASCAK  
Gerald T. Montague  
Army Research Laboratory  
Cleveland, Ohio

Gerald V. Brown  
LeRC-NASA  
Cleveland, Ohio

Alan B. Palazzolo  
Texas A&M  
College Station, Texas

510-09

029109

141

078105

## INTRODUCTION:

NASA and the Army are currently exploring the possibility of using magnetic bearings in gas turbine engines. The use of magnetic bearings in gas turbine engines could increase the reliability by eliminating the lubrication system. The use of magnetic bearings could also increase the speed and the size of the shafts in the engine, thus reducing vibrations and possibly eliminating third bearings. Magnetic bearings can apply forces to the shafts and move them so that blade tips and seals do not rub. This could be part of an active vibration cancellation system. Also, whirling (displacing the shaft center line) may delay rotating stall and increase the stall margin of the engine. Magnetic bearings coupled with an integral starter generator could result in a more efficient "more electric" engine. The IHPTET program, a joint DOD- industry program, has identified a need for a high temperature, (as high as 1200°F), magnetic bearing that could be demonstrated in a phase III engine.

A magnetic bearing is similar to an electric motor. The magnetic bearing has a laminated rotor and stator made out of cobalt steel. The stator has a series of coils of wire wound around it. These coils form a series of electromagnets around the circumference. These magnets exert a force on the rotor to keep the rotor in the center of the cavity. The centering force is commanded by a controller based on shaft position, (measured by displacement probes). The magnetic bearing can only pull and is basically unstable before active control is applied. The engine shafts, bearings, and case form a flexible structure which contain a large number of modes. A controller is necessary to stabilize these modes. A power amplifier is also necessary to provide the current prescribed by the controller to the magnetic bearings. In case of very high loads, a conventional back up bearing will engage and stop the rotor and stator from rubbing.

The magnetic bearing, the displacement probes, and the backup bearing are the only components in the hot section. The cobalt steel has a curie point greater than 1700°F and is heat treated about 1550°F. It begins to oxidize about 1000°F and practical limitations associated with the maximum magnetic field strength and the yield strength of the cobalt steel, limit the temperature to about 1200°F. Copper wire has a melting point beyond 2000°F but conventional wire insulation is only good to about 500°F. We need a ceramic wire insulation with high electrical resistivity, good heat conduction, and a high thermal expansion. Displacement probes can be optical, inductive, eddy current, or capacitive. All these probes can be built to operate at high temperature, but the capacitance probe seems to be the most

stable and linear. The backup bearing will be a conventional bearing with solid lubrication mounted in a high temperature damper.

#### APPROACH:

The objective is to determine the limits in temperature and speed of a magnetic bearing operating in an engine environment. Our approach is to use our in-house experience in magnets, mechanical components, high temperature materials, and surface lubrication to build and test a magnetic bearing. The tests will include both rig and engine tests and will be done in-house or through cooperative programs in industrial facilities.

A 1000°F magnetic bearing test rig has been built. The rig consists of a shaft supported on two grease-packed ball bearings with the magnetic bearing between the bearings. The rig is designed to run to 20,000 RPM. The grease packed bearings have shims between the shaft and the inner race. Removing the shims leaves a clearance between the shaft and the inner race, allowing these bearings to act as backup bearings. The magnetic bearing is mounted in a 9 inch cavity which is heated by electrical band heaters to as high as 1200°F.

The rig has a dual purpose. The first purpose is to measure the bearing coefficients. The second purpose is to do rotordynamic tests. When the rig is configured in the bearing coefficient mode, the rotor of the magnetic bearing is mounted on the shaft and the shims are inserted between the shaft and the ball bearings. The stator is mounted in a housing that can be shaken by four orthogonal piezo-electric actuators. The force transmitted to the stator, the acceleration of the stator, and the relative displacement of the rotor and stator are measured. With these measurements both the magnetic bearing displacement stiffness and current stiffness can be measured at speed. With the shims removed the magnetic bearing stability, controllability, and blade loss tests can be performed.

#### SUMMARY:

The first bearing tested will be a high temperature modification of the homopolar design previously tested at cryogenic and room temperatures. The second bearing tested will be a heteropolar design. The tests will first concentrate on various wire insulations and then we will try to re-enforce the laminations to reach higher speeds. A neural net controller is being developed to cope with nonlinearities and will be tested.

#### FUTURE RESEARCH:

We are applying magnetic bearings to other areas. Our "Spin Rig", a blade vibration test facility, is being retrofitted with magnetic bearings. The magnetic bearings will be used as actuators to excite blade vibrations. Our rotordynamics rig is being retrofitted with magnetic bearings to do redundancy tests on the coils. We have plans to retrofit a compressor rig to do active stall control tests. And lastly, we have begun a program in magnetic bearing suspension for flywheel energy storage for space applications.

## High Temperature Magnetic Bearing Applied to Gas Turbine Engine

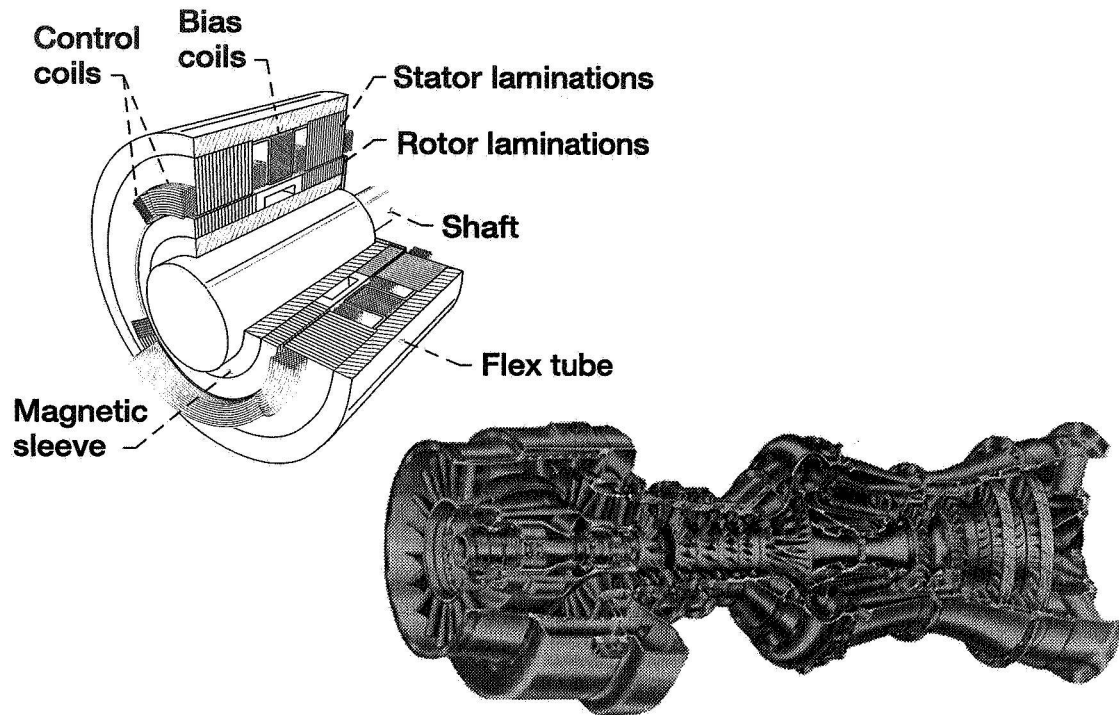


Fig. 1

## Who is Interested?

- Engine Manufacturers: (GE, Pratt & Whitney, Allison, and AlliedSignal have in-house programs)

- Government:

Navy—Magnetic bearing retrofitted on existing engine

Air Force—IHPTET engine supported on magnetic bearings and integral starter generator (ISG)

Army—Flight weight controller for magnetic bearings

Fig. 2

## Parts of a Homopolar Magnetic Bearing

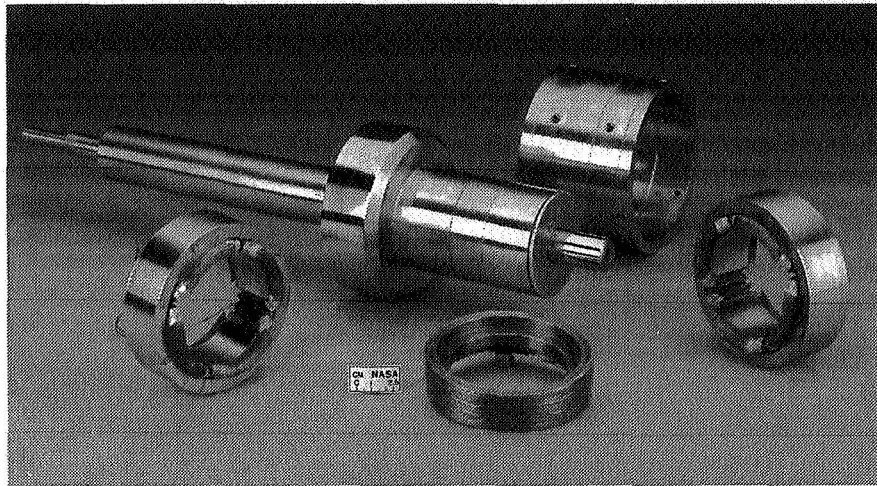


Fig. 3

## Homopolar Magnetic Bearing

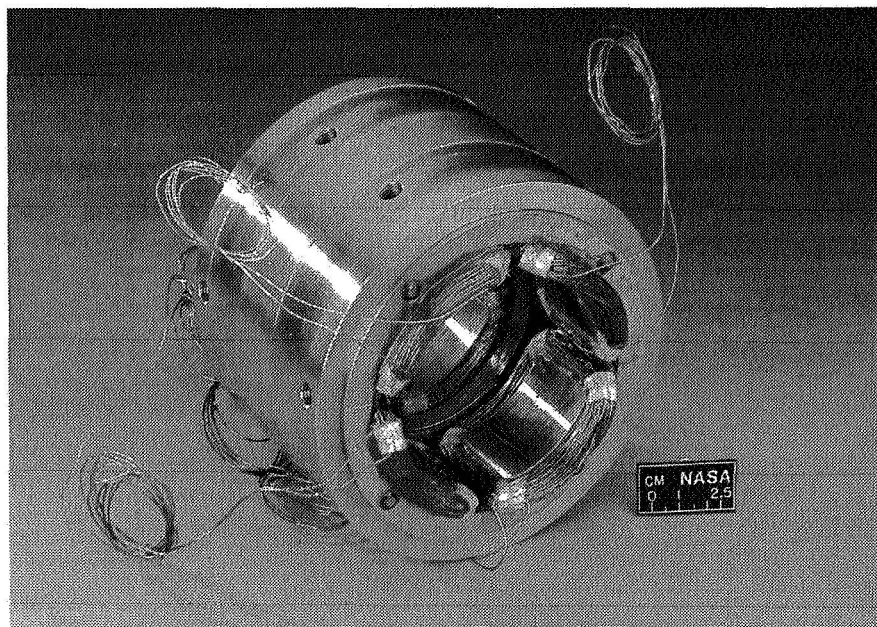


Fig. 4

## Heteropolar Magnetic Bearing

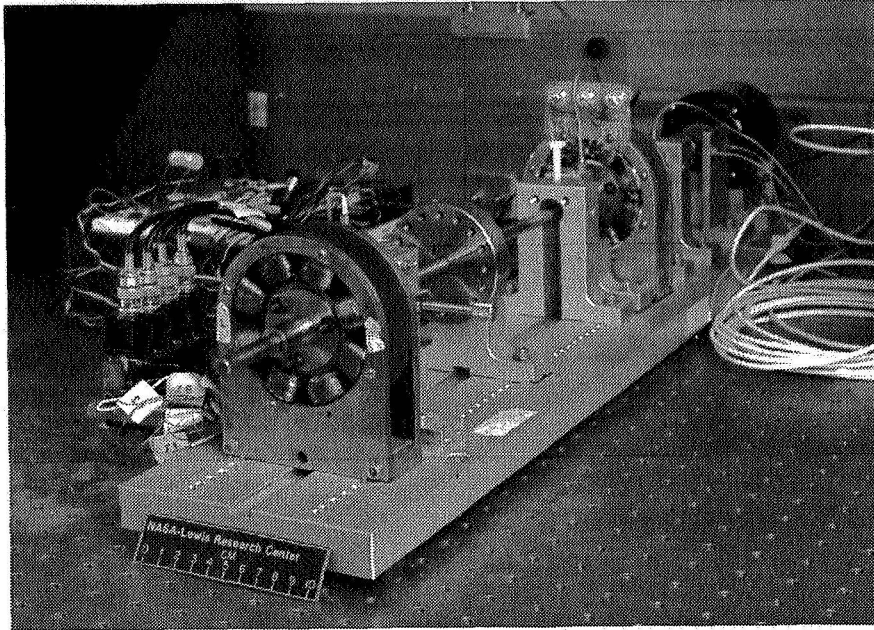


Fig. 5

## Magnetic Bearing Components

- Radial or Thrust Magnetic Actuator  
(Rotor, Stator, Coil)
- Displacement Probe  
(Eddy Current, Inductive, Capacitive, Self Sensing)
- Power Amplifier  
(Linear or Pulse Width Modulator)
- Controller  
(Analog or Digital)
- Auxiliary Bearing  
(Rub, Ball or Roller, Foil, Air, Powder)

Fig. 6

# Benefits of Using More Electric Engines

- **Safer and More Reliable**  
No oil cooler, pumps, plumbing, oil seals, & oil leaks  
Health monitoring and vibration control
- **Higher Efficiency—7 to 15% in specific fuel consumption (P&W, Allison)**  
Less secondary air flow and higher temperature limits—1 to 2%  
Blade tip clearance control—1 to 2%  
Stall line management—5 to 11%
- **Larger Design Envelope & Clean Engine Design**  
Higher rotational speeds & larger diameter stiff rotors

Fig. 7

## Active Vibration Control Controlled Blade Loss; 2.06 g-cm at 8000 rpm

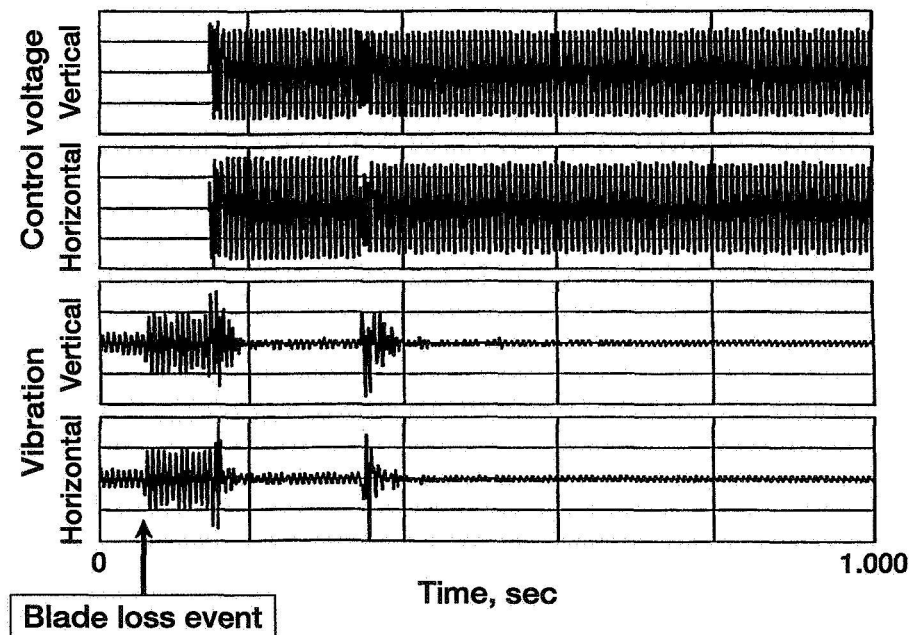


Fig. 8

Figure 10 is a graph showing Derivative gain (Y-axis, 0 to 40) versus Proportional gain (X-axis, 1 to 10). The graph compares three configurations:

- 0% cond. in lam. w/o skin depth, coarse mesh (Squares)
- 0% cond. in lam. with skin depth, fine mesh (Circles)
- Experiment (Triangles)

The graph is divided into two regions by a dashed line:

- Stable:** Region to the left of the dashed line (Proportional gain < 5.5).
- Unstable:** Region to the right of the dashed line (Proportional gain > 5.5).

The data points for the three configurations are approximately as follows:

Proportional gain	Derivative gain (coarse mesh)	Derivative gain (fine mesh)	Derivative gain (Experiment)
1.5	7	2	1
2.0	10	2.5	4
3.0	15	3	7
4.0	20	3.5	10
5.0	25	4	15
6.5	-	5	-
8.0	-	6	25
9.5	-	7	-



## Capacitive Probe Calibration at 1100 °F

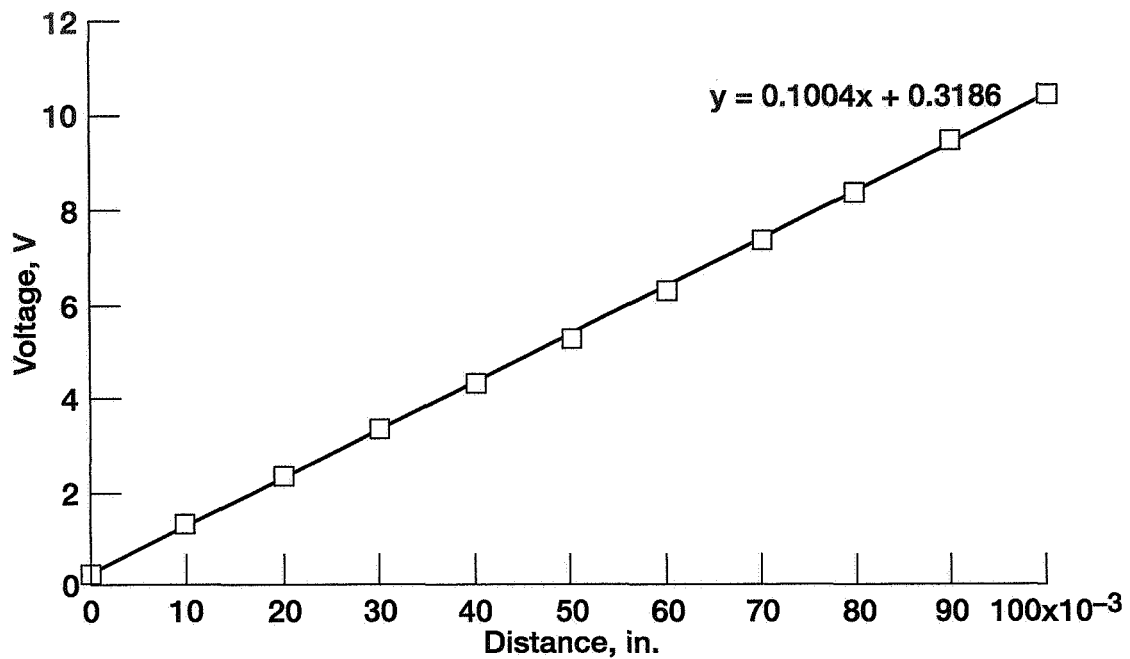


Fig. 10

## Tensile Properties of Hipercro 50

0.008-in. -thick sheet

Temperature, °F	0.20-Percent offset yield strength, psi	Tensile strength, psi	Elongation in 2-in. specimen, percent	Modulus of elasticity, psi
Longitudinal				
72	41 650	41 650	0.5	28.9×10 <sup>6</sup>
500	37 950	71 250	5.5	27.1
800	36 750	67 900	7.0	27.0
1100	33 750	62 600	6.0	20.0
Transverse				
72	-----	37 700	---	38.0×10 <sup>6</sup>
500	38 950	55 250	1.5	33.2
800	38 050	60 150	4.9	29.7
1100	34 700	55 250	12.0	28.9

Fig. 11

## Magnetic Properties of Hiperco 50

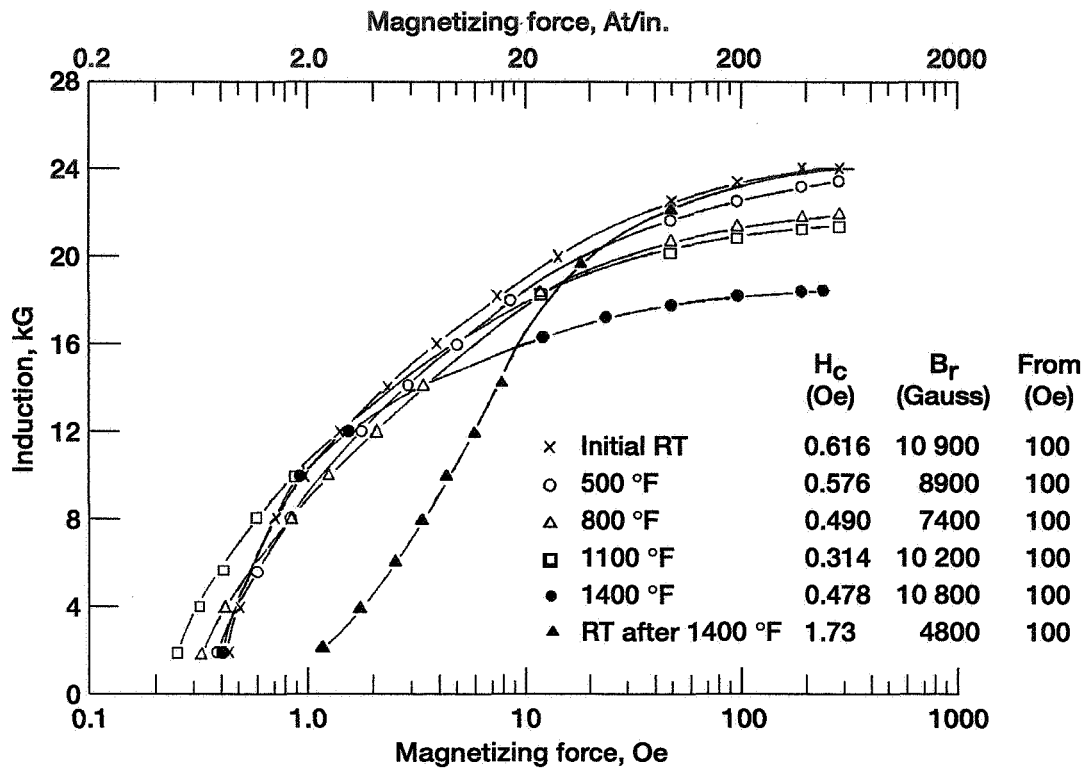
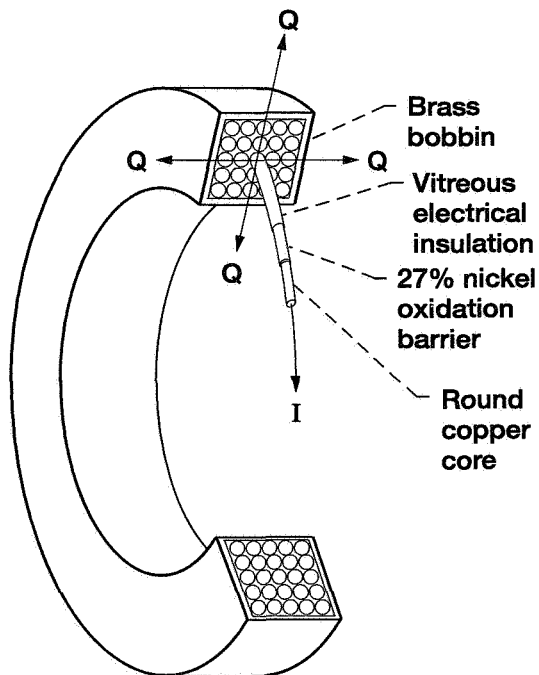


Fig. 12

## Coil Design

### Conventional Technology



### Advanced Technology

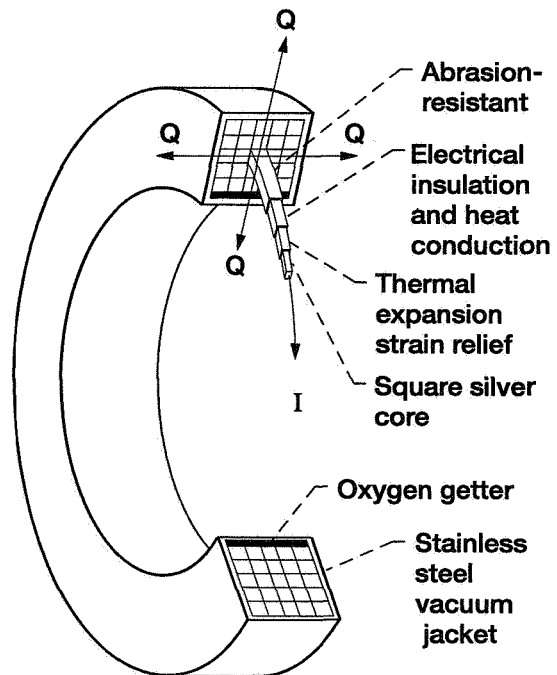


Fig. 13

# Objective

The objective is to determine the limits in temperature and speed of a magnetic bearing operating in an engine environment

- Design and Build Test Rig to accommodate 1000 °F and 20,000 rpm
- Design and Build Test Bearing
- Test Various Wire Insulation, Displacement Probes, and Lamination Designs
- Measure Bearing Coefficients, Stability, and Controllability
- Conduct Rotordynamic Test (Blade Loss, Seal Rub, FOD, etc.)

Fig. 14

## High Temperature Magnetic Bearing Test Rig

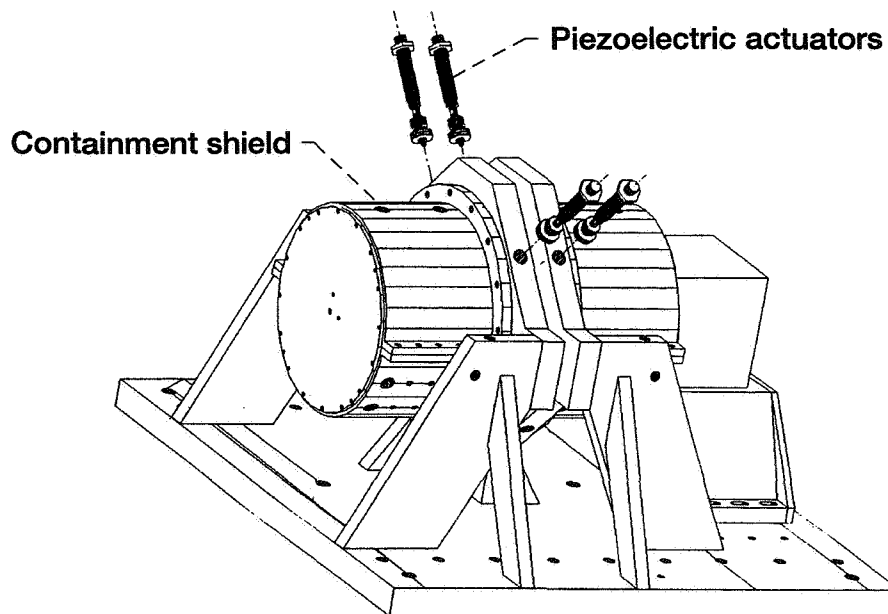


Fig. 15

## High Temperature Magnetic Bearing Rig

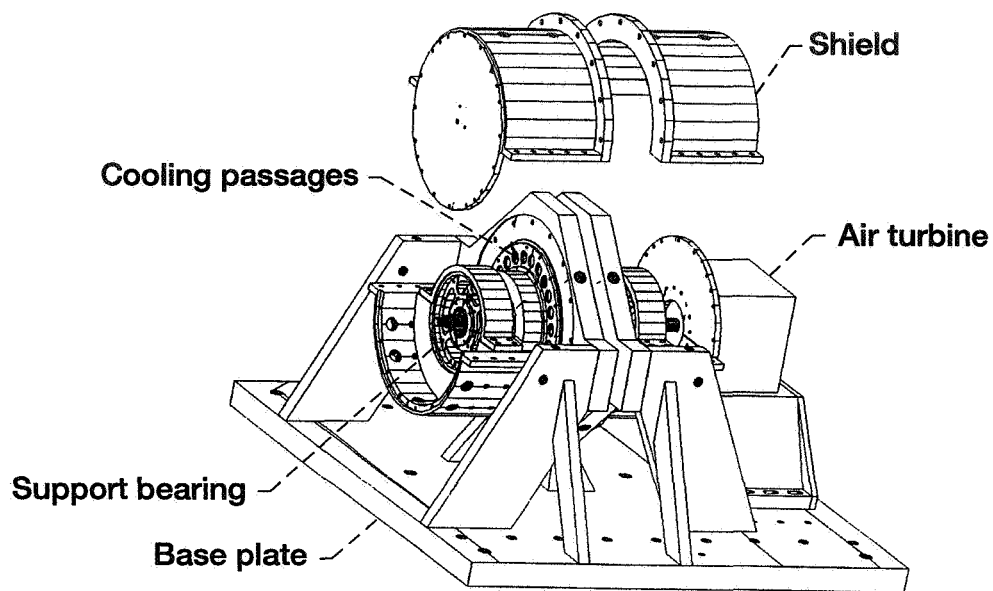


Fig. 16

## High Temperature Magnetic Bearing Rotor Assembly

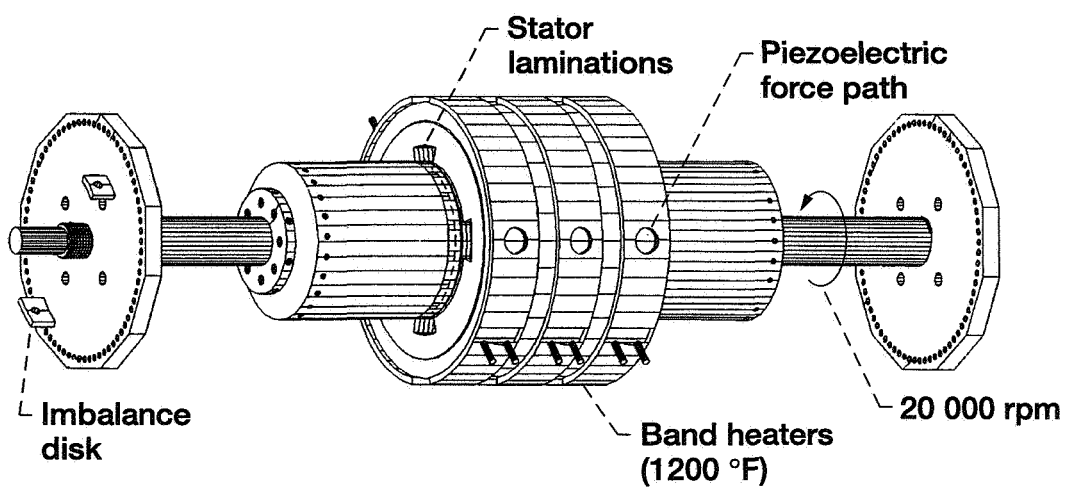


Fig. 17

## Piezoelectric Actuator

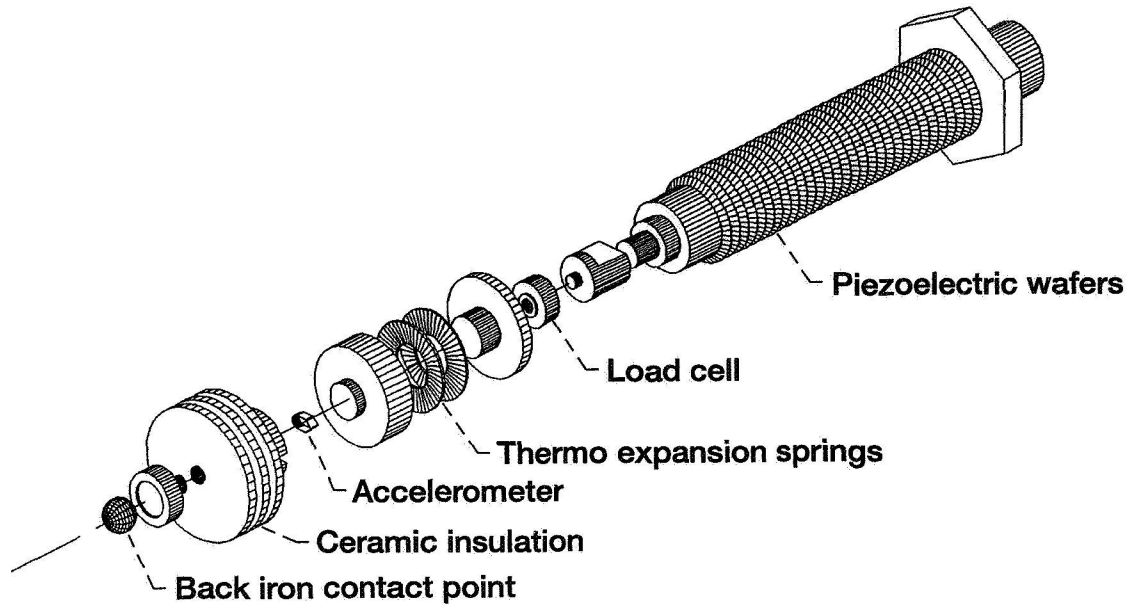


Fig. 18

## Summary

### First Test

- Capacitive probes are linear to 1200 °F; but require the shaft to be grounded
- The wire will be nickel clad copper with magnesium oxide coating
- Hiperc 50 laminations with oxide coating

### Second Test

- Square silver wire rapped with S-glass

### Third Test

- Ungrounded capacitive probes

Fig. 19

## Conclusions

- We were able to design a magnetic bearing to operate to 1000 °F and 20,000 rpm
- We were able to design a test rig to measure the bearing coefficients and run a rotordynamic test at temperature and speed

Fig. 20

## Future Research

(Apply Magnetic Bearings To Other Areas)

- Spin Rig—excite blade vibrations
- Rotordynamics Rig—redundancy test
- Compressor Rig—active stall control
- Flywheel Energy Storage—space applications

Fig. 21

511-63  
029110  
8P.  
295556

**NEURAL NETWORK CONTROL OF  
A MAGNETICALLY SUSPENDED ROTOR SYSTEM**

**BENJAMIN CHOI, Gerald Brown, and Dexter Johnson  
NASA Lewis Research Center  
Cleveland, Ohio 44135**

**Abstract**

Magnetic bearings offer significant advantages because of their noncontact operation, which can reduce maintenance. Higher speeds, no friction, no lubrication, weight reduction, precise position control, and active damping make them far superior to conventional contact bearings. However, there are technical barriers that limit the application of this technology in industry. One of them is the need for a nonlinear controller that can overcome the system nonlinearity and uncertainty inherent in magnetic bearings.

This paper discusses the use of a neural network as a nonlinear controller that circumvents system nonlinearity. A neural network controller was well trained and successfully demonstrated on a small magnetic bearing rig. This work demonstrated the feasibility of using a neural network to control nonlinear magnetic bearings and systems with unknown dynamics.

**Introduction**

Developing a controller for magnetic bearings has been one of the critical issues because magnetic bearings are inherently unstable and highly nonlinear. Also, the shaft may have unknown dynamic properties. However, the analysis and control of a magnetic bearing system have been developed primarily on the basis of linear system theory. Because of system uncertainty and nonlinearity, the resulting simplifications degrade overall system performance and reliability.

Thus, one possible approach to be considered first is to develop a conventional nonlinear controller that takes account of system nonlinearity and uncertainty. However, according to refs. 1 and 2, a nonlinear controller design requires a very accurate system model, otherwise the performance with the inaccurate model is worse than with the linear controller. Furthermore, the nonlinear controller might be computationally too intensive for practical real-time applications. Currently the common modeling methods for magnetic bearings are based on linear system theory, wherein nonlinearity and unknown dynamic properties cannot be fully taken into account.

The other possible approach to circumvent system nonlinearity and uncertainty in the magnetic bearing and the plant is to use an artificial intelligence technology, such as a neural network, fuzzy logic, or a genetic algorithm. In refs. 1 to 3, researchers have already successfully implemented such technology as system controllers for magnetic bearings. For nonlinear controller development on our small magnetic bearing rig in the Machine Dynamics Branch, the neural network was selected because it generates a neural model without any detailed information regarding the internal working of the magnetic bearing system, even though it might be too complex or impossible to derive an accurate system model.

This neural approach consists of two steps: the first is to train a neural plant model to emulate the magnetic bearing system and the plant; the second is to use that emulator to train a neural controller. MatLab, SimuLink, and Neural Network Toolbox software (ref. 4) are used to train the neural plant emulator and the neural controller, and to simulate the whole system. A feed-forward architecture with a back-propagation learning algorithm (ref. 5) was selected because of its proven performance, accuracy, and relatively easy implementation.

### **Neural Network Emulator Development**

The neural net plant emulator is first trained to emulate a theoretical model of the nonlinear plant. In order to train the emulator, the appropriate inputs and outputs for modeling the magnetic bearing system plant need to be determined. A discrete theoretical model of the plant dynamics in state-space notation is utilized to choose the present states of the plant (rotor displacement and velocity) and the plant input (control current) as the inputs to the emulator. The next states, the rotor displacement and velocity after one sample time, are chosen as the outputs from the plant emulator (see Fig. 3(a)). During the learning procedure, the errors between the actual network output and the training output (from the theoretical model) are minimized by upgrading the weights. The updating scheme is implemented so that changes recursively propagate back through the network, changing weights that had a large effect on the output more than those which did not. This process is repeated until the training and computed output are within a predefined training error (see ref. 5 for details).

Fig. 4 shows how well the neural emulator was trained with 405 training sample data. The emulator generated the almost exact target values (the next state of rotor displacement and velocity) for the training input data. Then the emulator was tested by simulating its response for the initial conditions of  $x_0 = 0$  in.,  $\dot{x} = 1$  in./sec, and  $I_c = 0$  amp (see Fig. 5). The neural net emulator response is so accurate that it perfectly overlaps the actual magnetic bearing response ('+' markers). In other words, the neural emulator perfectly predicts the next states (delayed by one sample time) of the magnetic bearing system for the current states and control force, which are not in the training sample data.

### **Neural Network Controller Training**

Our goal is to find a neural net controller that makes the whole system meet conventional performance specifications such as bandwidth, settling time, and overshoot, etc. We want the controller to take the current magnetic bearing states  $\bar{x}(t)$  and demand  $r$  as input parameters, and to output a control force  $u(t)$  to the magnetic bearing system. These current state values should make the magnetic bearing's next state vector  $\bar{x}(t+1)$  be identical to that defined by the desired linear reference system, which satisfies performance specifications in either the frequency or the time domain (see Fig. 3(b)). By replacing the magnetic bearing and plant with the neural plant model developed in the previous section, the errors between the actual magnetic bearing behavior and the desired linear behavior can be backpropagated through the model network to the control network. The derivatives are then backpropagated through the controller and used to adjust its weights and biases. Notice that during the controller training the neural plant model's weights and biases are not changed. Thus, the controller network must learn how to control the magnetic bearing system, represented temporarily by the neural plant emulator, so that it behaves like the linear reference model (see refs. 4, 5, and 1 for details).



Fig. 6(a) shows the Bode plot of a simple 2<sup>nd</sup> order linear reference model derived from frequency domain specifications; Fig. 6(b) shows the closed-loop magnetic bearing system after training. Both are almost identical even after 200 training epochs. Another neural controller based on time domain specifications is trained and tested by simulating its response for the initial condition and by comparing the results to the actual magnetic bearing response (see Fig. 7). The neural net controller is so accurate that it perfectly overlaps the magnetic bearing response ('+' markers). As can be seen here, the network does a near perfect job of making the nonlinear magnetic bearing system act like the linear reference model.

### **Controller Demonstration on Hardware**

The neural net controller algorithm trained from the theoretical plant model as just described was used to control our small Bentley-Nevada magnetic bearing rig by simply substituting it for the existing PID (proportional, integral, and derivative) controller code. Fig. 8 shows the orbits of rotor displacements from levitation to a rotor speed of about 12,000 rpm. When the controller powers on, the rotor is levitated to the desired reference position  $r$ , and then as rotor speed increases, the rotor orbits are getting bigger because of the disturbance force caused by mass imbalance. Notice that the neural plant emulator was trained only on purely theoretical data obtained from a nonlinear analytical plant model, where we neglect amplifier dynamics, sensor dynamics, and system noise and uncertainty.

### **Summary**

In this work, a neural network controller that circumvents the magnetic bearing's nonlinearity was developed and successfully demonstrated on a magnetic bearing rig. The neural plant emulator and neural controller were so accurate that the neural network controller did a near perfect job of making the nonlinear magnetic bearing system act like the linear reference model.

In future work, real experimental data for the nonlinear, unidentified plant will be used to train the neural plant emulator, which will then be used to train the neural controller, to improve system performance and reliability. Eventually, on-line training techniques should be utilized to adapt the neural controller to the changing dynamic characteristics of the magnetic bearing and plant system.

### **References**

1. Fittro, R.: Magnetic Bearing Control Using Artificial Neural Networks. MAG'93 Magnetic Bearings, Magnetic Drives and Dry Gas Seals Conf., pp. 201-210, Alexandria, VA, 1993.
2. Bleuler, H. et al.: Nonlinear Neural Network Control for a Magnetic Bearing. Swiss Federal Inst. of Tech., Zurich, Switzerland, 1992.
3. Chen, H.; and Lewis, P.: Rule-Based Damping Control for Magnetic Bearings. Proc. 3<sup>rd</sup> Intl. Symposium on Magnetic Bearings, pp. 25-32, 1992.
4. MatLab User's Guide, Neural Network Toolbox and SimuLink Toolbox, The MathWorks, Inc.
5. Rumerlhart, D.E.; and McClelland, J.L.: Parallel Distributed Processing: Exploration in the Microstructure of Cognition, vol. 1, MIT Press, Cambridge, MA, 1986.

# WHY A NEURAL NET CONTROLLER?

## Current Problems With Linear Controllers

- Inherently Unstable and Highly Nonlinear
- Unknown Dynamic Properties
- Analysis and Control Based on Linear System Theory

## ☛ To Increase Overall System Performance and Reliability

### ■ Conventional Nonlinear Controller

- Very accurate system model required.
- Computationally too intensive for real-time applications.

### ■ Neural Net Controller

- No mathematical model required.
- System nonlinearity and uncertainty circumvented.
- Relatively simple implementation.

Fig. 1

## Control Block Diagram of Bentley-Nevada Magnetic Bearing System

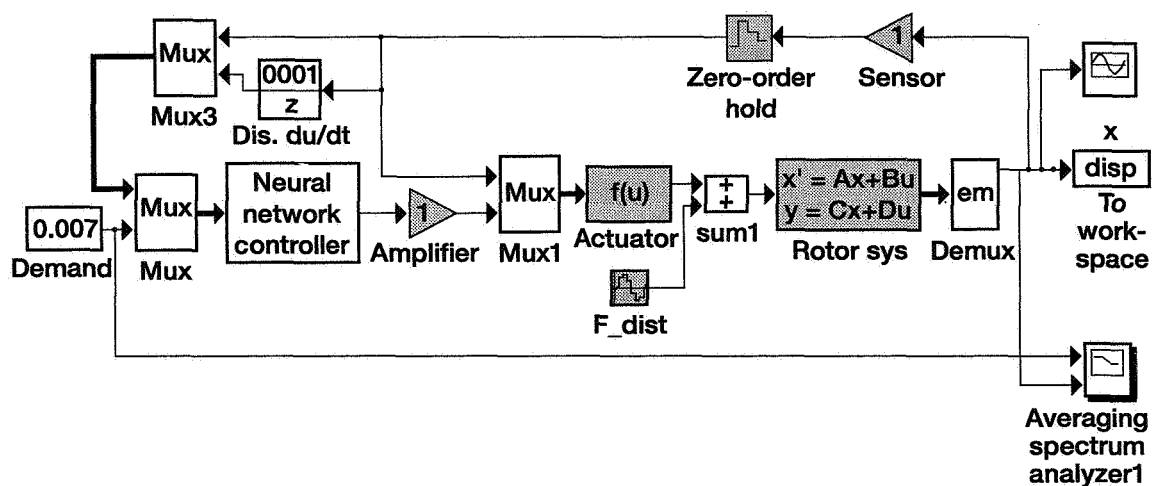
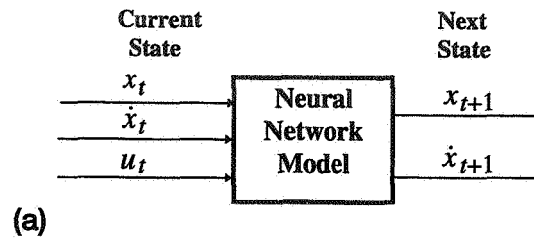


Fig. 2

# Nonlinear System Identification Using Neural Network



## Neural Controller/Model System

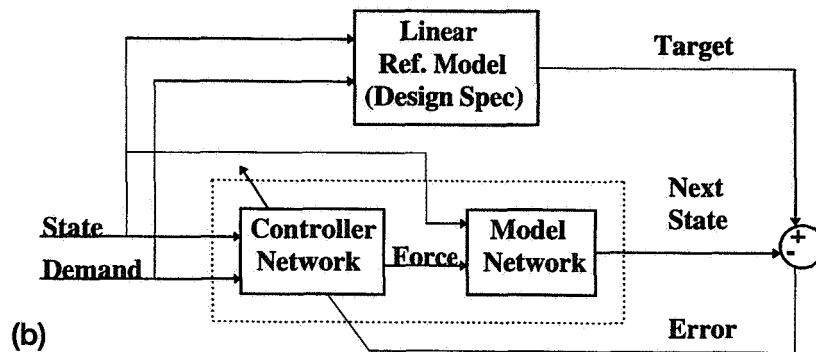


Fig. 3

## Target Values and Actual Neural Net Response for 405 Training Points

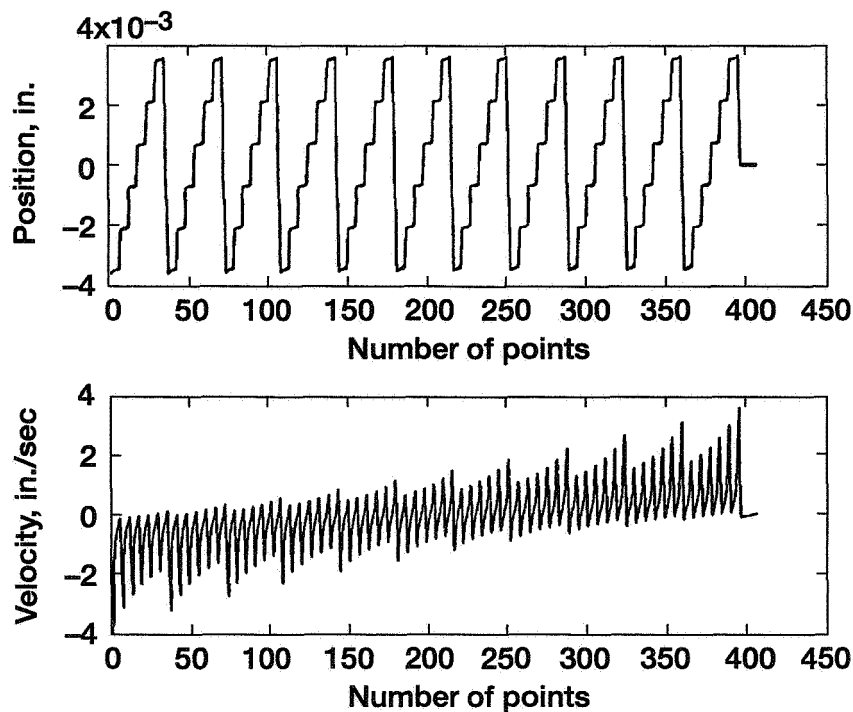


Fig. 4

## MB and Neural Net Response for Initial Conditions of $x_0 = 0$ in., $\dot{x}_0 = 1$ in./sec, and $u_0 = 0$ amp

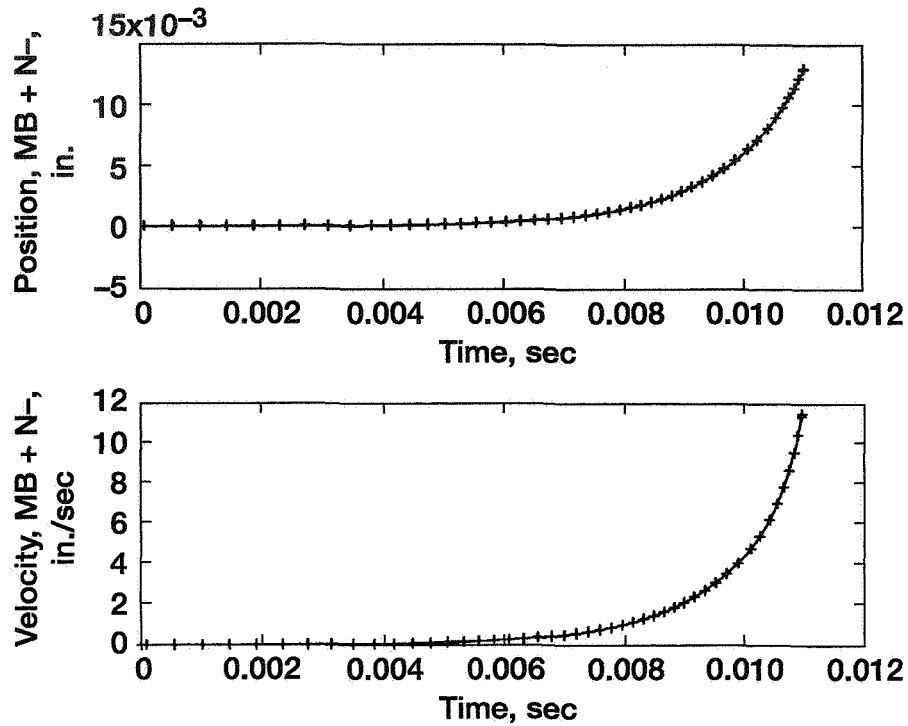


Fig. 5

## Bode Plots of Desired and Neural Network Models

Bode plot of a simple 2nd order  
 linear reference model in  
 frequency domain spec of  
 $m_p = 1.1$  and  $w_c = 1000$  Hz

Bode plot of trained  
 closed-loop system

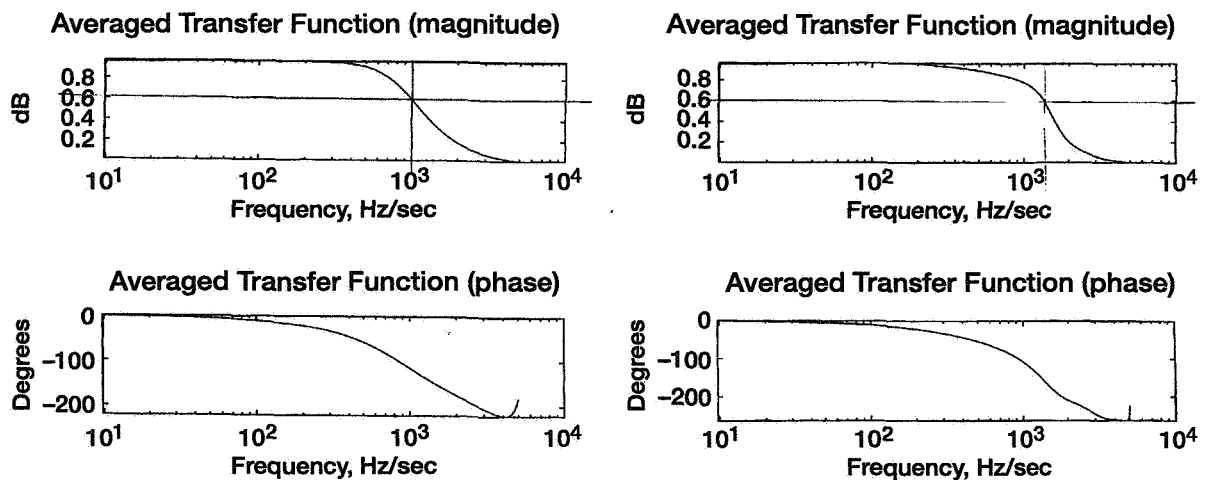


Fig. 6

A Simple 2nd Order Linear Reference Model Response in Time Domain Spec of  $P_O = 4.3\%$  and  $T_S = 0.0001$  sec, and a Trained Closed-Loop System Response for  $x_o = 0.011$  in.,  $\dot{x}_o = -6$  in./sec, and  $r_f = -0.005$  in.

Desired and Actual Response

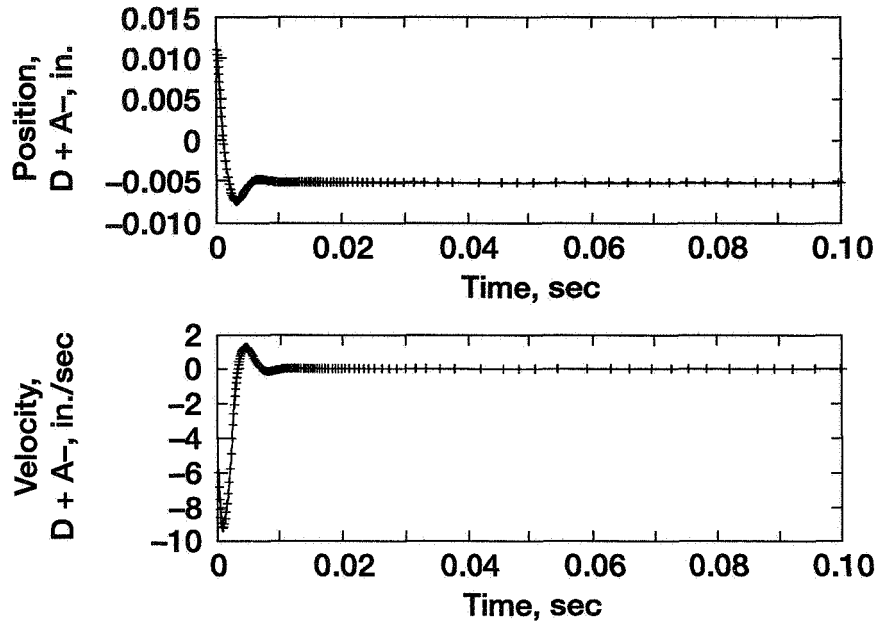


Fig. 7

## Rotor Orbits on the Bentley-Nevada Magnetic Bearing Rig

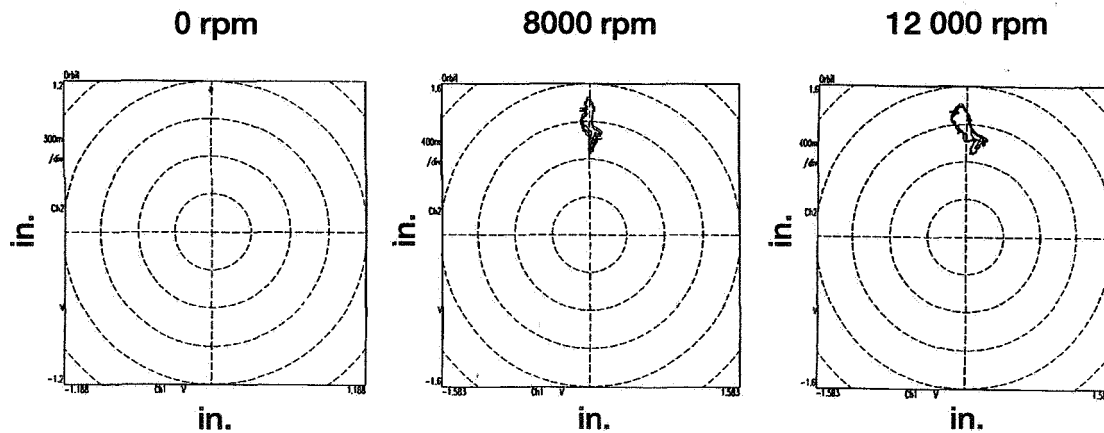


Fig. 8

## **SUMMARY**

- An accurate neural net model that emulates a nonlinear magnetic bearing system was well trained with sample data.
- From this neural model, two controllers (based on frequency and time domain specifications) were developed and demonstrated on the magnetic bearing rig.

⇒ Demonstrates the capability of the adaptive neural network controller for highly nonlinear and/or unknown magnetic bearing system.

Fig. 9

## **FUTURE WORK**

- Train neural net model by using experimental data including
  - Actuator dynamics and rotor system
  - Amplifier and sensor dynamics
- Develop on-line training scheme to adapt changing dynamic characteristics
- Include genetic algorithm for appropriate architecture

Fig. 10

# DIAMOND-FILM LUBRICANTS FOR CERAMICS

KAZUHISA MIYOSHI  
NASA Lewis Research Center  
Cleveland, Ohio 44135

512-27

029111

14p.

295559

## Introduction

Diamond's excellent tribological properties make it an ideal material for many tribological applications. Its extreme hardness, high abrasion resistance, good fatigue strength, high thermal conductivity, good radiation and temperature resistance, chemical and thermal inertness, high corrosion resistance, and environmental compatibility (refs. 1 and 2) suit it for applications such as bearings, valves, and engine parts in the harsh environment found in internal-combustion and jet engines. For example, diamond is being considered as a replacement for the sapphire that slides against tungsten carbide poppets which are used in check valves for the Space Shuttle's forward reaction control subsystem and orbital maneuvering subsystem.

Both natural and high-pressure synthetic diamond have limited application because of the small size and the high cost of the crystals. Another limiting factor for tribological applications is the separate operation that is required to bond the crystals to a substrate. Chemical-vapor-deposited (CVD) diamond, on the other hand, offers a broader potential since size and, eventually, cost are less of a limitation. CVD diamond, which is available in planar film or sheet form, opens the door for design engineering and tribology to take full advantage of the intrinsic properties of diamond in such areas as wear, solid lubrication, erosion, and corrosion applications.

The major drawbacks of CVD diamond, which restrict its use as a tribological coating, are its very rough surface, its low bending strength, and its very high deposition temperature. These obstacles must be overcome before practical, reliable, and cost-effective diamond coatings will become available as wear-resistant self-lubricating barriers for many moving mechanical assemblies. A process must be developed that will keep the deposition temperature below 400 °C and provide consistently satisfactory adhesion to metallic and nonmetallic substrates, including steel and  $\text{Si}_3\text{N}_4$ .

## Experimental

Sliding friction experiments were conducted with CVD diamond films and diamondlike carbon (DLC) films in contact with natural diamond or with a polished CVD diamond pin in humid air, in dry nitrogen, and in ultrahigh vacuum. The diamond films were produced by microwave plasma CVD and hot-filament CVD techniques. The DLC films were produced by an ion-beam deposition technique. Various analytical techniques, including Raman spectroscopy, hydrogen forward scattering (proton recoil analysis), Rutherford backscattering, transmission and scanning electron microscopy, X-ray photoelectron spectroscopy, and X-ray diffraction, were utilized to characterize the films.

## CVD Diamond Films

In humid air and dry nitrogen, as-deposited fine-grain diamond films and polished coarse-grain diamond films both had a low coefficient of friction ( $<0.1$ ) and a low wear rate ( $\leq 10^{-6} \text{ mm}^3/\text{N}\cdot\text{m}$ ). In ultrahigh vacuum, however, they had a high coefficient of friction ( $>0.4$ ) and a high wear rate ( $\geq 10^{-4} \text{ mm}^3/\text{N}\cdot\text{m}$ ),

making them unacceptable for tribological applications. Thus, it is clear that surface modifications which provide acceptable levels of friction and wear properties, regardless of environment, will be necessary before diamond films can be widely used for tribological applications.

### Ion-Implanted Diamond Films

Bombarding diamond films with carbon ions at 60 keV or nitrogen ions at 35 keV produced a thin, superficial layer of amorphous nondiamond carbon ( $<0.1\ \mu\text{m}$  thick). The carbon- or nitrogen-ion implantation had little effect on the coefficient of friction in humid air or in dry nitrogen: The ion-implanted diamond film retained a low coefficient of friction ( $\leq 0.1$ ) and a low wear rate ( $\leq 10^{-6}\ \text{mm}^3/\text{N}\cdot\text{m}$ ). In this respect, the ion-implanted CVD diamond was similar to the as-deposited fine-grain or the polished coarse-grain CVD diamond. In ultrahigh vacuum, however, the effect of carbon- or nitrogen-ion implantation was significant: An amorphous nondiamond carbon layer was formed on the diamond films, thereby reducing the coefficient of friction to 0.1 or lower and the wear rate to  $10^{-6}\ \text{mm}^3/\text{N}\cdot\text{m}$ , making them acceptable for tribological applications. The much lower friction of the ion-implanted diamond films can be attributed to the combination of the low shear strength of the thin, amorphous nondiamond carbon surface layer and the small contact area resulting from the high elastic modulus and hardness of the underlying diamond film.

We know that ion implantation does not create an interface of demarcation between the host material and the implanted species. Instead, it produces a graded interface. The ion implantation process can be easily controlled by adjusting the operating variables of the accelerator, such as the accelerating energy, current density, and time. One disadvantage of ion implantation technology is that the depth of penetration of the implanted species is very shallow (the thickness of ion-implanted layers ranges from 0.01 to  $0.5\ \mu\text{m}$ ) compared with that of conventional coatings; this may limit the tribological applications of ion-implanted coatings to light loads or short-term operations. In other words, the endurance life (wear life) of the ion-implanted layer that contributes to the tribological benefits is limited.

### Diamondlike Carbon Films on CVD Diamond

The thickness of (DLC) films can range from 0.1 to  $5\ \mu\text{m}$ , which is an order of magnitude greater than that of the ion-implanted layer. As a result, the endurance life of DLC can be longer than that of the ion-implanted layer. For this reason, studying an amorphous DLC film coated on a fine-grain CVD diamond film was a logical approach to enhancing tribological properties—especially, increasing the endurance of CVD diamond films.

As part of this study, DLC films were produced on fine-grain CVD diamond coatings by the direct impact of an ion beam (composed of a 3:17 mixture of Ar and  $\text{CH}_4$ ) at ion energies of 1500 and 700 eV. In ultrahigh vacuum the ion-beam-deposited DLC films on fine-grain CVD diamond (like the ion-implanted CVD diamond) greatly decrease both the friction and wear of fine-grain CVD diamond films and provide solid lubrication. In dry nitrogen and in humid air, the ion-beam-deposited DLC films on fine-grain CVD diamond films also had a low steady-state coefficient of friction and a low wear rate. Such enhanced tribological performance, coupled with a wider range of coating thicknesses, means a longer endurance life and improved wear resistance for the DLC deposited on fine-grain CVD diamond in comparison to the ion-implanted diamond films. Thus, DLC deposited on fine-grain CVD diamond films can be an effective wear-resistant, lubricating coating regardless of environment.

In this investigation the main criteria for judging the performance of a potential diamond-film lubricant were the coefficient of friction and the wear rate, which had to be less than 0.1 and  $10^{-6}\ \text{mm}^3/\text{N}\cdot\text{m}$ ,



respectively. The following films met the requirements regardless of environment:

- Carbon- or nitrogen-ion-implanted, fine-grain CVD diamond
- DLC deposited on fine-grain CVD diamond

### References

1. Pierson, H.O.: Handbook of Carbon, Graphite, Diamond, and Fullerenes. Properties, Processing, and Applications. Noyes Publications: Park Ridge, NJ, 1993.
2. Davies, G., ed.: Properties and Growth of Diamond. Inspec., Institution of Electrical Engineers, London, UK, 1994.

### Bibliography

Some earlier data and experimental details on this research are given in the following:

- Wu, R.L.C., et. al.: Synthesis and Characterization of Fine Grain Diamond Films. J. Appl. Phys., vol. 72, no. 1, July 1992, pp. 110-116.
- Miyoshi, K., et. al.: Friction and Wear of Plasma-Deposited Diamond Films. J. Appl. Phys., vol. 74, no. 7, Oct. 1993, pp. 4446-4454.
- Wu, R.L.C., et. al.: Ion-Implanted Diamond Films and Their Tribological Properties. Sur. Coat. Technol., vol. 62, 1993, pp. 589-594.
- Miyoshi, K., et al.: Physical and Tribological Characteristics of Ion-Implanted Diamond Films. NASA TM-106682, 1994.
- Miyoshi, K., et. al.: Friction and Wear of Ion-Beam-Deposited Diamondlike Carbon on Chemical-Vapor-Deposited, Fine-Grain Diamond. NASA TM 107316, 1996.

### **Acknowledgments**

The author gratefully acknowledges

- R.L.C. Wu, W.C. Lanter, S. Heidger, A. Garscadden, and P.N. Barnes of the Wright Laboratory for
  - depositing the microwave plasma CVD diamond films and preparing the ion-beam-deposited DLC films
  - performing Rutherford backscattering spectroscopy, hydrogen forward scattering, x-ray diffraction, and Raman analysis
- P.J. Wilbur and B. Shogrin of the Colorado State University for carbon ion implantation
- M. Murakawa and S. Miyake of the Nippon Institute of Technology for
  - hot-filament CVD diamond film deposition
  - nitrogen ion implantation

Fig. 1

CD-97-74268

## Sapphire and Diamond Sliding Against Tungsten Carbide Poppet

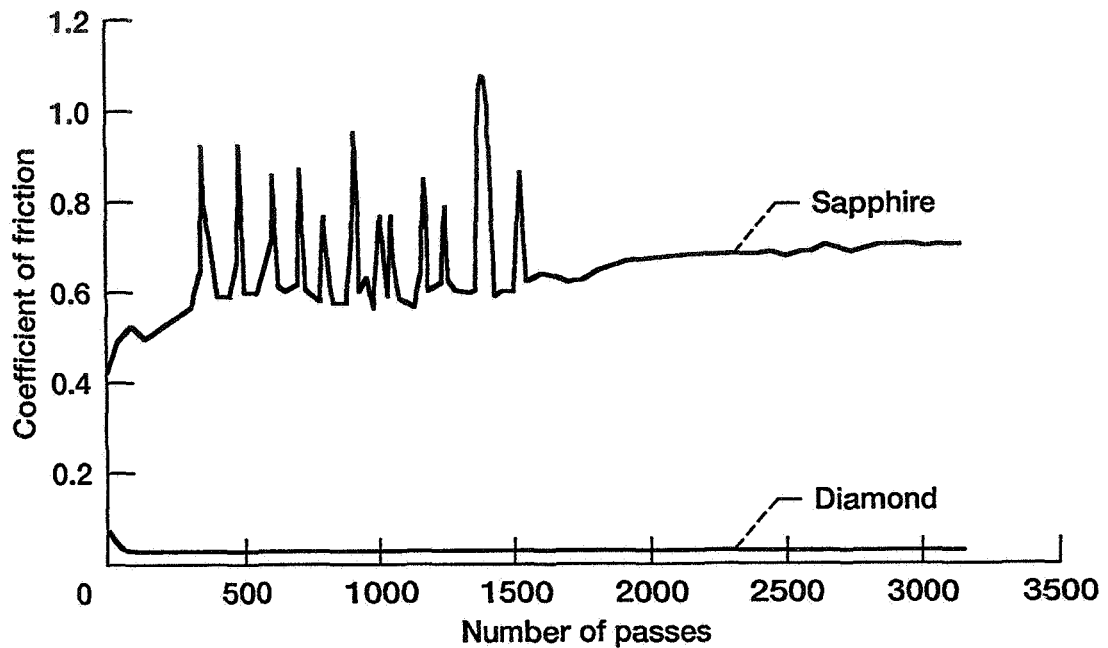


Fig. 2

CD-95-71024

## Why Diamond?

### Tribological Advantages

- Extreme hardness
- High abrasion resistance
- Good fatigue strength
- High thermal conductivity
- Good radiation and temperature resistance
- Chemical and thermal inertness
- High erosion and corrosion resistance
- Environmental compatibility

### Aeropropulsion and Rocket Propulsion Applications

- Self-lubricating, wear resistant barriers for moving mechanical assemblies such as bearings, valves, and engine parts
- Film lubricants for ceramics such as  $\text{Si}_3\text{N}_4$ ,  $\text{SiC}$ ,  $\text{Al}_2\text{O}_3$ , . . .
- Hard-to-machine applications for metals, ceramics, and composites

Fig. 3

CD-95-73140

## Hardness of Diamond and Other Hard Materials

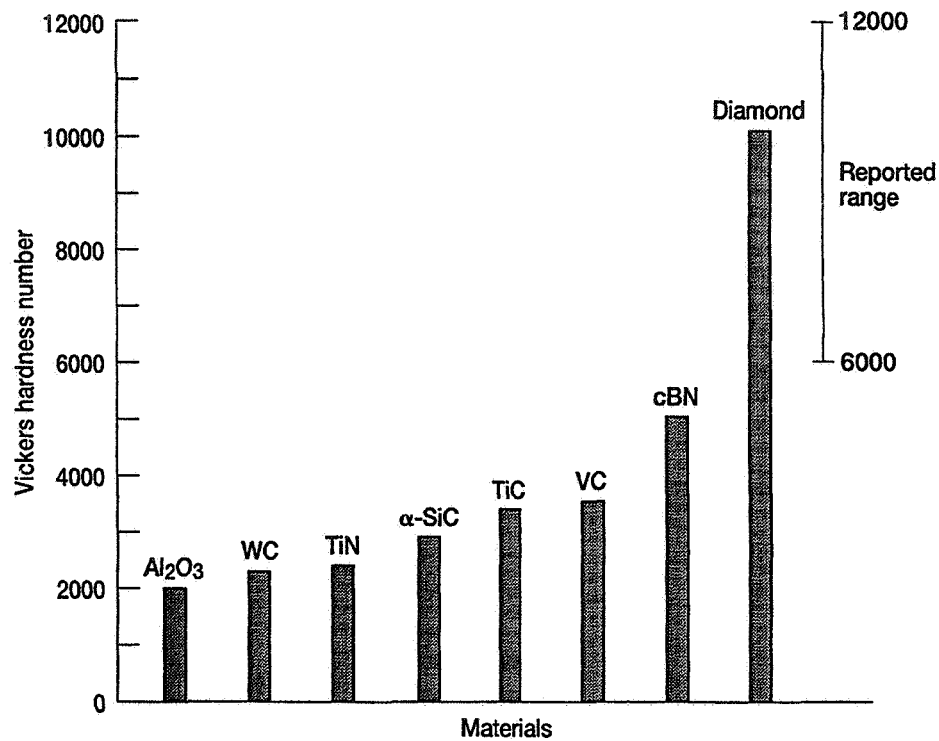


Fig. 4

CD-97-74264

## Advantages of CVD Diamond

- Planar film or sheet
- Large area
- Properties of diamond

Fig. 5

CD-97-74272

## Objective

- To provide diamond films with acceptable levels of friction and wear properties regardless of environment

## Goals

- Coefficient of friction  $\leq 0.1$
- Wear rate  $\leq 10^{-6} \text{ mm}^3/\text{N}\cdot\text{m}$

Fig. 6

CD-97-74271

## Analytical Techniques

- Scanning and transmission electron microscopy (SEM and TEM)
  - to determine surface morphology and grain size
- Rutherford backscattering spectroscopy (RBS)
  - to identify impurities and
  - to determine carbon and impurity concentrations
- Raman spectroscopy and Fourier transform infrared spectroscopy (FTIR)
  - to characterize diamond quality and structure
- Hydrogen forward scattering (Proton recoil detection)
  - to measure the hydrogen concentration
- X-ray photoelectron spectroscopy (XPS)
  - to characterize surface chemistry
- X-ray diffraction
  - to determine the crystal orientation

Fig. 7

CD-95-71961

## Chamber Tribometer

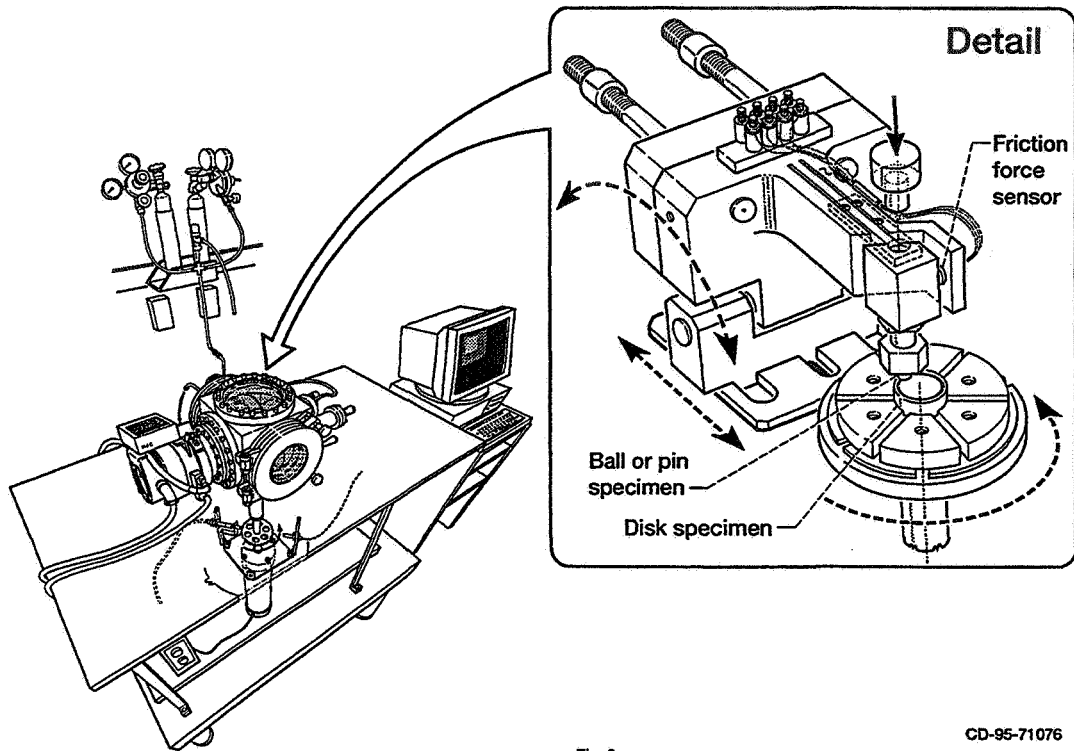


Fig. 8

CD-95-71076

## Tribological Characterization

- Humid air (40% relative humidity)
- Dry nitrogen (< 1% relative humidity)
- Ultrahigh vacuum ( $10^{-7}$  Pa)

Fig. 9

CD-95-72064

## Fine-grain Diamond and Diamondlike Carbon Films

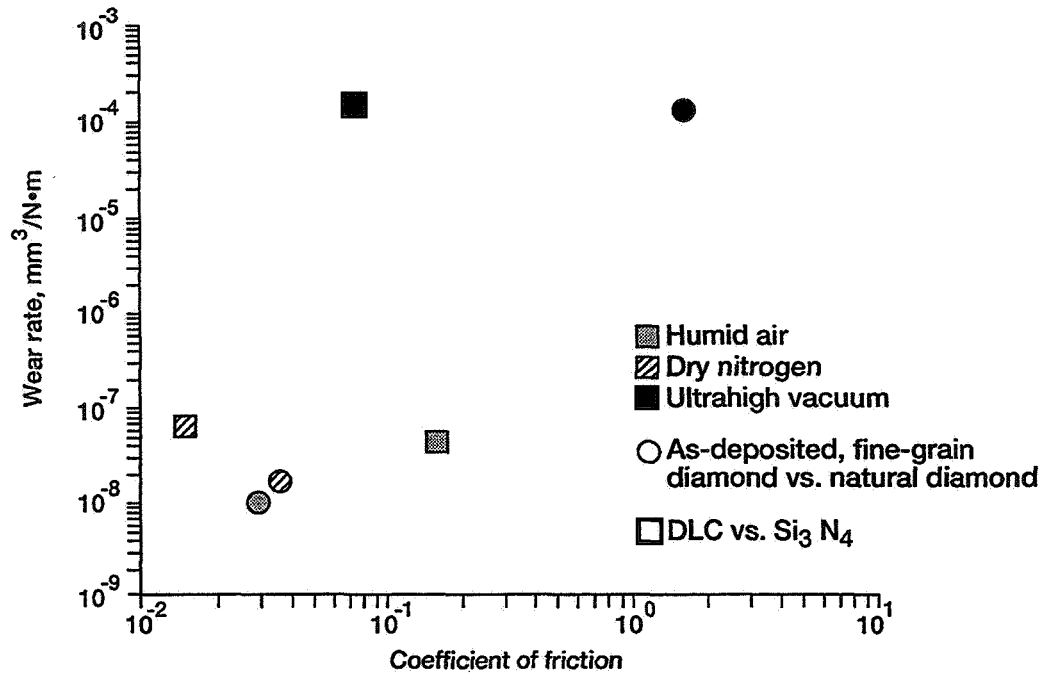


Fig. 10

CD-95-72016

## High Adhesion, Friction, and Wear in Ultrahigh Vacuum

- Removing some contaminant surface layer from the contact area yielded stronger interfacial adhesion, friction, and wear
  - Coefficient of friction > 1
  - Wear rate 10<sup>-4</sup> mm<sup>3</sup>/N·m

Fig. 11

CD-97-74269

## Approach

To use fine-grain diamond and DLC films  
regardless of environment, we must modify films  
(e.g., by ion implantation) to obtain acceptable  
levels of friction and wear properties

Fig. 12

CD-97-74261

## Types of Diamond Films

- As-deposited, smooth surface of fine-grain CVD diamond  
Microwave-plasma-assisted CVD technique
- Polished, smooth surface of coarse-grain CVD diamond  
Hot-filament CVD technique
- Carbon-ion-implanted surface of fine-grain CVD diamond  
60 keV and 50  $\mu\text{A}/\text{cm}^2$ ,  $1.2 \times 10^{17}$  carbon ions/ $\text{cm}^2$
- Nitrogen-ion-implanted surface of coarse-grain CVD diamond  
35 keV,  $5 \times 10^{17}$  nitrogen ions/ $\text{cm}^2$

Fig. 13

CD-97-74270

## Raman Spectra of Diamond Films

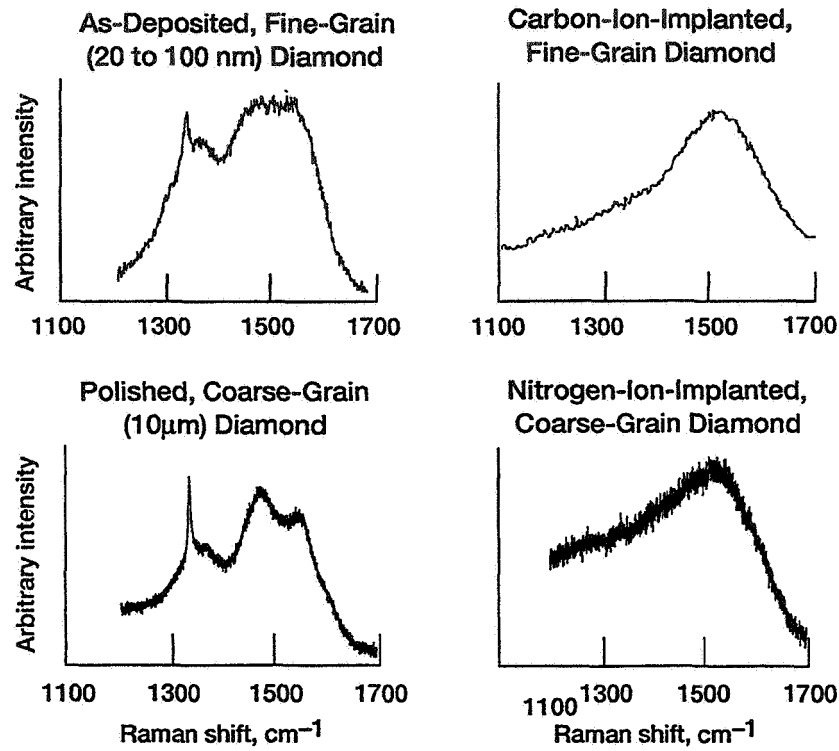


Fig. 14

CD-96-72705

## Coefficients of Friction and Wear Rates for CVD Diamond Films

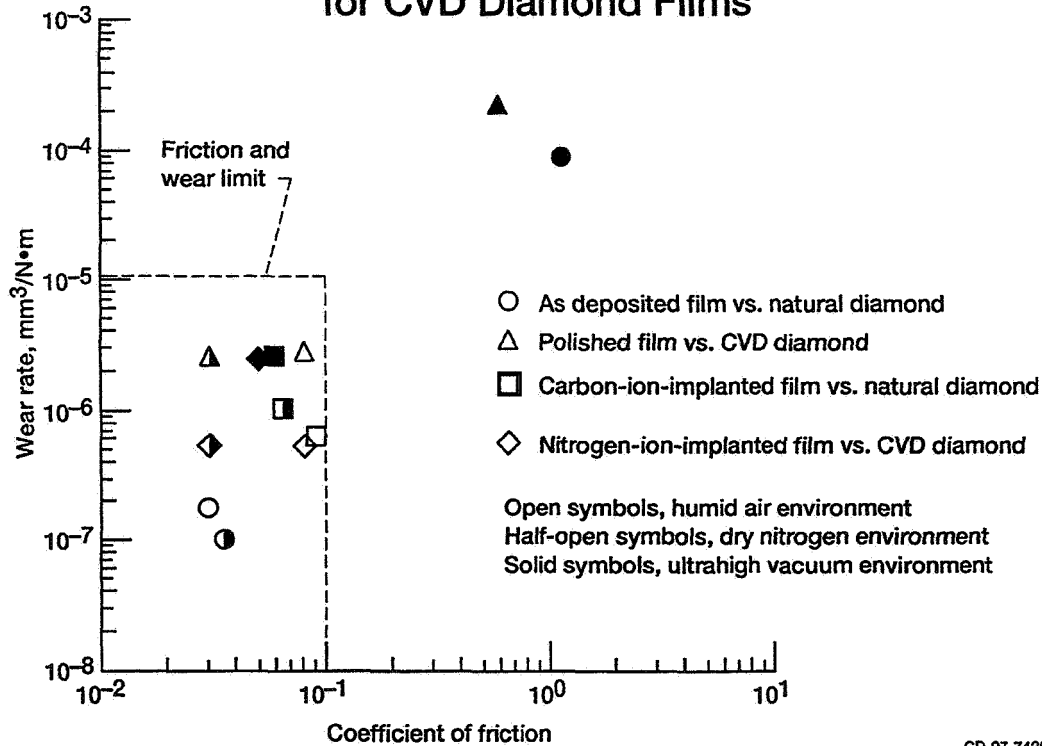


Fig. 15

CD-97-74262



## Ion-Implanted Diamond Film

- Ion implantation had a substantial effect on friction and wear
  - Coefficient of friction  $\leq 0.1$
  - Reduced friction by factors of 10 to 30
  - Wear rate  $10^{-6} \text{ mm}^3/\text{N}\cdot\text{m}$
  - Reduced wear by factors of 30 to 90

Fig. 16

CD-97-74273

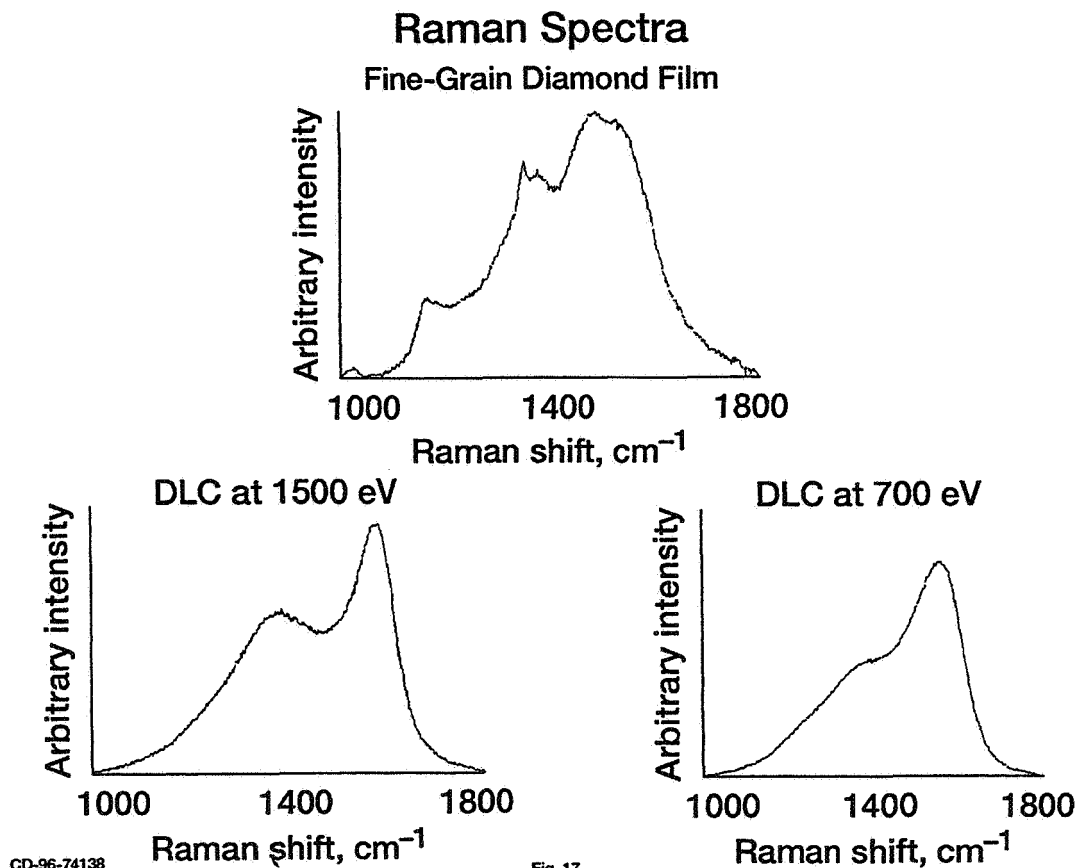


Fig. 17

## Coefficients of Friction and Wear Rates In Sliding Contact With CVD Diamond Pins in UHV

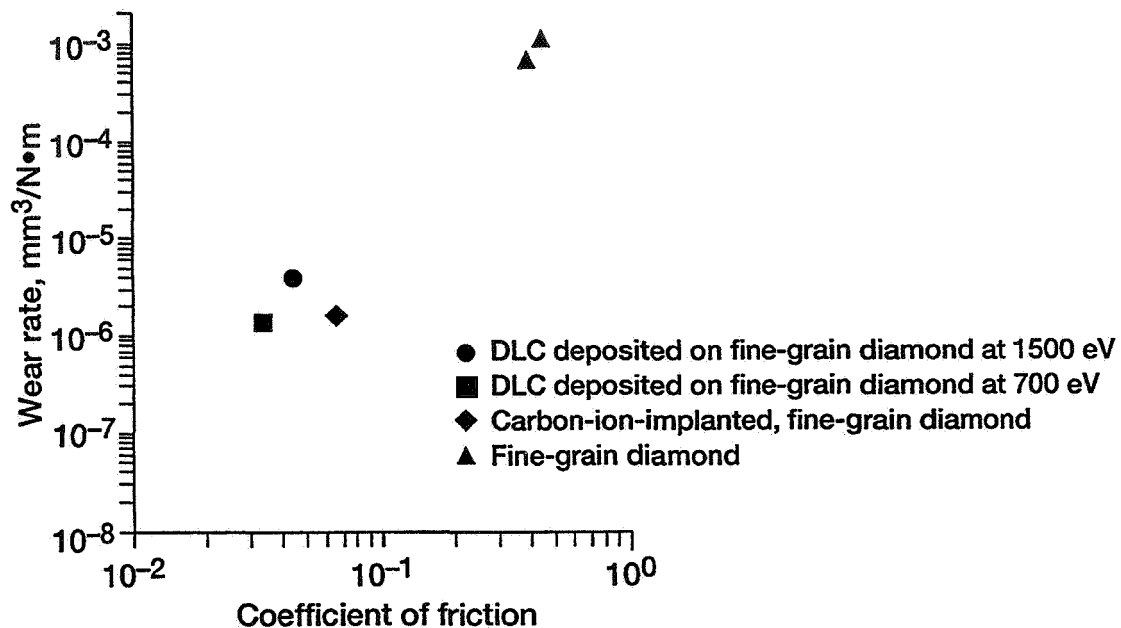


Fig. 18

CD-96-74139

## Summary

The DLC film produced by direct ion-beam deposition at ion energies of 1500 and 700 eV greatly decreased both the friction and wear of fine-grain CVD diamond films in ultrahigh vacuum without sacrificing the low friction and low wear properties attainable in dry nitrogen and in humid air.

Fig. 19

CD-97-74265

## Mechanisms of Friction

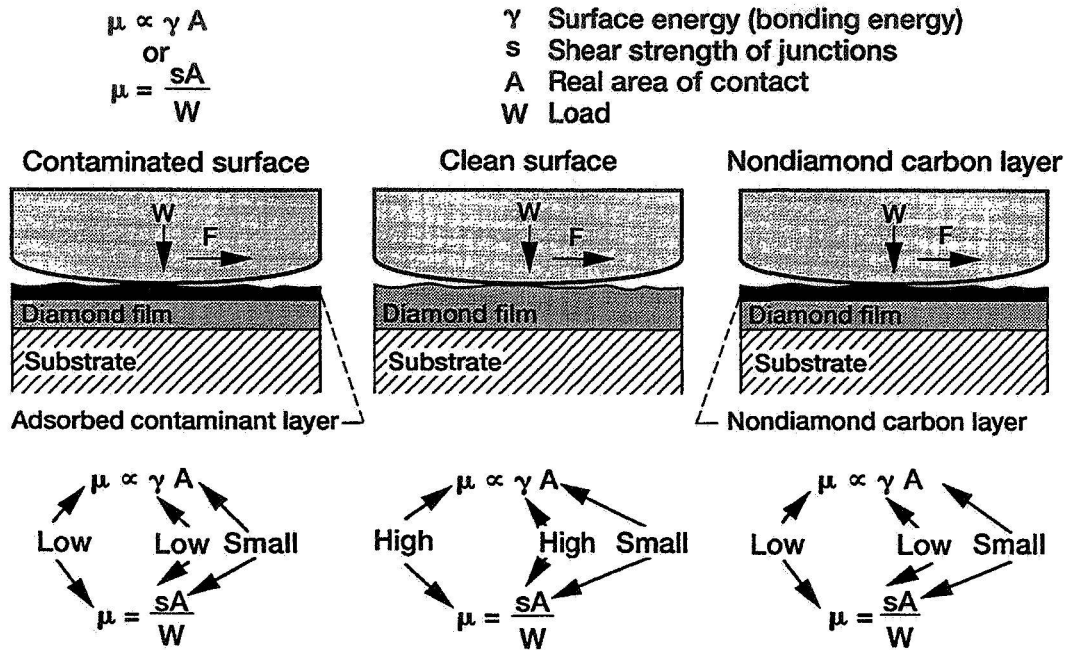


Fig. 20

CD-97-74263

## Concluding Remarks

The main criteria for judging the performance of a potential diamond-film lubricant were the coefficient of friction and the wear rate, which had to be less than 0.1 and  $10^{-6} \text{ mm}^3/\text{N}\cdot\text{m}$ , respectively.

The following films met the requirements regardless of environment:

- Carbon- or nitrogen-ion-implanted, fine-grain diamond
- DLC deposited on fine-grain diamond

Fig. 21

CD-97-74266

## **Future Work**

- **Complete tribological evaluation of CVD diamond-film lubricants and related multilayer coatings at temperatures up to 600 °C**
- **Determine optimum multilayer thin film materials for antiwear/antifretting applications**

Fig. 22

CD-97-74267

# A HIGH TEMPERATURE VAPOR PHASE LUBRICATION STUDY UTILIZING A THIOETHER LIQUID LUBRICANT

WILFREDO MORALES  
NASA Lewis Research Center  
Cleveland, Ohio

and

E. Earl Graham and Thomas Galvin  
Cleveland State University  
Cleveland, Ohio

513-27

029112

295561

8p.

## Introduction

Much of the experimental work on vapor phase lubrication has employed certain organo phosphorous compounds as the vapor phase lubricant. Graham and Klaus (ref. 1), for instance, used tricresyl phosphate (TCP) and tributyl phosphate to vapor phase lubricate a four-ball wear tester using M50 steel balls at 370°C. Makki and Graham (ref. 2) were able to vapor phase lubricate a reciprocating pin on plate tribometer using 1018 steel at 280°C with TCP vapor.

Although a few organo phosphorous compounds, such as TCP, have been successfully used as vapor phase lubricants in many laboratory experiments, many problems remain unsolved. Two areas of concern relate to the "durability" of phosphate deposited films and to the ability of the lubricating system to "self-recover" when vapor phase lubricated with an organo phosphorous compound.

Durability refers to the ability of the deposited film to provide effective lubrication, for a period of time, after the vapor flow to the lubricating surfaces has been interrupted. Vapor phase lubrication tests, conducted at Cleveland State University with their high temperature tribometer, revealed that when TCP vapor flow to the lubricating surfaces was interrupted the frictional coefficient of the system rapidly increased from a value less than 0.1 to a value of 0.3 which was selected as our failure point.

Self-recovery means the ability of the vapor phase lubricant to reduce the frictional coefficient of the lubricating system back down to value less than 0.1 after startup of the interrupted vapor flow. Lubrication tests conducted at Cleveland State University revealed that the high temperature tribometer could not self-recover after startup of the interrupted TCP vapor flow.

These studies led to the consideration of an alternative compound, a polyphenyl thioether organic liquid, as a vapor phase lubricant.

A review of previous research, conducted at NASA Lewis, indicated that polyphenyl thioethers (Fig. 2) possessed chemical properties which might make them suitable as vapor phase lubricants. First of all, they are thermally and oxidatively very stable under static conditions as shown by isosteniscope measurements and microoxidation tests (ref. 3). In one experiment a polyphenyl thioether was heated, in air, for 60 minutes at 350°C in the presence of M-50 steel with no detectable decomposition of the thioether.

The behavior of the thioethers under boundary lubricating conditions was, however, a different matter. They reacted to form insoluble organic deposits. A thioether was used to lubricate a vane pump loop in one study (ref. 4). Unexpected deposit formation jammed the pump vanes and rotor forcing the termination of the test. In a different study (ref. 5), substantial quantities of a deposit, referred to as "friction polymer", was formed in a sliding ball-on-disk friction apparatus. In an elegant electrochemical study by Morales (ref. 6), the author demonstrated the polymer forming properties of the thioethers when heated in the presence of a free radical source.

Figure 3 is a schematic representation of the friction and wear tester used in these studies. Briefly, a load (4 kg) is applied to a pin (cast iron) which is in contact with a rectangular plate (cast iron). The temperature of the plate can be varied between room temperature and 750°C. The reciprocating motion of the plate results in the pin rubbing against the surface of the plate over a 4 cm long wear track. A measured amount of thioether is vaporized into a flowing air stream which is directed to the rubbing cast iron surfaces.

Figure 4 are the results of the first test where the plate temperature was maintained at 500° C, and the vapor concentration of the thioether (by volume in air) was varied from 0.07% to 0.009%. The coefficient of friction, initially at 0.13, dropped to 0.03 over the first 15 minutes and leveled off at 0.07. As the thioether vapor concentration was reduced, a corresponding decrease in frictional coefficient values occurred. This test confirmed that polyphenyl thioethers can function as vapor phase lubricants.

Figure 5 are the results of a subsequent test where the vapor lubricant flow was turned off (air flow continued) and then on over a period of time, and later both the lubricant and air flow were turned off and on. The thioether vapor concentration was maintained constant at 0.07% in this test. With both the lubricant and air flow on, the coefficient of friction dropped to values below 0.05 during the first 115 minutes of the test. At 115 minutes, the lubricant flow was turned off. For about 30 minutes, the coefficient of friction remained at 0.02 and then rose sharply to 0.3. The lubricant flow was turned on again at 175 minutes and the frictional coefficient dropped back down to 0.02 within 15 minutes. At 190 minutes, both the lubricant and air flow were turned off. The frictional coefficient stayed below 0.02 for about 15 minutes before rising sharply to 0.3. At 220 minutes, both the lubricant and air flow were turned back on and the coefficient of friction dropped back down to values below 0.1.

The first test where the lubricant flow was turned off would simulate a partial failure where the only supply of lubricant would come from residual thioether in the delivery system. The second test where both lubricant and air flow were turned off would simulate a total failure of any supply of vapor to the rubbing parts. These results revealed that the thioether deposit, unlike the phosphorous deposit, was durable and able to self-recover.

## References

1. Graham, E.E. and Klaus, E.E.: Lubrication from the Vapor Phase at High Temperatures. ASLE Trans., 29, 2, pp. 229-234, 1986.
2. Makki, J.F. and Graham, E.E.: Formation of Solid Films from the Vapor Phase on High Temperature Surfaces. Lubr. Eng. 47, 3, pp. 199-206, 1991.
3. Morales, W.: High Pressure Liquid Chromatography: A Brief Introduction and Its Application to Analyzing the Degradation of a C-ether (Thio-ether) Liquid Lubricant. NASA TM 83474, 1983.

4. Jones, W.R., Jr.; Hady, W.F. and Swikert, M.A.: Lubrication with Some Polyphenyl Ethers and Super Refined Mineral Oils in a 600 F (316 C) Inerted Vane Pump Loop. NASA TN D-5096, 1969.
5. Jones, W.R., Jr.: The Effect of Oxygen Concentration on the Boundary Lubricating Characteristics of a C-ether and a Polyphenyl Ether to 300 C. Wear, 73, pp. 123-116, 1981.
6. Morales, W.: Simulation of Lubricating Behavior of a Thioether Liquid Lubricant by an Electrochemical Method. ASLE Trans., 29, 1, pp. 67-74, 1986.

## **Vapor Phase Lubrication**

### **BACKGROUND**

- **Successful vapor phase lubrication (VPL) studies have been demonstrated using certain organo-phosphorous compounds**
- **Many problems remain unsolved. Two areas of concern are**
  - (1) Low durability of the lubricating deposit**
  - (2) Inability of the system to self-recover**

### **OBJECTIVES**

- **Investigate the use of a polyphenyl thioether as a vapor phase lubricant**
- **Assess the durability of thioether deposits, and their ability to self-recover**

Fig. 1

## Polyphenyl Thioethers

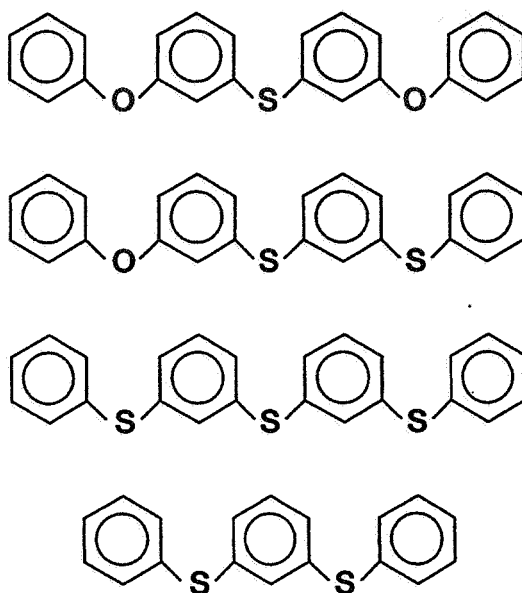


Fig. 2

## Schematic of High Temperature VPL Apparatus

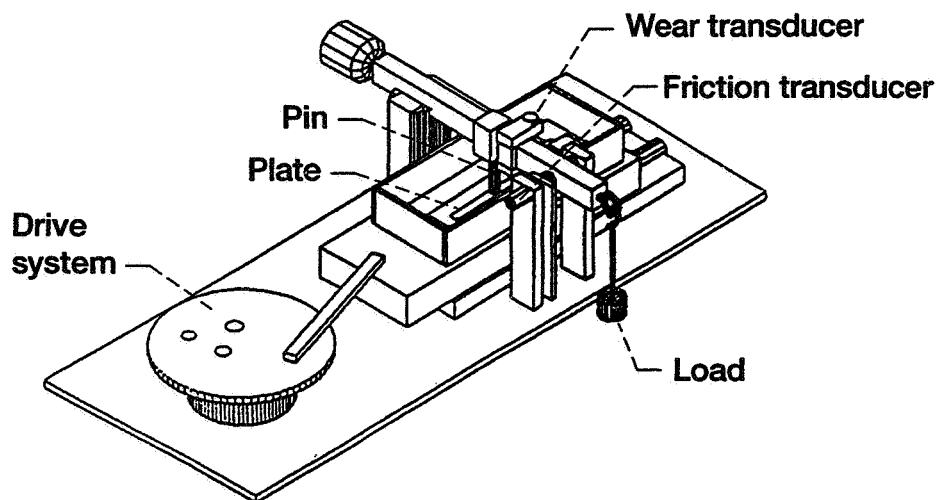


Fig. 3



## Coefficient of Friction vs. Time for Various Concentrations of Thioether in Air on Cast Iron

Plate Temperature, 500 °C; Vapor Temperature, 400 °C; Load, 4 kg

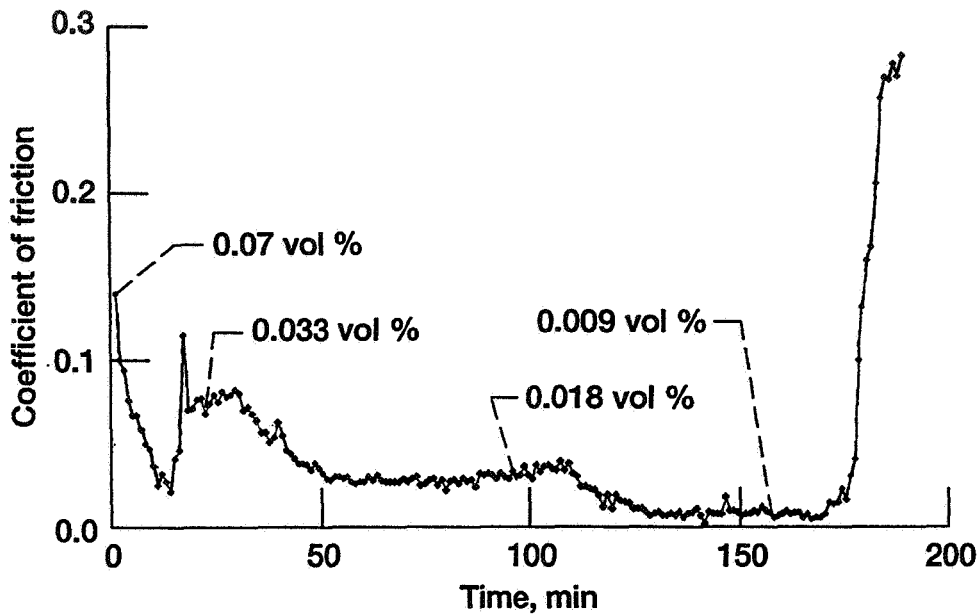


Fig. 4

## Coefficient of Friction Versus Time For Lube Off/On and for Lube/Air Off/On

Thioether Concentration 0.07%

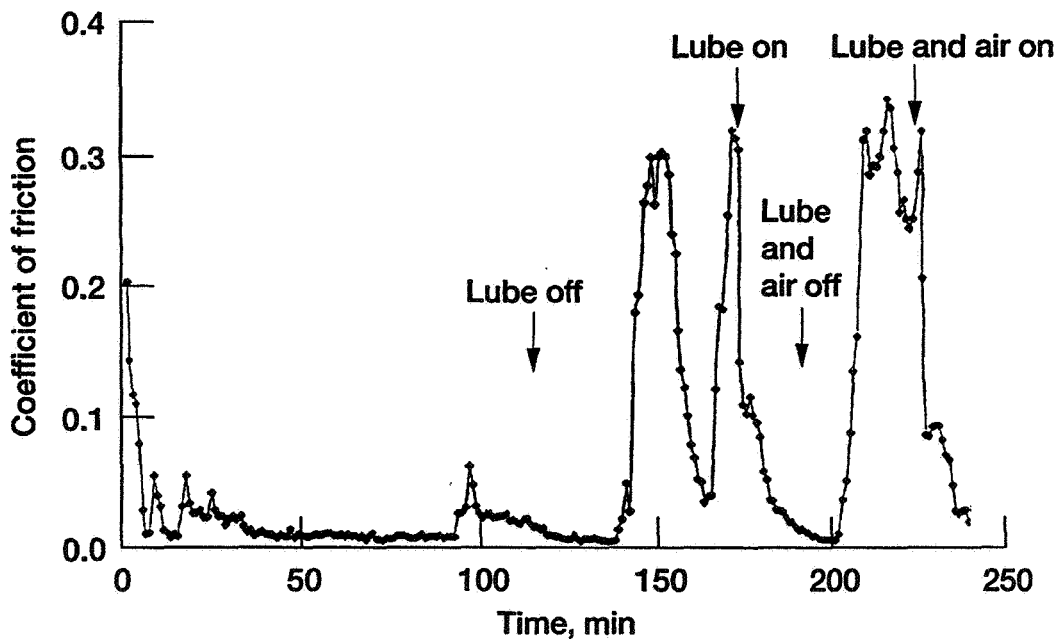


Fig. 5

### Raman Spectrum of Unused Thioether

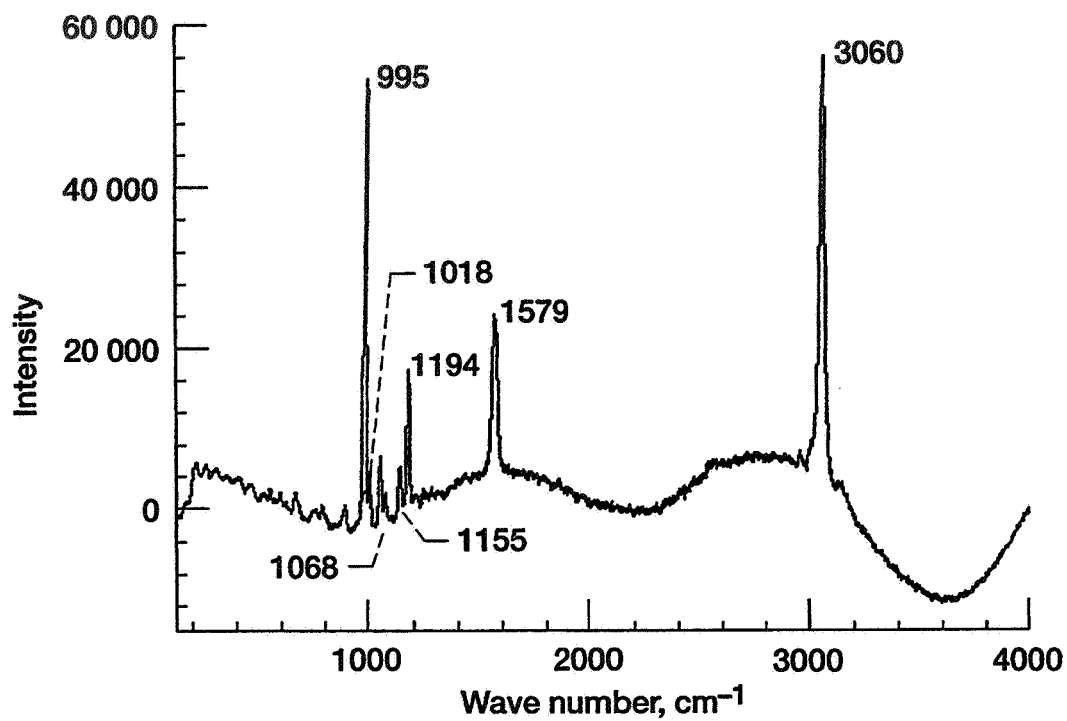


Fig. 6

### Raman Spectrum of Wear Debris

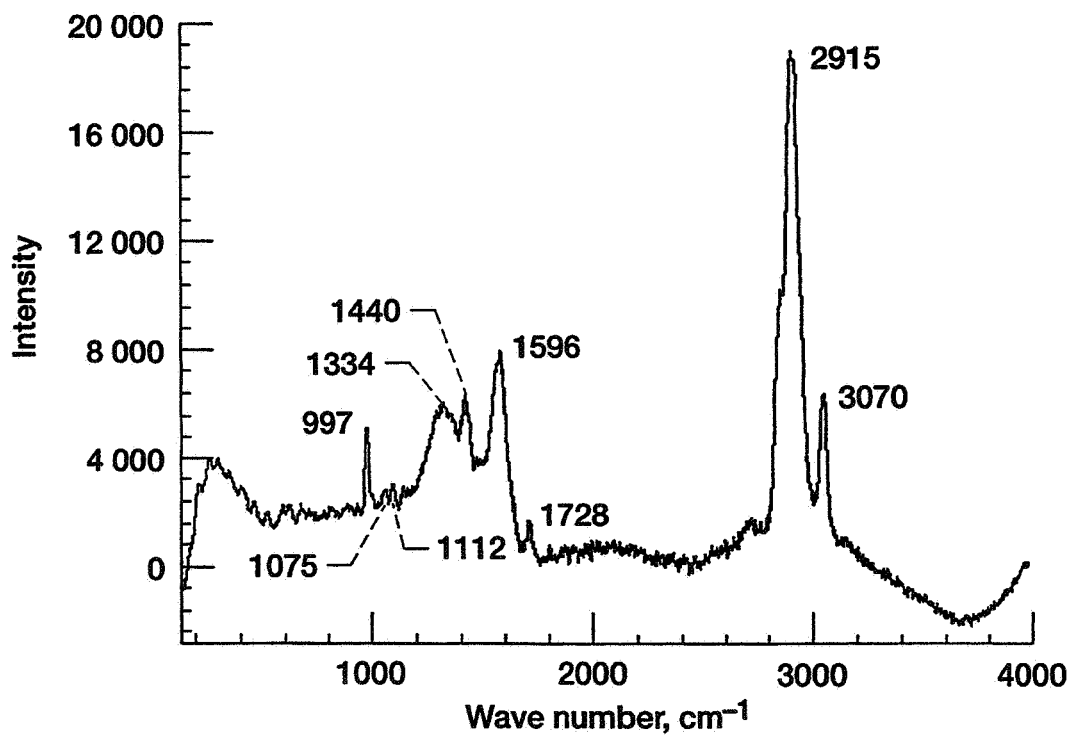


Fig. 7

## Raman Spectral Features and Their Assignments

Polyphenyl thioether (cm <sup>-1</sup> )	Assignment	Wear debris (cm <sup>-1</sup> )	Assignment
995 } 3060 }	C <sub>6</sub> H <sub>6</sub>	997 } 3070 }	C <sub>6</sub> H <sub>6</sub>
-----	-----	2915	- CH <sub>2</sub> -
1018 } 1068 } 1579 }	C <sub>6</sub> H <sub>5</sub> - S	1020 } 1075 }	C <sub>6</sub> H <sub>5</sub> - S
1155 } 1194 }	C <sub>6</sub> H <sub>5</sub> - O	-----	-----
-----	-----	1440 1596 } 1334 }	----- Graphitic
-----	-----	1728	C = O
-----	-----	1112	Alkyl - S

Fig. 8

## Summary

- Lubrication studies utilizing a reciprocating, pure sliding friction and wear apparatus revealed
  - That a very low concentration of thioether vapor in air was able to reduce the coefficient of friction for sliding cast iron specimens (at 500 °C) to values as low as 0.02
  - That interrupting the lubricant flow or the lubricant/air flow did not result in an immediate increase in the frictional coefficient of the system

Fig. 9

## Conclusions

- This study demonstrated that polyphenyl thioethers can function as vapor phase lubricants.
- The thioether lubricious deposit was found to be much more durable than the phosphorous deposit.
- The thioether-lubricated system was able to self-recover, unlike the phosphorous-lubricated system.

Fig. 10

## Future Research

- Quantify the term "durability" with respect to time as a function of various system variables (i.e., load, speed, temperature, etc.)
- Extend these studies to lubrication of stainless steels, superalloys, and ceramics

Fig. 11

# THE ROLE OF TRIBOLOGY IN THE DEVELOPMENT OF AN OIL-FREE TURBOCHARGER

CHRISTOPHER DELLACORTE  
NASA Lewis Research Center  
Cleveland, Ohio 44135

5/4-37  
029119  
40.  
295563

Gas-turbine-based aeropropulsion engines are technologically mature. Thus, as with any mature technology, revolutionary approaches will be needed to achieve the significant performance gains that will keep the U.S. propulsion manufacturers well ahead of foreign competition.

One such approach is the development of oil-free turbomachinery utilizing advanced foil air bearings, seals, and solid lubricants. By eliminating oil-lubricated bearings and seals and supporting an engine rotor on an air film, significant improvements can be realized. For example, the entire oil system including pipes, lines, filters, cooler, and tanks could be removed, thereby saving considerable weight. Since air has no thermal decomposition temperature, engine systems could operate without excessive cooling. Also, since air bearings have no diameter-rpm fatigue limits (D-N limits), engines could be designed to operate at much higher speeds and higher density, which would result in a smaller aeropropulsion package.

Because of recent advances in compliant foil air bearings and high temperature solid lubricants, these technologies can be applied to oil-free turbomachinery. In an effort to develop these technologies and to demonstrate a project along the path to an oil-free gas turbine engine, NASA has undertaken the development of an oil-free turbocharger for a heavy duty diesel engine. This turbomachine (see Fig. 1) can reach 120 000 rpm at a bearing temperature of 540 °C (1000 °F) and, in comparison to oil-lubricated bearings, can increase efficiency by 10 to 15 percent because of reduced friction. In addition, because there are no oil lubricants, there are no seal-leakage-induced emissions.

The oil-free turbocharger is an excellent technology tested for high temperature compliant air bearings and solid lubricants that are applied to the shaft during startup and shutdown. The turbocharger, which is composed of a compressor directly coupled through a shaft to a turbine, closely resembles the core of a small gas turbine generator. The main difference is that the turbocharger uses a diesel engine as its combustor.

NASA Lewis Research Center has an ongoing research program to investigate the performance and durability issues of foil bearings and start and stop solid lubricant coatings. Some results of this program are presented here. Figure 2 shows the load capacity performance of advanced bearing designs at temperatures from 25 to 650 °C (75 to 1200 °F) as a function of speed. In Fig. 3, a plot of the bearing torque as a function of load at 40 000 rpm shows that power loss increases with applied load, an expected result (see ref. 3). These data are important for applications of this technology development.

Photomicrographs of a new plasma-sprayed solid lubricant coating (PS300) are shown in Fig. 4. This coating was designed to lubricate the bearing during the initial startup and shutdown. The coating reduces friction and wear through the use of solid lubricant additions in a metal/ceramic matrix. Figure 5 depicts the results of an effort to tailor the composition of the coating so as to match its coefficient of thermal expansion (CTE) to that of the intended superalloy substrates. With a correct CTE match, modified coatings have successfully lubricated nickel-base superalloy shafts operating with Inconel-X 750 foil bearings for more than 30 000 start and stop cycles from 75 to 1200 °F (25 to 650 °C).

Breakthrough technologies in bearings and coatings enable new applications of oil-free turbomachinery. If we follow a path of ever increasingly challenging applications, a fully functional, oil-free aeropropulsion unit may be less than a decade away.

### References

1. DellaCorte, C.; and Wood, J.C.: High Temperature Solid Lubricant Materials for Heavy Duty and Advanced Heat Engines. NASA TM-106570, 1994.
2. Laskowski, J.A.; and DellaCorte, C.: Friction and Wear Characteristics of Candidate Foil Bearing Materials From 25 to 800 °C. NASA TM-107082, 1995.
3. DellaCorte, C.: A New Foil Air Bearing Test Rig for Use to 70 000 rpm. NASA TM-107405, 1997.
4. DellaCorte, C.; and Fellenstein, J.A.: The Effect of Compositional Tailoring on the Thermal Expansion and Tribological Properties of PS300: A Solid Lubricant Composite Coating. NASA TM-107332, 1997.

## Oil-Free Turbocharger

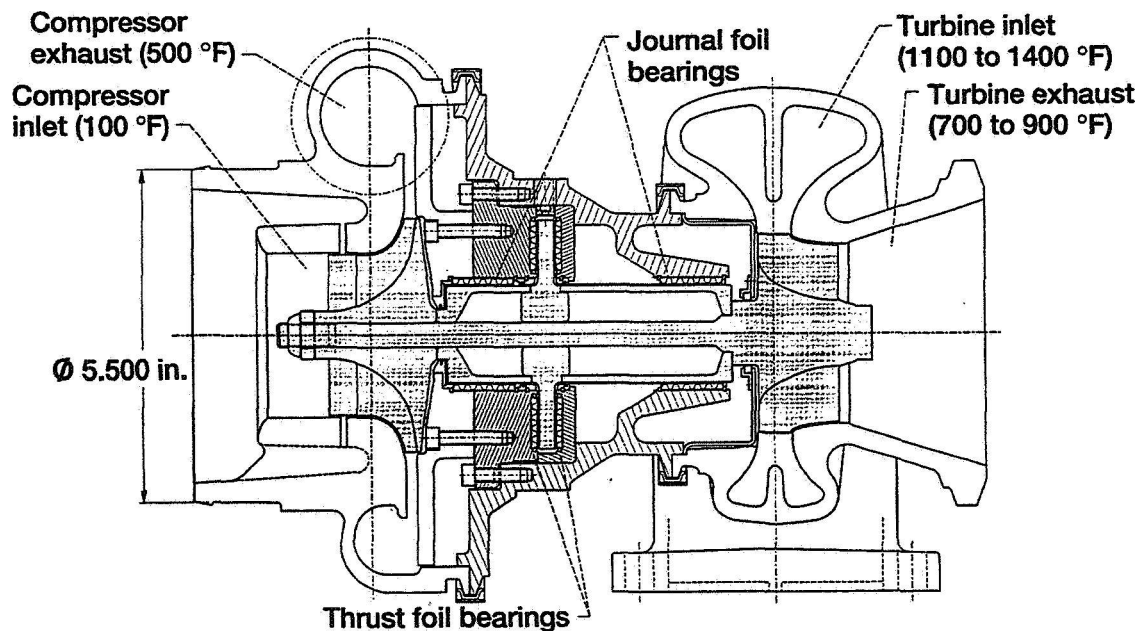


Fig. 1

CD-97-74362

## Bearing Load Capacity

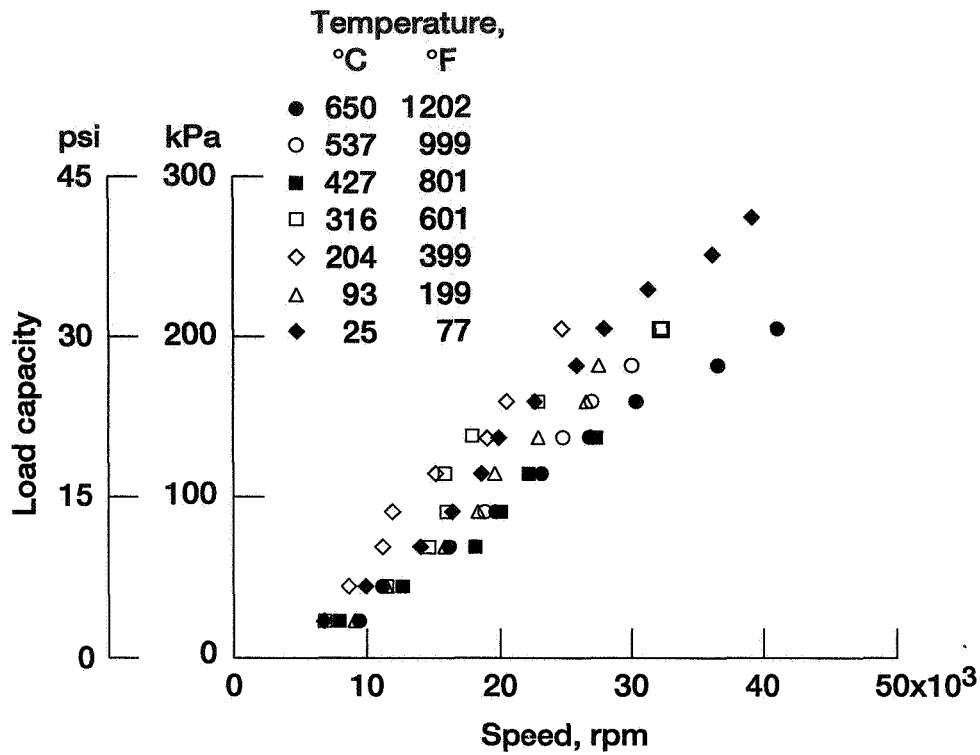


Fig. 2

CD-97-74363

## Bearing Torque

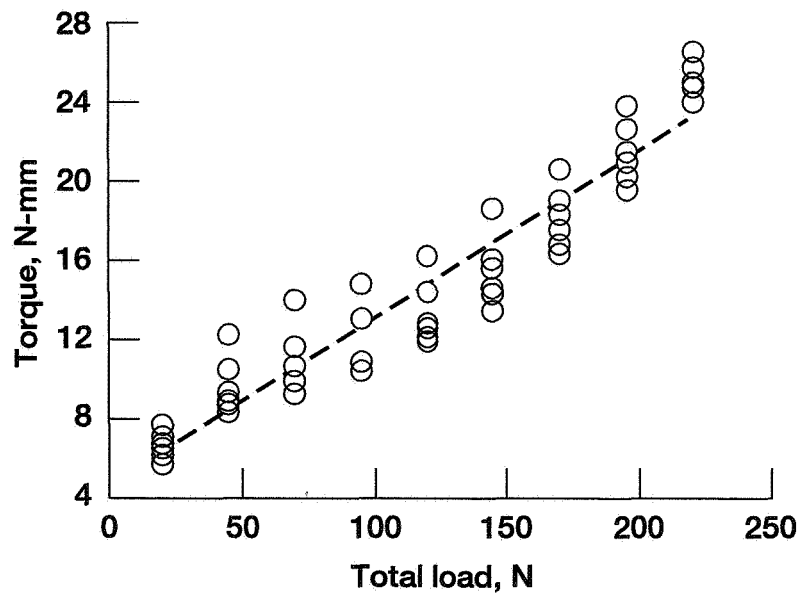


Fig. 3

CD-97-74364

## NASA PS300 Shaft Coating

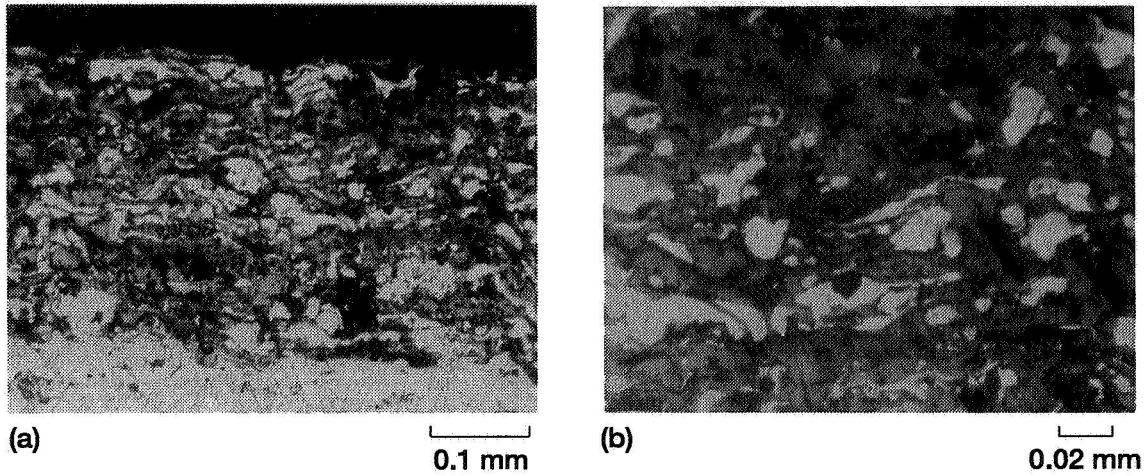


Fig. 4

CD-97-74365

## Effect of Composition on CTE

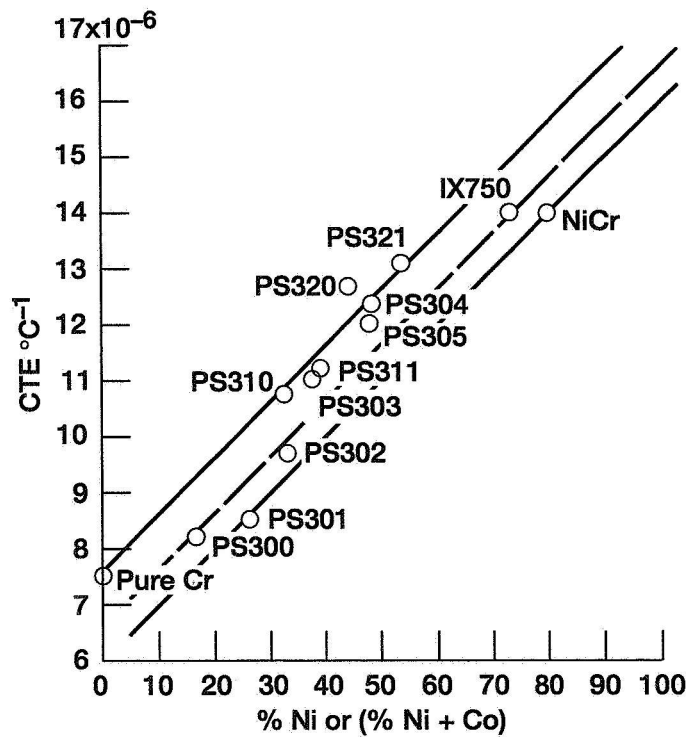


Fig. 5

CD-97-74366



# TUFT TESTING FOR ADVANCED OIL-FREE TURBOMACHINERY BRUSH SEALS

JAMES A. FELLENSTEIN\*  
Ohio Aerospace Institute  
Cleveland, Ohio

515-37

02 9/15

89.

295565

## Introduction

A typical brush seal is made with fine wires densely packed between two plates (Fig.1). To prevent bristle buckling during any shaft excursion the bristles are angled at approximately a forty-five degree angle. This ability to respond to shaft eccentricities without losing sealing performance gives the brush seal an advantage over traditional labyrinth seals. Brush seals, even when worn line-to-line with the shaft, have lower leakage rates than typical labyrinth seals. However, the optimal sealing performance of a brush seal occurs before the designed interference fit between the seal and shaft wears away. Therefore, to maximize overall turbomachinery efficiency, brush seal interfacial wear should be minimized (ref. 1).

Brush seals are designed with sacrificial brushes and hard shaft coatings to minimize shaft wear and reduce the cost of engine overhauls. Replacing a worn seal is more cost and time effective than refinishing an engine shaft. However, this tribopair causes excessive brush wear and reduces long term seal efficiency. An alternative design is to coat the shaft with a high temperature solid lubricant. Solid lubricants reduce the risk of microcrack formation and can potentially improve long term seal performance by acting like an abradable labyrinth seal. In other words, the seal would wear line-to-line below the shafts unworn outer diameter causing any leakage to flow down through the wear track or directly through the brush bristle pack.

To investigate the possibility of using solid lubricants for brush seal applications, three NASA developed coatings were tested against four metallic bristle materials. Characterization of each tribopair included measuring the friction coefficient, brush wear factor, and journal wear factor (Fig. 2). The results of these tests are also compared to previously completed tuft tests with three metallic bristles (Haynes 25, Inconel 718, and Haynes 230) versus plasma sprayed chrome carbide (refs. 2 and 3). Haynes 25 against plasma sprayed chrome carbide represents the industry standard and the baseline for this study.

These tests were completed on the Brush Seal Tuft Test Rig at the NASA Lewis Research Center (Fig. 3). One advantage of this facility is it allows tufts to be tested with a constant contact pressure. This constant load allows accurate brush and journal wear measurements without the confounding effects of unsteady loads, oxidation, and pressure differentials. This facility has been shown to accurately characterize candidate brush seal material at about 1/10<sup>th</sup> the cost of full scale seal testing (refs. 2 and 3).

The three coatings tested were PS212, PS300, and HVOF300. PS212 is a plasma sprayed chrome carbide based solid lubricant. Two versions of the chrome oxide based 300 series coating were tested (plasma sprayed and high velocity oxygen flame sprayed). Both the 200 and 300 series coatings have added silver for low temperature lubrication and a barium fluoride/calcium fluoride eutectic for high temperature lubrication (refs. 4, 5, and 6). The final test journal configuration is shown in Figure 4.

---

\*NASA Resident Research Associate at Lewis Research Center

The four wire materials tested were Haynes 25, Inconel 718, Haynes 230, and Haynes 242. These materials were all selected because of their high temperature capabilities and their availability in wire form. Each tuft is made with 920 bristles welded into an Inconel 718 collar. The wire diameter for each material was 0.071 mm (0.0028 in). After welding, the tufts are diamond ground to a 45° angle simulating an actual brush seal interface (Fig. 5).

The test temperature, surface speed and contact pressure were 650 °C (1200 °F), 24 m/s (78.5 ft/s), and 75.8 kPa (11 psi) respectively (Fig. 6). During each test the friction force, temperature, and speed are measured with a ±250 gram linear voltage displacement transformer (LVDT load cell), a Type K thermocouple and an optical speed pick-up. Post test analysis of the brush wear is completed by measuring the change in length of the bristles from inscribed witness marks in pre and post test photomicrographs. Post test analysis of the journals is completed by measuring the circumferential wear track cross sectional area with a stylus type surface profilometer at 90° intervals around the journal. Finally, wear factors for both the brush and journal are calculated based on the measured wear, test load, and sliding distance.

The results of these tests are summarized in Figures 7, 9, and 10. As seen in Figure 7 the friction coefficients ranged from 0.25 to 4.5 except for the tests conducted with the Haynes 242. In both tests completed with Haynes 242 the friction coefficient was above 0.60. Brush wear factors ranged from  $2.9 \times 10^{-7}$  (low wear) for Inconel 718 against PS300 to  $4.8 \times 10^{-6}$  (moderate wear) for Haynes 230 against PS300 (Figs. 8 and 9). Journal wear factors ranged from  $2.7 \times 10^{-8}$  (low wear) for Inconel 718 against plasma sprayed chrome carbide to  $6.6 \times 10^{-6}$  (moderate wear) for Haynes 25 against PS212 (Figs. 8 and 10).

Among the metallic brush/lubricant coating combinations tested, I718/PS300 was the best. However, compared to the baseline H25/PSCr<sub>2</sub>C<sub>3</sub>, the I718/PS300 wear couple exhibited more than 7 times greater journal wear without a significant improvement in friction or brush wear. Based on these results the metallic brush/solid lubricant tribopairs tested did not provide any additional tribological benefits over the industry standard of H25 against plasma sprayed chrome carbide.

Future work will include both ceramic and metallic bristles for higher temperature seal applications. Work will also continue on developing improved high temperature solid lubricants specifically tailored for brush seal applications.

## References

1. Mahler, F., and Boyes, E., "The Application of Brush Seals in Large Commercial Jet Engines," AIAA paper 95-2617, 1995.
2. Fellenstein, J.A., and DellaCorte, C., "A New Tribological Test for Candidate Brush Seal Materials Evaluation," NASA TM-106753, 1995.
3. Fellenstein, J.A., DellaCorte, C., Moore, K., and Boyes, E., "High Temperature Brush Seal Tuft Testing of Metallic Bristles Versus Chrome Carbide," NASA TM-107238, AIAA paper 96-2908, 1996.
4. DellaCorte, C., and Sliney, H., "Composition Optimization of Self-Lubricating Chromium-Carbide-Based Composition for Use to 760°C," ASLE volume 30, 1,77-83, 1986.

5. DellaCorte, C., and Edmonds, B.J., "Preliminary Evaluation of PS300: A New Self-Lubricating High Temperature Composition Coating for Use to 800°C," NASA TM-107056, 1996.
6. DellaCorte, C., and Laskowski, J.A., "Tribological Evaluation of PS300: A New Chrome Oxide Based Solid Lubricant Coating Sliding Against  $\text{Al}_2\text{O}_3$  From 25 to 650°C," NASA TM-107163, 1996.

### Typical Brush Seal Design

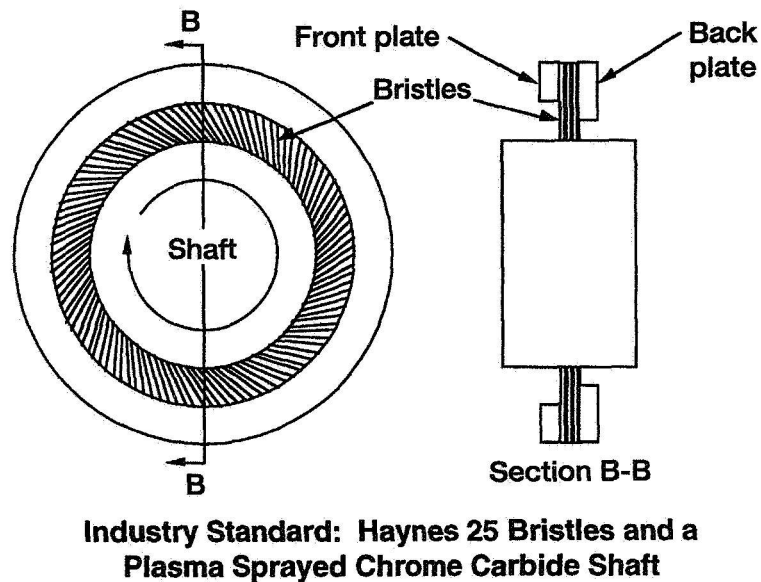


Fig. 1

### Project Objectives

- Expand the current database for candidate brush seal materials
- Characterization of candidate brush seal tribopairs
  - Friction Coefficient

$$\mu = \frac{\text{Friction Force}}{\text{Normal Load}}$$

- Wear Factor ( $K = \text{mm}^3/\text{N m}$ )

$$K = \frac{\text{Volume Worn}}{(\text{Sliding Distance})(\text{Normal Load})}$$

Fig. 2

## Cross Section and End View of Brush Seal Tuft Tester

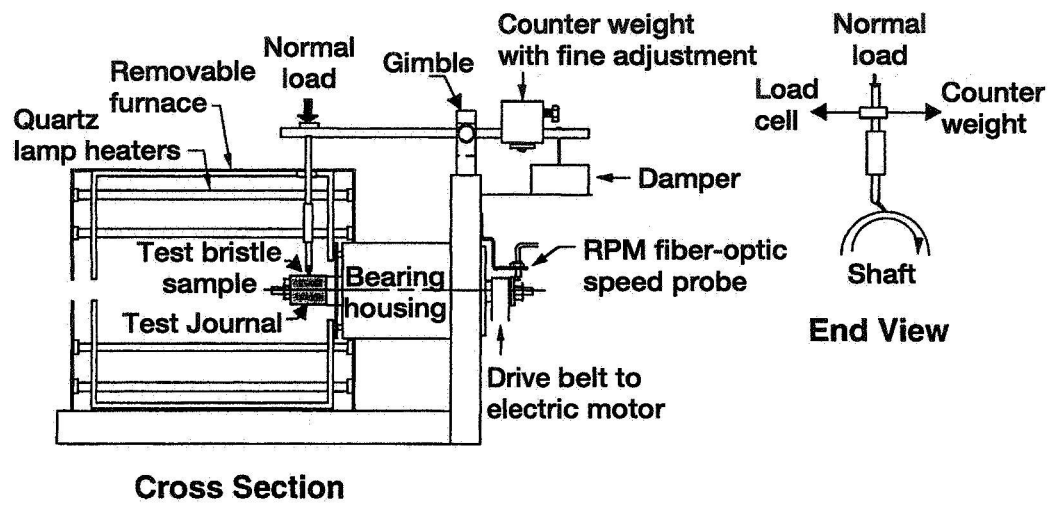


Fig. 3

## Journal Specimen Configuration Showing Dimensions and Geometry

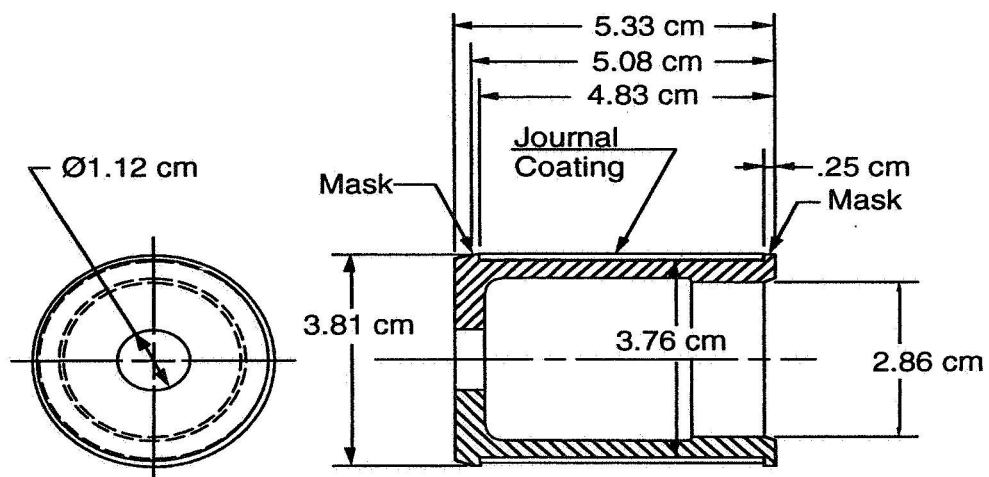


Fig. 4

## Tuft Specimen Configuration Showing Dimensions and Geometry

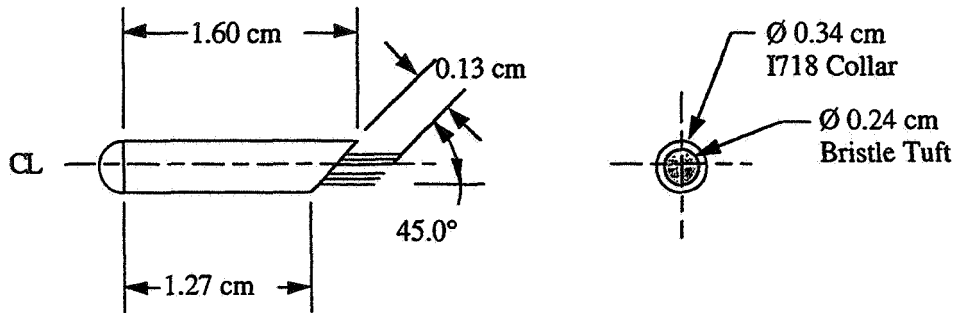


Fig. 5

## Brush Seal Tuft Test Parameters

Variable	Value
Temperature	650 °C (1200 °F)
Surface Speed	24 m/s (78.5 ft/s)
Contact Pressure	75.8 kPa (11 psi)

Fig. 6

## Average Friction Coefficients for Four Metallic Bristle Materials Tested Against Three Solid Lubricants and Chrome Carbide at 650 °C

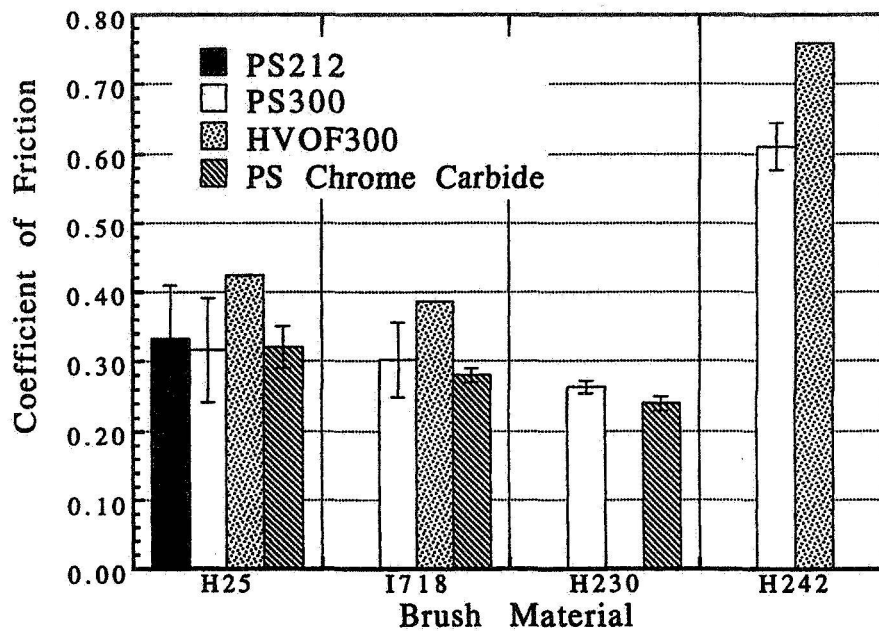


Fig. 7

## Wear Factor Interpretation

Wear Factor K (mm<sup>3</sup>/ N·m)

> 10 <sup>-4</sup>	High Wear
10 <sup>-5</sup> to 10 <sup>-6</sup>	Moderate to Low Wear
< 10 <sup>-7</sup>	Low Wear

Required brush wear factor for 10 000 hours  
and 0.127 mm of bristle wear is  
1.36 x 10<sup>-9</sup> mm<sup>3</sup>/ N·m.

Fig. 8

# **Average Brush Wear Factor for Four Metallic Bristle Materials Tested Against Three Solid Lubricants and Chrome Carbide at 650 °C**

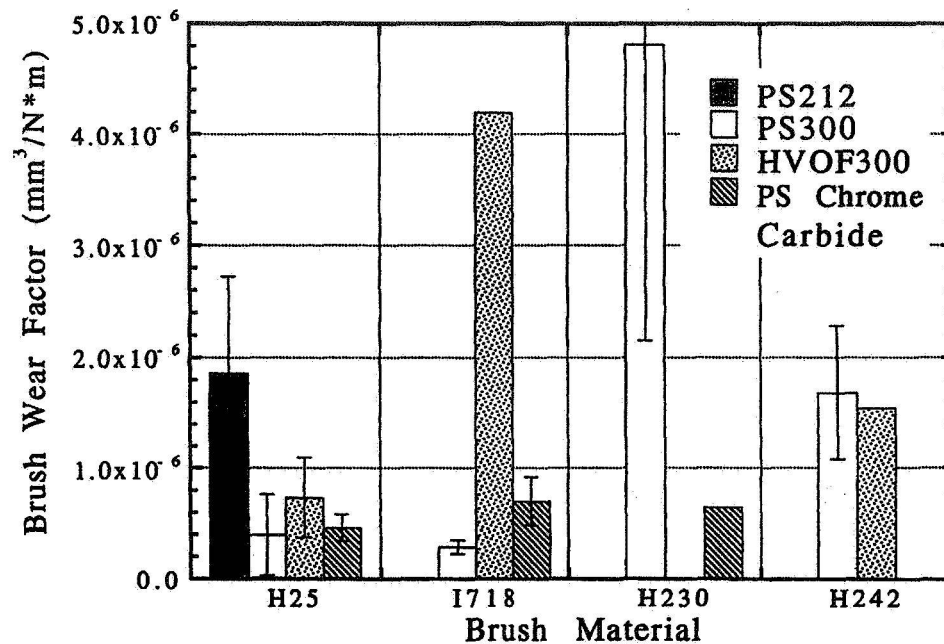


Fig. 9

# **Average Journal Wear Factor for Four Metallic Bristle Materials Tested Against Three Solid Lubricants and Chrome Carbide at 650 °C**

Brush Material	Journal Coating			
	PSCr <sub>2</sub> C <sub>3</sub>	PS212	PS300	HVOF300
H25	7.2x10 <sup>-8</sup>	<b>6.6x10<sup>-6</sup></b>	2.0x10 <sup>-6</sup>	1.1x10 <sup>-7</sup>
I718	<b>2.7x10<sup>-8</sup></b>		5.2x10 <sup>-7</sup>	7.4x10 <sup>-7</sup>
H230	4.2x10 <sup>-8</sup>		2.8x10 <sup>-7</sup>	
H242			2.1x10 <sup>-7</sup>	8.9x10 <sup>-8</sup>

Fig. 10

## **Brush Seal Tuft Test Conclusions**

- **Plasma-sprayed chrome carbide exhibited the lowest journal wear rates**
- **PS300 showed lower journal wear than PS212**
- **HVOF300 performed better than the plasma sprayed version**

**The industry standard of Haynes 25 against  $\text{PSCr}_2\text{C}_3$  performed just as good or better than any of the metallic bristle/solid lubricant tribopairs**

Fig. 11

## **Focus on Future Research**

- **Future brush seal tuft testing includes both ceramic and metallic bristle materials for higher temperature seal applications**
- **Development will continue on NASA's solid lubricant coatings**
- **Research will continue on developing lower wear and friction tribopairs**

Fig. 12



# ROTORDYNAMIC DESIGN ANALYSIS OF AN OIL-FREE TURBOCHARGER\*

SAMUEL A. HOWARD\*\*  
Case Western Reserve University  
Cleveland, Ohio

516-37  
029116 121  
295567

## Introduction

Modern heavy duty diesel engines utilize turbochargers for increased power output. Also, a wide range of power levels can be achieved with one engine displacement through the use of different turbocharger configurations, eliminating the need for several different sized engines. These are the reasons that virtually all diesel truck engines currently marketed use turbochargers. However, because these turbochargers rely on ring seals and oil-lubricated floating sleeve bearings, they often suffer breakdowns. These turbochargers operate at elevated temperatures which often causes the oil to degrade and even coke to the bearing surfaces. This can lead to catastrophic failure, increased particulate emissions from oil leaks, and, in extreme cases, engine fires.

Replacing the oil lubricated bearings from these turbochargers with some other device is desirable to eliminate these inherent problems. Foil bearings (figure 3) are compliant self-acting bearings lubricated by air and are well suited to high speed, light load applications. Thus, foil bearings present one potential replacement for oil-lubricated sleeve bearings. Their use as such is investigated in this work.

Air cycle machines are the turbocompressors used in commercial airliners to provide cabin cooling. These machines have successfully utilized air foil bearings for the last thirty years (ref. 1). These machines, however, are powered by compressor bleed-off and operate at steady speed and load conditions, and relatively low temperatures (ref. 2). To advance the technology of foil bearings to varying speed and high temperature applications, the modification of a turbocharger has been proposed. The goal of this work is to show that air-lubricated foil bearings can be designed for use in high variable speed, high temperature machines.

## Methodology

To conduct the design study, a finite element computer code developed for NASA called Analysis of Rotor Dynamic Systems (ARDS) is used to model the rotor and check for stability (ref. 3). The rotor bearing system is modeled using published bearing data (ref.

---

\* Work funded under NASA Grant # NCC3-409

\*\* NASA Resident Research Associate at Lewis Research Center.

4), and the stiffness of the bearings is chosen such that the operating speed range is clear of any critical speeds. The stability of the system is checked with a range of bearing damping coefficients in order to determine the necessary amount of damping to force the instability threshold speed out of the operating range. Lastly, centrifugal stresses, shaft growth, and bearing locations are considered in the final design as these factors affect the manufacturing ease and performance. The design is identified that gives the best balance of stability, ease of manufacture, and acceptable structural properties of the designs studied.

## **Results**

Three rotor bearing configurations were analyzed in this study to determine if air foil bearings are capable of supporting a turbocharger rotor operating at high speed, high temperature, and variable load conditions, and to determine which of these configurations is optimum. The first rotor system analyzed has a 2.54 cm (1.0 inch) outside diameter and 1.9 cm (0.75 inch) inside diameter. For simplicity and manufacturing considerations, the bearing L/D ratios are constrained to be 1. Therefore, the bearings are 2.54 cm (1.0 inch) long. Figure 8 shows this configuration. Upon plotting the critical speed map (Figure 9), it can be seen that bearing stiffness below 21,000 N/cm (12,000 lb/in) will guarantee that the operating speed range (20,000 to 117,000 RPM) is free of critical speeds. The stability of the rotor system is measured in terms of the log decrement. From experience in the literature, it has been found that if the log decrement is positive and larger than 0.2, then the system is considered stable (ref. 5). Figure 10 shows that in order for the log decrement to be larger than 0.2, the bearing damping coefficients need to be larger than 315 Ns/m (1.8 lb s/in). Since bearings of this type are expected to deliver damping values in the range 350 to 2630 Ns/m (2.0 to 15 lb s/in), the system is capable of stable operation in this speed range.

Since the damping required in the previous analysis is very small compared to the expected level of damping, it is desirable to analyze a rotor with bigger bearings. Bigger bearings will be inherently less stable because they will have a higher load capacity than the smaller bearings, therefore, they will run less eccentric for the same applied load. The less eccentric a bearing is, the less stable it is as well. The result of this is that the system will simply require more damping in order to remain stable, but this is not a problem because the bearings offer more damping than is needed for stability. However, the benefit of larger bearings is higher load capacity and therefore, higher tolerance to shock loads.

In order to use bigger bearings, the original turbocharger shaft has to be increased from 9.68 cm (3.81 in) to 12.80 cm (5.04 in), which was determined to be the largest possible bearing span. In this configuration, the shaft outside diameter is 3.8 cm (1.5 in), and inside diameter is 3.3 cm (1.3 in). Again keeping the L/D ratio of 1, the bearings are 3.8 cm (1.5 in) long (Figure 11). A critical speed analysis similar to that of Figure 9, reveals

that bearing stiffness must be chosen below 31,500 N/cm (18,000 lb/in). The stability analysis shows that damping values over 482 Ns/m (2.75 lb s/in) are needed in order for the system to be stable (Figure 13). As expected, this value is higher than the previous system, but is still acceptable.

A third analysis with 5.1 cm (2.0 in) bearings was considered, but the stress in the shaft at maximum speed is near that of the material's yield strength. Therefore, this design was not analyzed. Since the maximum stress and the maximum shaft growth for both the smaller shaft and the larger shaft are acceptable, and both appear to be stable in the speed range, another criteria for deciding which is better must be used. Based on the load capacity of the smaller bearings at the minimum speed, the maximum shock that the small rotor can sustain is found to be approximately 6g. While the larger shaft can sustain roughly 11g. Since the turbocharger is expected to be able to survive extended exposure to accelerations as high as 5-6g, the larger rotor is clearly the best design of the two.

## **Conclusions**

The feasibility of supporting a diesel truck engine turbocharger on air-lubricated foil bearings has been demonstrated. A design which offers sufficient damping for system stability, as well as ample load capacity for the expected high shock loads sustained in the environment has been chosen. This design, 3.8 cm (1.5 in) long bearings with 3.8 cm diameter as well, is capable of delivering the desired performance in the turbocharger studied, and demonstrates the capability of air foil bearings to be utilized in similar applications of high speed, high temperature, and extreme conditions.

## **References**

1. Saville, M., A. Gu, and R. Capaldi. "Liquid Hydrogen Turbopump Foil Bearing," AIAA-91-2108, 1991.
2. Meacham, W.L., et. al. "Dynamic Stiffness and Damping of Foil Bearings for Gas Turbine Engines," SAE paper 931449, 1993.
3. Nelson, H.D., And W.L. Meacham. "Transient Response of Rotor-Bearing Systems Using Component Mode Synthesis," NASA TN D-7385 (August 1973).
4. Heshmat, H., et. al., "Analysis of Gas-Lubricated Foil Journal Bearings," ASME Paper 82-Lub-40 (October 1982).
5. Heshmat, H., "Gas-Lubricated Foil Bearings for Heat Pumps with Counter-Rotating Heat Exchangers," ASME paper 82-DET-139 (September 1982).

## Objectives

- The primary objective of this project is to show, through rotordynamic analysis of the turbocharger, that air-lubricated foil bearing technology offers a feasible design option for lightweight, high speed, high temperature rotating machinery.
- A secondary objective is to choose a preliminary set of design parameters for this particular application by studying the rotordynamic response of three different rotor/bearing geometries.

Fig. 1

## Background

- Diesel truck engine turbochargers, which currently use floating sleeve oil journal bearings, are subject to frequent breakdown due to oil degradation and coking.
- The oil delivery system is also a source of many reliability and leakage problems.
- Air-lubricated foil bearings offer a possible solution to these problems by eliminating the turbocharger from the oil lubrication system of the engine.

Fig. 2

## Typical Foil Bearings

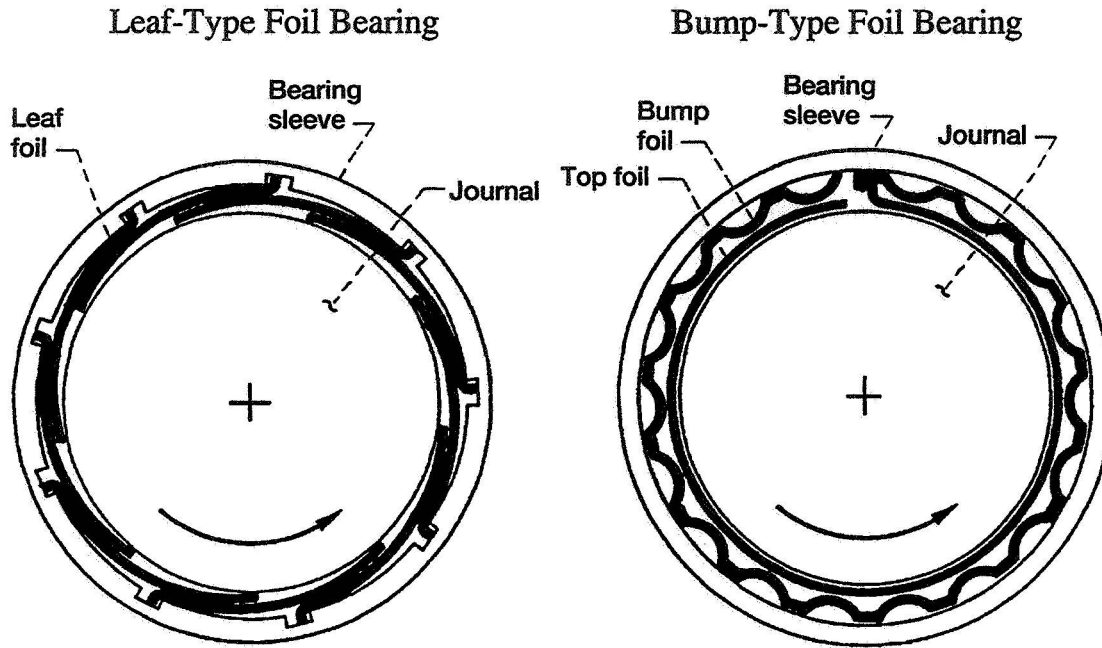


Fig. 3

## Advantages of Air Foil Bearings

- Eliminating the turbocharger from the oil lubrication system extends the life of engine oil, and in many cases lowers emissions.
- Oil-lubricated bearings are limited to operation below the maximum oil temperature, whereas air-lubricated bearings are limited only by the maximum temperature of the bearing material.
- Air-lubricated bearings can reduce the overall power loss by an order of magnitude over floating sleeve oil bearings.
- With a demonstrated 100,000 hours mean time between failures, there are virtually no maintenance requirements for the foil bearings.

Fig. 4

## Disadvantages of Air Foil Bearings

- Air foil bearings have much lower unit load capacities than oil film bearings in general.
- Air-lubricated bearings generally do not offer as much damping as oil film bearings because of the lower viscosity of air, this could lead to stability problems.
- There are no boundary lubrication additives in air to aid in start-up and shut-down conditions; therefore, metal-to-metal contact during start-up/shut-down can be a life limiting factor.

Fig. 5

## Some Possible Applications for Air Foil Bearings

- Turbochargers
- Turbogenerators
- Air Cycle Machines
- Automotive Gas Turbines
- High Speed Heat Pumps
- Aircraft Gas Turbine Engines

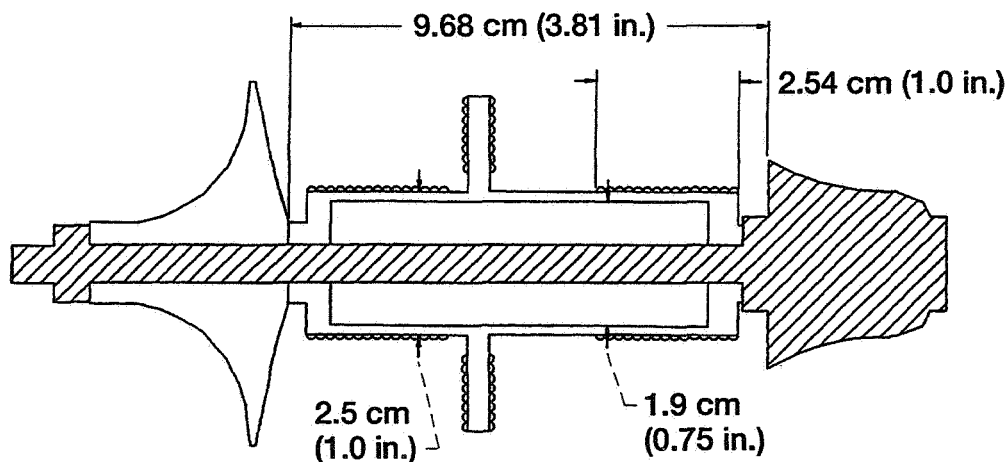
Fig. 6

## Present Work

- Three rotor configurations were analyzed to determine the best bearing based on the characteristics of load capacity, centrifugal stresses, and rotor stability.
- The rotor response is mapped as it varies with bearing stiffness to determine the range of stiffness that results in a rotor that has no critical speeds within the operating speed range of the turbocharger.
- The log decrement of the resulting rotor/bearing system is plotted as a function of damping coefficients in order to determine if the system will be stable.
- The rotor/bearing system that demonstrates the best compromise between load capacity and stability, and whose stress levels are acceptable, is chosen as the final design.

Fig. 7

## Small Rotor Configuration



Not to scale

Fig. 8

# Critical Speed vs. Bearing Stiffness for the Small Rotor $(K_{xx} = K_{yy} = K, K_{xy} = K_{yx} = 0)$

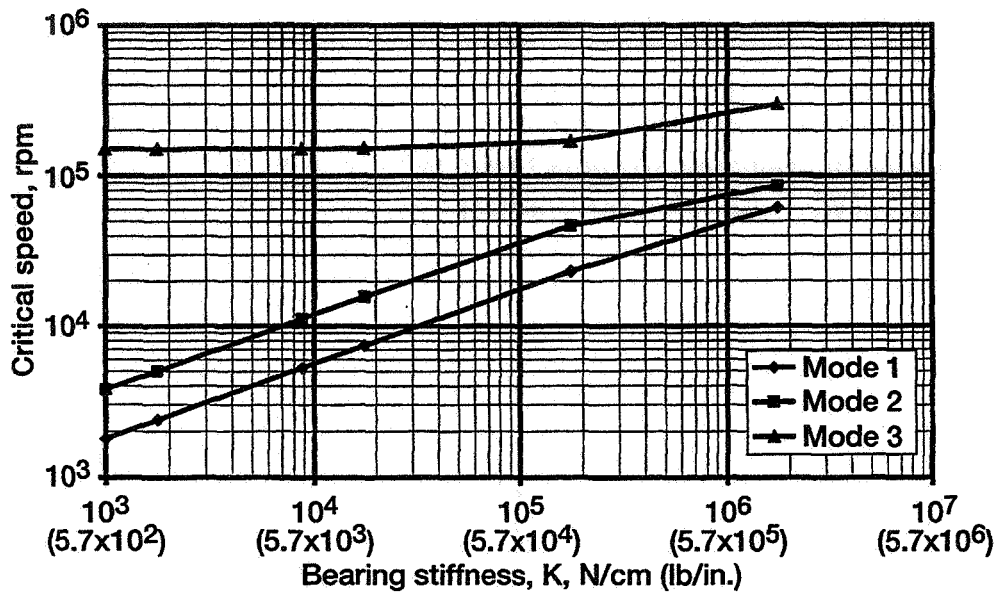


Fig. 9

# Log Decrement vs. Bearing Damping Coefficient for the Small Rotor $(B_{xx} = B_{yy} = B, B_{xy} = B_{yx} = 0)$

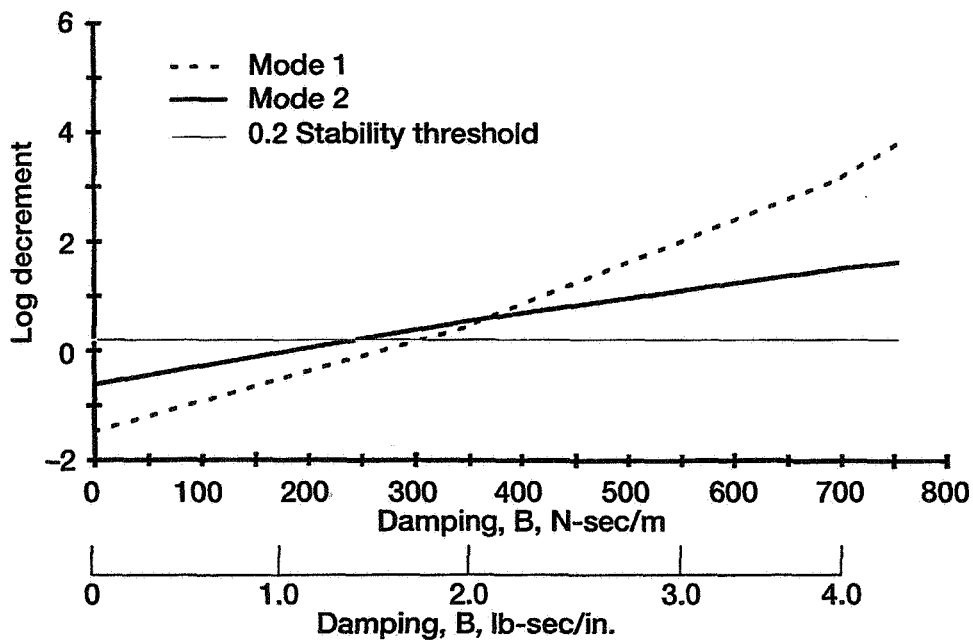
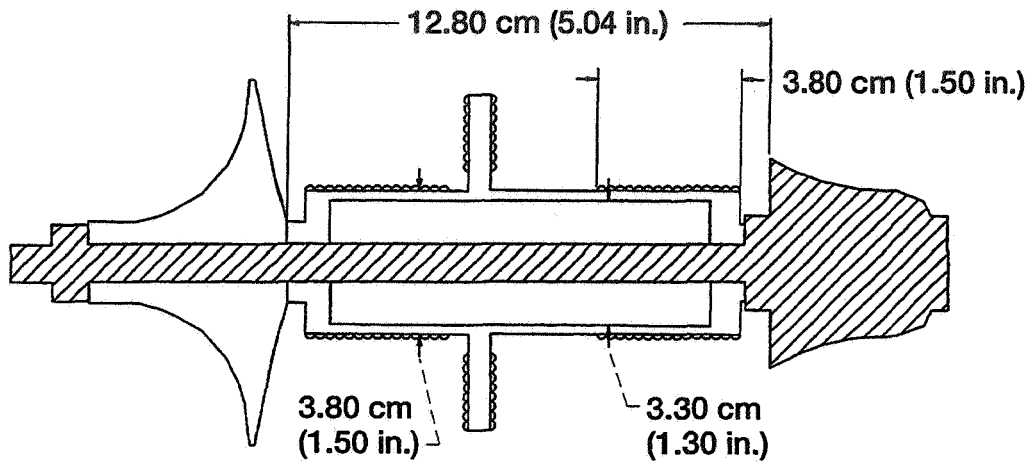


Fig. 10



## Large Rotor Configuration



Not to scale

Fig. 11

## Critical Speed vs. Bearing Stiffness for the Large Rotor ( $K_{xx} = K_{yy} = K$ , $K_{xy} = K_{yx} = 0$ )

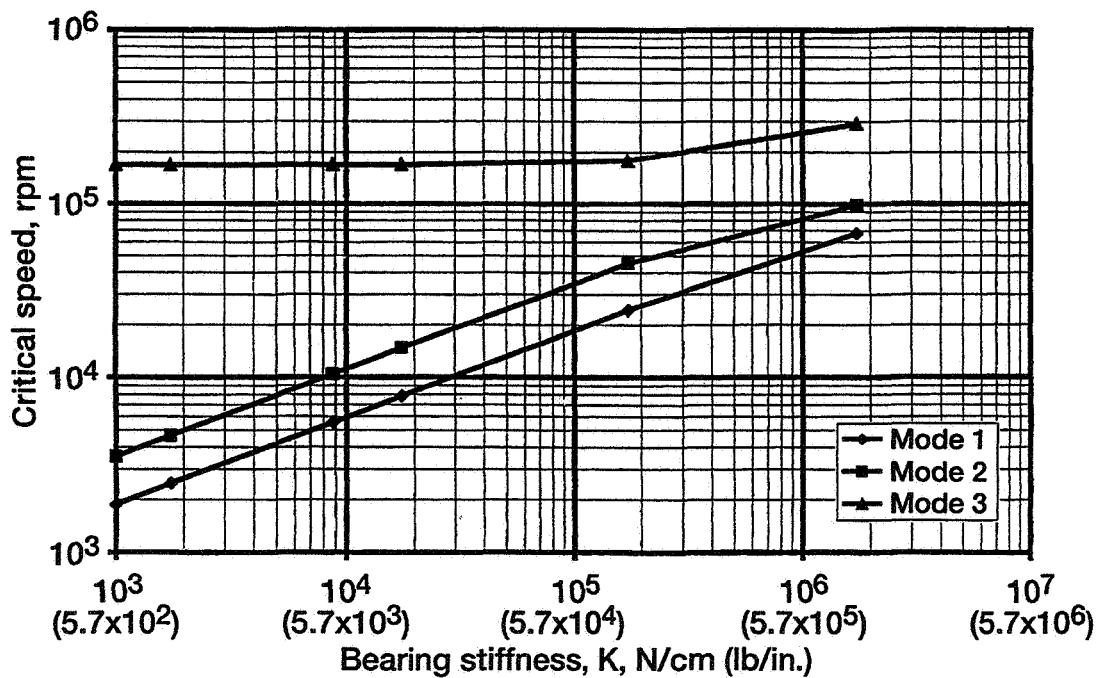


Fig. 12

## Log Decrement vs. Bearing Damping Coefficient for the Large Rotor ( $B_{xx} = B_{yy} = B$ , $B_{xy} = B_{yx} = 0$ )

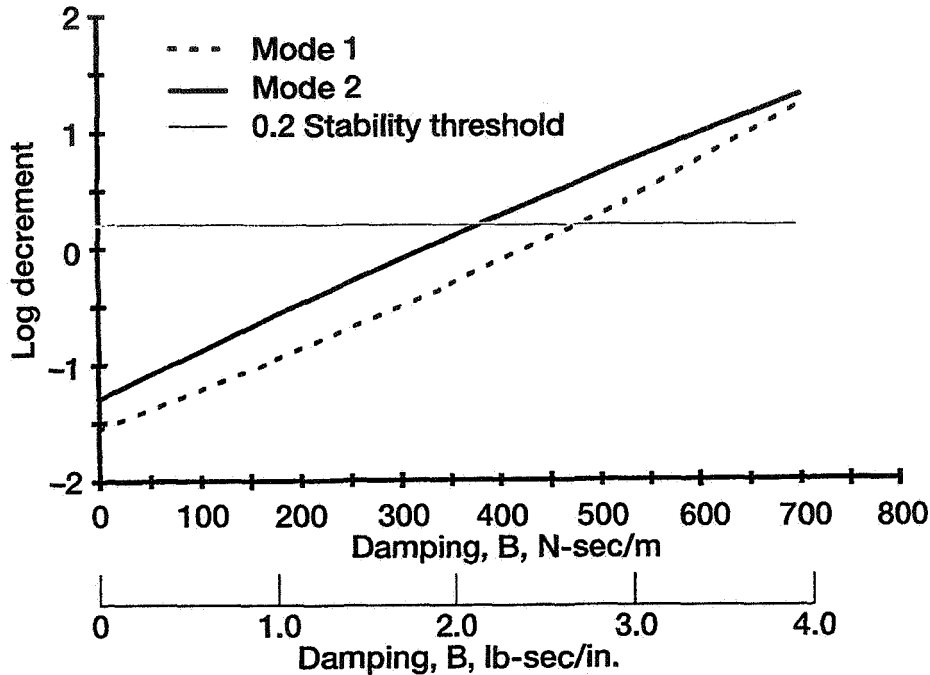


Fig. 13

## Summary of Results

- Two of the three rotor designs analyzed (the 2.54-cm (1.0-in.) and the 3.8-cm (1.5-in.) diameter shafts) have maximum stress levels sufficiently below the materials yield strength. The third (5.1-cm (2.0-in.)) shaft has maximum stress levels approximately equal to the material's yield strength; therefore, it is not analyzed any further.
- Both of the remaining rotor designs have ample load capacity to support the static load of the rotor. However, on the basis of an estimate of the maximum load capacity, the small rotor can only sustain a 6g dynamic loading, whereas the large rotor can sustain up to 11g.
- Both rotor/bearing systems are capable of stable operation. The small rotor bearings must supply 315 N-sec/m (1.8 lb-sec/in.) of damping to be stable, whereas the large rotor bearing must supply 482 N-sec/m (2.75 lb-sec/in.) of damping to be stable. Both are well below the expected maximum level of damping in these bearings of 2630 N-sec/m (15.0 lb-sec/in.).

Fig. 14

## Original Turbocharger Configuration

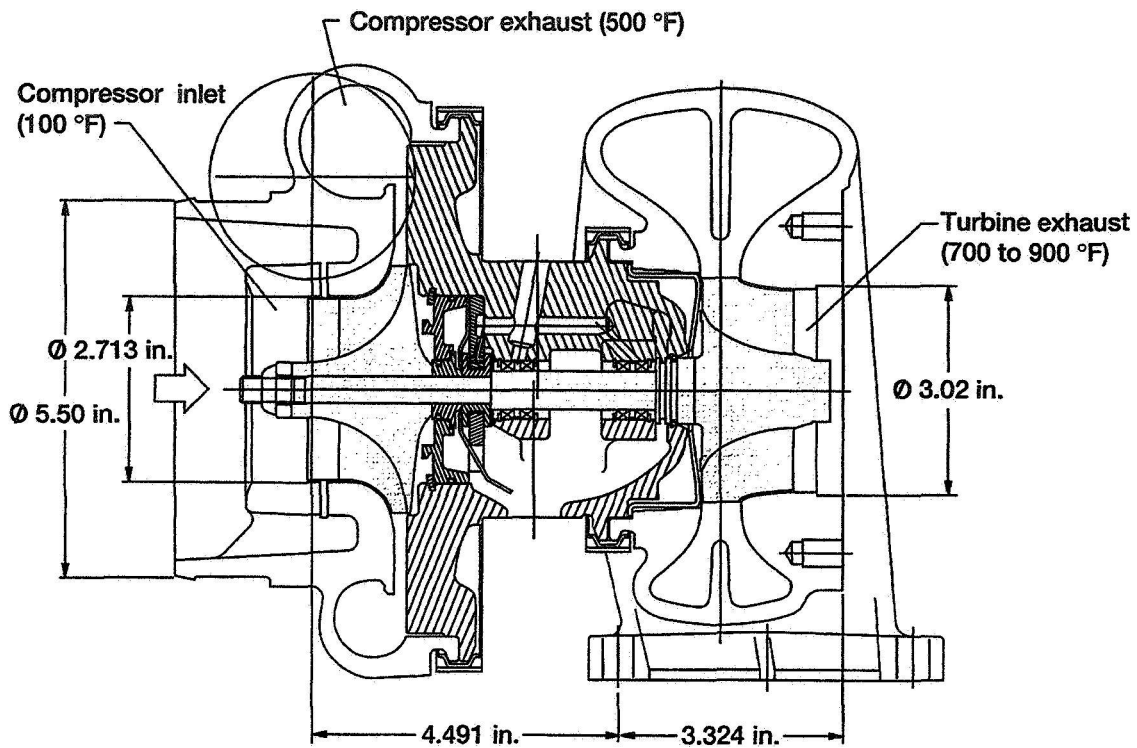


Fig. 15

## Proposed Turbocharger Configuration

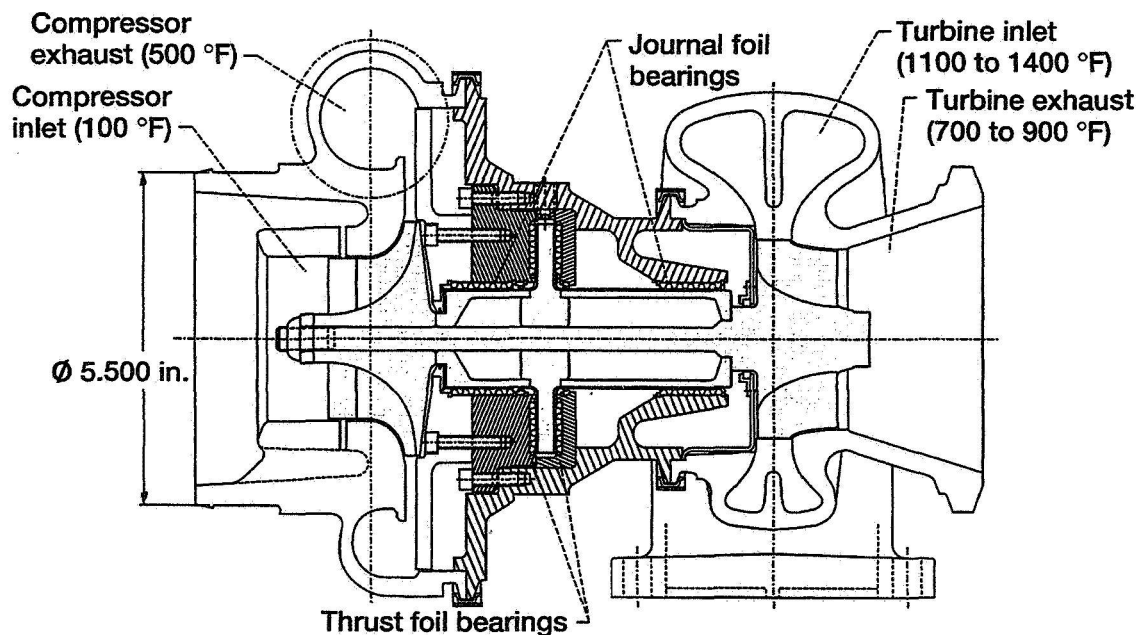


Fig. 16

## Conclusions

- Since the large rotor system is stable, and it can sustain more dynamic load than the small rotor, this is the chosen design.
- The feasibility of designing a diesel truck engine turbocharger utilizing air-lubricated foil bearings has been demonstrated.
- The success of this design indicates that foil bearings could offer an alternative for oil-lubricated bearings in many other similar applications as well.

Fig. 17

## Future Research

- The design resulting from this project will be built into a dummy turbocharger for testing.
- Once the testing of the dummy turbocharger is complete, a working turbocharger will be built and tested. This stage of the project is slated for September 1997.
- The final step will be to compare the test results of the oil-free turbocharger with similar results from an oil-lubricated turbocharger to determine the performance increases realized.

Fig. 18

517-37  
029118 C265E  
295569  
120.

# RECENT ADVANCES IN THE ANALYSIS OF SPIRAL BEVEL GEARS

ROBERT F. HANDSCHUH  
U.S. Army Research Laboratory  
NASA Lewis Research Center  
Cleveland, Ohio

## INTRODUCTION

Spiral bevel gears are currently used in all helicopter power transmission systems manufactured in the United States. These gears are required to transfer power from the horizontal engines to the vertical rotor shaft. Spiral bevel gears used in this capacity, are typically required to carry high loads and operate at very high rotational speeds. The requirements of a typical aerospace spiral bevel gear application is shown in figure (1) (Ref.[1]). When designers are faced with requirements outside of their experience, failures can occur or the resultant design will not be optimal. Therefore analytical tools that can enhance the design process are needed.

Over the last ten years many studies have been conducted on understanding, analyzing, and improving the surface geometry and meshing characteristics of spiral bevel gears (Refs.[2-3]). Research in this area requires understanding and kinematically representing the manufacturing process. The basic configuration of the machine for manufacture of spiral bevel gears is shown in figure (2).

Building on the very important fundamentals of gear manufacturing kinematics has permitted the extension of these techniques to produce 3-D finite element models (Ref.[4]). Utilizing this numerical technique has resulted in sophisticated analysis of these complex gears for thermal and structural / contact analysis (Refs.[5-8]).

The objective of this paper is to summarize the differential geometry approach to modeling the gear tooth surface geometry, document how three-dimensional models are developed, and provide examples using the finite element technique for solving thermal and structural/contact problems (figure (3)).

## GEAR GEOMETRY

The modeling of spiral bevel gears is dependent on the proper kinematic analysis of the manufacturing process. Many researchers have spent a great deal of time and effort to accurately describe the resultant surfaces generated in the manufacturing process. The first step is in formulating the so called "equation of meshing" (Ref.[3]). This equation states that the scalar product between the normal to the cutting (grinding) surface and gear being generated and the relative velocity between the cutter and gear being generated must equal zero at the specified location. Next, the basic gear design data to be analyzed must be given. This information includes the number of teeth of both members, the mean cone distance, spiral angle, shaft angle, and other basic data.

As part of the complex analysis of References [2,3], the shape and slope of the transmission error curve (the deviation from uniform motion), as shown in figure (4), and the contact between pinion and gear are input as desired quantities into the computer program. This analysis procedure is commonly known as Tooth Contact Analysis (TCA). Based on the input data, the machine tool settings are determined for the pinion and gear to accomplish the model requirements.

### **THREE-DIMENSIONAL FINITE ELEMENT MODEL DEVELOPMENT**

The next logical step beyond having the TCA description of the meshing gear system was to extend the information already determined by this analysis (machine settings for the pinion and gear) to calculate the gear tooth surface coordinates (Ref.[4]). The equation of meshing for one member, pinion or gear, is an equation with three variables. Two more equations are constructed by determining the radial and axial positions known to be on the active profile from the basic gear geometry (fig. 5). This set of 3 nonlinear algebraic equations are then solved by numerical methods simultaneously.

The procedure for fully describing the active profile of the concave and convex sides of the gear profiles is currently accomplished by choosing a grid of radial and axial positions and numerically solving for the actual coordinates in the coordinate system fixed to the pinion or gear under study. Utilizing this data and orienting the surfaces with the correct tooth thickness results in the model as shown in figure (6).

### **THERMAL AND STRUCTURAL/CONTACT ANALYSIS METHODOLOGY**

The procedure to conduct the thermal analysis using the finite element method will now be discussed. The overall flow chart to conduct the analysis is shown in figure (7). As shown in the flow chart, the basic design data is required to initiate the analysis. Based on this information, the manufacturing machine tool settings are determined and a tooth contact analysis performed. Several other analytical codes are then run to produce the finite element model and boundary conditions.

The procedure to conduct a full 3-D structural/contact analysis requires having at least several teeth from the pinion and gear, oriented such that the meshing process can be simulated. Contact algorithms have been developed without the use of gap elements and have permitted realistic analysis of contact for mismatched surfaces (figure(8)). Information to this level of detail has not been available with the current design standards. Many researchers and manufacturers may gain this type of information empirically using strain gages.

The geometric and resultant finite element modeling described herein were obtained using the program of Reference [9]. A nonlinear finite element analysis from Ref.[10] was used for the thermal and structural results reported. The basic model arrangement used for the results reported herein are given in figure (9).

### **EXAMPLE APPLICATIONS**

**Thermal Analysis:** Two different portions of the thermal analysis will now be described. First a grid point of the active profile (meshing surface) will be followed for several revolutions. This is shown in figure (10). The solution using the time and position varying boundary conditions is shown initiating from the time averaged boundary condition solution. This particular grid point was at a location on the active profile that received a large heat flux during meshing.

The other part of the solution to look at is the entire temperature field. The results are shown in figure (11) during the meshing (heat flux application) portion of the analysis. The maximum temperature for this time increment was approximately 200 degrees C. By looking at the entire temperature field for all the time increments for a revolution provides the analyst with the temperature variation as a function of angular position.

**Structural / Contact Analysis:** The structural / contact analysis will now be described (Ref.[7]). Three pinion teeth and four gear teeth were used to construct the model. The pinion was fixed at the locations shown in figure (12) and the gear was constrained from moving axially, but was allowed to rotate. The torque was input to the model via a force on the gear body at a known radial position. This caused the gear to rotate into the pinion and initiate the contact between the two members. For conditions representative of the full load conditions for this gear mesh resulted in the stress field shown in figure (13) for one of the gear teeth. The stresses plotted are the minimum principal. Note the concentration of stresses on the active profile showing the region of contact between the surfaces. Similar plots could have been produced to show the maximum bending in the fillet or some other region of concern.

Therefore the analysis procedures presented in this paper can provide detailed results of these complex gear members (figures (14) and (15)). Much work, however, still needs to be completed (figure (16)) and the proper validation with experiments are paramount to designers using advanced finite element tools.

## REFERENCES

1. Oswald, F.: Gear Tooth Stress Measurements on the UH-60A Helicopter Transmission. NASA TP-2698, 1987.
2. Litvin, F.: Theory of Gearing. NASA RP-1212, 1989.
3. Litvin, F.; and Zhang, Y.: Local Synthesis and Tooth Contact Analysis of Face-Milled Spiral Bevel Gears. NASA CR-4342, 1991.
3. Handschuh, R.; and Litvin, F.: A Method for Determining Spiral Bevel Gear Tooth Geometry for Finite Element Analysis. NASA TP-3096, Aug., 1991.
4. Handschuh, R.: Thermal Behavior of Spiral Bevel Gears. Ph.D. Dissertation, Case Western Reserve University, August, 1993.
5. Handschuh, R.; and Kicher, T.: Experimental and Analytical Assessment of the Thermal Behavior of Spiral Bevel Gears. 1996 AGMA Fall Technical Meeting, NASA TM-107009, ARL-CR-852.
6. Bibel, G.; Kumar, A.; and Reddy, S.: Contact Stress Analysis of Spiral Bevel Gears Using Nonlinear Finite Element Static Analysis. NASA TM-106176, ARL-TR-158, AIAA-93-2296, May, 1993.
7. Bibel, G.; Tiku, K.; and Kumar, A.: Prediction of Contact Path and Load Sharing in Spiral Bevel Gears. NASA CR-195305, ARL-CR-146, April, 1994.
8. Bibel, G.; Tiku, K.; Kumar, A.; and Handschuh, R.: Comparison of Gap Elements and Contact Algorithm for 3D Contact Analysis of Spiral Bevel Gears. NASA TM-106643, ARL-TR-478, 1994.
9. Bibel, G.; and Handschuh, R.: Meshing of a Spiral Bevel Gearset with 3D Finite Element Analysis, NASA TM-107336, ARL-TR-1224, October, 1996.
10. PATRAN Users Manual, PDA Engineering, Costa Mesa, California, 1991.
11. MARC K-5.1 User Manual, MARC Analysis Research Corporation, Palo Alto, California, 1981.

## Section View of UH-60A Helicopter Transmission

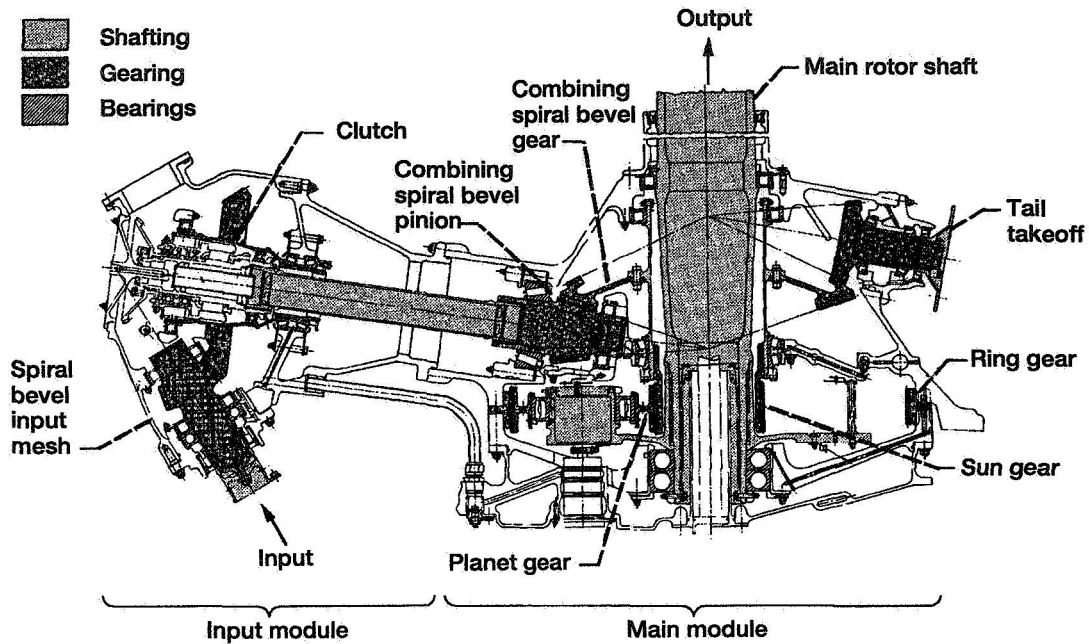


Fig. 1

CD-97-74367

## Orientation of Spiral Bevel Gear During Manufacture Relative to the Generating Machine

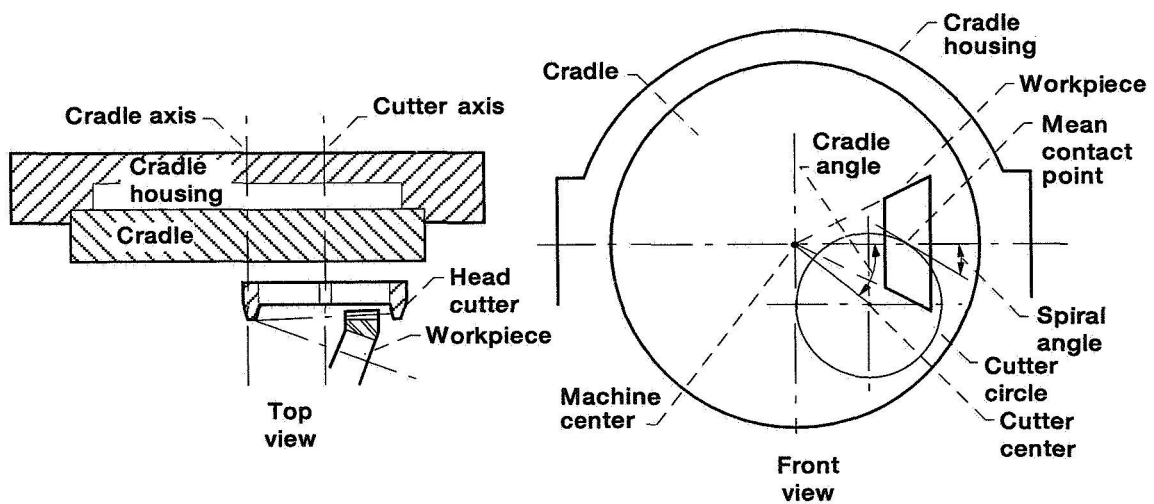


Fig. 2

CD-97-74368



## Objectives

- Use differential geometry approach to define the tooth surface geometry of spiral bevel gears
- Use geometric modeling program to build 3-D finite element models
- Develop required boundary conditions
- Conduct thermal and structural/contact analysis

Fig. 3

## Transmission Error Curve of the Preferred Type

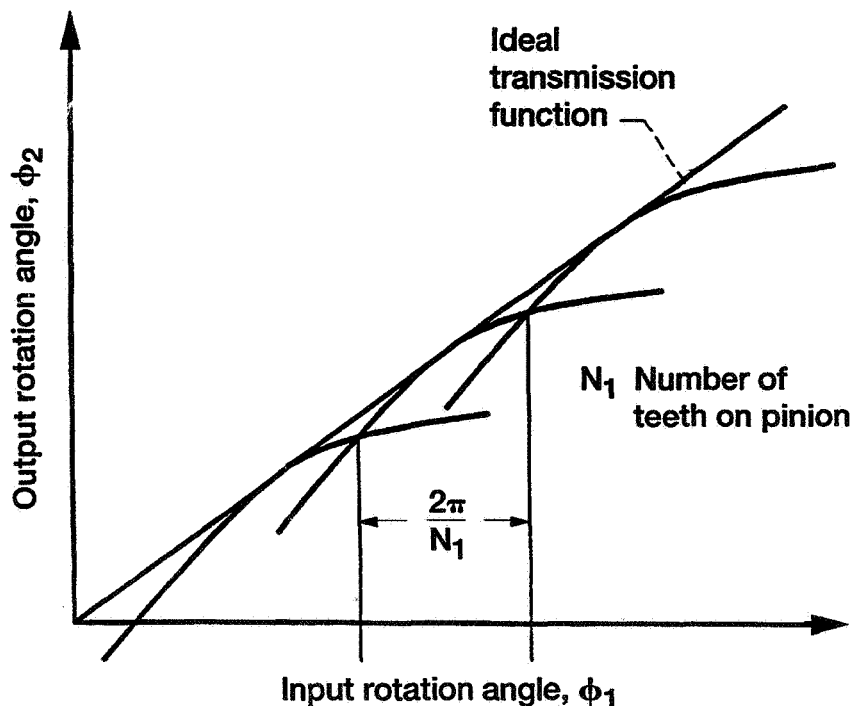


Fig. 4

CD-97-74369

## Orientation of Gear Design Requirements With Respect to the Gear Manufacturing Coordinate Systems

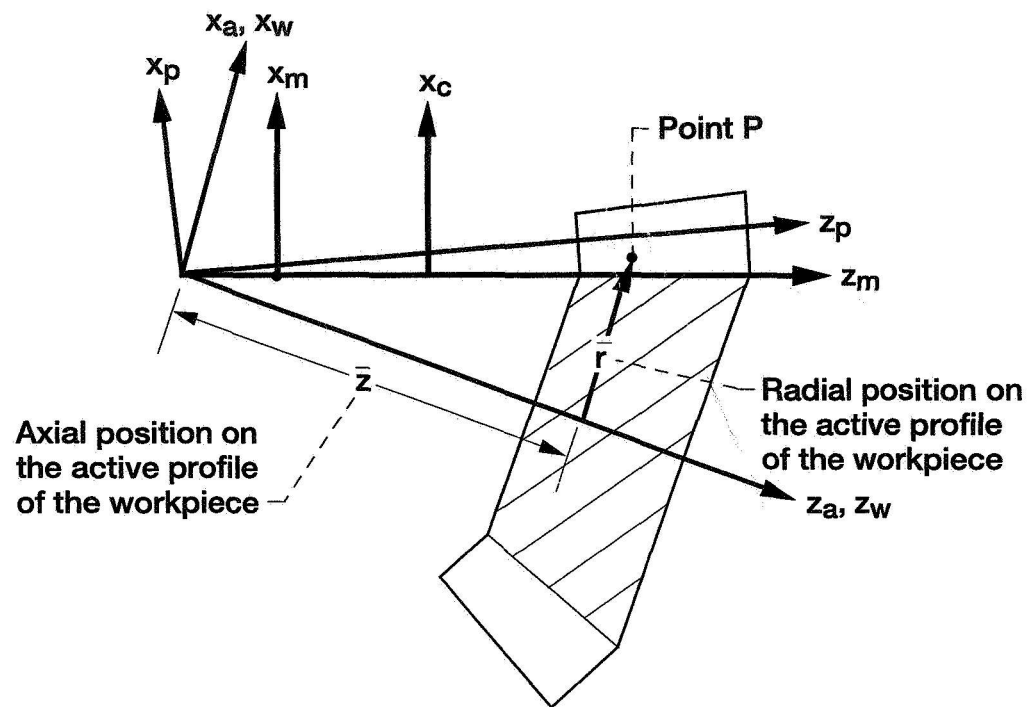


Fig. 5

CD-97-74370

## Finite Element Model

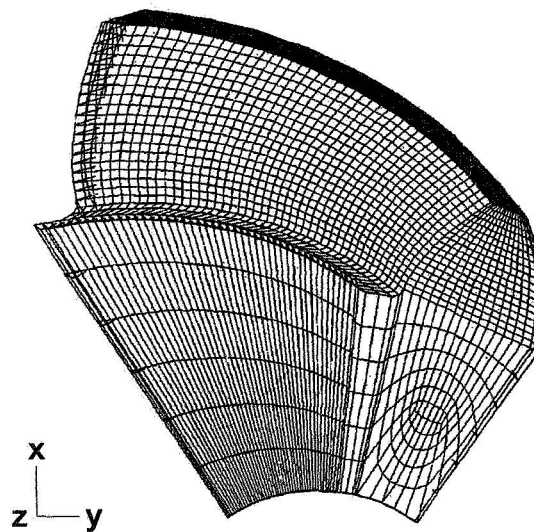


Fig. 6

CD-97-74372

## Flow Chart for the Thermal Analysis Procedure

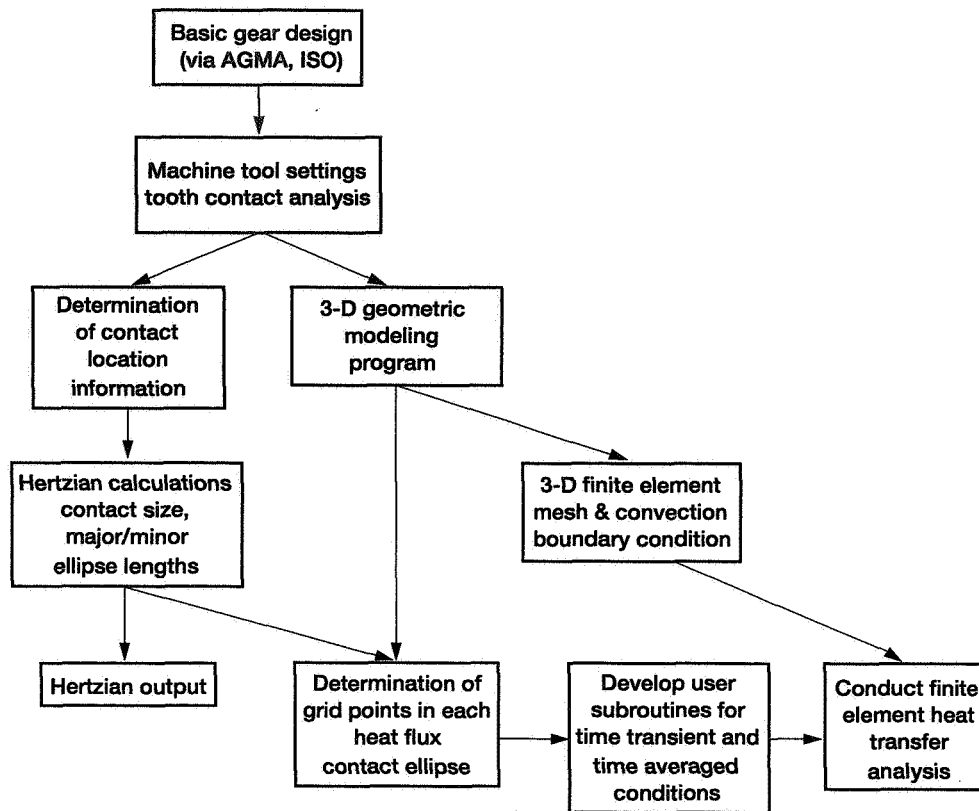


Fig. 7

CD-97-74373

## Contact Algorithm Used for the 3-D Structural Analysis

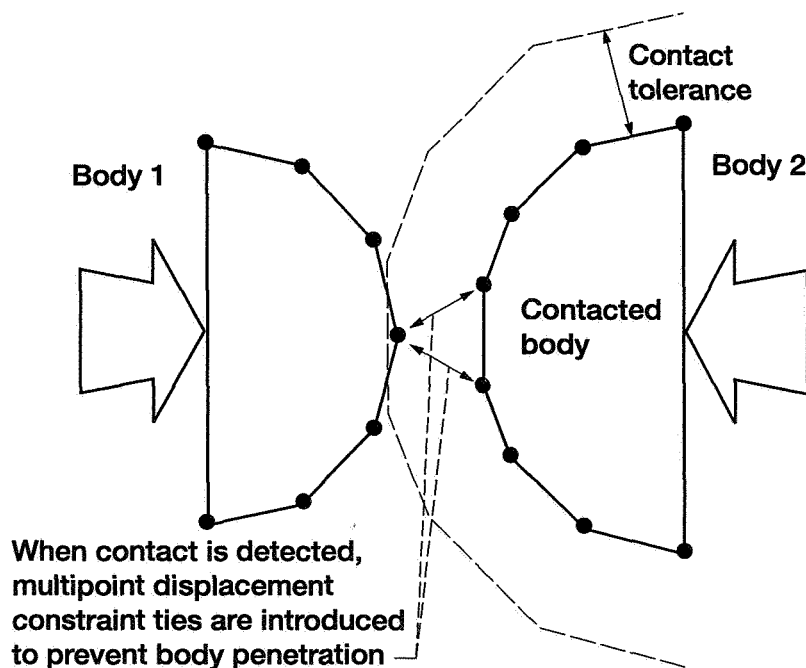


Fig. 8

CD-97-74374

## Pinion and Gear Design Data

	Pinion	Gear
Number of teeth pinion	12	36
Dedendum angle, deg	1.5666	3.8833
Addendum angle, deg	3.8833	1.5666
Pitch angle, deg	18.4333	71.566
Shaft angle, deg	90	
Mean spiral angle, deg	35	
Face width, mm (in.)	25.4 (1.0)	

Fig. 9

CD-97-74375

## Temperature Variation for an Active Profile Grid Point

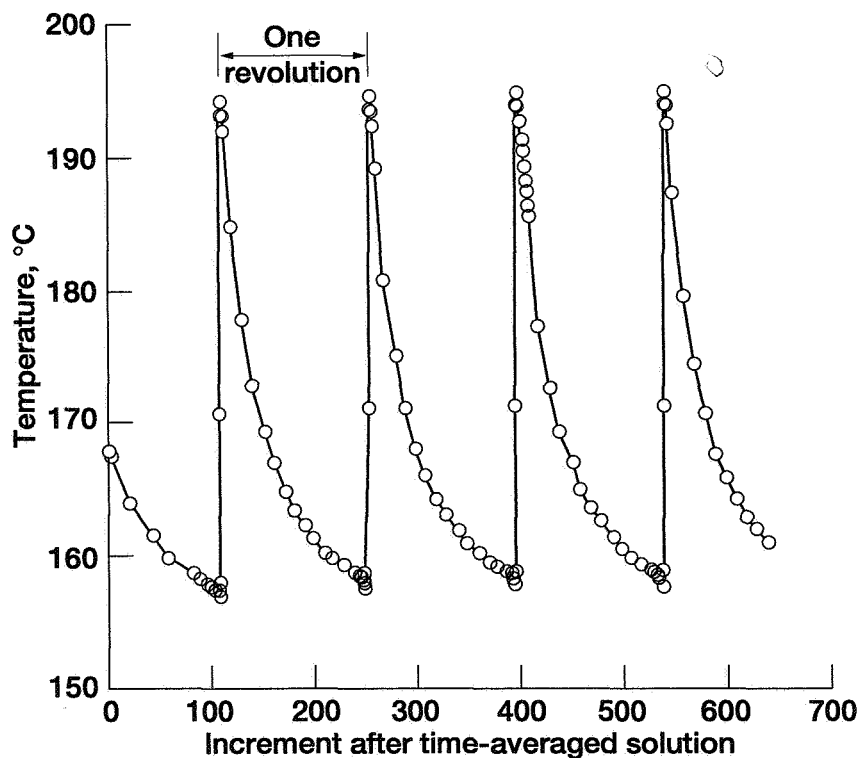


Fig. 10

CD-97-74376

## Temperature Variation Shown for the Entire Model During a Meshing Step

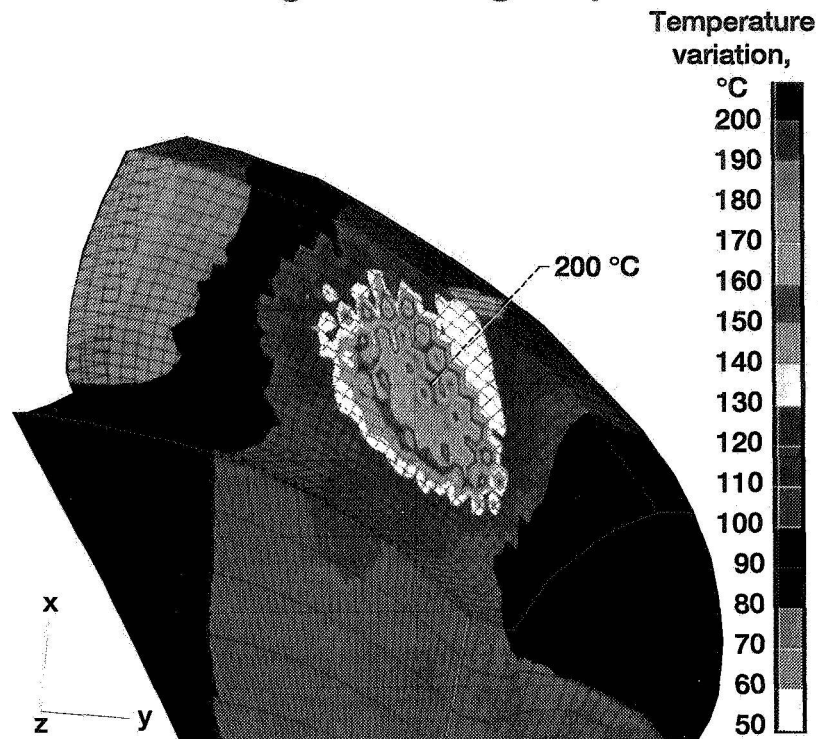


Fig. 11

CD-97-74377

## Model Used in the 3-D Structural Analysis

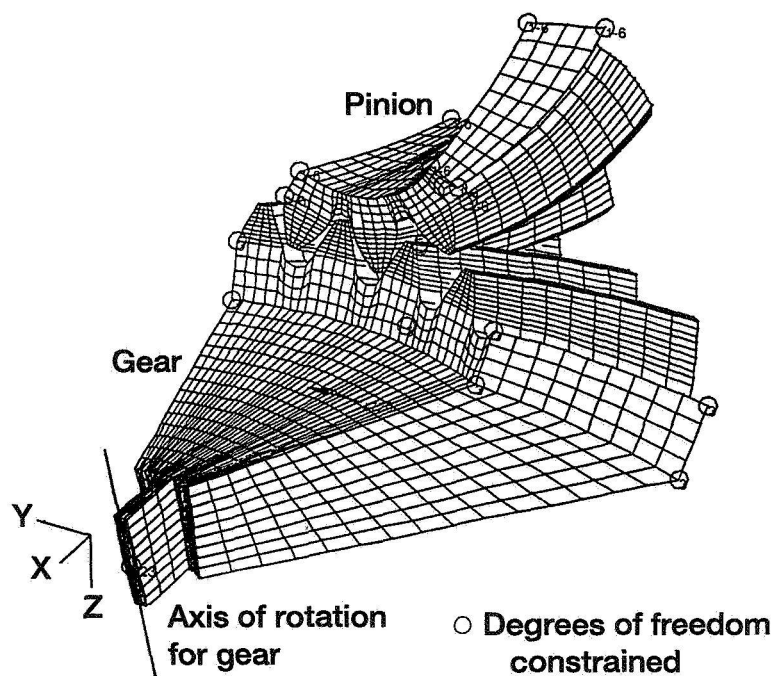


Fig. 12

CD-97-74378

## Gear Tooth Stress Field From the Structural Analysis

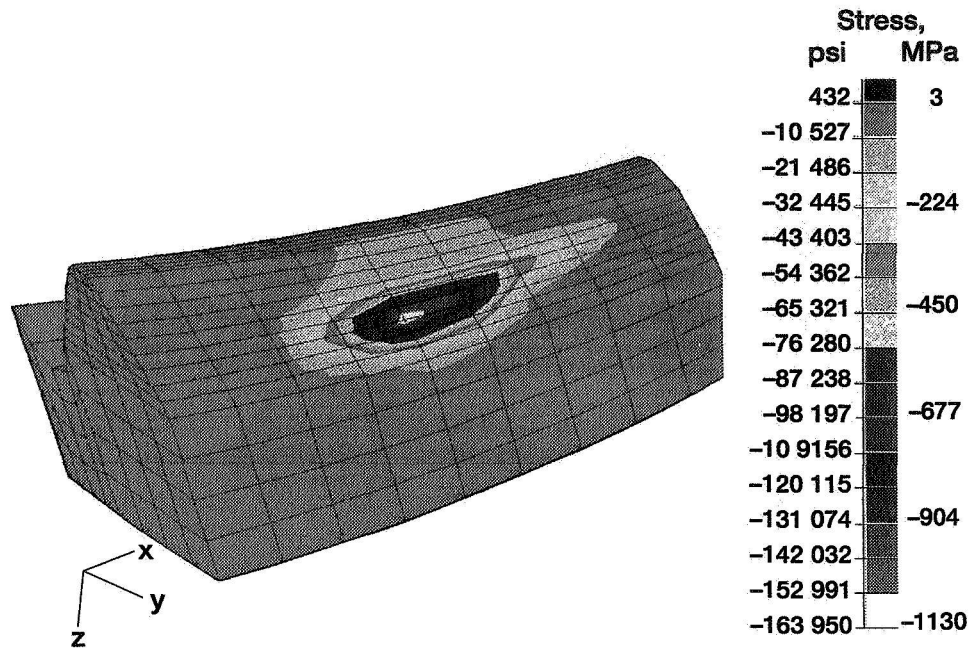


Fig. 13

CD-97-74379

## Summary of Results

- Complex 3-D modeling of spiral bevel gears is now possible
- Methodology to build finite element models has been developed
- Thermal and structural analyses have been successfully conducted

Fig. 14

## Conclusions

- Spiral bevel gear modeling using finite elements has been developed
- Thermal analysis has analytically predicted behavior as that found in experimental tests
- Structural/contact analyses have been successfully applied to in-house component and helicopter transmission test hardware

Fig. 15

## Focus of Future Research

- Work with present codes and finite element analysis to make them operational in workstation or PC environment
- Improve automation of finite element model development
- Continue validation with experiments and broaden data base of successful applications

Fig. 16

## APPENDIX—CONTENTS OF VOLUME I

### MATERIALS PROCESSING

Paper

The Effect of Hydrogen Annealing and Sulfur Content on the Oxidation Resistance of PWA 1480 James L. Smialek, NASA LeRC .....	1
Factors Influencing Residual Stresses in Yttria Stabilized Zirconia Thermal Barrier Coatings Roy T. R. McGrann, Edmund F. Rybicki, and John R. Shadley, The University of Tulsa; and William J. Brindley, NASA LeRC .....	2
In-situ Cure Monitoring of the Immidization of PMR-15 Sheryl Cossins, Jon J. Kellar, and Robb M. Winter, South Dakota School of Mines and Technology .....	3
Electron Beam Cured Epoxy Resin Composites for High Temperature Applications Christopher J. Janke, Oak Ridge National Laboratory; George F. Dorsey, Lockheed Martin Energy Systems, Inc.; Stephen J. Havens, Oak Ridge Institute for Science and Education; Vincent J. Lopata, Atomic Energy of Canada Ltd.—Whiteshell Laboratories; and Michael A. Meador, NASA LeRC ...	4
Joining of Silicon Carbide-Based Ceramics by Reaction Forming Method Mrityunjay Singh, NYMA, Inc.; and James D. Kiser, NASA LeRC .....	5

### MATERIALS CHARACTERISTICS

Thermodynamic Studies of High Temperature Materials via Knudsen Cell Mass Spectrometry Nathan S. Jacobson and Michael P. Brady, NASA LeRC .....	6
Mechanical Properties of Cu-Cr-Nb Alloys David L. Ellis, Case Western Reserve University .....	7
MoSi <sub>2</sub> -Base Composite for Engine Applications Mohan G. Hebsur, NYMA, Inc.; and Michael V. Nathal, NASA LeRC .....	8

### MATERIALS MODELING

Mechanical Characterization and Micromechanical Modeling of Woven Carbon/Copper Composites Brett A. Bednarczyk and Marek-Jerzy Pindera, University of Virginia; and David L. Ellis and Robert V. Miner, NASA LeRC .....	9
Computational Modeling Method for Superalloys Guillermo Bozzolo, OAI; and Ronald D. Noebe and John Gayda, NASA LeRC .....	10



## **LIFING MODELS (1)**

<b>Characterization of Damage Accumulation in a C/SiC Composite at Elevated Temperatures</b> Jack Telesman and Mike Verrilli, NASA LeRC; Louis Ghosn, Case Western Reserve University; and Pete Kantzos, Ohio Aerospace Institute .....	11
<b>Accelerated Testing Methodology for the Determination of Slow Crack Growth of Advanced Ceramics</b> Sung R. Choi, Cleveland State University; and Jonathan A. Salem and John P. Gyekenyesi, NASA LeRC .....	12
<b>Robust Integration Schemes for Generalized Viscoplasticity With Internal-State Variables</b> Atef F. Saleeb, W. Li, and Thomas E. Wilt, The University of Akron .....	13
<b>Parameter Estimation for Viscoplastic Material Modeling</b> Atef F. Saleeb, Atef S. Gendy, and Thomas E. Wilt, The University of Akron .....	14

## **LIFING MODELS (2)**

<b>A Viscoplastic Constitutive Theory for Monolithic Ceramic Materials—I</b> Lesley A. Janosik, NASA LeRC; and Stephen F. Duffy, Cleveland State University .....	15
<b>Creep Life Prediction of Ceramic Components Using the Finite Element Based Integrated Design Program (CARES/Creep)</b> Osama M. Jadaan, University of Wisconsin-Platteville; Lynn M. Powers, Case Western Reserve University; and John P. Gyekenyesi, NASA LeRC .....	16
<b>CARES/Life Software for Designing More Reliable Ceramic Parts</b> Noel N. Nemeth, NASA LeRC; Lynn M. Powers, Case Western University; and Eric H. Baker, Cleveland State University .....	17
<b>Fiber Contraction Approaches for Improving CMC Proportional Limit</b> James A. DiCarlo, NASA LeRC; and Hee Mann Yun, Cleveland State University .....	18
<b>Thermal Fatigue Limitations of Continuous Fiber Metal Matrix Composites</b> Gary R. Halford, NASA LeRC; and Vinod K. Arya, University of Akron .....	19

REPORT DOCUMENTATION PAGE			Form Approved OMB No. 0704-0188	
Public reporting burden for this collection of information is estimated to average 1 hour per response, including the time for reviewing instructions, searching existing data sources, gathering and maintaining the data needed, and completing and reviewing the collection of information. Send comments regarding this burden estimate or any other aspect of this collection of information, including suggestions for reducing this burden, to Washington Headquarters Services, Directorate for Information Operations and Reports, 1215 Jefferson Davis Highway, Suite 1204, Arlington, VA 22202-4302, and to the Office of Management and Budget, Paperwork Reduction Project (0704-0188), Washington, DC 20503.				
1. AGENCY USE ONLY (Leave blank)	2. REPORT DATE April 1997	3. REPORT TYPE AND DATES COVERED Conference Publication		
4. TITLE AND SUBTITLE  Physics & Process Modeling (PPM) and Other Propulsion R&T Volume II: Applied Life Models, Design, Vibration Control, Mechanical Components, Tribology		5. FUNDING NUMBERS  WU-523-22-13		
6. AUTHOR(S)				
7. PERFORMING ORGANIZATION NAME(S) AND ADDRESS(ES)  National Aeronautics and Space Administration Lewis Research Center Cleveland, Ohio 44135-3191		8. PERFORMING ORGANIZATION REPORT NUMBER  E-10644		
9. SPONSORING/MONITORING AGENCY NAME(S) AND ADDRESS(ES)  National Aeronautics and Space Administration Washington, D.C. 20546-0001		10. SPONSORING/MONITORING AGENCY REPORT NUMBER  NASA CP-10193		
11. SUPPLEMENTARY NOTES This is a compilation of 36 technical presentations from the PPM and Other Propulsion R&T in the format of extended abstracts followed by tables and figures. Volume I includes papers presented in the sessions on Materials Processing, Materials Characteristics, Materials Modeling, and Lifting Models. Volume II is a compilation of the papers presented at sessions on Applied Life Models, Design, Vibration Control; Mechanical Components, and Tribology. Responsible person, Doug Rohn, organization code 2200, (216) 433-3325.				
12a. DISTRIBUTION/AVAILABILITY STATEMENT  Unclassified - Unlimited Subject Categories 23, 39, and 37  This publication is available from the NASA Center for AeroSpace Information, (301) 621-0390.		12b. DISTRIBUTION CODE		
13. ABSTRACT (Maximum 200 words)  This CP contains the extended abstracts and presentation figures of 36 papers presented at the PPM and Other Propulsion R&T Conference held in Cleveland, Ohio, on May 1, 1997. The focus of the research described in these presentations is on materials and structures technologies that are parts of the various projects within the NASA Aeronautics Propulsion Systems Research and Technology Base Program. These projects include Physics and Process Modeling; Smart, Green Engine; Fast, Quiet Engine; High Temperature Engine Materials Program; and Hybrid Hypersonic Propulsion. Also presented were research results from the Rotorcraft Systems Program and work supported by the NASA Lewis Director's Discretionary Fund. Authors from NASA Lewis Research Center, industry, and universities conducted research in the following areas: material processing, material characterization, modeling, lifting, applied life models, design techniques, vibration control, mechanical components, and tribology. Key issues, research accomplishments, and future directions are summarized in this publication.				
14. SUBJECT TERMS  Processing; Modeling; Alloys; Composites; Ceramic matrix; Gears; Bearings; Optimization; Tribology			15. NUMBER OF PAGES 188	
			16. PRICE CODE A09	
17. SECURITY CLASSIFICATION OF REPORT Unclassified	18. SECURITY CLASSIFICATION OF THIS PAGE Unclassified	19. SECURITY CLASSIFICATION OF ABSTRACT Unclassified	20. LIMITATION OF ABSTRACT	